An STM Study of C_{60} Molecule on Au(111): Close-Packed Single Layer and Magic Number Clusters

By Yangchun Xie

A thesis submitted to
The University of Birmingham
for the degree of
DOCTOR OF PHILOSPHY

Nanoscale Physics Research Laboratory
School of Physics and Astronomy
The University of Birmingham
September, 2013

Abstract

This thesis includes the results of the investigation of the C_{60} layer on Au(111), and the self-assembled C_{60}/Au complex supported on Au(111) by Scanning Tunnelling Microscopy.

The characteristics of the close packed C_{60} layer on metallic surfaces indicate a complex bonding geometry of the molecules with the surfaces, where the mechanisms behind various observations remain to be uncovered. The interfacial interaction of the C_{60} layer on the Au(111) substrate under ultra high vacuum conditions is investigated. The symmetry and lattice mismatch of the C_{60} layer and the Au crystalline substrate leads to the formation of three phases of the molecular layer, with brightness contrast among the C_{60} molecules. The epitaxial configuration of the molecules on the substrate is analyzed from a geometric point of view. And the interfacial diffusion and nucleation of Au atoms deposited on the C_{60} layer covered Au(111) sample, reveals the bonding difference between the dim and the normal (also named bright) C_{60} molecules. We also propose that the C_{60} layer can be used as a mask to guide the structures of Au islands nucleated at the interface between the C_{60} overlayer and the metallic substrate.

Self-assembly of molecules on well-defined surfaces is a promising route to producing functional structures with nanoscale dimensions. Taking advantage of this approach, we obtained C_{60}/Au clusters with specific size, shape, and organization of nanostructures, based on both the van der Waals interaction between C_{60} molecules and the interaction between the molecule and the Au atoms through charge transfer. The structural models for the C_{60}/Au clusters observed are presented, based on knowledge about the C_{60} molecules on the Au(111) surface. The Au(111) substrate with the $22\times\sqrt{3}$ reconstruction acts as a template to regulate the growth of the cluster, and plays a vital role in the size distribution and in the thermal stability of the clusters.

To My Parents and My Younger Brother

Acknowledgement

During my journey in obtaining my PhD, I have got a lot of support and encouragement from many people including my supervisor, my friends, and colleagues. At the beginning of this thesis, I would like to thank all these people who contributed in many ways to the success of this study.

First and foremost, I would like to express my sincere gratitude to my supervisor Dr. Quanmin Guo for providing guidance, support and encouragement during my PhD study and research. Under his supervision, I successfully overcame the difficulties met in experiments and learned a lot. He used to review my thesis progress, give suggestions and made corrections. I gratefully acknowledge Prof. Richard Palmer, head of the NPRL group and also my co-supervisor, for his support and guidance during the past four years.

My sincere thanks also go to Dr Lin Tang for providing me experimental hands-on training on the operation of STM, and Dr Fangsen Li who devoted much time in giving guidance to me at the beginning of my PhD study. I thank my fellow labmates in NPRL: Dr Tianluo Pan and the PhD student Scott Holmes for motivating discussion during experiments. I thank all the present members of the NPRL group. The NPRL group is a source of friendships as well as good advice and collaboration.

Besides, I would like to thank Clive Weston, my friend also my landlord, and his wife Margaret Weston. Clive gave me valuable suggestions concerning the English of my PhD thesis as well as my Mphil report. The Weston couple also provide me a comfortable home during my PhD life.

I take this opportunity to acknowledge the Midlands Physics Alliance Graduate School (MPAGS) for their funding for my PhD study in University of Birmingham. And I also acknowledge the Engineering and Physical Sciences Research Council (EPRC), UK for their financial assistance for my scientific researches.

My time at Birmingham was made enjoyable in part due to my friends that became a part of my life. I am grateful for time spent with roommates and friends, and for their valuable help during my difficult time.

Lastly, I would like to thank my family for their love, encouragement and support throughout my life. My parents Jianjun Xie and Junting Yang support me in all my pursuits, and my younger brother Jianzhou Xie can always cheer me up during the time when I felt down. I owe everything to them.

List of Publications

Yangchun Xie, Lin Tang, and Quanmin Guo, *Cooperative Assembly of Magic Number C_{60}-Au Complexes,* Phys. Rev. Lett. 111, 186101 (2013)

Yangchun Xie, Lin Tang, and Quanmin Guo, *Underlayer Growth of a Nanoporous Single Atomic Layer of Gold,* J. Phys. Chem. C 116, 5103 (2012)

Lin Tang, **Yangchun Xie**, and Quanmin Guo, *Complex Orientational Ordering of C60 Molecules on Au(111),* J. Chem. Phys. 135, 114702 (2011)

Lin Tang, **Yangchun Xie**, and Quanmin Guo, *Probing the Buried C60/Au(111) Interface with Atoms,* J. Chem. Phys. 136, 214706 (2012)

Contents

Chapter 1. Introduction **1**

References **8**

Chapter 2. Literature Review **11**

2.1 Scanning Tunnelling Microscopy **11**

2.1.1 Electron Tunnelling 11

2.1.2 STM Atomic Resolution 16

2.1.3 General Application of STM 19

2.2 The Au Atoms and Surfaces **23**

2.2.1 The Features of the Au(111) Surface 24

2.2.2 Atomic Steps 38

2.2.3 Au(111) Supported Metal Nanostructures 43

2.2.4 Au_n Cluster: Structure and Catalytic Property 47

2.3 Pt Oxide **51**

2.4 The C_{60} Molecule **54**

2.4.1 C_{60} Molecule: Synthesis and General Properties 54

2.4.2 C_{60} Molecule on the (111) Surfaces of Noble Metals 63

2.4.2.1 C_{60} Molecules on the Au(111) Surface 63

2.4.2.2 C_{60} Molecules on Cu(111) and Ag(111) 72

2.4.3 C_{60} Molecule and Related 2D Molecular Assemblies 75

Reference **82**

Chapter 3. Experimental Techniques and Methodology **98**

3.1 The Ultra-High Vacuum **98**

3.1.1 The Definition of Ultra-High Vacuum 98

3.1.2 Attaining UHV 99

3.1.3 Venting and Baking 100

3.1.4 The Leakage Detection 102

3.2 Tip Treatment **102**

3.2.1 Tungsten Tip – Electrochemical Etching 103

3.2.2 Tip Treatment – High Temperature Annealing 105

3.3 Sample Preparation **107**

3.3.1 The Preparation of the Clean Au(111) Surface 107

3.3.2 Au Atom and C_{60} Molecule Deposition 110

3.4 The VT and LT STM System **110**

3.4.1 The Features of the VT STM 112
3.4.2 The Features of the LT STM 117
References 118

Chapter 4. Probing the C_{60}/Au(111) Interface with Au Atoms 119
4.1 C_{60} Monolayer on the Au(111) Surface 119
4.1.1 The Phases of C_{60} Layer on Au(111) 121
4.1.2 The Periodic Phases 125
4.1.3 Au Atom Diffusion on C_{60}/Au(111) Substrate at Room Temperature 132
4.2 Au Island Sandwiched at the Interface of C_{60}/Au(111) at Low Temperature 138
4.2.1 The Au Islands beneath the C_{60} Overlayer in the R30° Disordered Phase 139
4.2.2 The Au Islands beneath the C_{60} Overlayer in the R0° Uniform Phase 143
4.3 Electron Irradiation of C_{60} Molecule in Monolayer on Au(111) 154
References 161

Chapter 5. Self-Defined $(C_{60})_m(Au)_n$ Nanoclusters 163
5.1 The Fabrication Process 163
5.1.1 The In-Situ Deposition of C_{60} Molecules and Au Atoms 163
5.1.2 The Formation of the C_{60}/Au Nanocluster 165
5.2 The C_{60}/Au Nanocluster at Room Temperature 170
5.2.1 Close-Shell Structure of $(C_{60})_7(Au)_{19}$ 170
5.2.2 Large C_{60}/Au Clusters 176
5.2.3 Relocation of C_{60}/Au Clusters 181
5.3 Structure Evolution of the $(C_{60})_m(Au)_n$ Clusters at Elevated Temperatures ... 184
5.3.1 Vanishing of the Open Structure 184
5.3.2 Structure Reorganization from Unstable to Stable during Annealing 186
5.4 The Importance of the Template – the Au(111) Substrate 192
5.4.1 Role in the Size Distribution of the Clusters 193
5.4.2 Role in the Stability of the Clusters 195
5.5 Other Self-Defined Structures 200
References 203

Chapter 6: Summary and Future Work 204
6.1 Summary 204
6.2 Future Plan 206
References 207

Appendix 208

I. Formation of Pt Oxide on Au(111): A Low Oxygen Pressure STM Study 208
I.1 Oxygen Dosing through A Hot Pt Tube on Au(111) 208
I.2 The Pt Oxide on Au(111) 209
II. Abbreviations 213
III. The Commensurability of the C_{60} Single Layer on Au(111) 214
References 227

Chapter 1: Introduction

With the invention of the Scanning Tunneling Microscope (STM) by Binning and Rohrer [1, 2] in 1982, surface science steps closer to the world of atoms. With the development of this surface sensitive technique, the function of the STM is not confined to imaging surfaces. People came to be amazed at the ability of the STM to manipulate atoms one by one, as has been demonstrated by Eigler and Schweizer [3]. They managed to write the IBM logo using Xe atoms on the surface of a nickel single crystal at 4 K [3]. And recently a nanoscale "car" assembled from molecules with functional units has been driven by a STM tip on the Cu(111) surface [4]. Through years of experimental practice and exploration, STM has proven itself as the backbone of surface science techniques to study the structural, chemical, electronic, and optical properties of surfaces and surficial nanostructures [5].

The work presented in this thesis is done using both variable temperature ultra-high vacuum STM (VT UHV STM), low temperature ultra-high vacuum STM (LT UHV STM), and the technique of physical vapour deposition. The subjects of the study are the interface interaction of C_{60} thin films on Au(111) using Au atoms as a probe, and the self-assembled nanostructures of C_{60} molecules and clusters of Au atoms.

The inertness of the Au surface makes it an ideal candidate for this study provided that the substrate surface stays free of oxidization and contamination for a long time in the UHV chamber. The Au(111) surface has been widely used in the study of nano-assemblies [6], multilayer alloys [7, 8, 9], catalysis[10] and so on. As observed by the STM, the clean Au(111) surface has a unique herringbone

reconstruction with a unit cell $22\times\sqrt{3}$ by uniaxial contraction of the top atomic layer [11]. When adsorbates cover the Au(111) surface, the reconstructed surface can either change to the unconstructed (1×1) structure via relaxation of the compressed top layer (the (111) surface of the FCC crystals exhibiting a hexagonal unit cell) or have an even larger atomic density, i.e., further compression of the top layer of the $22\times\sqrt{3}$ reconstructed Au(111) [8, 9, 12]. The structural transformation of the reconstruction pattern reflects changes in the long-range strain field [13]. The divergence of the two opposite changes of the reconstructed clean Au(111) surface comes from the different electronegativity of the adsorbates. The adsorbates which are more electronegative than Au obtain electron charges from the Au(111) substrate, and this helps to relieve the stress in the top Au(111) layer, i.e., lifting of the herringbone reconstruction [14]. By contrast, charge transfer from the adsorbates to the Au(111) increases the strain in the top layer and leads to the further compression of the surface Au atoms [9]. The herringbone structure can be preserved if adsorbates are weakly bound with the Au(111) surface, e.g. the self-assembled monolayer (SAM) of many organic molecules [15].

One important application of the Au(111) surface is using it as a template to grow ordered arrays of molecules or clusters [16]. The molecules or clusters are always trapped at the elbow sites, where surface dislocations are present, of the herringbone structure.

The Fullerene molecules, especially the C_{60} molecule, are of great scientific research interest for both their chemical and physical properties with applications that span novel material engineering, energy storage, and electronics. The knowledge of the C_{60} structure and the mechanism for its formation is now quite complete [17] since the first spectroscopic proof for its existence in 1943 [18] and

the achievement of C_{60} massive production in optimized conditions in 1985 [19]. The electronic properties and physical structures of the C_{60} molecule in the form of individual molecule, or close packed film or bulk have been extensively studied by surface-sensitive experimental techniques [17, 20] and theoretical calculations [21, 22]. Each carbon atom is connected with three other carbon atoms by two single bonds (bond length ~ 1.45 Å) along the sides of pentagon carbon rings and one double bond (bond length ~ 1.40 Å) shared by two hexagonal carbon rings with equal chemical reactivity [23]. The band gap of a free C_{60} molecule between the highest occupied molecular orbital (HOMO) and the lowest unoccupied molecular orbital (LUMO) is about 1.5 eV, and the ionization potential is 7.6 eV and the electron affinity 2.65 eV [17].

One of the major research subjects concerning C_{60} in surface science is the interface interaction of the C_{60} layer with various substrates. STM is of particular importance in the characterization of the film growth features of C_{60} on surfaces, especially the (111) surface of the noble metals (Cu, Ag, and Au). Temperature programmed desorption experiments show that the order of the binding energy of C_{60} single layer to the (111) surface of the three noble metals, from strongest to weakest is Cu, Ag, and Au [17, 24]. C_{60} molecules readily form close packed layers on the (111) surfaces of noble metals, grown out from step edges.

The C_{60} single layer on Au(111) takes on different phases [25] with a dim and bright contrast among the C_{60} molecules in STM images, which is also observed for the C_{60} layer on the (111) surface of Cu, Ag, Pt etc [26, 27]. According to the distributions of the dim C_{60} molecules in the close packed layer, the phases are classified into three categories, namely the uniform phase, the disordered phase, and the periodic phase. Each phase is associated with superstructures defined by

the relation between the overlayer lattice to the crystalline substrate lattice. The uniform phase is assigned the 38 × 38-R0° superstructure, and the disordered phase the $2\sqrt{3} \times 2\sqrt{3}$-R30° superstructure, which corresponds to a commensurate epitaxy C_{60} layer on Au(111), where every overlayer lattice point is in coincidence with a substrate lattice point [14, 24, 28]. The superstructures for the periodic phases are not single option due to the complex distributions of the dim C_{60} molecules [25]. In the periodic phases, the dim-molecule overstructures are rotated to the molecular layer, and have different periodicities concerning the arrangement of the dim molecules [25].

The understanding of an interface is the first step towards design of new interfaces in nanoscale systems, which is critical for the fabrication of functional electronic devices. The final observed epitaxial molecular layers on substrates result from the delicate balance of the overlayer-substrate interface energy, the energy of the molecules within the overlayer, and the lattice registry between the two interacting layers [28]. If the interaction between the molecules of the overlayer to the substrate is much larger than that among the molecules within the overlayer, a commensurate overlayer forms at the expense of close packing within the molecular overlayer [28]. One example is the self-assembled monolayers (SAMs) of alkanthiols on Au(111), where the alkanthiols strongly adsorb on the Au(111) substrate through the S-Au chemical bond. If the intramolecular bonding is much stronger than the interlayers interaction, the overlayer will conserve its native structure [28].

Due to the large size difference between the C_{60} molecule and the metal atom, and the strong intralayer bonding (the Van der Waals force) within the C_{60} layer, incommensurate growth is common for a C_{60} overlayer on metallic surfaces [24],

and such growth is always accompanied by a change of strain at the interface, e.g., the lifting of the herringbone reconstruction of Au(111). The adsorption of C_{60} molecules on metal surfaces, e.g., Au, Ag and Pt, can sometimes induce the reconstruction of the metal surfaces, with the formation of atomic pits, where metallic atoms are missing from the close-packed surface [29, 30]. The adsorption site of the dim C_{60} molecules is considered to be over the nanopit [25]. And thus the dim C_{60} molecules bind more strongly than other C_{60} molecules do, which can be reflected from the diffusion and nucleation of Au atoms at the interface of the C_{60} overlayer on Au(111) with dim and bright contrast among the molecules. The nature of the interface formed upon physical or chemical adsorption on the substrate greatly influences the properties of the overlayer, e.g. its order and stability. Therefore, part of this thesis concentrates on the question of what the interface between the C_{60} overlayer and the Au(111) looks like.

Another research subject during my PhD study is about the self assembled nanostructures. The study of the properties of the self-assembled monolayer is an active research field because of its ease of fabrication, the diversity of the possible structures of the SAM with specific functionalities and potential applications, in the areas of electronics, catalysis, optics and so on [16, 31, 32]. The linkages that connect the molecules within the extended networks of SAM are usually hydrogen bonding [33, 34] and metal-ligand bonding [35, 36], which all are directional bondings. The improvement of the spatial order in nanostructure growth is one topic under intensive study via the choice of molecules with different functional groups [16].

A second way to regulate molecules is through their interactions with substrates, especially when the substrates have periodic structures through reconstruction.

The surface defects of the reconstruction are usually where the molecules can be trapped, as in the growth of ordered arrays of metal clusters on Au(111) with the herringbone reconstruction [37, 38] as the template. We also take advantage of the Au(111) herringbone reconstruction to grow self-assembled C_{60}/Au clusters, where no directional bond is needed to form structures with well-defined size and shape.

The thesis is constructed as follows.

Chapter 2 is the literature review. The Au(111) surface is used as the template in my study. The (111) surface of gold in the FCC bulk structure has the lowest surface energy compared with other surfaces, and on the basis of STM studies with atomic resolution, its characteristics especially the herringbone reconstruction are described in detail. Theoretical simulations provide more information concerning the energies and forces behind the reconstruction based on empirical observations. The Au(111) surface supported growth or adsorption is another area under intense investigation, which is vital for the application potentials of Au in the development of nanoscience and nanotechnology. The lowest-energy structures and electronic properties of small Au clusters (Au_n, $n \leq 20$ integer) in the gas phase are also included in the review as Au clusters are the stable cores in the fabrication of the self-assembled C_{60}/Au clusters in my experiments, whose geometry decides the electron distribution, and the electronic density of states, and thus their stability.

The properties of the C_{60} molecule are introduced in the subjects regarding its physical and electronic structures, thin film growth on metallic substrates and C_{60} related nanostructures. Theoretical models provide complementary insights into

the interpretation and prediction of the intramolecular interaction and the interlayer interaction with metallic substrate, as well as band structures.

Chapter 3 introduces the techniques, deposition methods and operation practice used in the experiments. The features of the two systems – the variable temperature (VT) STM and the low temperature (LT) STM are presented, which are designed respectively for the demand of different experiments. Experiments were carried out at temperature ranging from 77 K to about 410 K. All the samples were kept in an ultra high vacuum.

Chapter 4 and chapter 5 deliver the experimental results. Chapter 4 is about the study of the interfacial interaction between the close-packed C_{60} layer and the Au(111) surface through the diffusion of Au atoms at various substrate temperatures. Different phases of the C_{60} overlayer are also observed. The emphasis is on the periodic phases, as for C_{60} domains more than one periodicity of the superstructures formed by dim C_{60} molecules exists. The diffusion of Au atoms at the interface between the C_{60} overlayer and the Au(111) substrate reveals the different bonding strength between the dim C_{60} molecule and the normal C_{60} molecule. And the Au islands nucleated at the interface imply complex modes of overlayer growth, where the surface strain needs taking into consideration.

Chapter 5 is about the self- assembled C_{60}/Au clusters on the Au(111) template. The first step for assembling the bi-component clusters took place at low temperature about 110 K following sequential deposition of Au atoms and C_{60} molecules. Then the introduction of a slow annealing process from 110 K to room temperature promotes the ripening process of the clusters and results in the population of one type of C_{60}/Au clusters of particular size, shape and composition due to the thermodynamic balance of binding energy and strength. The structure

of this cluster is interpreted, based on existing knowledge of the physical dimensions of the molecule and the atom as well as the optimized bonding lengths of C_{60}-C_{60}, Au-Au and C_{60}-Au. Other minor structures of the clusters are also discussed. The thermal stability of the clusters was studied with in-situ annealing and the structure evolution was followed by STM.

The importance of the Au(111) surface is that it acts like a template during the whole fabrication process, when the elbow sites anchor the clusters at low temperatures and regulate the changes of the size and shape of the clusters during the annealing process from low temperature to room temperature.

The final chapter gives a summary of the results already obtained, and a future plan.

References

[1] G. Binning and H. Rohrer, C. Gerber, and E. Weibel, Surface Studies by Scanning Tunneling Microscopy. Phys. Rev. Lett. **49**, 57 (1982).
[2] G. Binning and H. Rohrer. In touch with Atoms. Rev. Mod. Phys. **71**, S324 (1999).
[3] D. M. Eigler and E. K. Schweizer. Positioning Single Atoms with A Scanning Tunneling Microscope. Nature **344**, 524 (1990).
[4] T. Kudernac, N. Ruangsupapichat, M. Parschau, B. Maciá, N. Katsonis, S. R. Harutyunyan, K. Ernst and B. L. Feringa. Electrically Driven Directional Motion of A Four-Wheeled Molecule on a metal surface. Nature **479**, 208 (2011).
[5] C. J. Chen. Introduction to Scanning Tunneling Microscopy 2nd Edition. Oxford University Press, New York (2007).
[6] R. Otero, J. M. Gallego, A. L. Vázquez de Parga, N. Martin, and R. Miranda. Molecular Self-Assembly at Solid Surfaces. Adv. Mater. **23**, 5148 (2011).
[7] B. Voigtländer, G. Meyer, and N. M. Amer. Epitaxial Growth of Thin Magnetic Cobalt Films on Au(111) Studied by Scanning Tunneling Microscopy. Phys. Rev. B **44**, 10354 (1991).
[8] M. Corso, L. Fernández, F. Schiller, and J. E. Ortega. Au(111) – Based Nanotemplates by Gd Alloying. ACS Nano **4**, 1603 (2010).
[9] M. Corso, M. J. Verstraete, F. Schiller, M. Ormaza, L. Fernández, T. Greber, M. Torrent, A. Rubio, and J. E. Ortega. Rare-Earth Surface Alloying: A New Phase for $GdAu_2$. Phys. Rev. Lett. **105**, 016101 (2010).

[10] J. Gong. Structure and Surface Chemistry of Gold-Based Model Catalysts. Chem. Rev. **112**, 2987 (2012).
[11] J. V. Barth, H. Brune, G. Ertl, and R. J. Behm. Scanning Tunneling Microscopy Observations on the Reconstructed Au(111) Surface: Atomic Structure, Long-Range, Superstructure, Rotational Domains, and Surface Defects. Phys. Rev. B **42**, 9307 (1990).
[12] J. V. Barth, R. J. Behm, and G. Ertl. Mesoscopic Structural Transformations of the Au(111) Surface Induced by Alkali Metal Adsorption. Surf. Sci. Lett. **302**, L319 (1994).
[13] S. Narasimhan and D. Vanderbilt. Elastic Stress Domains and the Herringbone Reconstruction on Au(111). Phys. Rev. Lett. **69**, 1564 (1992).
[14] E. I. Altman and R. J. Colton. Nucleation, Growth, and Structure of Fullerene Films on Au(111). Surf. Sci. **279**, 49 (1992).
[15] A. Kühnle. Self-Assembly of Organic Molecules at Metal Surfaces. Current Opinion in Colloid & Interface Science **14**, 157 (2009).
[16] J. V. Barth, G. Costantini, and K. Kern. Engineering Atomic and Molecular Nanostructures at Surfaces. Nature **437**, 671 (2005).
[17] M.S. Dresselhaus, G. Dreeselhaus, and P.C. Eklund. Science of Fullerenes and Carbon Nanotubes. Academic Press, London (1996).
[18] R. Taylor. Lecture Notes on Fullerene Chemistry: A Handbook for Chemists. Imperial College Press, London (1999), 6-7.
[19] H. W. Kroto, J. R. Heath, S. C. O'Brien, R. F. Curl, and R. E. Smalley. C_{60}: Buckminsterfullerene. Nature **318**, 162 (1985).
[20] P. Damay and F. Leclercq. Molecular Geometry in Fullerene C_{60}: A Direct Determination of the Bond-Length Difference $d_{C\text{-}C} - d_{C=C}$. Phys. Rev. B **49**, 7790 (1994).
[21] Q. M. Zhang, J. Y. Yi, and J. Bernholc. Structure and Dynamics of Solid C_{60}. Phys. Rev. Lett. **66**, 2633 (1991).
[22] S. Saito and A. Oshiyama. Cohesive Mechanism and Energy Bands of Solid C_{60}. Phys. Rev. Lett. **66**, 2637 (1991).
[23] R. D. Jonhson, G. Meijer, and D. S. Bethune. C_{60} Has Icosahedral Symmetry. J. Am. Chem. Soc. **112**, 8983 (1990).
[24] E. I. Altman and R. J. Colton. The Interaction of C_{60} with Noble Metal Surfaces. Surf. Sci. **295**, 13 (1993).
[25] J. A. Gardener, G. A. D. Briggs, and M. R. Castell. Scanning Tunnelling Microscopy Studies of C_{60} Monolayers on Au(111). Phys. Rev. B **80**, 235434 (2009).
[26] W. W. Pai, C. Hsu, M.C. Lin, K. C. Lin, and T. B. Tang. Structural Relaxation of Adlayers in the Presence of Adsorbate-Induced Reconstruction: C_{60}/Cu(111). Phys. Rev. B **69**, 125405 (2004).
[27] K. Aït-Mansour, P. Ruffieux, P. Gröning, R. Fasel, and O. Gröning. Positional and Orientational Templating of C_{60} Molecules on the Ag/Pt(111) Strain-Relief Pattern. J. Phys. Chem. C **113**, 5292 (2009).
[28] D. E. Hooks, T. Fritz, and M. D. Ward. Epitaxy and Molecular Organization on Solid Substrates. Adv. Mater. **13**, 227 (2011).
[29] X. Torrelles, M. Pedio, C. Cepek, and R. Felici. $2\sqrt{3}\times2\sqrt{3}R30°$ Induced Self-Assembly Ordering by C_{60} on A Au(111) Surface: X-Ray Diffraction Structure Analysis. Phys. Rev. B **86**, 075461 (2012).

[30] X. Q. Shi, M. A. Van Hove, and R. Q. Zhang. Adsorbate-Induced Reconstruction by C_{60} on Close-Packed Metal Surfaces: Mechanism for Different Types of Reconstruction. Phys. Rev. B **85**, 075421 (2012).
[31] A. D Jewell, E. C. H. Sykes, and G. Kyriakou. Molecular-Scale Surface Chemistry of a Common Metal Nanoparticle Capping Agent: Triphenylphosphine on Au(111). ACS Nano **6**, 3545 (2012).
[32] J. Lu, P S. E. Yeo, Y. Zheng, Z. Yang, Q. Bao, C. K. Gan, and K. P. Loh. Using the Garphene Moiré Pattern for the Trapping of C_{60} and Homoepitaxy of Graphene. ACS Nano **6**, 944 (2012).
[33] R. Madueno, M. T. Raisanen, C. Silien, and M. Buck. Functionalizing Hydrogen-Bonded Surface Networks with Self-Assembled Monolayers. Nature **454**, 618 (2008).
[34] G. Pawin, K. L. Wong, K. Y. Kwon, L. Bartels. A Homomolecular Porous Network at a Cu(111) Surface. Science **313**, 961 (2006).
[35] F. Klappenberger, D. Kühne, W. Krenner, I. Silanes, A. Arnau, F. J. García de Abajo, S. Klyatskaya, M. Ruben, and J. V. Barth. Tunable Quantum Dot Arrays Formed from Self-Assembled Metal-Organic Networks. Phys. Rev. Lett. **106**, 026802 (2011).
[36] F. Hanke, S. Haq, R. Raval, and M. Persson. Heat-to-Connect: Surface Commensurability Directs Organometallic One-Dimensional Self-Assembly. ACS Nano **5**, 9093 (2011).
[37] M. M. Biener, J. Biener, R. Schalek, and C. M. Friend. Surface Alloying of Immiscible Metals: Mo on Au(111) Studied by STM. Surf. Sci. **594**, 221 (2005).
[38] D. D. Chambliss, R. J. Wilson, and S. Chiang. Nucleation of Ordered Ni Island Arrays on Au(111) by Surface-Lattice Dislocations. Phys. Rev. Lett. **66**, 1721 (1991).

Chapter 2. Literature Review

The creation of the Scanning Tunnelling Microscope (STM) opens the door of the atomic world for people to explore. The idea of making a microscope to see atoms comes from the quantum effect of electron tunnelling through a vacuum gap. But the fulfilment of the STM is a combination of electronic control, vibration isolation, vacuum technology, feedback control and data collection.

2.1 Scanning Tunnelling Microscopy

Simply speaking, the STM is an electron microscope that detects the tunnelling current between a metal tip and a conductive sample to study surface-related subjects at the atomic level. From the conception of electron tunnelling to the final fulfilment of the STM, a lot of effort has been devoted to STM-based research. At the same time, STM also stimulates the rapid progress of surface science. STM is a complex system involving not only the quantum physical phenomenon which people knew a long time before the fulfilment of the STM, but also other technologies closely related to controlling the system working with the precision at the nanometer scale.

2.1.1 Electron Tunnelling

In classical mechanics, if the energy of an electron is lower than that of a potential barrier, the electron cannot penetrate through the barrier to the other side. But from the view of quantum mechanics, there is always a probability that the electron can go through the barrier. The basic physical concepts are as follows [1].

For simplicity, the quantum tunnelling effect is described in one dimension. In quantum mechanics, particles such as the electron have wave properties and can

be represented by wave functions ψ(z) in which z represents the positions of the particle along its propagation direction. The Schrödinger equation, representing one of the basic rules in quantum mechanics, predicts the states of the particles. As shown in Figure 2.1 below, an electron with energy E propagates along direction z and meets a barrier of height U(z) (U=0 for z<0 and U=U_0 for 0≤z≤a). The Schrödinger equation describing the electron is as follows

$$-\frac{\hbar^2}{2m}\frac{d^2}{dz^2}\psi(z)+U(z)\psi(z)=E\psi(z). \quad (2.1)\ [1]$$

For E > U(z), the solution for Eq. 2.1 is

$$\psi(z)=\psi(0)e^{\pm ikz}. \quad (2.2)\ [1]$$

The $e^{\pm ikz}$ part in Eq. 2.2 indicates the wave nature of the electron when it propagates. And

$$k=\frac{\sqrt{2m(E-U)}}{\hbar} \quad (2.3)\ [1]$$

is the wave vector[2]. If E < U(z), the solutions for Eq. 2.2 is

$$\psi(z)=\psi(0)e^{-kz}, \quad (2.4)\ [1]$$

in which $k=\frac{\sqrt{2m(U-E)}}{\hbar}$ is called the decay constant which comes from the fact that the wave function with the part e^{-kz} decays exponentially with z when the electron crosses the barrier and travels in the +z direction. The probability to see an electron in the barrier region is proportional to $|\psi(0)|^2e^{-2kz}$, the further in +z direction, the smaller the probability. The electron can tunnel through the barrier U_0, even if the electron energy E is smaller than U_0, and further propagates in +z direction (Figure 2.1).

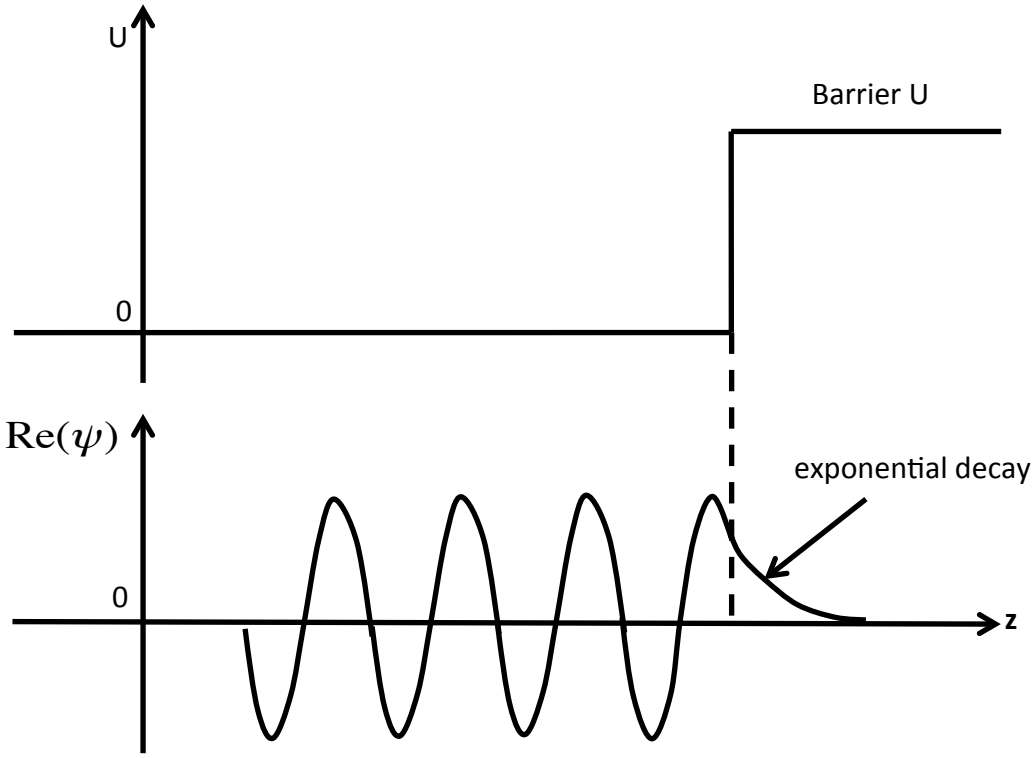

Figure 2.1 A basic model of the quantum tunnelling effect in one dimension. A electron travels in the +z direction. The wave function of the electron exponentially decays to zero in the forbidden region where the barrier U is larger than the electron energy.

In the situation of STM, the tunnelling junction can be depicted as in Fig. 2.2 below. When there is no bias voltage applied between the tip and the sample, electrons from each side can tunnel to the other side through the vacuum barrier with the same probability, Fig. 2.2(a). When a negative bias V is applied to the sample, Fig. 2.2(b), there is a possibility for electrons with energy E_n between E_F-eV and E_F penetrating through the vacuum to the tip. And tunnelling current is recorded from the tip by electronic circuits of high sensitivity.

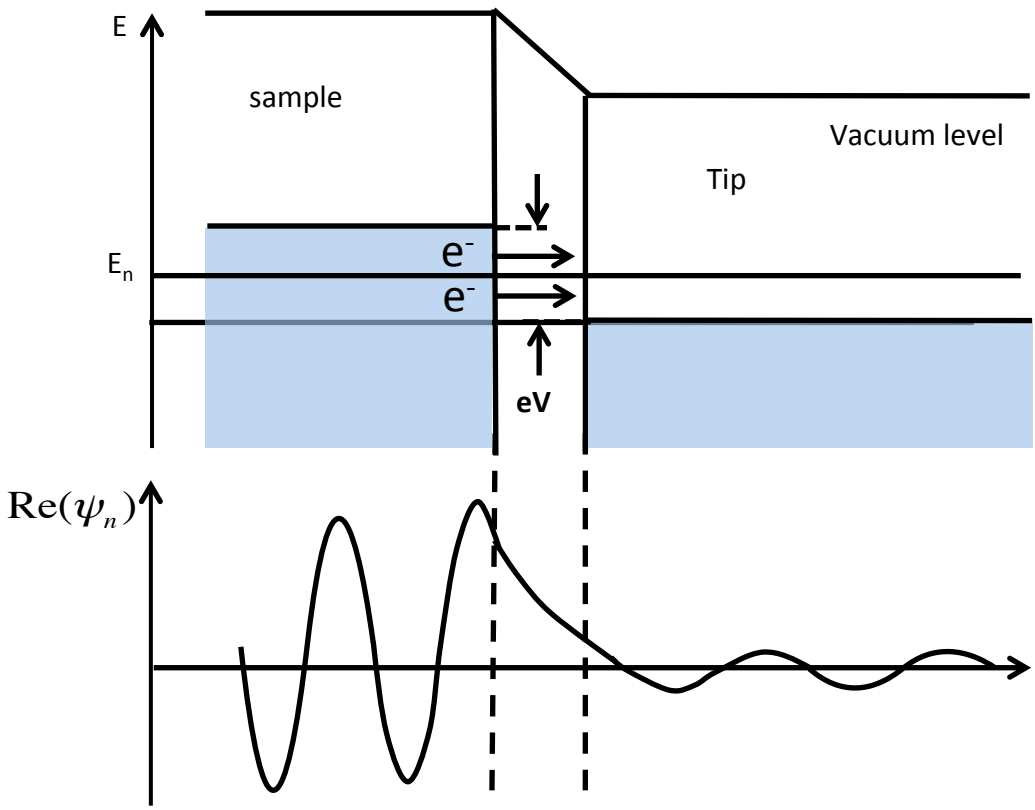

Figure 2.2 An elementary model of a metal-vacuum-metal tunnelling junction. When there is no bias applied between the sample and the tip, electrons have an equal possibility of tunnelling through the barrier in either direction. If a negative bias is applied to the sample, a net electron current flows from sample to tip through a vacuum gap.

The tunnelling current can be given as

$$I \propto exp\left(-2z\sqrt{\frac{2m}{\hbar^2}\left(\phi - \frac{e|V|}{2}\right)}\right), \qquad (2.4)\ [2]$$

where ϕ is the work function of the sample, z the separation between the tip apex and the counterpart - atoms in the sample surface during scanning, m the electron mass, e the electron charge, $\hbar = \frac{h}{2\pi}$, $\hbar$ the Dirac constant, V the bias applied to the sample.

From Eq. 2.4, we can extract the information of tip-sample separation from the change of tunnelling current. If $\phi - \frac{e|V|}{2}$ is 5 eV, 1 Å change of z leads to the change of the exponent part in Eq. 2.4 by 9.8 times. The fact that the tunnelling current exponentially depends on the barrier gap z between the tip and the sample is one of the reasons that gives the STM a vertical resolution of about 0.01 Å.

Compared with theoretical calculations, larger corrugations of surface atoms are observed by STM. More factors beside the tunnelling effect need to be considered for the detected tunnelling current. Imaging force [3] should be expected to exist during scanning. As from basic electrostatics, the electrons for example on the tip induce positive charges on the scanned conductive surface. The negative and positive charges would interact with each other. This interaction further modifies the wave function between the tip and the sample, and can account for the observed much larger tunnelling current compared to that from theoretical calculations without considering the imaging force.

In 1960, Bardeen [4] applied perturbation theory to explain the electron tunnelling current for STM imaging. The tip and the sample were treated as two isolated systems. The tunnelling current came from the overlap of the wave functions of the two systems when the tip and the sample were close enough. This calculation shows more complex consideration of the tunnelling current.

Another important constant in the STM tunnelling junction is the tunnelling conductance (quantum conductance) G which is defined as

$$G = \frac{I_t}{V} = G_0 T, \qquad (2.5)\ [2]$$

where I_t is the tunnelling current, V the bias voltage and G_0 is the conductance constant [2]. G is found to be a quantized quantity with the value to be $n\frac{2e^2}{h}$, where n is an integer and T is the transmission coefficient. [5].

2.1.2 STM Atomic Resolution

The resolution of the STM inaugurates experiment and working on an atomic scale [6]. The atomic resolution achieved by STM prompts theoretical researches to understand the mechanisms behind the images obtained. Tersoff and Hamann proposed an s-wave-tip model [7, 8]. In the s-wave-tip model, the tip with a curvature of R is treated as a spherical potential well. The s-wave solution for the Schrödinger equation plays the only important role for the tunnelling current. The STM image shows the contours of charge density of simple metal surfaces. The s-wave-tip succeeds in explaining the superstructures for example Au(110) with periodicities of 0.815 nm and 1.223 nm, or large atoms [9, 10] on metal surfaces, but it is not sufficient to reveal the principles behind the atomic resolution of about 0.2 nm achieved by STM. Theoretically the corrugation that an s-wave tip can achieve is one magnitude smaller than has been observed by STM.

If the STM image only shows the local density states (LDOS) at the Fermi level of a surface for example the Al(111) surface, the corrugation of Al atoms should be within 0.03 Å [11]. However, the observed corrugation [12] is one order of magnitude higher than 0.03 Å. The tip electronic states play an important role during imaging. Chen [13] interprets the atomic resolution of STM from the p_z and d_{z^2} states of a tip made of a *d*-band metal or semiconductor. When the higher angular momenta of a tip are considered, the STM topography is not simply the contour of LDOS of the surface [14], which could give an insight to the origin of the

large corrugations observed. The *d* band metals have higher corrugations of charge density near the Fermi level than those of free electron metals as the d_{z^2} state near the Fermi level [15]. If both the tip and the surface are *d* band metals with the d_{z^2} state, the theoretical corrugation amplitude could be two orders of magnitude larger than that predicted using the s-wave tip model.

The p_z [16] state tip increases the corrugation amplitude by a factor a little larger than 1 at K of the Brillouin zone of the surface [17]. The d_{z^2} state tip [13] shows a corrugation amplitude Δz 10 times larger than the corrugation amplitude of the charge-density state probed by the *s*-state tip from theoretical calculations [8, 18]. There are also other states, e.g. d_{xz} and d_{x^2} of a tip considered for STM imaging, which give inverted corrugation of metal atoms [17] as shown in Fig 2.3. The Au atoms in the STM image (Figure 2.3) are imaged as hollow instead of protrusions.

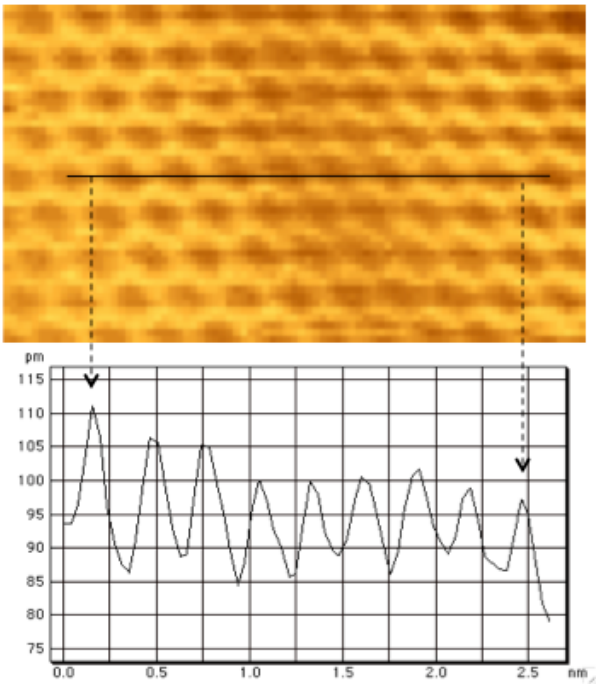

Figure 2.3 Atomic-resolution STM image of Au(111) with Au atoms imaged as inverted corrugation. (I_t: 11 nA, V_{sample}: -20 mV, Image from my own work.)

Due to the tip proximity, the density of electron states of the surface is supposed to be modified [19] as long as the tunnelling current comes into effect. During the tip approach, the tunnelling barrier is observed to decrease substantially and more tip-induced states such as a hybridized sp_z and a $p_{x,y}$-like states arise in-between the gap accompanying increased charge density. According to theoretical calculation of the Al tip - Al(111) system [19], when the tip is 4.2 Å from the surface, a bondlike channel connects the tip states and the surface states. When the effective barrier for electrons becomes negative, electrons are transported in a quantum ballistic manner. The effective barrier varies on different surface sites, which amplifies the electronic features of a flat metal surface and may be used to explain the atomic resolution of STM.

The atomic forces between the tip and surface also contribute to the improved resolution of STM. The forces existing in vacuum tunnelling were first studied by Teague [20]. In his experiment, the attractive force, the van der Waals force between two gold electrodes and the electrostatic force originating from the applied voltage could possibly deflect the electrode surface in the tunnelling region, which affect the observed profile between the tunnelling current I and electrodes separation S. The atomic forces existing during scanning leads to the realization of the atomic force microscope (AFM), which is another powerful tool to study surfaces.

At long distances, the interaction between the tip and the sample is dominated by the van der Waals force when there is no overlap between the wave functions of tip and sample in quantum mechanics, which means there is no exchange of electrons between the two.

When the tip comes close to the surface in the intermediate region where the van der Waals force and the repulsive force are negligible, the electron tunnelling effect induces the interaction between a metal tip and a metallic surface, in which attractive force, the exchange force or the resonance force, is discovered [21]. Dürig et al. measured the force gradient originating from the resonance interaction, linearly increasing with the gap width before mechanical contact happened between the tip and the sample.

The local deformations of tip and surface caused by strong repulsive force between the apex atoms of the tip and their counterparts on the surface, are also considered to contribute to the observed large corrugation of simple metal surfaces. Atomic resolution on a metal surface whose surface-density-states corrugations are small is always obtained when the tip gets very close (~ 3 Å) to the metal surface, which requires an imaging condition of a large tunnelling current of the order of 10 nA and a small bias voltage of the order of 10 mV. Under these imaging conditions, it is supposed that there exists a repulsive force between the tip and the surface, which induces local elastic deformations [3] of both tip and surface. The local elastic deformations caused by the repulsive force as a result of core-core interaction amplify the motion of the tip with respect to the surface and therefore the electronic corrugation.

2.1.3 General Applications of STM

STM has been proved to be one of the most powerful tools in surface science study [22]. The basic and most important application of STM is studying surface features such as metal or semiconductor surfaces. The first atomic-resolution STM image was obtained on the Si(111) surface [23]. The real-space image shows detailed

information about the 7×7 reconstruction of Si(111) shown in Figure 2.4 where the rhombus outlines the unit cell. Each bright dot represents one Si atom.

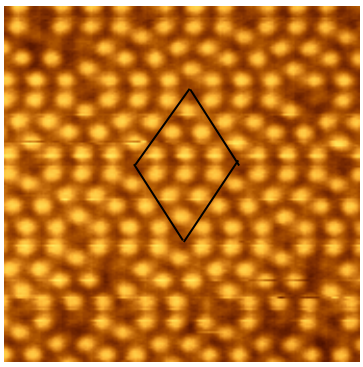

Figure 2. 4 Topographic STM image of the Si(111)-7×7 reconstruction surface. Each bright dot corresponds to one Si atom and the rhombus outlines the unit cell. (I_t: 0.3 nA, V_{sample}: 1V. STM image size: 9nm ×9nm, image from my own work.)

The corrugation observed on Si(111) is as large as 0.9 Å [23] which exceeds that expected from theoretical calculations. After the achievement of atomic resolution on Si(111), more and more STM images with atomic resolution were obtained on clean metal surfaces. It is always hard for STM to detect the atomic corrugations on metal surfaces due to their rather smooth surface charge density distribution. Individual Au atoms on the Au(111) surface were first resolved in 1987 [24] by STM with a vertical corrugation of 0.3 Å. Later, in 1990, the Au(111)-22×$\sqrt{3}$ reconstruction [25] was observed. This will be introduced in detail in the next subsection.

Molecular orbitals are also observed by STM under different tunnelling conditions [26]. On hydrogen saturated Si(100), after annealing at 690 K, the occupied π-orbital formed by coupling of Si dangling bonds is observed under negative sample

bias by STM as a bright feature symmetrically distributed around a Si dimer row. On the contrary, under positive sample bias, the unoccupied π-orbital shows a node structure where the node sits between the two Si dimer rows.

Although STM images can hardly show any chemical information, different atoms of bimetallic surfaces [27, 28, 29] sometimes exhibit an obvious contrast under STM imaging due to their large difference in electronic structure. An amplitude difference of about 0.3 Å between Pt and Ni atoms on a single crystal surface is observed by STM [27]. On the (111) surface of $Pt_{25}Ni_{75}$ single crystal, a bright and dark contrast exists for different species of metal atoms, with Pt atoms appearing dark and Ni atoms bright. As the bright dark contrast largely depends on the tip conditions, it is possible that some adsorbate, such as sulfur or oxygen, attached to the STM tip interacts differently with the surface atoms, which leads to chemically resolved STM images. A similar height contrast of about 0.2 Å is also observed on the PtRh(100) surface [28] with Pt atoms imaged darker than Rh atoms. In this case, the chemical contrast is considered to come from the difference in electronic structure of Pt and Rh, unlike Pt and Ni that are in the same column of the Periodic Table. Here the chemical contrast is reflected as brightness contrast in STM images. The STM study of bimetallic alloys, for example PdAu alloy [29], with catalytic properties shed light on the understanding of the catalytic origin of metallic alloys from the view of surface composition, the distribution of respective metallic atoms in the surface layer and the active sites for activating chemical reactions on the surface.

Besides the basic function of imaging surfaces in real space, the atomic scale manipulation carried out by STM tip shows more and more exciting results with the advance of STM. One of the famous examples is the IBM logo written on a single

crystal Ni(110) surface using Xe atoms [30]. A “sliding” process invented by Eigler and his colleagues is used to precisely position each Xe atom on the surface. During normal scanning, the tip was at a distance when its interaction with Xe atoms is weak. When moving a targeted Xe atom, scanning was stopped, and the tip was drawn near the Xe atom and stopped at a distance when the interaction between the tip and the Xe atom was large enough to drag the Xe atom sliding on Ni(110). Then the scanning resumed until the tip reached the final destination and dropped the Xe atom there when a voltage pulse was applied on the tip. At last, the tip was withdrawn from the surface and the targeted Xe atom stayed where it was positioned. Later Eigler and his colleagues built a corral of radius 71.3 nm [31] with a STM tip by placing individual iron atoms in a circle on Cu(111) at low temperature. Inside the nanostructure, surface state electrons are confined and scattered by Fe atoms. The density of states inside the corral studied via tunnelling spectroscopy show resonance features of atomic states, whose peaks lie close to the electron eigenstates inside a 2D circular potential box. Beside 2D confinement of surface electrons, 1D electronic states existing within the 1D Cu chain on Cu(111) are also detected by tunnelling spectroscopy [32]. The combination of STM manipulation and tunnelling spectroscopy provides an effective tool for studying the fundamental electron states in nanosystems, which is of practical importance for the miniaturization of electronic devices and possible catalytic and magnetic applications.

The STM tip can be treated as an electron or hole source during scanning. Electron or hole injection has been discovered to drive molecular reaction on surfaces. Organic molecules with certain tails such as thiol, can form an ordered monolayer on flat surfaces while molecules with the alkyne group without an anchor to attach

themselves to surfaces hardly follow the thermally activated pathway to form an uniform layer [33], as the activation barrier to their binding with surface atoms is too high to overcome. When the STM tip scans over disordered layer of phenylacetylene molecules on Au(111) at positive sample bias [33], injection of electrons activates phenylacetylene molecules to self-assemble into ordered domains, when the organic molecules are supposed to bind with Au atoms in the (111) surface. This electron-assisted process opens up a new way to control self-assembly of desired molecules for possible electronic applications.

STM can also drive a molecular motor in the nanometer scale on a metal surface [34, 35]. The molecule motor is a meso-(R, S-R,S) isomer with four chiral units acting as four wheels when driven by the tip. The molecule can move in a fixed direction when tip injects a positive pulse (electron tunnelling from the tip to the sample) over the molecule, which induces the concerted action of the four motor units. The directional movement of the isomer is achieved by an appropriate choice of the chirality of each wheel unit. This design conception initiates the study of nanoscale mechanical system with directionally controllable motion.

2.2 The Au Atoms and Surfaces

Gold is one of the most inert metals in nature. Clean Au surfaces are widely used in surface science and nanoscience as a support in various environments such as acid solution, air and UHV due to its inertness. However, when gold comes in the form of nanoclusters, it exhibits important and interesting chemical, catalytic and electronic properties. In section 2.2, I will give a detailed introduction about the structure and properties of Au surfaces and Au clusters.

The Face Centred Cubic (FCC) and the Hexagonal Close Packed (HCP) stacking are two different ways that atoms accommodate to form regular structures of

occupying the minimum volume. The FCC structure is denoted as ABC stacking and the HCP corresponds to ABA stacking. Au single crystal shows the FCC stacking.

2.2.1 The Features of the Au(111) Surface

Before the advent of the STM, Au surfaces with different crystallographic orientations, such as the (111), (110) and (100) had been widely investigated by transmission electron microscope (TEM) [36, 37, 38], low energy electron diffraction (LEED) [39] and High-Resolution Helium-Atom Scattering (HRHAS) [40]. As early as 1935, Finch et al. [41] studied electro-deposited Au films with electron diffraction and obtained a diffraction pattern exhibiting normal and "extra" rings. They attributed these "extra" rings to an interstitial entry of gas molecules into the top layer of the Au thin film, as the pattern was only shown after the sample was sufficiently heated in air or oxygen at a temperature of 773 K, and gradually disappeared when the sample was heated in vacuo. That was the first discovery of the reconstruction of the Au(111) surface but the reasons for and detailed structure of the reconstructed surface remained unknown. Later from the LEED pattern [39], an anomalous structure, corresponding to the extra rings seen from transmission electron diffraction (TED) results, of Au(111) was also observed after cleaning the surface, which is believed to originate from a reconstruction that the hexagonally packed top layer of Au was contracted by 5%. The reconstructed Au surface was further verified by TEM. From high vacuum TEM images with topographic information, the Au(111) surface after cleaning and heating [36, 37, 38] showed a reconstructed structure with a contracted top surface layer with 6.3 nm spaced fringes in the ⟨110⟩ direction (see Figure 2.5). The fringes were very sensitive to surface contamination, which is why they were not discovered in other

similar experiments lacking of high vacuum environment. It was also confirmed by a TEM study that the surface was compressed in the $[1\bar{1}0]$ direction, by about 4.2% compared to the bulk [37] which also exhibits a bright and dark contrast at the fringe boundaries (see Figure 2.5c, indicated by arrowheads).

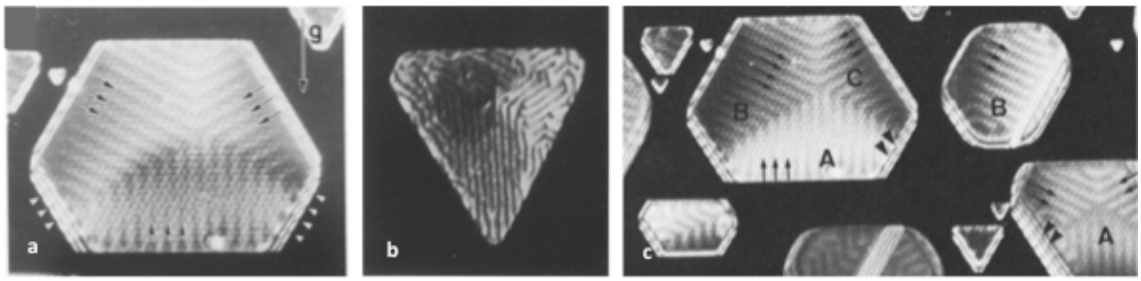

Figure 2.5 Electron micrographs of reconstructed Au(111) surfaces. (a) Au islands grown on MoS_2 dark field image formed by $(\bar{1}1\bar{1})$ reflection. Arrowheads point to Moiré fringes and arrows the fringes from reconstruction [36]. (b) Fringes inside a Au crystallite [37]. (c) Au platelets on MoS_2. Arrows indicate the fringes and arrowheads the Moiré fringes. The surfaces are divided into three domains − A,B, and C− with differently oriented fringes [38]. (Images reproduced from [36, 37, 38])

Takayanagi and Yagi [42] proposed a model of the Au(111) reconstruction based on their TEM observation, as shown in Figure 2.6a. The unit cell of the Au(111) reconstruction is denoted as $p\times1$ with p ranging from 22 to 24, in correspondence to surface layer contraction by 4.2-4.6 % on average in the $[\bar{1}10]$ direction. Au atoms (open circles) in the second layer are located at site A of the FCC crystal structure while there is a transition part to connect the two area of Au atoms (solid circles) in the top layer occupying site B or site C. The Burgers vectors of $b_1 = 1/6\,[\bar{2}11]$ and $b_2 = 1/6\,[\bar{1}2\bar{1}]$ indicate displacement of Au atoms in the transition area. Figure 2.6b is a modified model proposed by Harten et al. [40] from their

High Resolution Helium-Atom Scattering (HRHAS) study. Au atoms in the top layer (circles) are divided into three kinds with respect to their positions in the FCC stacking, some of which are situated at the sites A or C while the rest sit in a so-called soliton area where they gradually transit from site A to site C stacking via intermediate bridge sites, which is the minimum energy path that connects the two sites. The transition process accompanies a vertical displacement of Au atoms in the z direction perpendicular to the x-y plane.

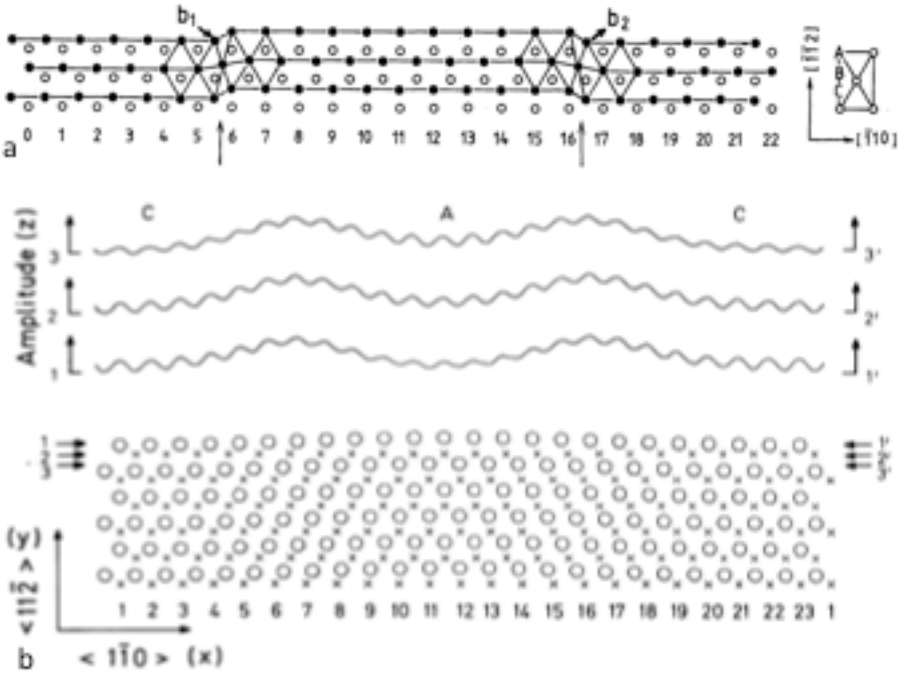

Figure 2.6 (a) Surface reconstruction model of Au(111) in top view. Solid and open circles represent top layer Au atoms and Au atoms in second layer. The compression of Au atoms in the top layer is realized by displacement of atoms in the Burgers vectors $b_1 = 1/6\,[\bar{2}11]$ *and* $b_2 = 1/6\,[\bar{1}2\bar{1}]$. *[42] (b) On the top is the vertical corrugation of three lines in the unit cell. At the bottom is a top view of the top two reconstructed layers of Au atoms in which circles represent atoms in the top layer and crosses in the second layer [40]. (Images reproduced from [40,42]).*

The TEM micrographs cannot provide enough information about how Au atoms arrange to bring about the reconstruction. However, with the assistance of STM, it is possible to reach conclusions about the atomic arrangement in the reconstructed Au(111) surface [43, 44, 45], not attainable with other surface sensitive techniques. At the early stages of STM development, the small corrugations of Au atoms, due to their free electron density, were hardly observed by STM, except steps of the Au(111) surface with a height of 2.35 Å [46]. The observation of Au(111) with the resolution of individual Au atoms was firstly obtained by Hallmark et al. [43] using STM in both air and UHV environments. The observation of hexagonally packed atoms with spacing of 3.0±0.3 Å confirms the assignment of the corrugation to Au atoms. For the reconstructed surface denoted as Au(111)- $22\times\sqrt{3}$, there are bright strips in the STM images named discommensuration lines (DLs). The DLs are the aforementioned transition areas that are between areas of Au atoms in FCC stacking (ABC) and HCP stacking (ABA) (see Figure 2.7) [44, 45].

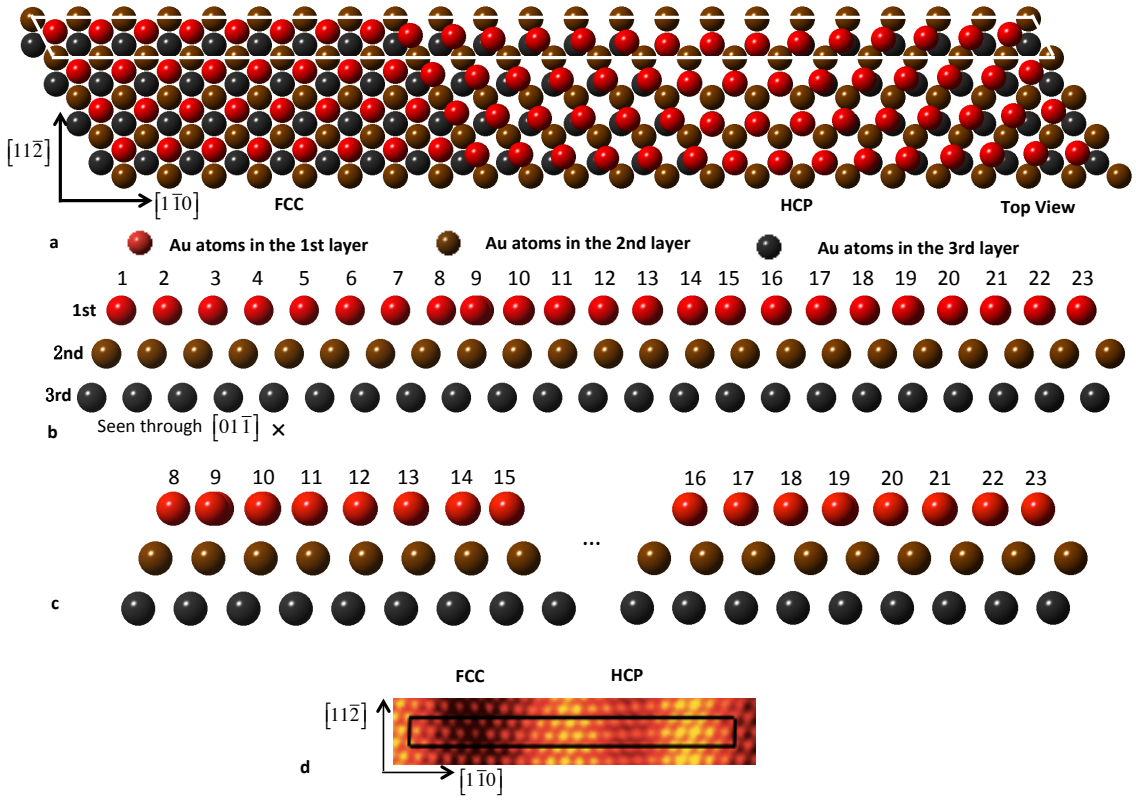

Figure 2.7 (a) A schematic diagram of the reconstructed Au(111). Three layers of Au atoms are shown in the image with the Au atoms in the first layer in red, in the second layer in grey and in the third layer in black. The 23 Au atoms (red) in the first layer and also 22 FCC hollow sites in the second layer are enclosed by a parallelogram (white). Surface Au atoms are compressed in the $[1\bar{1}0]$ *direction. (b) The occupation shift of the 23 Au atoms in the first layer seen through the* $[01\bar{1}]$ *direction. (c) A zoom-in image of the transition area. From Au atom 9 to Au atom 14, the occupations of the Au atoms in the first layer shift from FCC hollow site to HCP hollow site, and from Au atom 17 to Au atom 22, shift from HCP hollow site to FCC hollow site. (d) Atomic resolution of Au(111) in real space, a unit cell highlighted by a rectangle.*

The transition area shows a corrugation of 0.15 ± 0.04 Å with respect to the surface plane [45]. The height difference can be readily obtained from a hard sphere model between atoms in bridge site and hollow site [40]. The areas of atoms in FCC stacking or HCP stacking are not equally separated by DLs with a larger FCC region and a narrower HCP region due to the fact that the energy at site A in HCP stacking is higher than that at site C in FCC stacking. The DLs bend by 120° to form a zigzag herringbone pattern, shown in Figure 2.8a below.

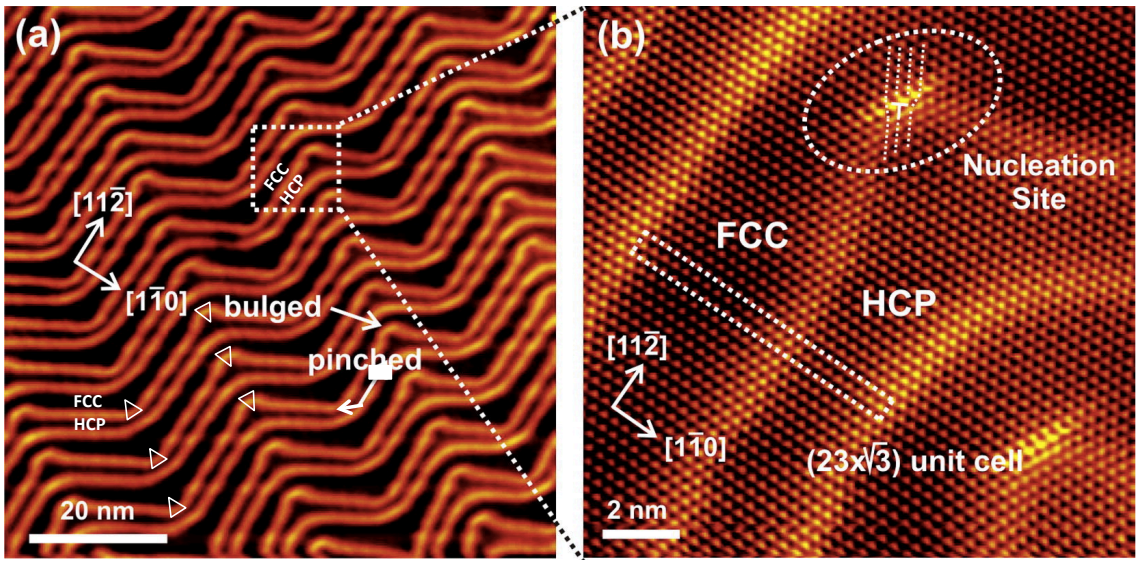

Figure 2.8 (a) STM image of reconstructed Au(111) with rotational domains. Bulged and pinched elbows are pointed by arrows. The herringbone zigzag pattern is clearly seen. Pairs of DLs run in $[11\bar{2}]$ *where the area of the FCC region is larger than that of the HCP region. (b) An extra atomic row is on the open side of the bulged elbow site, marked by an oval, where the DLs bend by 120°. (Images taken from [47].)*

DLs come in pairs, one of which has a dislocation at every bending site (elbow site, marked in Figure 2.8a with triangles) while the other one is free of dislocation, and both of them run in $\langle 11\bar{2} \rangle$, orthogonal to the uniaxial contraction direction $\langle 1\bar{1}0 \rangle$.

The width of a pair is 22 Å and the distance between two pairs is 44 Å [44]. The bending sites of DLs are of two types, named as bulged elbow and pinched elbow. At the bulged elbow, one of the paired DLs is pushed toward the FCC area where an additional atomic row exists on the open side of the bent DL, shown in Figure 2.8b marked by an oval resulting in a larger HCP area, seen in Figure 2.8a with triangles pointing down. On the contrary, at the pinched elbow, the FCC area is enlarged due to the shift of the DLs towards the HCP region, as seen in Figure 2.8a with triangles pointing up, where an additional atomic row exists in the HCP region. Sometimes, surface defects such as screw dislocation on the surface and steps, interfere with the DLs and disturb the zigzag pattern as the strain in the top layer is changed. The elbows have been used as nucleation sites for the growth of many types of atomic and molecular structures.

These various features of the clean Au(111) surface were the focus of theoretical study when the reconstruction was first observed. Theoretical physicists devoted their efforts to simulate the reconstruction pattern of Au(111) using the Frenkel-Kontorova model based on the "Double-Sine-Gordon" (DSG) potential [48, 49] and inclusion of the long-range elastic stress [50, 51, 52], as well as embedded atom method [53, 54], in which both the many-body surface strain and near-surface elastic properties are considered. However, the large unit cell of the reconstruction makes theoretical calculations difficult to produce all the features of the reconstruction. The double-sine-Gordon soliton model discriminates the energetic difference between the ABC and ABA stacking, which gives rise up to a different size distribution of the FCC and HCP areas. The DSG potential applied to surface Au atoms can produce the solitons with misfit dislocations and the zigzag pattern of solitons but cannot get a right size of the unit cell [48]. Ravelo and El-Batanouny

associated molecular dynamics with the DSG model to explain the observed softening of surface phonon branches in the shear horizontal and longitudinal directions in their model by introducing a proper size of dislocation and misfit between the substrate and the surface, which causes a decrease of surface force constants that induces the reconstruction [49, 55]. Wang also used a well-tested many-body interatomic potential in molecular dynamics simulation, to perfectly reproduce the surface phonon spectra [56] observed from experiments and the unit cell of the reconstruction. All the theoretical calculations mentioned above can at best reproduce the unit cell of Au(111) reconstruction without the rotational domain. More factors need to be included for theoretical simulation of the Au(111) reconstruction.

Surface stress is supposed to be one of the reasons for inducing surface reconstruction. Atoms at the surface have lower coordination numbers than those in the bulk due to which they tend to have, in most cases, a shorter bonding length within the plane. Theoretical calculations [57] found the unreconstructed Au(111) surface experiencing a tensile stress, which is in accordance with the compression of the reconstructed Au(111) surface. The compression reaches maximum at elbow sites, three times larger than that of the DLs, which accounts for the preferential nucleation at the elbow sites [52]. Surface strain is also believed to modify the secondary structure [51], the rotational domain of the Au(111) reconstruction. The formation of elbows probably lowers surface energy, and therefore externally exerted elastic deformation (compression) of Au thin film on mica eliminates the number of elbow sites, as is confirmed from both theoretical calculations [50, 51] and experimental observations [58].

Another way to study the Au(111) reconstruction is from the view of the difference in the electronic structures of surface-layer and bulk Au atoms [54, 56, 59, 60, 61]. Heine and Marks studied the forces in bulk Au, a competition between the *d* shell repulsion and the *sp* electron attraction, and further inferred what the Au(111) surface would likely to react to forces that are present when the electron density of the surface was chopped off [60]. They discussed the *sp* electron redistribution within the top surface and concluded that the local geometry affects the charge redistribution, based on the fact that the *sp* electrons go into the attractive mantle core region to lower their energy. Therefore, for a large flat surface, Au atoms with additional electron density lying in-between experience compressive stress while Au atoms at the step edge with a different charge distribution undergo tangential expansive stress. Their studies provided an insight into the possible causes of the observed compression of the Au(111) surface. The charge distributions within the Au surface, clusters and particles are of great interest for the study of structures of organic networks, catalytic activities etc. Later Layanthi et al. [61] applied the many-body interaction approach to the study of surface lattice dynamics. From their theoretical calculated surface-phonon dispersion curves, both charge redistribution and surface lattice instability (surface reconstruction) of Au(111) were shown.

Reconstruction is a common way for crystal surfaces to lower free energy when the bulk symmetry is discontinued by the surface. Temperature [62, 63, 64], adsorbates [65, 66, 67], and electrochemical potentials in electrolytes [68, 69, 70] can lead to phase transitions of the reconstructed Au(111). STM worked in atmosphere when it was invented. Later it was also enabled to work in various conditions including high vacuum, extreme temperatures, and solutions of

electrolytes for the study of the properties of surfaces in different environments. When the reconstructed Au(111) surface is in contact with air or solution, the herringbone reconstruction gradually disappear with the transition of surface structure from 22 ×√3 to 1×1 [69], which may be due to the release of strain by adsorbates from air or liquid. Adsorbates of different electronegativity from that of Au, can also affect the reconstruction of the Au(111) surface, due to the change of electronic states of the surface. If the adsorbates, for example C_{60} molecules, are less electronegative than Au, i.e., charges transferred from the Au to the adsorbates, the Au(111) surface with herringbone reconstruction is believed to fully or partly recover to the 1×1 structure [71, 72, 73] – the same as the bulk structure. On the other hand, if the adsorbates, for example K and Na, are more electronegative than Au in the (111) surface, i.e., donating charges to Au, the Au(111) surface experiences further compression, resulting in a greater atomic density of the first Au(111) layer compared with the 22×√3 herringbone reconstruction [65, 66]. The temperature-dependent phase transition (change of reconstruction pattern) of the Au(111) surface is studied by X-ray diffraction [62, 63] and STM [64]. In the temperature range from 300 K to 865 K, Sandy et al. [62, 63] observed the normal herringbone construction of Au(111) from the X ray diffraction pattern. If the temperature was further increased to 1250 K, a new structure named the discommensuration fluid phase formed in the surface layer of Au(111), in which the compression of the surface layer is isotropic on average with disordered arrangement of discommensuration lines and elbow sites. Both the periodicity of reconstruction unit cell and the separation of elbow sites decrease with increasing temperature. There is coexistence of both phases at the temperature range from 865 K to 879 K. STM observed shortening of DLs in every rotational domain [64].

The electronic structure of the Au(111) surface dictates various surface processes and exhibits features of great interest due to its structural and energetic inhomogeneity from the reconstruction. It has been studied experimentally using both high-resolution angle-resolved photoemission Spectroscopy (HRARPES) [74, 75, 76, 77] and STM [78, 79, 80, 81, 82], as well as theoretical simulations on the basis of first principle calculation [83] and density functional theory [84, 85]. Surface resonance states, in the research category of electronic surface properties, are split off from bulk bands. Paniago et al. [75] discovered a localized *d*-like surface resonance state within the uppermost layer of reconstructed Au(111). The *d*-like surface resonances can be identified by comparing a series of normal-emission photoelectron spectra at different temperatures with the Au(111) surface in the (1×1) structure at the low temperature of 72 K and 135 K, or in the (22×√3) structure at the temperature of 205 K, 262 K and 307 K. Besides *d*-like states, there are also *sp*-derived states from hybridization of crossed bands. LaShell et al. [76] observed spin-split of the *sp*-derived surface state origin from spin-orbit coupling, which can be explained by inversion symmetry breaking of the system [76, 84, 85].

Scanning tunnelling spectroscopy (STS), another function of STM, probes both the filled and empty states on surfaces shown as I tunnelling current or dI/dV differential tunnelling conductance vs V bias curves. The spectra are taken when the tip is fixed over an area in certain tunnelling conditions such as 0.3nA 1.0V, and the bias ramps over a range of about ±3V depending on what kind of material is studied, while the feedback is turned off to keep the tip static. The parabolic dispersion relation between the wave vectors of surface electron states versus electron energy can also be obtained using STS [74, 78, 82, 86], providing

information about both the empty and occupied states on the surface at around the Fermi level. Typical STS curves over regions of HCP, FCC and DL on Au(111) are shown in Figure 2.9 [82].

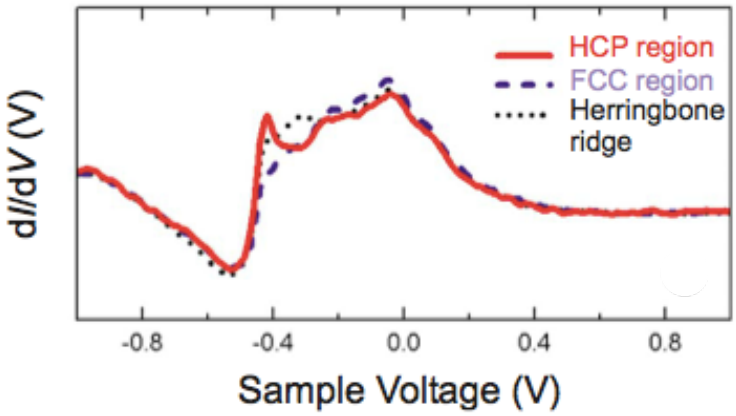

Figure 2.9 STS curves obtained by STM over the regions of HCP, FCC and Herringbone ridge (DL) of the clean Au(111) surface. (Image cited from [82].)

Due to the existence of surface states, free surface electron waves can propagate on the surface and form standing waves because of the interference of incident and scattered electron waves near a potential barrier such as a step [87, 88]. Standing waves formed by interference of surface state electrons [78, 86] are also detected by STM at both room temperature and a low temperature of 30 K. Hasegawa and Avouris [86] studied surface electron scattering by point defects and steps using STS mapping, which provides a rough measurement of the LDOS on the surface when the electronic structure is isolated from the geometric structure to clearly show the oscillation of the surface state electron. The step has a higher LDOS, the brighter feature in the map, than other areas, and therefore acts as a potential barrier to reflect propagating electron waves. Fujita et al. measured the wave

number $k_{//}$ at the Fermi level which is about 1.7 nm^{-1} in accordance with photoemission measurements [74]. They also proposed anisotropy of the two dimensional Fermi surface as they observed the enhancement of the amplitude of the standing waves at the regions of HCP and DL. Moreover, they proposed the possible existence of a quasi-one-dimensional surface state along DLs due to the continuity of the standing wave even when the DL was rotated by 120° into another stress domain [78]. Standing waves on Au(111) were also discovered near the DLs by Fujita et al. using low temperature STM [78]. Au atoms that form the DLs occupying the bridging sites are energetically higher than these at the hollow sites, and therefore, they form potential barriers for reflecting electron waves. From dI/dV spectra carried out at 4 K using STM, Chen et al. [79] found a surface state at 0.52 eV below the Fermi level (E_F) well consistent with photoemission results. The spectra also reveal a difference in LDOS between the FCC and HCP regions, with the HCP region having a lower potential to accommodate more delocalized surface electrons. The external electron potential map in Figure 2.10b of the reconstructed Au(111) surface was imaged by Bürgi et al. [89] based on the Hohenberg-Kohn theorem [90] and the assumption that the total electron density is linearly correlated with the external potential. Their findings agree with the findings of Chen et al. [79]. What is more, they found that the regions around the DLs are the most attractive area, shown as darker areas in Figure 2.10b, to surface electrons, which can also be seen from Figure 2.10d - averaged line profile of the $U(x)$ external potential across the DLs.

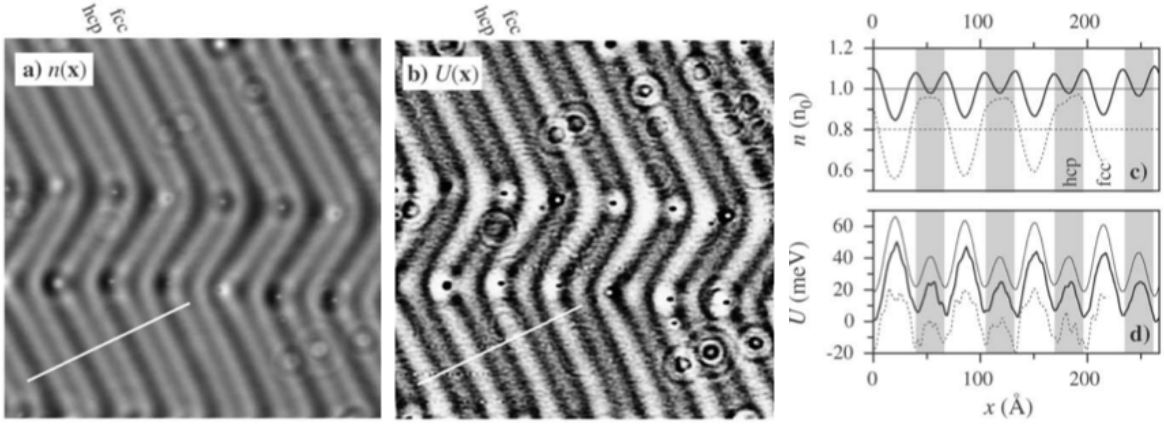

Figure 2.10 (a) A 512 Å × 512 Å electron density $n_{2D}(-320\,meV, x)$ map of reconstructed Au(111). (b) External potential $U(x)$ map of the same area in a. The solid lines in c and d correspond to averaged electron density $n_{2D}(-320meV, x)$ and external potential $U(x)$ over lines that are parallel to the white line in a and b. The dashed lines are similar to the solid lines but obtained at 450mV. (Images and data cited from [89].)

Schouteden et al. [82] investigated surface states of Au(111) from Fourier transform (FT) and inverse FT images of STM, which enables the study of broader energy ranges up to 3 eV than previous studies carried out using STS and STM. Besides the standing waves, they also found traces of bulk states, which vanish quickly on the surface and contribute to the oscillation of standing waves.

2.2.2 Atomic Steps

There are two kinds of Au steps on Au(111) originating in the intrinsic characteristic of the (111) surface, hexagonally packed, of FCC crystals [91], where there are two types of close packed ⟨110⟩ step edge as shown in Figure 2.11 [92, 93, 94, 95, 96]. The crystallographic structures of step A and step B are related

with a rotation of $2\pi/6$. Step A descends along $[11\bar{2}]$ and exposes a {111} facet, while the other step B ascends along $[11\bar{2}]$ and exhibits a {100} facet.

The difference in the step free energy of the step A and step B also greatly influences the equilibrium shapes of a metallic island grown on the (111) surface. For instance, silver islands on Ag(111) and copper islands on Cu(111) show hexagonal shape in three fold symmetry [97], because similar free energy of step A and step B leads to comparable growth rates of all the step edges. On the contrary, the equilibrium shapes of Au islands on Au(111) are more or less truncated triangles as step B advances more slowly in the $[11\bar{2}]$ direction perpendicular to the step edge than step A in the $[\bar{1}\bar{1}2]$ direction during the growth process (Figure 2.11). The final shape of a metallic island is a result of minimization of the overall step energy.

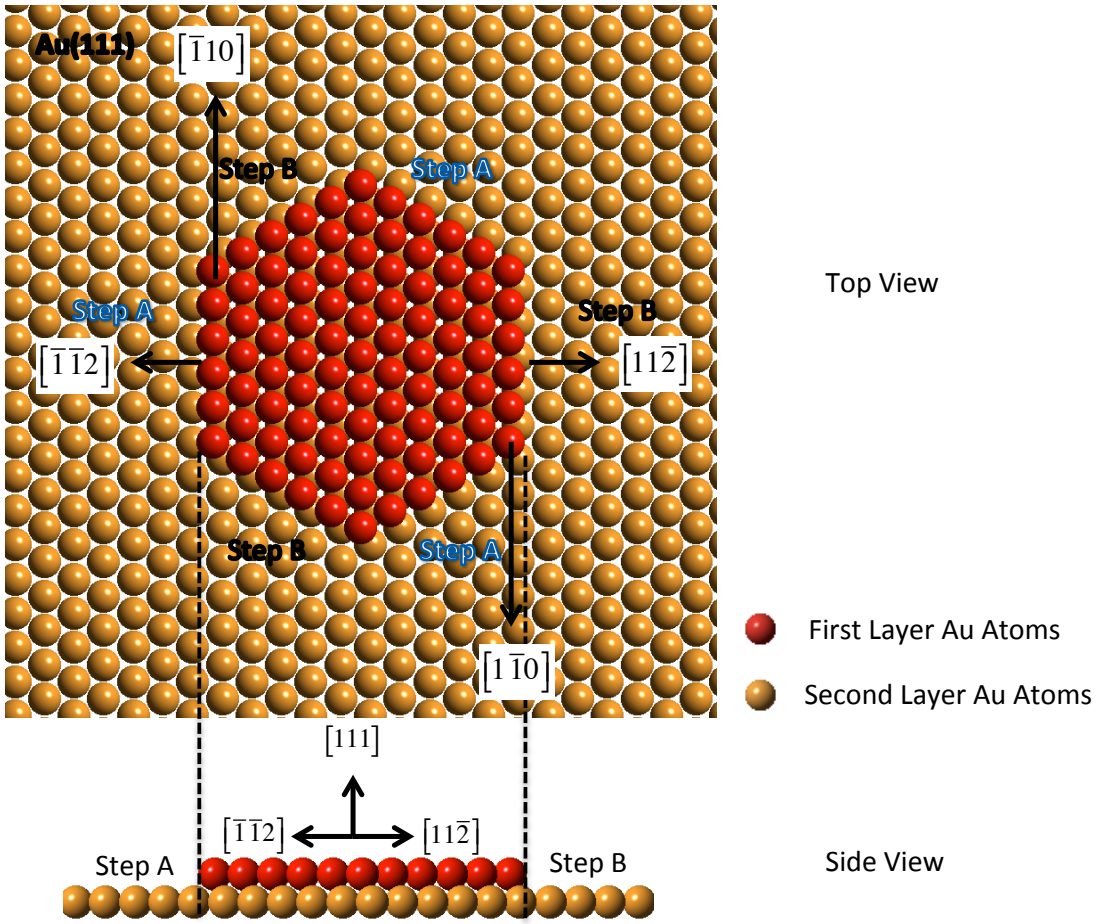

Figure 2.11 Model of a hexagonal Au island on Au(111). The island exposes two types of steps A and B with growth direction in $[\bar{1}\bar{1}2]$ *and* $[11\bar{2}]$ *respectively. The step A forms a (100) microfacet and the step B forms a (111) microfacet. (Image cited from [94].)*

The atomic steps of Au(111) attract great interest as they are a kind of surface defects where, when the DLs approach steps, the reconstruction diverges into different patterns [92, 93, 95]. When the DLs extend beyond a step of {111} microfacet vertically, their structure is not disturbed by the step, i.e., the DLs on both the upper and lower terraces can be connected directly as seen in Figure 2.12a. On the other hand, a step of {100} microfacet cuts off the connection between the DLs on the upper and lower terraces with a slender area, nearest to

the step edge, of atoms in FCC stacking followed by a DL parallel to the step edge on the lower terrace seen Figure 2.12b.

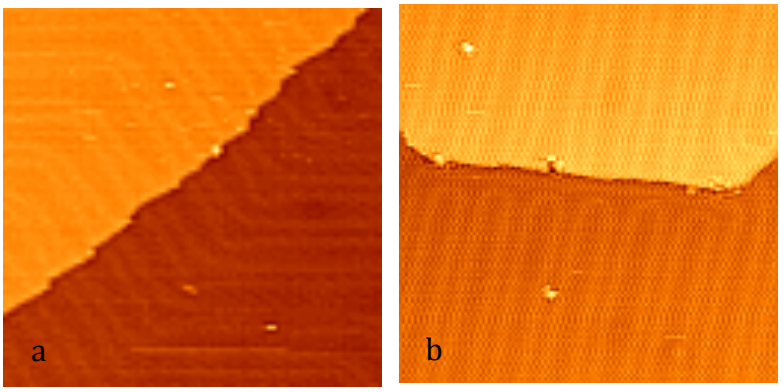

Figure 2.12 (a) The DLs can cross the step with {111} microfacet without disturbance. (b) A DL forms on the lower terrace and is parallel to the step, which stops the DLs on the upper terrace extending continuously to the lower terrace. The DLs on the lower terrace bend when they approach the {100} microfaceted step.

Also Au steps can be manipulated by the STM tip [96, 98, 99, 100] through external force resulting from a large local electrical field between the tip and sample. The restructuring of Au steps is due to the different stability of the steps mentioned above [91] and anisotropic diffusion. In an ambient environment, Au steps were observed moving during the course of continuous scanning by the tip of STM [98]. The density of Au steps on the surface of Au thin films on mica is closely related to the moving rates: from STM statistical observation [98], the higher the density, the faster the rate. However, different sections of a moving step don't advance at the same pace, so a nanostructure named gold finger [96, 99, 100] grown from step edge is fabricated through surface diffusion assisted by the STM tip. The growth of

gold fingers is direction dependent due to the anisotropy of the Au(111) surface and the difference of energetic stability of Au steps, and a fast growth rate can be achieved by a proper combination of scan direction and step orientation. The $[1\bar{1}0]$ direction, the compression direction of the Au surface, and its rotational counterparts $[01\bar{1}]$ and $[\bar{1}01]$ are found to be the preferred directions that gold fingers align along [100]. The gold finger is unstable on the surface when temperature is above 380 K. After annealing, the step appearance of gold fingers on both sides diverge from each other, as the step of {111} microfacet stays smooth while the other one of {100} microfacet has the FCC area of the herringbone reconstruction projecting out from the edge to form a serrated structure Figure 2.13 [96]. The serration of the step minimizes the step energy by changing the step with {100} microfacet in high energy into small segments of the step with {111} microfacet in low energy arranging in a saw-tooth pattern. An STM image and a schematic diagram are shown in Figure 2.13 to show the change.

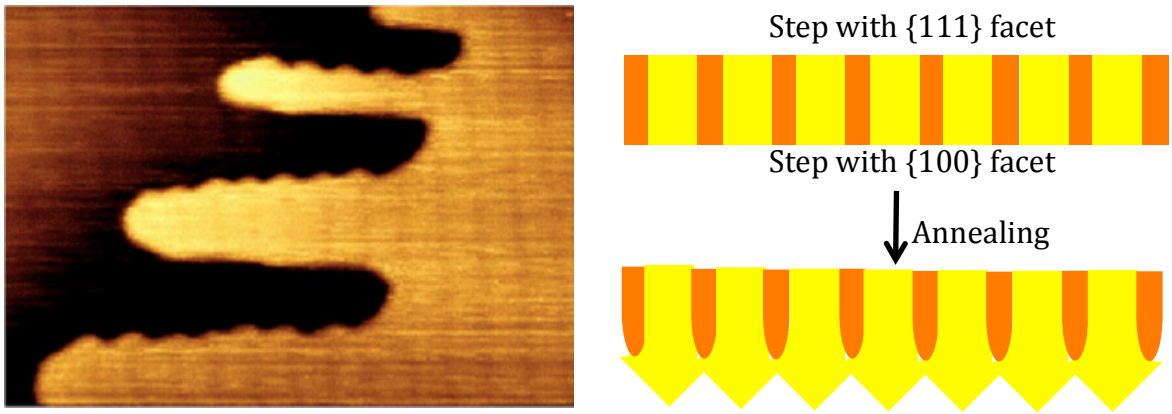

Figure 2.13 On the left is an STM image of gold fingers after annealing. The gold fingers grew in the direction perpendicular to the DLs, i.e., $[1\bar{1}0]$*. After annealing, one of the two long step edges with {100} microfacet was transformed to serrated*

structure with {111} microfacet as shown in the schematic diagram on the right. (Images cited from [96].)

The long range organization and stability of Au(111) vicinal surfaces populated with steps, are also closely related to the atomic structure of the steps [95, 101, 102]. A vicinal surface is always related to a low-index surface in crystal and consists of a series of consecutive steps with low-index terraces. An ordered array of steps in the vicinal surfaces of Au(111) with preferential separation between steps was reported from STM observation [103], which can be explained by the mechanism of surface energy minimization through surface reconstruction. The terrace sizes between the steps of vicinal surfaces from theoretical study [101] are closely related to the surface reconstruction, specifically the width of the terraces being multiples of the reconstruction periodicity of the Au(111) surface when the surface free energy is in a local minimum. The Au(455) surface, one of the Au(111) vicinal surfaces, misoriented to the (111) surface by 5.76°, was studied by X-ray diffraction and STM [104]. The steps of the (455) surface are equally spaced at room temperature after the treatment of being annealed at a temperature of 880 K and then cooled to room temperature, the surface is in a hill-and-valley morphology with steps divided into two phases of orientational angles 4° and 10° with respect to (111), and superperiodicities 80 nm and 100 nm respectively [102, 104]. The two phases of the clean Au(455) surface further evolve at high temperatures from 550 K to 1000 K with one phase showing an increasing misorientation angle from 4° to 5.2° and larger step density while the other phase stays intact with no change of misorientation angle and step density. Many other vicinal surfaces of Au(111) [93, 102, 104, 105, 106] have been studied from the

view of thermal dynamics, surface stress etc. to explore the original nature of vicinal surfaces and their potential applications.

The monoatomic steps of Au(111) and its vicinal surfaces are used as template for the growth of one dimensional (1D) nanostructures due to their tunable terrace sizes and site selectivity [107, 108, 109]. For instance, the Au(677) vicinal surface with a {111} microfacet has alternative FCC and HCP segments along the step edges, which leads to a clear adsorption selectivity as various molecules tend to attach to the FCC region at a low coverage [107, 108, 110]. Theoretical calculation explains the site selectivity through a mechanism of relaxation in the HCP region where atoms in the lower edge relax outward and thus gain extra coordination resulting in a passivated step edge [111]. Beside the site selectivity, size-regulated and parallel-aligned growth of graphene nanoribbons of subnanometer width is also realized on the step terraces [112].

2.2.3 Au(111) Supported Metal Nanostructures

Due to the inertness surface of Au and the large terrace easily obtained by thermal deposition of Au on mica or Highly Ordered Pyrolytic Graphite (HOPG), Au surface is an ideal substrate to study atoms/molecules deposited on Au in air [113] or in high vacuum. Therefore, beside Au single crystals, Au thin films grown on mica and HOPG can also exhibit the Au(111) surface with atomic flat terraces extending to hundreds of nanometers. The study of gold epitaxial growth was characterized by STM, as the direct imaging of the surface provides the growth mode in atomic scale [114]. At the initial stage of epitaxial growth, i.e., submonolayer coverage, Au atoms, after landing on the freshly cleaved mica surface, nucleate into islands of single-layer height. The gold islands can expand to large terraces of several

hundred Å with a continuous supply of Au atoms. A second layer starts to grow before the first layer is completely filled. For Au thin films of hundreds of layers, hill-and-valley surface topography is observed. Moderate annealing at temperature of about 300 °C during epitaxy growth can lead to a smoother surface morphology as thermal activation promotes Au atom diffusion across the surface, which is indirectly proved by depressions on Au surface filling in and the movement of steps [115] at room temperature.

Another important system of Au(111) supported growth is the bimetallic system using gold as a base and other metals such as Ni, Pd, Pt etc. as dopants [116]. This system is extensively used in heterogeneous catalysis to improve selectivity and efficiency via the interplay of the two metallic elements. The growth mechanism and long-term post deposition changes for these metals on Au(111) are the focus of scientific research as the size and shape of the metallic clusters on Au(111) are crucial in the field of nano devices fabrication, and catalysis. Some metals such as Ag, Cu and Al stay anchored after landing on the surface while some metals, for example Pd, Ni, Co and Pt, diffuse to preferred nucleation sites in most cases the elbow sites and step edges, on the Au(111) surface. Generally, from the aspect of surface diffusion, the metals deposited can be classified into two categories, where the difference mainly comes from the interaction between the cluster and the surface.

Ag clusters deform from incoming structures to a flattened structure even after being soft-landed on substrates [117, 118]. The height of the Ag clusters shifts from a maximum of four layers to a minimum single layer with increasing deposition energy from 1 eV to 340 eV, i.e., the kinetic energy of a cluster. When the kinetic energy of Ag clusters is below 3 eV, the cluster-surface interaction is the

key factor for cluster height distribution: the larger the cluster size the higher the cluster height. There exists a post-deposition decay process for Ag clusters soft-landed on Au(111), which is explained from theoretical simulations [118, 119, 120]. Grönhagen et al. [118] suggests that the downwards diffusion of Ag atoms from step edge of the top layer cluster is assisted by a nonlocal effect that the increasing binding energy of lower-part cluster with Au surface lowers the migration barrier of Ag atoms on the top of a cluster. For Ag thin film on Au, at low coverage, Ag islands grow continuously in fingerlike rows until expanding to large terraces at high coverage [121, 122]. For coverage over a monolayer, there is a mixing of Ag and Au atoms at the interfacial layer [123].

The Cu adlayers on Au(111) have been widely studied in electrochemical environments [124, 125, 126]. Similarly to Ag, in underpotential deposition of liquid environment, the nucleation behavior of Cu is homogeneous on Au(111) due to its lower surface energy than Au(111) [127]. Ordered structures, $\left(\sqrt{3}\times\sqrt{3}\right)R30°$ and (1×1) are observed in situ by STM [124, 125]. Yet, under vacuum conditions, at a coverage of ~0.02 ML, Cu atoms are shown as dark features at elbow sites in the area where dislocations exist, i.e., the FCC area of bulged elbows and the HCP area of pinched elbows [128]. When the coverage reaches 0.062 ML, small islands, formed at coverage of 0.02 ML, grow further into triangular islands [128]. Copper islands begin to merge from a coverage of 0.36 ML [128] and a second Cu layer has developed before the completion of the first layer. Similar discommensuration lines to these on Au(111) are observed on both first and second Cu layer on Au(111) but grow unidirectionally [128].

The metal atoms Ni and Pd both prefer to grow at elbow sites of reconstructed Au(111) from small 2D clusters to truncated triangular islands [129, 130]. There is

a place exchange mechanism for the nucleation of 2D Ni clusters at the very beginning, in which Au atoms at the elbow sites are substituted by deposited Ni atoms and these Ni atoms in the top Au layer further anchor incoming Ni atoms [131]. The growth of the first and second layers can proceed at the same time, as long as the 2D Ni islands on Au(111) are large enough to accommodate incoming Ni atoms [132]. Annealing ultrathin Ni layers on Au(111) lead to smoothness of the surface, and at 570 K Ni film is submerged by Au atoms forming bimetallic Ni/Au alloy under top Au layer, as shown in the schematic diagram Figure 2.14 [132].

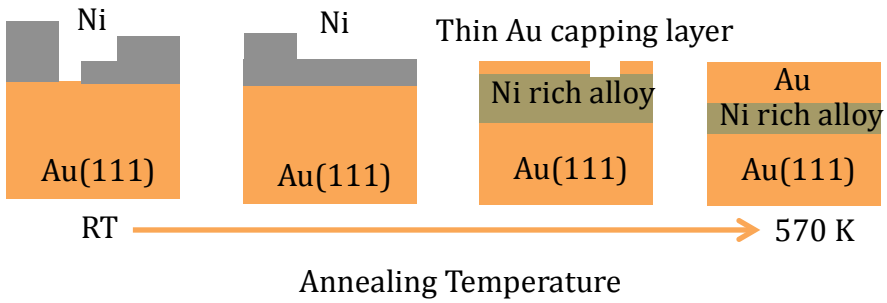

Figure 2.14 Schematic diagram showing the annealing process of Ni thin layers on Au(111) from room temperature (RT) to 570 K and the process of Ni atoms submerging into the Au substrate [132].

Theoretical calculations based on the embedded-atom method [133] further confirm that Ni clusters on Au(111) diffuse into Au substrate in a two-step manner by firstly incorporation into Au surface layer and then expulsion of Au atoms in the surface, which is an energetic and kinetic tendency of the Ni/Au system.

Another widely studied bimetallic system is Pt/Au in the application of catalysis. Before the formation Pt islands, a single Pt atom on Au(111) is imaged, similarly to Cu, as a dark void on the Au surface, which is due to the place exchange with the

surface Au atom. An opposite STM contrast for Pt atoms on an Au substrate has also been obtained in different tip conditions [134]. Pt clusters can also form ordered structures on Au(111) at very low coverage. The growth tendency shows random distribution, accompanying the modification of the herringbone pattern at higher coverage of Pt due to the change of local stress [135]. The ordered structures of Pt islands are fabricated on the vicinal Au surface – Au(788) [135] as in the case of Ag [136]. In UHV deposition, the growth of 2D multilayers of Pt can be observed by STM [136]. The growth of Pt cluster on Au(111) is also studied by in situ X-ray absorption spectroscopy (XAS) for the purpose of catalytic application in fuel cells [137], where Pt as a catalyst is of great interest to scientists and widely studied for the oxidation of CO and its reaction with oxygen. When Pt is oxidized by oxygen, the resulting Pt oxides behave totally different from pure metal on the Au(111) surface, as is discussed in section 2.3.

2.2.4 Au_n Cluster: Structure and Catalytic Property

The electronic structure and geometric structure of nanoparticles and nanoclusters are key factors in determining their physical and chemical properties, stability, and electronic characters, all of which could possibly influence their commercial potentials in industry and manufactory. Extensive scientific research in various disciplines unveils more and more knowledge of gold clusters and nanoparticles [138]. So far, Au clusters have been proposed to take on 2D planar and 3D caged structures.

The thermal stability of Au nanoparticles or clusters [139, 140] in the size range of hundreds of angstroms in diameter plays an important role in applications in fuel cells, catalysis [141] etc. that require high energy to activate reactions such as CO

oxidation [142] and nitrogen oxide reduction [143]. Sintering of Au nanoparticles during catalytic reactions can lead to serious deterioration of their efficiency. One way to stabilize Au clusters on substrate is to find a surface that can pin the clusters and sometimes assist the performance of the clusters [139]. Direct observation of Au clusters in images always needs the assistance of a different substrate such as a metallic or oxide surface as support, which will interact with the clusters and affect the properties of Au clusters to some extent. In this section, the structures of Au clusters in the gas phase with atomic number $n < 20$ will be discussed, which are free from any effects of substrates [138]. Theoretical modelling is focused on the geometric structures and correlated electronic properties of neutral, anionic, and cationic Au clusters in gas phase to explain the catalytic activity in terms of active reaction sites and size sensitivity. The electronic information can be obtained using photoelectron spectroscopy and optical spectroscopy [144]. And the structural information can be indirectly deduced from quantum chemical calculation by comparison between the spectra of theoretically proposed structure and experimentally obtained spectra [144].

Häkkinen and Landman studied the anionic and neutral Au clusters Au_n $2 \leq n \leq 10$ by comparing theoretical structures with photoelectron spectroscopy data, and found that optimal structures changed from planar when $n \leq 7$ to three dimensional [145]. They calculated that the binding energy per atom with respect to the number of atoms in the cluster and discovered an odd-even oscillation for Au_n clusters with even numbers more stable than odd-numbered $Au_{n\pm1}$ clusters [145], and that the anionic even-numbered Au_n^- cluster can attribute electrons to the anti-bonding LUMO of O_2 adsorbed on the clusters, due to their higher affinity levels, which could induce a high reactivity of the oxygen/Au cluster system. Wang

et al. through a unconstrained global search for lowest energy structures for small Au_n clusters, found that the structural transition happened at the Au_7 cluster which was in a flat cage shape – a pentagonal bipyramid and that an odd-even fluctuation – similar to the discovery of Häkkinen and Landman mentioned above, of cluster properties in the aspects of HOMO-LUMO gap, and ionization energy, i.e., the even-numbered Au_n clusters more stable [146] existed. The lowest energy structure of Au_{12} is a flat cage – a transitional structure from 2D planar ($n \leq 6$) to 3D compact and spherical ($n \geq 15$) with binding energy per atom 2.5 eV and HOMO-LUMO gap 0.82 eV [146].

P. Gruene et al. investigated Au clusters in the size of 7, 19 and 20 by means of vibrational spectroscopy and quantum mechanical calculations [147]. The vibrational spectra from infrared multiple-photon dissociation spectroscopy and corresponding DFT calculations of the Au_7 structure imply a nonsymmetric geometry – a flat edged-caped triangle – to be the ground state structure [147], which is at variance with most studies.

Gilb et al. obtained the geometry of positively charged Au_n^+ ($n < 14$) via ion mobility measurement [148] where the mass of clusters is determined by the travel time for the ion drifting through a gas (helium) cell accelerated by a static field and the cross section of a given Au_n cluster isomer corresponds to one certain value, therein containing the structural information of the cluster. Their DFT calculation shows that Au_n cluster dimension expands to three dimensions at $n = 8$ and the theoretical cross-sections of lowest energetic structures agree well with experimental data within the measurement error except when n equals 4, 10 and 13 [148].

The dimensional structure transition occurs due to the lowering of the cluster energy by increasing the number of bonds for each atom the transitional numbers as shown before usually being around 6 or 7. In contrast to previous theoretical calculations, fairly large planar clusters with a maximum of 12 gold atoms are expected to exist in ion mobility measurement [149]. In the ion mobility experiment [149], the dodecamer has two peaks in the plot of arrival times versus intensity, which indicates the existence of two isomers for Au_{12}, one of 3D structure and the other of 2D symmetric structure. One plausible explanation for the formation of a large planar Au_{12} anionic cluster is the relativistic effects in the clusters made of coinage metals (Cu, Ag and Au). The electron distribution of a Au atom has a fully filled 5*d* shell and a single electron at the 6s shell, where the relativistic effect stabilizes the $6s^1$ electron and delocalizes $5d^{10}$ electrons, and causes a hybridization of the *s* and *p* electrons associated with shortened interatomic bonding lengths for the Au_n (n = 4-14) clusters [150, 151, 152]. The significant relativistic effect of gold clusters can possibly change their chemical reactivity and physical stability in the gold-related system [153]. A planar quantum dot model can also be applied to explain the planar structure of Au_{12} because the outer electron shell of orbitals in the Au_{12} cluster is fully occupied by the 12 Au $6s^1$ electrons in a configuration of $1s^21p^42s^21d^4$, the origin of its structural stability [138, 153]. The Au clusters in a closed-shell electron configuration show low binding energy and a large energy gap in photoelectron spectra [151]. The 2D to 3D transition at the critical cluster size 12 is further proved from the Argon tagging experiment [154]. Ar atoms can be physisorbed on the Au(111) plan of Au clusters via weak van de Waals interaction, therefore favouring adhesion on 2D Au_{12}^- more than its 3D isomer. The planar 2D Au_{12}^- cluster condensed with Ar atoms can be

picked out of the cluster beam and, as a result, an increasing portion of 3D Au_{12}^- is observed from photoelectron spectra [154]. This method is limited to the situation of subtle energy difference between the 2D and 3D structure of Au_n^- clusters and this is the case for the 2D and 3D structures of Au_{12}^- cluster. Also, due to the reason aforementioned and depending on the computational methods applied, 3D isomers of Au_{12} cluster have also been proposed to be the ground state [155, 156]. It is difficult to observe the structures of neutral Au clusters in mobility measurement although theoretical calculation indicates little structural divergence between the neutral and negatively charged clusters [151]. Placing neutral Au clusters on a inert substrate is a possible way to study their properties.

Besides atomic arrangements in the Au_n clusters, charge state [157, 158, 159] is another critical factor concerning applications, which can be greatly influenced by the interaction with substrate [158]. Au atoms in either surface or cluster form tend to be electron acceptors [152], and even within the cluster, the charge distribution among the Au atoms is not uniform with atoms at the corners - lowest coordinated atoms - negatively charged, on the edges less negative, and in the center of a plan – high coordinated atoms - in the positive charge state [157]. This charge distribution can assist charge transfer from the cluster to adsorbates to lower the activation energy of a chemical reaction or enhance the bonding strength within the molecular clusters of multi-elements.

2.3 Pt Oxide

The oxidization of Pt has been widely studied, by various techniques such as XPS [160], XAS and STM [161, 162] on different Pt crystalgraphic plans [160, 161, 163, 164] or Pt clusters [137], in different environment – vacuum of low oxygen partial

pressure or ambient condition [160]. The exploration of Pt-based system helps to understand catalytic reactions such as in CO oxidization [165] and the reduction of NO and oxygen [166] where Pt plays a key role. The knowledge leads to practical industrial applications in the design of catalytic reactor [167].

The adsorption states of oxygen on Pt(111) undergo transition from physisorbed to chemisorbed through kinetic activation at a temperature as low as 40 K as revealed by XPS detection [168]. Oxygen atoms from dissociative adsorption on Pt(111) arrange in an ordered (2×2) structure at a low temperature of ~ 150 K under STM observation [169, 170]. Atomic oxygen is imaged as a dark spot on the Pt(111) surface occupying a FCC hollow site [169, 171]. When CO molecules and O atoms coadsorb on the Pt(111) surface, both of them arrange in a regular structure - c(4×2) for CO and (2×2) for O as mentioned before. The transformation of CO_{ad} and O_{as} to CO_2, which will be released from the surface, takes place at low temperature and from the boundary of the islands of CO and O [170]. With a continuous supply of CO, the Pt(111) surface is fully covered by CO until the depletion of O_{ad} [170]. Under high oxygen pressure ~ 1 Torr, and at elevated temperatures, Pt surfaces undergo oxidization [161]. From XPS and XAS data [160], Miller et al. proposed that the oxidization process of Pt(111) started from the formation of a PtO surface oxide with chemisorbed oxygen, proceeded to a thin PtO_2 trilayer and at last bulk oxidization. On Pt(110) Figure 2.15a where every other close-packed Pt row is missing, oxygen atoms prefer the FCC sites aside the Pt ridges [163, 164]. A possible structure of PtO_2 is proposed, based on STM observations and DFT calculation with oxygen coverage of 2 ML, to be like what is shown in Figure 2.15b [163, 164, 172]. Due to the oxygen adsorption, Pt atoms in the row are supposed to experience vertical relaxations induced by an effective

attractive interaction between every pair of oxygen atoms in the direction perpendicular to [1$\bar{1}$0] [163, 164]. The uniformity of this kind of PtO chain along the ridge can be improved by performing O exposure at elevated substrate temperatures up to about 600 K [164].

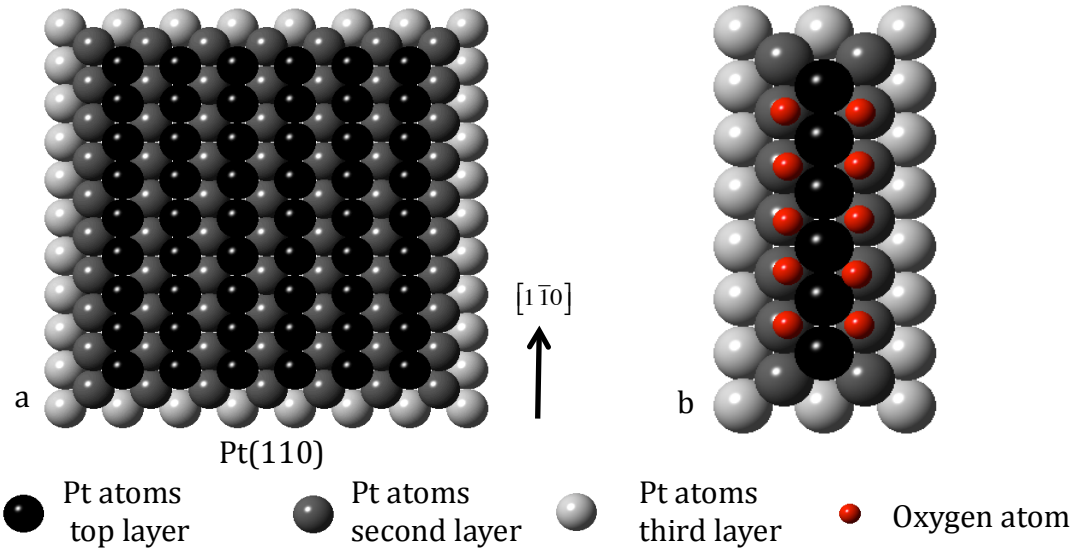

Figure 2.15 Ball model of Pt oxide on Pt(110). (a) The Pt(110) surface crystallographic structure, dark balls are Pt atom in the top layer, dark grey in the second layer and light grey in the third layer. In the [1$\bar{1}$0] *direction are rows of close-packed Pt atoms. (b) Proposed model of the Pt oxide based on DFT calculations when oxygen coverage is 2 ML. Oxygen atoms occupy FCC sites on the sides of the Pt row [172].*

The steps of Pt substrate are energetically preferred sites for oxygen adsorption, dissociation and formation of Pt oxide [173, 174] which, comparing with gas-phase O_2, may be due to that the Pt steps assist in lowering the dissociation barrier for absorbed molecular oxygen [175], or stabilize the molecular precursor state and the transition state after oxygen adsorption [174], according to theoretical

modelling. Miller et al. associate the variation of dissociation barriers with the oxygen coverage [176, 177] in which small dissociation barriers of about 0.3 ~ 0.4 eV are yielded. Their calculation shows that the interatomic interaction of O-O in different supercells which are closely correlated with different oxygen coverage, influences the final state of oxygen atoms, thus giving a dissociation barrier of 0.24 eV comparable with experiment evidence.

2.4 The C_{60} Molecule

Fullerene usually refers to molecules made only of carbon atoms in closed structures of cages. One member, the most famous and well studied, of the fullerene family is C_{60} which is given a specific name – buckminsterfullerene or buckyball [178]. The C_{60} molecule in a nearly spherical cage has attracted a lot of attention due to its unique and symmetric structure and a variety of properties, which can be used in different disciplines, e.g. in surface science C_{60} molecules always acting as building blocks in nanostructures. In this section, the knowledge about C_{60} from synthesis, isolation to its physical and chemical properties in the form of a single molecule or a thin film on the Au(111) substrate or solid is introduced. Some interesting discoveries of C_{60} related nanostructures are included at the end.

2.4.1 C_{60} Molecule: Synthesis and General Properties

So far three methods have been employed to synthesize C_{60} molecules. The arc-discharge process [178, 179] was the first discovered, and mostly convenient way to produce C_{60} molecules, where more than 50% of the fullerene production was C_{60} molecules by optimizing the time interval between the evaporation of carbon flakes using laser pulses firing on graphite and the expansion of the carbon flakes

through the He stream to an integration cup [178]. C_{60} molecules can also made by pyrolysis of naphthalene at 1273 K, in which the naphthalene provides aromatic fragments to be patched together to form the molecule [180]. Howard et al. succeeded in the production of C_{60} and C_{70} molecules from hydrocarbon combustion [181, 182]. The chemical way to synthesize C_{60} molecules is not as straightforward as the first three methods as it takes 12 steps [183]. However, the significance of the chemical method lies in the fullerene ramification, whose properties can be tuned to fit the purpose of use. Extraction and purification of C_{60} molecules can be achieved using either solvent methods on the basis of liquid chromatography [184], or sublimation methods taking advantage of the different evaporation temperatures of the members in the fullerene production [185].

The physical structure of C_{60} molecule was proposed to be a truncated icosahedron, shape of a football, with 12 pentagonal rings and 20 hexagonal rings [178, 185]. The 60 carbon atoms are located at the 60 equivalent vertices [185] with all the valence electrons paired, with therefore 60 single bonds – adjoining two pentagons and 30 double bonds – classified into two different types: adjoining one pentagon and one hexagon (5:6) or adjoining two hexagon (6:6) as indicated in Figure 2.16a. In the ^{13}C Nuclear Magnetic Resonance (NMR) experiment [186] at 77 K, when the rotation of C_{60} molecules is thermodynamically frozen [187], the average nearest C-C bond lengths were measured to be 1.45 ± 0.015 Å for the single bond shared by one pentagonal and one hexagonal carbon rings, and 1.40 ± 0.015Å for the double bond shared by two hexagonal carbon rings. The diameter of the buckyball fullerene is 7.1 Å from electron diffraction measurement in the gas phase [188]. If including the size of the π-electron cloud in the circumambience of carbon atoms, the electronic diameter of a C_{60} molecule is 7.09+3.35=10.34 Å [189].

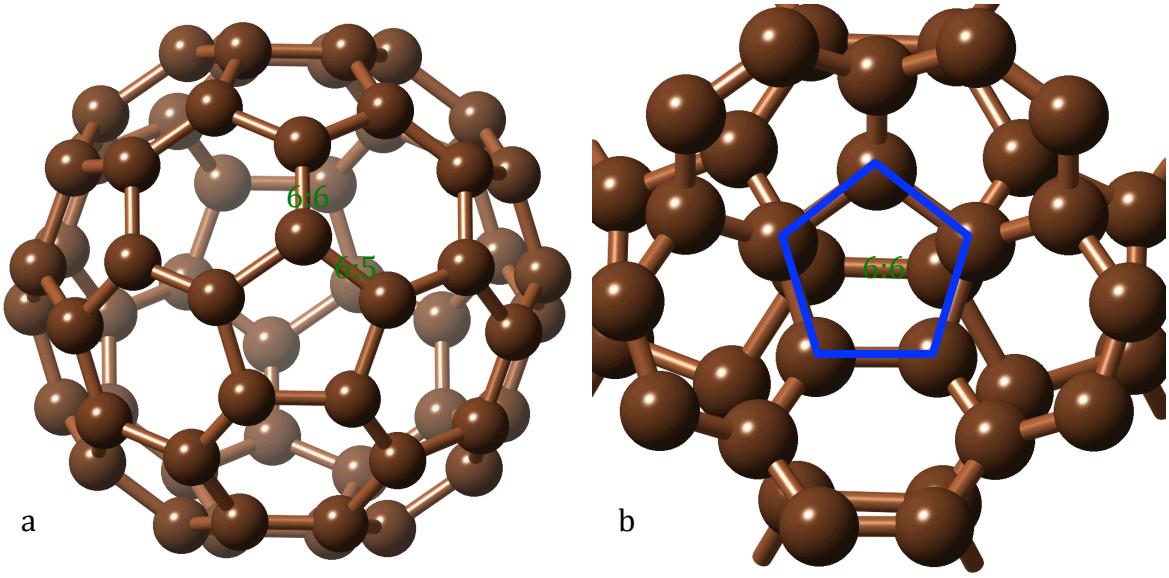

Figure 2.16 (a) A schematic diagram of a C_{60} molecule in icosahedral structure made of pentagonal and hexagonal rings. The bond between two hexagonal ring is denoted as 6:6 bond and the bond between a hexagon and a pentagon is denoted as 6:5 bond. (b) The projection of the relative orientation between two C_{60} molecules in solid. Only parts of the two molecules are shown. The blue pentagon highlights the electron-poor carbon ring that a electron-rich 6:6 bond of the neighbouring molecule faces to [190].

C_{60} molecules in solid form can form a crystal structure in FCC configuration at room temperature and ambient pressure in a rapid and isotropic rotating state and at temperatures below 249 K [191], in a simple cubic (SC) structure with orientational order of each molecule which results from both the high symmetry of the icosahedral and near-spherical structure of the molecule, and optimized bonding with least overlap of carbon atoms among neighbouring C_{60} molecules in the solid. This configuration is that the electron-rich 6:6 carbon bond faces the centre of the electron-poor pentagonal carbon ring [190] as shown in Figure 2.16b. At high pressure, 1.2 Gpa, the van der Waals cloud between molecules in the solid

can be compressed from 2.9 Å to 2.5 Å [192] measured by energy-dispersive X-ray diffraction. The solid has the same linear compressibility as graphite in the out-of-plan direction and a volume compressibility 6.9×10^{-12} cm/dyne (1 dyne = 1 gcm/s^2), about three times as large as that of graphite until the limit of the compression, with little distortion of the stiff molecular cage [193]. The transition temperatures T_c from SC to FCC are linearly and directly proportional to hydrostatic pressure, in a rate of +10.4 K/kbar, due to a possible change in the orientation barrier [194]. The phase transition of bulk C_{60} is summarized in Figure 2.17 [195 and references therein]. The left line corresponds to the solid-state transition from SC to FCC. At pressures below atmosphere, the transition temperature changes little, in great contrast with the tendency at high pressures. Further to the right is the solid-to-vapor phase line which ends at a point where a narrow liquid phase may exist above 1800 K [196, 197]. High pressure (solid line on the top in the phase diagram) [198] or high temperature (vertical solid line to the far right in the phase diagram) ~ 5000 K from theoretical predication [199] can both lead to the degradation of C_{60} molecule.

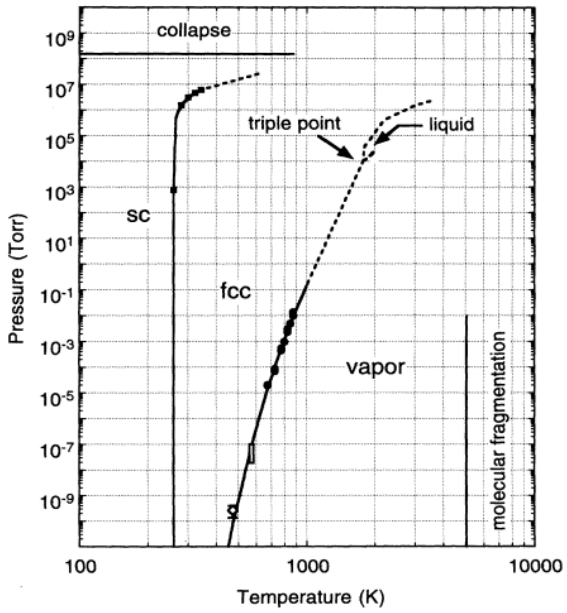

Figure 2.17 Phase diagram of the C_{60} molecule. The left solid line is the crystalline transition of solid C_{60} from SC to FCC. Below 10^5 Torr, the pressure-dependent transition temperature shows no obvious change, therefore there is almost a straight vertical relation between the transition temperature and the pressure below 10^5 Torr. The curve on the right is the boundary between the solid phase and the vapor phase. There may be a triple point on this line where a liquid phase exists, at around 1800 K. The horizontal line on the top of the diagram and vertical line on the right of the diagram are the limits of pressure and temperature when C_{60} molecule can stay intact. [195 and references therein]

Accompanying with phase transition between FCC and SC at 261 K, there is a discontinuity during the process of lattice constant diminution, with decreasing temperature with a variation of 0.044 ± 0.004 Å (Figure 2.18) from X-ray measurement with a hysteresis of less than 0.5 K [200]. An abnormal volume expansion is also observed at ~ 90 K during heating or cooling studied by high-resolution capacitance dilatometry [201]. In the thermal expansivity measurement,

a hysteresis of 1.5 K between heating and cooling process prevails in the relation between temperature and volume expansivity, and the onset temperatures of the transition shift to smaller values with decreasing heating or cooling rates from 0.15 mK/s to 20 mK/s, which both are the characteristics of glass transition with freezing in of orientational freedom [201, 202]. This anomaly at 90 K is related to a local relaxation of disordered regions in the solid with measured activation energy of 288 ± 5 meV [201]. The disordered region has an electron-rich double bond in conjunction with a hexagonal ring [203] instead of a pentagonal ring [190] as aforementioned. The solid contains about 16.5 % C_{60} molecules in "disordered" phase – a second preferred orientation of C_{60} molecule as shown in Figure 2.18b inset B. This phase composition remains constant until the temperature goes beyond 90 K. Then the proportion of orientation B increases continuously as it approaches 260 K, a counterpart to the temperature-occupation relationship in Figure 2.18b [203]. At temperatures above 260 K, C_{60} molecules are in orientational disorder with no fixed axial rotation.

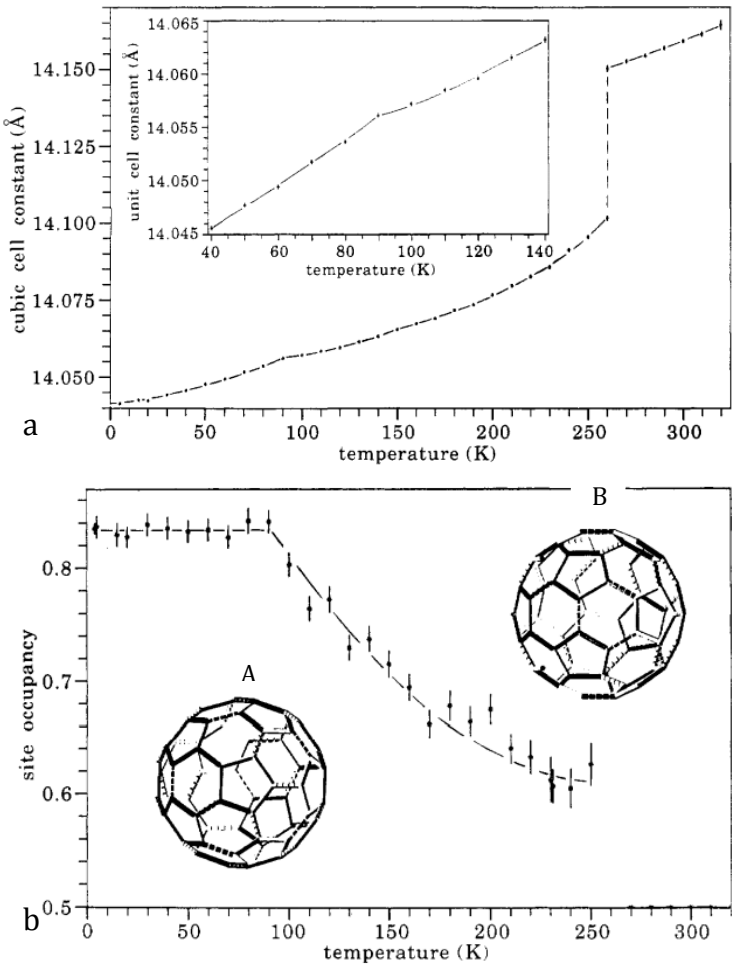

Figure 2.18 (a) The variation of the lattice constant of C_{60} solid with temperature. An obvious jump of lattice constant happens at 260 K in correspondence with the first-order phase transition between FCC and SC. A second-order phase transition starts from 90 K as shown in the inset. From 5 K to 90 K, a minority of C_{60} molecules (about 16.5 %) orientates in a direction close to the optimized van der Waals arrangement. (b) A phase change in orientational orders as temperature increasing from 5 K to 310 K. At temperatures below 90 K, about 16.5 % of C_{60} molecules take on the orientation as in inset B and 83.5 % as in inset A. From 90 K to 260 K, more and more C_{60} molecules gradually transit to the orientation of inset B [203, 204].

The orientational phase transition temperature is frequency dependent. Therefore, different transition temperatures have been reported, around 80 K from thermal expansion experiments [201, 203] and around 160 K from sound velocity measurement [205] and dielectric response observation [206]. Essentially, the observed phase transition has the same origin [207].

The electronic structure of the C_{60} molecule has been extensively studied by both experimental [208, 209, 210, 211, 212] and theoretical methods [213, 214, 215, 216], which is critical for the understanding of molecular adsorption and desorption, the formation of thin film and multi-element nanoclusters etc. The photoemission (PES) technique can probe the occupied states of the C_{60} molecule below the Fermi energy level (E_F) [209, 210], where studies are often carried out on C_{60} molecules in condensed form on different substrates. The PES spectrum is obtained from the information in the emitted electrons excited by incident photons of energy $h\nu$. The ionization energy of a C_{60} molecule was reported to be 7.6±0.2 eV, from the X-ray photoemission study [209], and its electron affinity to be 2.65±0.05 eV [217], this high value making the C_{60} molecule an electron acceptor in interactions with other atoms such as alkali metals or noble metal surfaces [218]. With increasing photoelectron energy, deeper energy levels of the molecule can be detected. The valence band structure of the C_{60} molecule is characterized by p_π derived bonding states within 5 eV below the E_F, s-p_σ derived bonding states, within 5eV to 12 eV below the E_F, and the deepest states derived from s-like σ bands, all inclusive in a bandwidth of about 23 eV, similar to that of graphite and diamond [210]. The inverse photoemission spectroscopy (IPES) technique can detect the unoccupied states of the C_{60} molecule, in which incident electrons enter the excited states with emission of photons of different energy [211]. The energy

gap between the ionization energy and the electron affinity is 4.9 eV for the C_{60} molecule in gas phase [219] (Figure 2.19), and is about 2.3±0.1 eV for the C_{60} molecule in solid [220], corresponding to the difference between the under edge of the lowest unoccupied molecular orbital (LUMO) and the upper edge of the highest occupied molecular orbital (HOMO). The impact of the substrate in photoemission and inverse photoemission measurement can be eliminated when the thickness of C_{60} films reaches a few layers with no mixing of molecular states and substrate states [221].

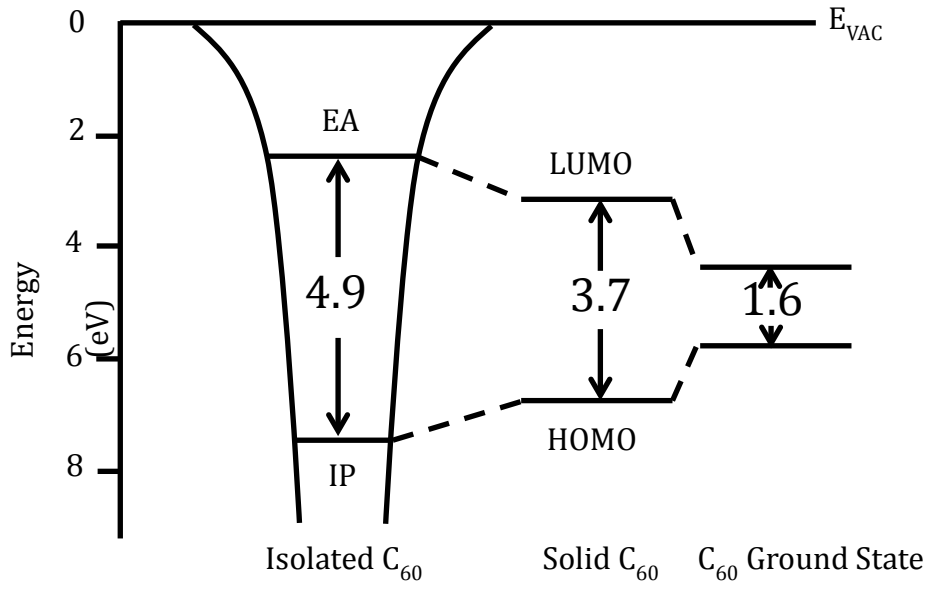

Figure 2.19 The energy gap between the electron affinity and ionization energy of isolated C_{60} is 4.9 eV. The energy difference between the centre of HOMO and the centre of LUMO is 3.7 eV while that between the under edge of LUMO and the upper edge of HOMO is about 2.3 ~2.6 eV, the intrinsic band gap. The band gap in ground state C_{60} is 1.6 eV, the lowest energy cost for the separation of a hole and an electron in a neutral C_{60} molecule. [212]

Both the PES and IPES measurements involve the changes of electrons in the studied system. Therefore, the PES spectrum shows the band information for the (60-1) electron, as one electron escapes from the molecule due to the excitation of photons, and the IPES spectrum contains the energy states for the (60+1) electron as one extra electron is injected into the molecule, occupying an excited state above the LUMO. The excited states observed in high-resolution electron-energy-loss spectroscopy (HREEL) are the states for a neutral C_{60} molecule. So far the smallest energy gap in HREEL is ~ 1.6 eV [222] as shown on the rightmost side of Figure 2.19.

2.4.2 C_{60} Molecules on the (111) Surfaces of Noble Metals

STM is an ideal technique to study C_{60} film on various substrates regarding the epitaxial growth mode of the film, the interface interaction between the C_{60} monolayer and the substrate as well as the properties of individual C_{60} molecule at low temperature when the rotation of the molecule is frozen. The structural, thermal and electronic properties of C_{60} molecules will be discussed in detail.

2.4.2.1 C_{60} Molecules on the Au(111) Surface

To deposit C_{60} molecules, one can thermally evaporate C_{60} molecules onto the substrate. The growth modes of C_{60} on metal surfaces vary with the different interactions between molecule and surfaces. The most commonly studied crystallographic surface for noble metals such as Au, Ag and Cu is the close packed (111) surface. The nucleation and growth of C_{60} molecules on the Au(111) surface will be presented as an introduction to the subject.

At room temperature, C_{60} molecules can diffuse freely on the Au(111) surface until they meet the step edge where the initial growth of two dimensional islands starts,

with a subsequent supply of C_{60} molecules, firstly on the lower terrace and then both on the lower and upper terraces [223, 224, 225]. The exclusive adsorption at the lower terrace side is due to the enhanced LDOS [86] there, and therefore the strong interaction between the molecule and the Au atoms. The unique $22\times\sqrt{3}$ herringbone reconstruction of Au(111) leads to an ordered growth of 2D C_{60} islands at the elbow sites at a low temperature of ~ 80 K [225], when the kinetic energy of C_{60} molecules cannot escape the confinement of the barrier at the elbow sites where a surface lattice dislocation exists [129]. Besides, the alternatively arranged FCC and HCP segments at the step edge have different affinity to C_{60} molecules. At low coverage, only the FCC segments are decorated with small molecular arrays [223]. With increasing coverage, close-packed molecular layers form in a layer-by-layer manner. C_{60} molecules in the second layer don't show any preference to step edge and little interaction with the substrate, as their desorption temperature is about 573 K, well below the desorption temperature of the first C_{60} layer from the Au substrate, which is about 773 K. In experiment, we can take advantage of this property to obtain a pure single layer of C_{60} molecules. In the close-packed multilayers, the nearest-neighbour distance is ~ 1.0 nm [226, 227], and the molecular height is about 0.7 nm on the Au(111) surface, and 0.81 nm on the first C_{60} layer where each molecule sits at the three-fold hollow site of the hexagonally packed first layer [223].

The close packed direction of the C_{60} overlayer is not always the same as that of the underlayer Au(111) surface. Using the DLs on the uncovered Au surface which runs in the $[11\bar{2}]$ direction as a reference, the relative orientations of the C_{60} overlayer on the Au(111) surface can be determined. So far four phases have been reported from STM and low energy electron diffraction (LEED) observations, the

superlattices denoting as $2\sqrt{3}\times2\sqrt{3}$-R30°, 38×38-R0°, $\sqrt{589}\times\sqrt{589}$-R14° or 7×7-R14° in bulk C_{60} lattice spacing to represent the size of a unit cell and 3×3-R34° [223, 228, 229, 230]. In each of the above expressions for the superlattices, the numerical value behind "R" represents the relative angle between the close packed direction of the Au(111) surface and that of the C_{60} layer. Large coincident unit cells are required to match the lattice difference. The molecule spacing of 1.0 nm is not in registry with the atom lattice constant 0.238 nm, except the $2\sqrt{3}\times2\sqrt{3}$-R30° phase. Therefore, in all the other phases the occupation sites of C_{60} molecule in a unit cell on the (111) substrate are not the same, and the occupations are at any of a hollow site, a bridging site, an on-top site and places in-between these sites [223]. The $2\sqrt{3}\times2\sqrt{3}$R30° phase is the only one where all C_{60} molecules in the overlayer sit on the same site over an unreconstructed Au(111) surface, and is named the commensurate phase. This phase is also experimentally observed to be the thermodynamically stable phase, and becomes abundant after the sample is annealed at 350 °C [229]. The 38×38 phase, which has a unit cell that contains 38×38 Au atoms or 11×11 C_{60} molecules, is called the "in-phase" superstructure because of the coincidence of the close packed direction of both the Au underlayer and the C_{60} overlayer [229]. The R14° phase has a unit cell comprised of 49 molecules. At a low temperature of 5.7 K, low enough to stop molecular rotation, Schull and Berndt reported the observation of orientational order in the superstructure [230], rotated by ±14° to the close packing direction of the (111) lattice.

The intramolecular structure of C_{60} can be differentiated under STM observation when the molecule is static at low temperature or anchored by strong interaction with the substrates [231]. Three intramolecular patterns, (Figure 2.20a) [230] of a

C_{60} molecule in STM images can be assigned to three different molecular orientations [232] based on the fact that at positive sample bias, the pentagonal ring is imaged bright [233].

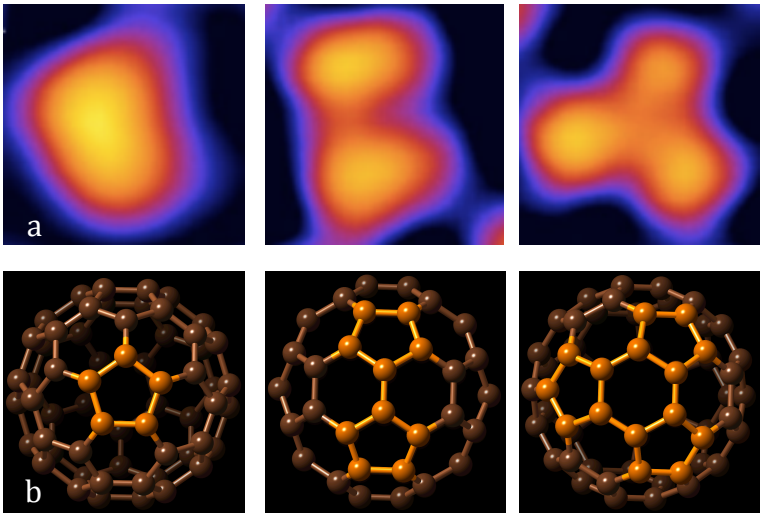

Figure 2.20 The assignment of three molecular orientations to corresponding intramolecular STM images. (a) Three STM images of intramolecular structures of C_{60} molecule. The bright lobe is the five-member pentagon ring. (b) Corresponding molecular orientations. The pentagon rings are in orange colour. One bright ring is a pentagon ring facing upwards or the Au substrate, two bright lobes a 6:6 double bond, and three bright lobes a hexagon ring. [230]

Figure 2.20a displays the three intramolecular structures obtained by STM at 5.7 K. Below these STM images are corresponding models. As is generally known, for free C_{60} molecules, the HOMO of the molecule is centred at the double bonds between two hexagonal carbon rings and the LUMO is at the bond of a hexagon and a pentagon. Therefore, the pentagonal carbon ring is an electron poor region, and is imaged bright at the positive bias when electrons tunnel from the tip to the

molecule [189]. If a C_{60} molecule is imaged as one bright lobe at positive bias, one of its pentagon rings sits on the substrate, and due to the symmetry of the quasispherical shape of C_{60}, also faces upwards from the top view. Two lobes indicate that a 6:6 bond as shown in the middle of Figure 2.20b, is in direct contact with the substrate, and a three-lobe structure means a hexagon ring on the substrate as shown on the right of Figure 2.20b. The internal structures of the C_{60} molecule are also observed if the molecule is attached to the tip of Q-plus AFM. The appearance of Si atoms in Si(111) - (7×7) changes with molecular orientations when different parts of the molecular cage interact with the dangling bonds of Si atoms[234].

In the 7×7-R14° structure, an orientational order is observed. The molecules in one edge of a unit cell rotate gradually by steps of 7° around the same axis with the change of adsorption sites from hexagon ring to a 6:6 bond and back to hexagon ring [230]. A fourth superstructure, 3×3-R34°, with a small size, in which every third molecule sits on the same site on the (111) surface is also confirmed by STM [73]. The close packed direction is only 4° different from the close packed direction of the R30° structure. The average separation between two dim fullerene molecules is about three molecules [73].

The photoemission and inverse photoemission study of C_{60} layer(s) on Au(111) indicates the existence of charge transfer from the Au substrate to the molecules and a shift of the LUMO to the Fermi level which is aligned with the Fermi level of the substrate [221, 235, 236]. The transferred electron, estimated to be about 0.8 e^- or less on Au(111), occupies the LUMO-derived state [229]. Thus the interaction between C_{60} and Au(111) is assigned to be chemisorption, yet the weakest interaction among the metal surfaces so-far studied. The charge transfer at the

interface is believed to be the dominant reason for the high desorption temperature of monolayer C_{60} on Au(111). STS study shows a 2.3 eV gap between the HOMO and the LUMO of molecule in a single C_{60} layer [237]. Differential conductance spectroscopy at 7 K locates the HOMO of a C_{60} molecule in a molecular layer at −1.7±0.2 eV, the LUMO at 1.0±0.2 eV and the LUMO+1 at 2.2±0.2 eV [238].

The charge transfer induces the decrease of HOMO-LUMO separation [235] resulting from the decrease of the charging energy U (Hubbard energy from Coulomb interaction among charges), which comes from the screening effect from charges at the surface and among molecules [238, 239]. The HOMO-LUMO gap measured by STS is the sum of the gap of a neutral C_{60} molecule and the Coulomb energy from the repulsion between the tunnelling electron and the charges in molecular cage [239]. The repulsive interaction decreases the energy gap. The STS over one single C_{60} molecule alone on Au(111) indicates a negligible charge donation from the substrate and hence the energy gap of HOMO-LUMO increases to 2.8 ± 0.1 eV, when the screening effect from surrounding molecules disappears [239]. The photoemission measurement of the work function gives a value of 4.7 eV for single layer C_{60} on Au(111), which is 0.6 eV smaller than that of the substrate, also contributed to the screening effect [229].

Theoretical calculations of the C_{60} layer on Au(111) obtain a covalent-like bonding with ionic features at the interface between the C_{60} overlayer and Au substrate [240, 241]. The theoretical prediction of charge transfer from Au to C_{60} is about 0.2 eV [240] less than the experimental measurement mentioned before. The lowest energetic adsorption site for a C_{60} molecule is the hollow site on Au(111), where a

hexagonal ring of the C_{60} molecular cage is parallel with the surface and sits on a hollow site with an adsorption energy of -1.3 eV [240, 241, 242].

A dim and bright contrast phenomenon exists among C_{60} molecules in the first monolayer on Au(111) and other metal surfaces. Under STM imaging, some C_{60} molecules look dimmer than other molecules on the same substrate. Gardener et al. carried out a thorough investigation about the dim C_{60} molecule [73] using STM. The height difference between the dim molecule and the bright molecule is dependent on the bias voltage used in scanning, and ranges from 0.35 Å to 1.2 Å with the largest value at −1.8 V which can be attributed to the difference in the LUMO of the dim and bright molecules [73]. They also studied the transition dynamics of switching from the dim to the bright or vice versa at room temperature as this thermally driven dynamics stops at low temperature 77 K.

What could be the mechanisms behind the formation of the dim C_{60} molecule? Because STM cannot get a direct image of the interface, theoretical simulation plays an important role in determination of the interfacial structure [243, 244, 245]. The formation of Au vacancies with the size of one Au atom or of seven Au atoms beneath the dim C_{60} molecule on the Au(111) substrate is established by theoretical calculation [244, 245]. The configuration with a C_{60} molecule placed on a gold vacancy is proposed to exist with reconstruction of the first atomic layer of the Au substrate [245, 246]. The formation of the Au vacancy is attributed to the interaction between the molecule and the Au surface, with hybridization of molecular π orbitals and metal *s* states [246]. An additional mechanism for the brightness contrast is that there is more charge gain from the Au substrate for the dim molecule than for the bright molecule, and therefore, larger tunnelling resistance of the dim C_{60} molecules when electrons tunnel to the LUMO of the dim

C_{60} molecule [73]. The dim C_{60} molecule is inclined to take on a certain polar and azimuthal orientation at 77 K [247]. The dim C_{60} molecule is imaged to have a hexagonal carbon ring in contact with the Au(111) substrate, as it shows three lobs on the STM image. The locking of the cages of dim molecules indicates a local effect from the underlying Au substrate [248], perhaps the single-atom Au vacancy.

The coverage of the C_{60} monolayer can lift the herringbone reconstruction as has been observed in many experiment [243, 244]. However, a fast deposition rate may lead to a slow process of lifting the herringbone reconstruction [71, 223]. Therefore, in some cases the reconstruction is still visible [71]. The formation of the dim molecules in the monolayer possibly leads to a second reconstruction of the Au(111) layer - the relaxation of the Au first underlayer to form Au vacancies.

Another relevant phenomenon resulting from the interaction between the C_{60} single layer and the Au(111) substrate is the various distributions of dim C_{60} molecules in different phases, as shown in Figure 2.21. As mentioned above, each phase is associated with a unique superlattice structure in the molecular layer where there is an angle between the close packed direction of the C_{60} layer and that of the substrate, and a periodic sequence for the occupation site of each molecule on the substrate. Therefore, the distributions of dim molecules in a close packed C_{60} layer are strongly correlated with which phase the molecule layer takes on. For different phases, the occupation sites of C_{60} molecules on the Au(111) repeat in various periods. Figure 2.21a shows an STM image in which the C_{60} layer is in the "disordered" phase with high density of dim molecules [73]. The term "disordered" here means contrast disorder in the image. The disordered phase is assigned to the $2\sqrt{3}\times2\sqrt{3}$-R30° superstructure, all molecule being at equivalent lattice sites. A uniform phase (Figure 2.21b) has a few dim molecules in random

distribution with the 38×38-R0° superstructure, every eleven C_{60} molecules occupying the same lattice site. If the dim molecules form 2D arrays of long-range orders, the C_{60} layers are in the quasiperiodic phase (Figure 2.21c and d). It seems that a unite cell can be roughly assigned to each periodic phase based on the positions of dim molecules or clusters of two or three dim molecules.

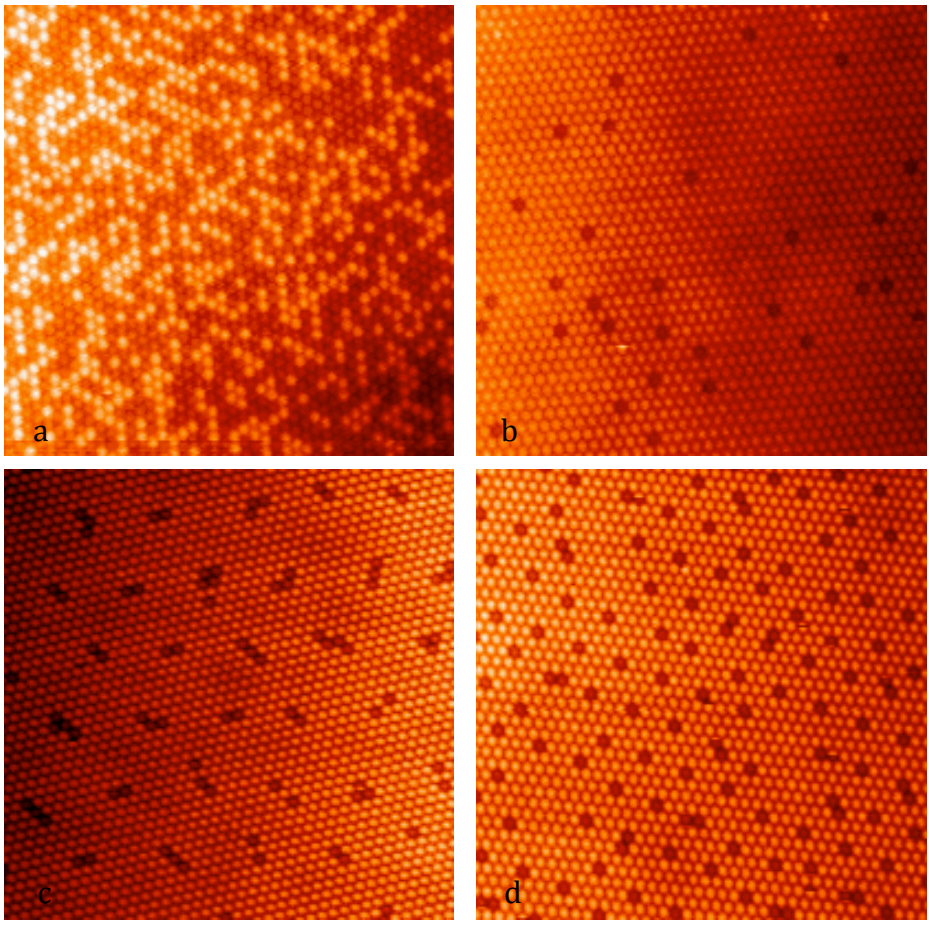

Figure 2.21 The different phases of C_{60} overlayer on the Au(111) surface. (a) STM image of a disordered phase as the dim molecule is randomly distributed. This phase is related to the $2\sqrt{3}\times2\sqrt{3}$-R30° structure. (b) The uniform phase with randomly distributed dim C_{60} molecules. This phase has the 38×38-R0° superstructure. (c) A quasiperiodic phase with the 7×7-R14° superstructure. (d) A second quasiperiodic phase with a small periodicity in the 2D array of dim molecules. This C_{60} layer shows the 3×3-R34° superstructure.

2.4.2.2 C_{60} Molecules on Cu(111) and Ag(111)

The growth mode of C_{60} molecules on the (111) surfaces of Cu, Ag, and Au follows the same pattern. 2D islands in hexagonally close-packed arrangement start to form after steps are fully covered by molecules. These three different metal surfaces all donate electrons to C_{60} molecules with differences in the amount of charge transferred, which reflect from the modification in the molecular orbital states [229, 249]. The binding energies along with the amount of charge gain from the substrates indicate an increasing bonding strength between the C_{60} layer with the (111) surface of metals from Au, Ag to Cu.

An annealing treatment at ~ 370 K of a C_{60} layer on Cu(111) during or after molecule deposition, promotes the growth of a well-ordered phase with a p(4×4) superlattice – a commensurate layer [250]. The intramolecular structures of C_{60} on Cu(111) are readily observable in STM even at room temperature due to the strong bonding with the substrate [250, 251]. A clover shape with three bright lobes in three-fold symmetry is obtained at sample positive bias, and a doughnut shape of the HOMO is observed at sample negative bias. The molecular orientation can also be inferred from X-ray photoemission diffraction patterns with the assistance of theoretical simulation [252]. The XPD further confirms that the C_{60} molecules are adsorbed on Cu(111) with a hexagonal ring in two azimuthal equivalent orientations of angular difference 60° [252].

On the basis of the intramolecular structure, the adsorption geometry of the molecule in the (4×4) phase is assigned to a hexagonal ring on the hollow site [250]. Other metastable superstructures of a C_{60} layer on Cu(111) can exist at temperature between 300 ~ 330 K, with unique brightness contrast among the C_{60} molecules in the layer [253]. All the phases of C_{60} layer on Cu(111) involve

different degree of relaxation in the atomic layer of the Cu substrate, and adjustment of nearest neighbour (NN) distance of C_{60}-C_{60} in the molecular overlayer due to the competing balance between the C_{60}-Cu (adsorbate-substrate) and C_{60}-C_{60} (adsorbate-adsorbate) interactions [253].

The electronic information from photoemission spectra suggests the HOMO at −1.7 eV and the partially occupied LUMO near the Fermi level, as well as a weak state in the HOMO-LUMO gap at −1 eV due to a strong hybridization effect of metal and carbon states [249]. There is a large discrepancy in the amount of charge transferred from the substrate, between theoretical calculation which is about 0.8 e^- [254] and photoemission measurements of about 1.5 ~ 2 e^- [249, 255]. Tamai et al. attributes this overestimation from experimental work to the hybridization state near Fermi level, which actually does not contribute to charge transfer [249]. The work function for single-layer C_{60} covered Cu(111) is about 4.86 eV smaller than that of a bare Cu surface (4.94 eV) [255].

The interaction of the C_{60} layer with Ag(111) is stronger than that with Au(111), given a higher desorption temperature ~ 785 K [72]. The stable molecular geometry on Ag(111) is confirmed from low-energy electron diffraction (LEED) and STM to be $2\sqrt{3}\times2\sqrt{3}$-R30° [224, 256, 257] the same as the stable structure of C_{60} on Au(111). The sample is usually annealed at high temperature of ~ 575 K to change metastable structures to stable ones. The LEED pattern obtained at 32 K without molecule-rotational motion, supplemented by DFT calculation, suggests that C_{60} molecules occupy Ag vacancies formed through substrate reconstruction [257]. The DFT calculation of the balance between the energy cost of vacancy formation and energy compensation of chemisorption favors the predication of the relaxation of the Ag(111) substrate [257].

A summary of superstructures for epitaxial C_{60} monolayer on the (111) surface of Cu, Ag, and Au is shown in Table 2.1. The NN distance (10.18 Å) of C_{60} molecule in the close packed monolayer is four times the lattice constant of Cu(111) 2.55 Å. Therefore, a commensurate (4×4) superstructure exists on Cu(111). For the C_{60} monolayer on Ag(111) and Cu(111), the stable phase $2\sqrt{3}\times2\sqrt{3}$-R30° has the smallest lattice mismatch as $2\sqrt{3}$ times the NN Ag-Ag (2.89 Å) or Au-Au (2.88 Å) distance is approximately the same as the NN C_{60} distance [189].

Substrate	a (Å)	Superlattice
Cu(111) [250]	2.55	(4×4)-R0°
Ag(111) [256]	2.89	$(2\sqrt{3}\times2\sqrt{3})$-R30°
Au(111) [73]	2.88	$(2\sqrt{3}\times2\sqrt{3})$-R30°
Au(111) [73]	2.88	(38×38)-R0°
Au(111) [73]	2.88	(7×7)-R14°

Table 2.1 The superstructures of C_{60} monolayer on the (111) surfaces of noble metals, Cu, Ag, and Au [73, 250].

In the three situations of C_{60} monolayer covered noble metal surfaces, vacancies in the first atomic layer of the substrate have been proposed from theoretical simulations to be due to strong interactions between the C_{60} layer and the noble metal surfaces, which could possibly be the reason for the observed dim and bright contrast among C_{60} molecules [241, 243, 246].

2.4.3 C_{60} Molecule and Related 2D Molecular Assemblies

The C_{60} molecule, due to its highly symmetric shape and rich electronic molecular structure, is a versatile candidate as a building block for various nanostructures on surfaces. Metal surfaces with surface defects, for example, step edges or surface dislocations from surface reconstruction where C_{60} molecules, when diffusing on the surfaces, would likely attach to, can be used as templates to grow well ordered arrays of 2D molecular assemblies. A further development involves fabrication of multi-element self-assembled structures by sequential deposition or codeposition of C_{60} molecule and other substances [258].

The Au surface is one of the most popular choices for the growth of nanostructures, due to the unique herringbone reconstruction of the surface and the long straight steps of vicinal gold surfaces with small segments of HCP and FCC stacking regions [107, 259]. As has been mentioned, C_{60} molecules can assemble at the step edges of the Au surface of high index in the form of nanochains at room temperature, as in Figure 2.22a [107]. At low temperature, 2D ordered arrays of C_{60} molecular clusters form at elbow sites of the herringbone on Au(111) [260]. The Graphene moiré pattern is a novel template to trap C_{60} molecules in the valleys and bumps, as shown in Figure 2.22b [261]. The C_{60} molecules trapped in the valley have a uniform bonding configuration, with the 6:6 bond facing the graphene. And molecular units spread over the surface with a bright molecule on the bump surrounded by six molecules [261].

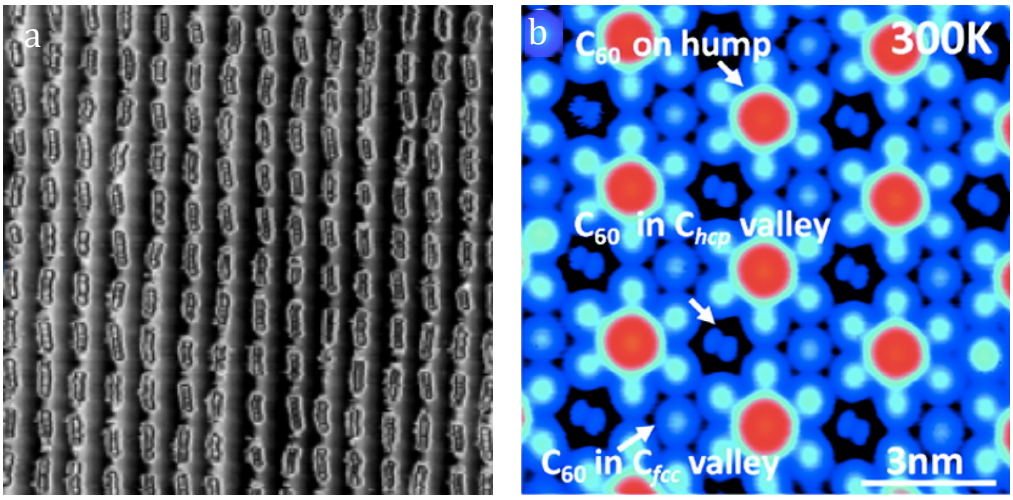

Figure 2.22 Ordered nanostructures formed by C_{60} molecules. (a) C_{60} molecules nanochains at the FCC segments of Au steps. [107] (b) C_{60} molecular assembly on graphene on Ru(0001). Molecules are trapped at both the valleys and bumps of the Moiré pattern, where bright C_{60} molecules stay at the bumps circumfused by six C_{60} molecules. The molecules in the valley interact with the substrate by the C-C 6:6 bond [261].

C_{60} molecules can also be trapped in nanoscale porous frameworks self-assembled by functional molecules [262, 263, 264, 265, 266]. If substrates are precovered with 2D networks, further deposition of C_{60} molecules leads to the formation of ordered binary molecular systems. Here, the organic networks decide the arrangement of C_{60} molecules. Directional bonding such as hydrogen bonding is of a necessity to form two-dimensional networks. Theobald et al. co-deposit melamine and PTCDI on a silver covered silicon surface, where melamine acts as the three-fold connector as shown in the middle of Figure 2.23a, and PTCDI molecule as the building edge. The two components together form three-fold junctions through hydrogen bonding (Figure 2.23a) [262]. The nano-junctions are further connected into a honeycomb network (Figure 2.23b) with the nearest

distance between two melamine molecules being 9.98 Å [262]. A schematic diagram in Figure 2.23b shows the packing of the hexagonal pores through the connection of three-fold junctions (highlighted by a truncated square in Figure 2.23c). After subsequent deposition of C_{60} molecules onto the 2D network, heptameric C_{60} clusters are trapped in the pores of the network [262].

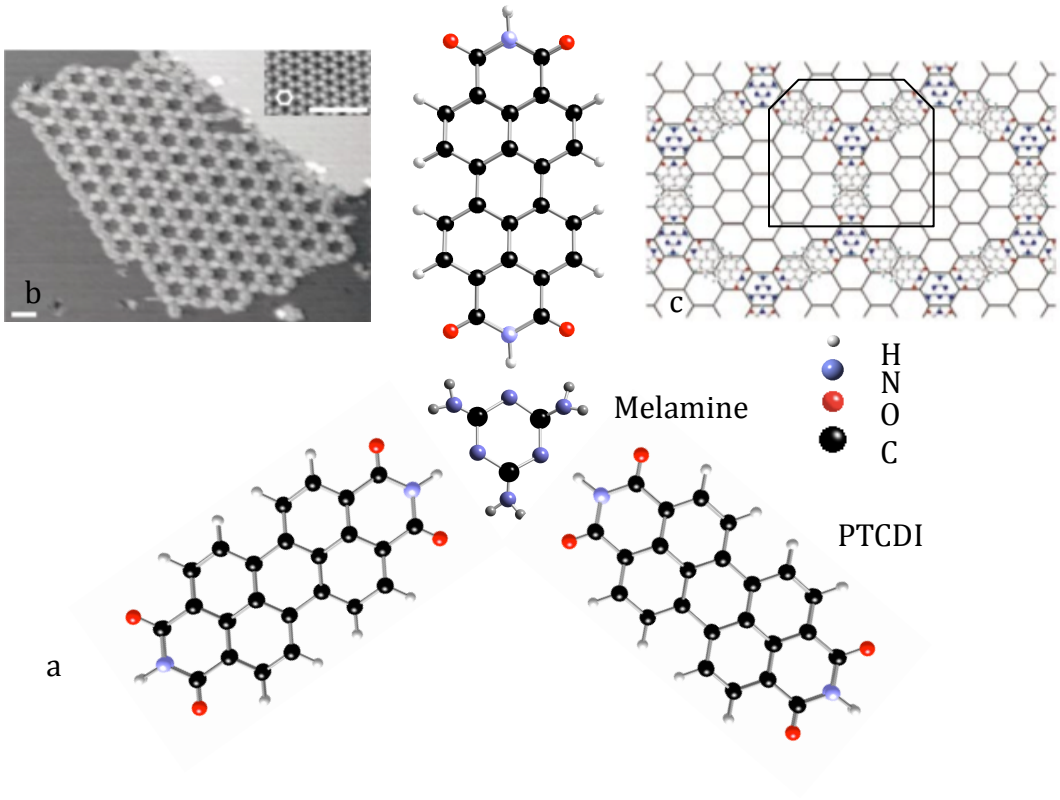

Figure 2.23 Schematic diagram and STM image of melamine-PTCDI self-assembled network. The structure of the three-fold nano-junction a with the melamine molecule in the middle and three PTCDI molecules attached to the connector (melamine) through hydrogen bonding. STM image of the organic network b and corresponding diagram c show how the two types of molecules form the porous network on the surface [262].

Some hetero-molecular architecture can also grow on the surface of semiconductors where the molecule-substrate interaction is pronounced [264].

Baris et al. succeeded in creating a 2D open scaffold with the 1,2,5-tri(4'-bromophenyl) benzene (TBB) molecule and the 1,3,4-tri(4"-bromo-4, 4'-biphenyl) benzene (BPB) molecule on a reconstructed semiconductor surface of Si(111)-B$\sqrt{3}\times\sqrt{3}$R30° [264], in which the substrate guides the growth of nanoscale template to accommodate subsequently deposited C_{60} molecules. An STM image with superimposed model of the molecular network is shown in Figure 2.24a. The hexagonal nanopore has edges of 1.1 nm in length, and the pore size is just right to fit in one C_{60} molecule (Figure 2.24b). Periodic arrays of C_{60} molecule formed on the open molecular framework where the bright protrusions are the C_{60} molecules as shown in Figure 2.24c.

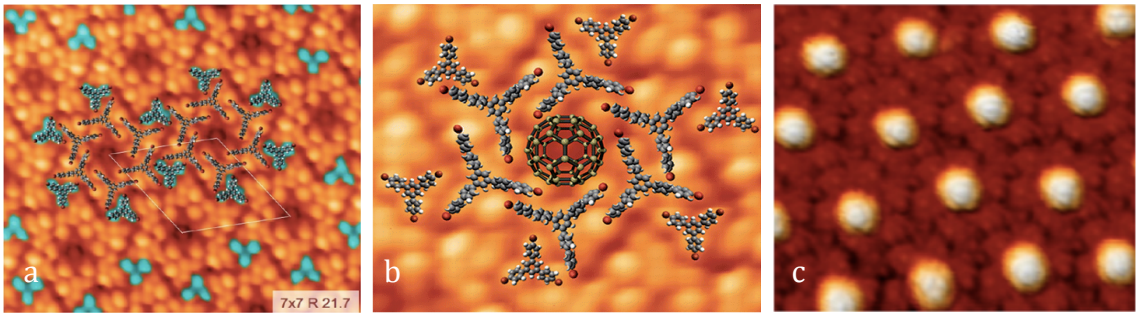

Figure 2.24 The bicomponent molecular assembly on a Silicon surface. (a) STM image of the 2D network with superimposed structure of the TBB/BPB layer. (b) Inclusion of a C_{60} molecule in a pore of the network. (c) STM image of the ordered arrays of C_{60} molecules (bright protrusions) accommodated on the porous template. [264]

Besides the above-mentioned examples of C_{60} molecules being of mainly physical incorporation into an open self-assembled template with porous structures, another approach to stabilize C_{60} molecules is through electron donor/acceptor interaction [267]. With an appropriate coverage of *p*-sexiphenyl (six benzene rings

connected in a row denoted as 6P) on Ag(111), the flat molecules organize into a 2D network of nano-stripes with alternative arrangement of molecules in face-on (molecular plane parallel to the substrate) and edge-on (molecular plane in upright orientation) configuration (Figure 2.25a) [267]. The separation between two edge-on molecules is about 1.1±0.02 nm. After deposition of C_{60} molecules and annealing treatment (380 K) of the C_{60}-6P nano-stripe system, the Ag(111) surface is covered with periodic C_{60} chains separated by face-on and edge-on nano-stripes [267]. The morphology of the C_{60}/6P nanojunctions and corresponding schematic diagram are shown in Figure 2.25b and c.

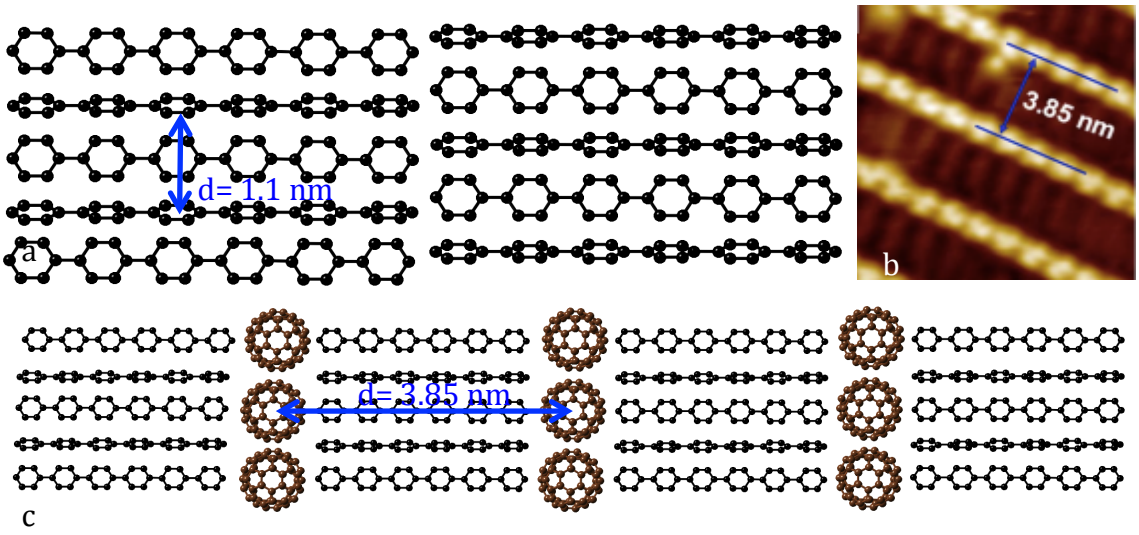

Figure 2.25 (a) A schematic drawing of the molecular configuration of 6P layer on Ag(111). The organic molecules arrange in a face-on (molecule facing parallel to the substrate) and edge-on (molecule sitting vertically on the substrate) manner. The distance between nearest two molecules of the same orientation in a strip is 1.1 nm. (b) STM image of the C_{60}/6P nanojunction arrays. The linear bright protrusions are C_{60} rows. In-between the C_{60} rows are nano-stripes of 6P molecule arranged in the face-on and edge-on fashion. (c) Illustration of the nanojunction arrays with alternating C_{60} chains and 6P nano-stripes. [267]

Thermal activation of the C_{60}-6P mixture promotes the insertion of C_{60} molecules in-between the nano-stripes, where the C_{60} molecules are closely packed along the long axis of nano-stripes forming rows separated by 3.85 nm – the single-molecule width (Figure 2.25b). The centre-to-centre distance between two C_{60} chains 3.85 nm is the sum of the van der Waals diameter of the C_{60} molecule (1.0 nm) and the length of the 6P molecule (2.95 nm) [268]. The C_{60} molecule is frequently the electron acceptor in many systems when in interaction with metals such as Cu, Ag, and Au. Here the 6P molecule acts as the electron donor and binds with the fullerene molecule through electrostatic interaction.

The coadsorption or codeposition of molecules offers a way to control the structure and property of self-assemblies on substrate by tuning the coverage and ratio of each component in the intermixed system [269, 270]. An example of the coadsorption method is the growth of C_{60}/acridine-9-carboxylic acid (ACA, structure shown in Figure 2.26b) intermixed layer with tunable spacing between C_{60} molecules, demonstrated by Xu et al. [269]. The ordered structure formed by C_{60} molecule and ACA is shown in Figure 2.26c. The protrusions in blue colour correspond to C_{60} molecules separated by 2.65 nm [269]. The proposed model of the structure (Figure 2.26d) consists of an ordered arrangement of a unit formed by one C_{60} molecule and six ACA molecules, and highlighted by the rhombus in Figure 2.26d. For a unit cell, the six ACA molecules can be classified into two "pinwheel" trimers (the two insets in Figure 2.26d) that each is organized in opposite rotation directions. Three ACA molecules of a trimer orient with the ring nitrogen atoms directing inward and are rotated by 120° with respect to each other. One C_{60} molecule sits directly on top of one trimer. This ordered structure is

observed when an equal coverage of C_{60} molecules and ACA molecules, each of 0.4 ML, is reached [270].

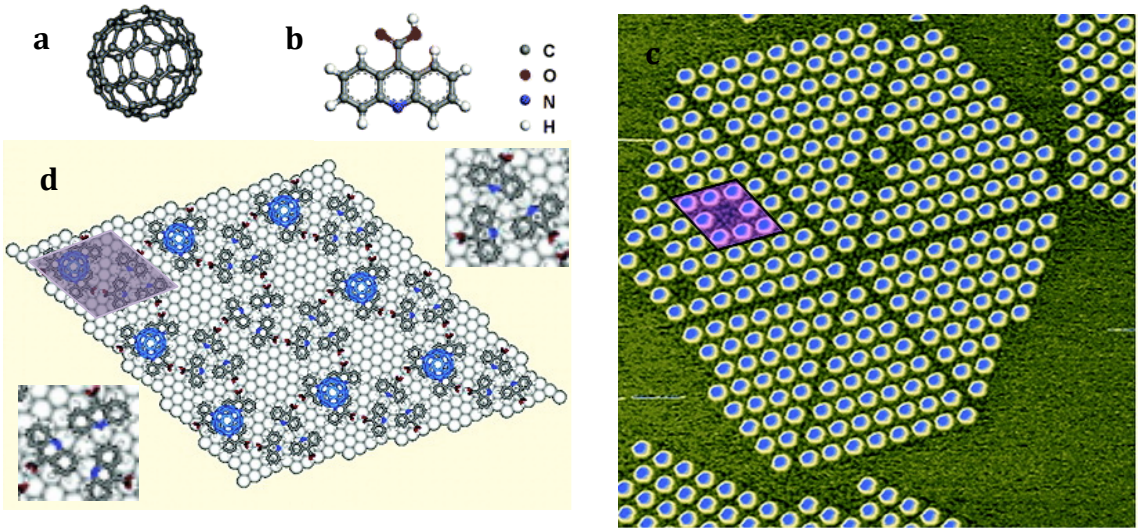

Figure 2.26 Ordered structure of C_{60} and ACA bimolecular layer. Chemical structures of C_{60} a and ACA b molecule. (c) An STM image of the ordered structure of C_{60} and ACA layer. Around the ordered structure is the ACA layer in gas phase. The pink rhombic shadow covers eight C_{60} molecules, each sitting on top of three ACA molecules. A corresponding diagram is in d. (d) The unit cell for the order structure is highlighted by a rhombus. It consists of one C_{60} and six ACA molecules. The ACA molecules can be divided into two "pinwheel" trimers (two insets) arranged in opposite rotation directions. One C_{60} molecule is located on top of one trimer. [269, 270]

The geometry and interaction of the C_{60} molecule with surrounding environments are the focus of much research because it is not only of basic scientific interest but also important in the design of molecular electronics. Application of C_{60} molecules in association with other organic molecules with functional groups in surface

science opens a new way to explore nanostructures with defined structures and properties.

References

[1] L. D. Landau and E. M. Lifshitz. Quantum Mechnics: Non-Relativistic Theory. Sixth Chinese Language Edition, Higher Education Press, Beijing (2008).
[2] C. J. Chen. Introduction to Scanning Tunnelling Microscopy. Second Edition, Oxford University Press, New York (2008).
[3] J. M. Soler, A. M. Baro, N. Garcia, and H. Rohrer. Interatomic Forces in Scanning Tunnelling Microscopy: Giant Corrugations of the Graphite Surface. Phys. Rev. Lett. **57**, 444 (1986).
[4] J. Barden. Tunnelling from A Many-Particle Point of View. Phys. Rev. Lett. **6**, 57 (1961).
[5] H. Ohnishi, Yukihito Kondo, and Kunio Tkayanagi. Quantized Conductance through Individual Rows of Suspended Gold Atoms. Nature **395**, 780 (1998).
[6] C. F. Quate. Vacuum Tunnelling: A New Technique for Microscopy. Physics Today. **39**, 26 (1986).
[7] G. Binning, H. Rohrer, Ch. Gerber, and E. Weibel. 7×7 Reconstruction on Si(111) Resolved in Real Space. Phys. Rev. Lett. **50**, 120 (1983).
[8] J. Tersoff and D. R. Hamann. Theory of the Scanning Tunnelling Microscope. Phys. Rev. B **31**, 805 (1985).
[9] N. D. Lang. Theory of Single-Atom Imaging in the Scanning Tunnelling Microscope. Phys. Rev. Lett. **56**, 1164 (1986).
[10] D. M. Eigler, P. S. Weiss, and E. K. Schweizer. Imaging Xe with a Low Temperature Scanning Tunnelling Microscope. Phys. Rev. Lett. **66**, 1189 (1991).
[11] K. Mednick and L. Kleinman. Self-Consistent Al(111) Film Calculation. Phys. Rev. B **22**, 5768 (1980).
[12] J. Wintterlin, J. Wiechers, H. Brune, and T. Gritsch. Atomic-Resolution Imaging of Close-Packed Metal Surfaces by Scanning Tunnelling Microscopy. Phys. Rev. Lett. **62**, 59 (1989).
[13] C. J. Chen. Origin of Atomic Resolution on Metal Surfaces in Scanning Tunnelling Microscopy. Phys. Rev. Lett. **65**, 448 (1990).
[14] W. Sacks and C. Noguera. Generalized Expression for the Tunnelling Current in Scanning Tunnelling Microscopy. **43**, 11612 (1991).
[15] D. Drakova, G. Doyen, and F. V. Trentini. Self-Consistent Calculations of Rare-Gas-Transition-Metal Interaction Potentials. Phys. Rev. B **32**, 6399 (1985).
[16] P. M. Morse and H. Feshbach. Methods of Theoretical Physics. London : McGraw-Hill, New York (1953).
[17] C. J. Chen. Introduction to Scanning Tunnelling Microscopy. First Edition, Oxford University Press, New York (1993).
[18] J. Tersoff and D. R. Hamann. Theory and Application for the Scanning Tunnelling Microscope. Phys. Rev. Lett. **50**, 1998 (1983).

[19] S. Ciraci, A. Baratoff, and I. P. Batra. Site-Dependent Electronic Effects, Forces, and Deformations in Scanning Tunnelling Microscopy of Flat Metal Surfaces. Phys. Rev. B **42**, 7618 (1990).
[20] E. C. Teague. Room Temperature Gold-Vacuum-Gold Tunnelling Experiments. Journal of Research of the National Bureau of Standards. **91**, 171 (1986).
[21] U. Dürig, O. Züger, and D. W. Pohi. Observation of Metallic Adhesion Using the Scanning Tunnelling Microscope. Phys. Rev. Lett. **65**, 349 (1990).
[22] F. Besenbacher. Scanning Tunnelling Microscopy Studies of Metal Surfaces. Reports on Progress in Physics. **59**, 1737 (1996).
[23] G. Binning, H. Rohrer, Ch. Gerber, and E. Weibel. 7×7 Reconstruction on Si(111) Resolved in Real Space. Phys. Rev. Lett. **50**, 120 (1983).
[24] V. M. Hallmark, S. Chiang, J. F. Rabolt, J. D. Swalen, and R. J. Wilson. Observation of Atomic Corrugation on Au(111) by Scanning Tunnelling Microcopy. Phys. Rev. Lett. **59**, 2879 (1987).
[25] J. V. Barth, H. Brune, G. Ertl, and R. J. Behm. Scanning Tunnelling Microscopy Observations on the Reconstructed Au(111) Surface: Atomic Structure, Long-range Superstructure, Rotational Domains, and Surface Defects. Phys. Rev. B **42**, 9307 (1990).
[26] J. J. Boland. Evidence of Pairing and Its Role in the Recombinative Desorption of Hydrogen from the Si(100)-2×1 Surface. Phys. Rev. Lett. **67**, 1539 (1991).
[27] M. Schmid, H. Stadler, and P. Varga. Direct Observation of Surface Chemical Order by Scanning Tunnelling Microscopy. Phys. Rev. Lett. **70**, 1441 (1993).
[28]P. T. Wouda, B. E. Nieuwenbuys, M. Schmid, and P. Varga. Chemically Resolved STM on A PtRh(100) Surface. Surf. Sci. **359**, 17 (1996).
[29]M. Ruff, N. Takehiro, P. Liu, J. K. Nørskov, and R. J. Behm. Size-specific Chemistry on Bimetallic Surfaces: A Combined Experimental and Theoretical Study. ChemPhysChem **8**, 2068 (2007).
[30] D. M. Eigler, and E. K. Schweizer. Positioning Single Atoms with A Scanning Tunnelling Microscope. Nature **344**, 524 (1990).
[31]M. F. Crommie, C. P. Lutz, D. M. Eigler. Confinement of Electrons to Quantum Corrals on A Metal Surface. Science **262**, 218 (1993).
[32] S. Fölsch, P. Hyldgaard, R. Koch, and K. H. Ploog. Quantum Confinement in Monatomic Cu Chains on Cu(111). Phys. Rev. Lett. **92**, 056803-1 (2004).
[33] Q. Li, Ch. Han, M. Fuentes-Cabrera, H. Terrones, B. G. Sumpter, W. Lu, J. Bernholc, J. Yi, Zh. Gai, A. P. Baddorf, P. Maksymovych, and M. Pan. Electronic Control over Attachment and Self-Assembly of Alkyne Groups on Gold. ACS Nano. **6**, 9267 (2004).
[34] T. Kudernac, N. Ruangsupapichat, M. Parschau, B. Maciá, N. Katsonis, S. R. Harutyunyan, L. Ernst, and B. Feringa. Electrically Driven Directional Motion of A Four-Wheeled Molecule on A Metal Surface. Nature **479**, 208 (2011).
[35] P. S. Weiss. A Molecular Four-Wheel Drive. Nature **479**, 187 (2011).
[36] K. Yagi, K. Takayanagi, K. Kobayashi, N. Osakabe, Y. Tanishiro, and G. Honjo. Surface Study by An UHV Electron Microscope. Surf. Sci. **86**, 174 (1979).
[37] J. C. Heyraud, and J. J. Métois. Anomalous 1/3 422 Diffraction Spots from {111} Flat Gold Crystallites: (111) Surface Reconstruction and Moiré Fringes between the Surface and the Bulk. Surf. Sci. **100**, 519 (1980).

[38] Y. Tanishiro, H. Kanamori, K. Takayanagi, K. Yagi, and G. Honjo. UHV Transmission Electron Microscopy on the Reconstructed Surface of (111) Gold. Surf. Sci. **111**, 395 (1981).
[39] J. Perdereau, J. P. Biberian, and G. E. Rhead. Adsorption and Surface Alloying of Lead Monolayers on (111) and (110) Faces of Gold. J. Phys. F: Met. Phys. **4**, 798 (1974).
[40] U. Haren, A. M. Lahee, J. P. Toennies, and Ch. Wöll. Observation of A Soliton Reconstruction of Au(111) by High-Resolution Helium-Atom Diffraction. Phys. Rev. Lett. **54**, 2619 (1985).
[41] G. I. Finch, A. G. Quarrell, and H. Wilman. Electron Diffraction and Surface Structure. Trans. Faraday Soc. **31**, 1051 (1935).
[42] K. Takayanagi and K. Yagi. Monatom-High Level Electron Microscopy of Metal Surface. Tran. Jpn. Insti. Met. **24**, 337 (1983).
[43] V. M. Hallmark, S. Chiang, J. F. Rabolt, J. D. Swalen, and R. J. Wilson. Observation of Atomic Corrugation on Au(111) by Scanning Tunnelling Microscopy. Phys. Rev. Lett. **59**, 2879 (1987).
[44] Ch. Wöll, S. Chiang, R. J. Wilson, and P. H. Lippel. Determination of Atom Positions at Stacking-Fault Dislocations on Au(111) by Scanning Tunnelling Microscopy. Phys. Rev. B **39**, 7988 (1989).
[45] J. V. Barth, H. Brune, G. Ertl, and R. J. Behm. Scanning Tunnelling Microscopy Observation on the Reconstructed Au(111) Surface: Atomic Structure, Long-Range Superstructure, Rotational Domains, and Surface Defects. Phys. Rev. B **42**, 9307 (1990).
[46] W. J. Kaiser and R. C. Jaklevic. Direct Observation of An Ordered Step Surface Reconstruction on Au(111) by Scanning Tunnelling Microscopy. Surf. Sci. **182**, L227 (1987).
[47] F. Besenbacher, J. V. Lauritsen, T. R. Linderoth, E. Lægsgaard, R. T. Vang, and S. Wendt. Atomic-Scale Surface Science Phenomena Studied by Scanning Tenneling Microscopy. Surf. Sci. **603**, 1315 (2009).
[48] M. El-Batanouny, S. Burdick, K. M. Martini, and P. Stancioff. Double-Sine-Gordon Solitions: A Model for Misfit Dislocations on the Au(111) Reconstructed Surface. Phys. Rev. Lett. **58**, 2762 (1987).
[49] R. Ravelo and M. El-Batanouny. Molecular-Dynamics Study of the Reconstructed Au(111) Surface: Low Temperature. Phys. Rev. B **40**, 9574 (1989).
[50] S. Narsimhan and D. Vanderbilt. Elastic Stress Domains and the Herringbone Reconstruction on Au(111). Phys. Rev. Lett. **69**, 1564 (1992).
[51] U. Tartaglino, E. Tosatti, D. Passerone, and F. Ercolessi. Bending Strain-Driven Modification of Surface Reconstruction: Au(111). Phys. Rev. B **65**, 241406 (2002).
[52] H. Bulou and C. Goyhenex. Local Strain Analysis of the Herringbone Reconstruction of Au(111) through Atomistic Simulation. Phys. Rev. B **65**, 045407 (2002).
[53] M. S. Daw and M. I. Basket. Embedded-Atom Method: Derivation and Application to Impurities, Surfaces, and Other Defects in Metals. Phys. Rev. B **29**, 6443 (1984).
[54] B. W. Dodson. Many-Body Surface Strain and Surface Reconstruction in FCC Transition Metals. Phys. Rev. Lett. **60**, 2288 (1988).

[55] R. Ravelo and M. El-Batanouny. Molecular Dynamics Study of the Surface Vibration of the Reconstructed Au(111) Surface. Journal of Electron Spectroscopy and Related Phenomena **54-55**, 255 (1990).
[56] X. Wang. Anomalous Surface Phonons of the Reconstructed Au(111): A Molecular-Dynamics Simulation. Phys. Rev. Lett. **67**, 1294 (1991).
[57] R. J. Needs and M. Mansfield. Calculations of the Surface Stress Tensor and Surface Energy of the (111) Surface of Iridium, Platinum and Gold. J. Phys.: Condens Matter **1**, 7555 (1989).
[58] O. Schaff, A. K. Schimid, N. C. Bartelt, J. De La Figuera, and R. Q. Hwang. In-site STM Studies of Strain-Stabilized Thin-Film Dislocation Network under Applied Stress. Mater. Sci. Eng. A **319-321**, 914 (2001).
[59] L. D. Marks, V. Heine, and D. J. Smith. Direct Observation of Elastic and Plastic Deformation at Au(111) Surface. Phys. Rev. Lett. **52**, 656 (1984).
[60] V. Heine and L. D. Marks. Competition between Pairwise and Multi-Atom Forces at Nobel Metal Surfaces. Surf. Sci. **165**, 65 (1986).
[61] C. S. Jayanthi, H. Bilz, W. Kress, and G. Benedek. Nature of Surface-Phonon Anomalies in Noble Metals. Phys. Rev. Lett. **59**, 795 (1987).
[62] K. G. Huang, D. Gibbs, D. M. Zehner, A. R. Sandy, and S. G. J. Mochrie. Phase Behavior of the Au(111) Surface: Discommensurations and Kinks. Phys. Rev. Lett. **26**, 3313 (1990).
[63] A. R. Sandy, S. G. J. Mochrie, D.M. Zehner, K. G. Huang, and D. Gibbs. Structure and Phases of the Au(111) Surface: X-Ray-Scattering Measurement. Phys. Rev. B **43**, 4667 (1991).
[64] P. Kowalczyk, W. Kozlowski, Z. Klusek, W. Olejniczak, and P. K. Datta. STM Studies of the Reconstructed Au(111) Thin-Film at Elevated Temperatures. Appl. Surf. Sci. **253**, 4715 (2007).
[65] J. V. Barth, R. J. Behm, and G. Ertl. Mesoscopic Structural Transformations of the Au(111) surface Induced by Alkali Metal Adsorption. Surf. Sci. Lett. **320**, L319 (1994).
[66] M. Corso, M. J. Verstraete, F. Schiller, M. Ormaza, L. Fernández, T. Greber, M. Torrent, A. Rubio, and J. E. Ortega. Rare-Earth Surface Alloying: A New Phase for $GdAu_2$. Phys. Rev. Lett. **105**, 016101 (2010).
[67] M. Corso, L. Fernández, F. Schiller, and J. E. Ortega. Au(111)-Based Nanotemplates by Gd Alloying. ACS Nano **4**, 1603 (2010).
[68] J. Wiechers, T. Twomey, and D. M. Kolb. An In-Situ Scanning Tunnelling Microscopy Study of Au(111) with Atomic Scale Resolution. J. Electroanal. Chem. **248**, 451 (1988).
[69] N. J. Tao and S. M. Lindsay. Observation of the $22\times\sqrt{3}$ Reconstruction of Au(111) under Aqueous Solutions Using Scanning Tunnelling Microscopy. J. Appl. Phys. **70**, 5141 (1991).
[70] F. C. Simeone, D. M. Kolb, S. Venkatachalam, and T. Jacob. The Au(111)/Electrolyte Interface: A Tunnel-Spectroscopic and DFT Inverstigation. Angew. Chem. Int. Ed. **46**, 8903 (2007).
[71] J. K. Gimzewski, S. Modesti, Ch. Gerber, and R. R. Schlittler. Observation of A New Au(111) Reconstruction at the Interface of An Adsorbed C_{60} Overlayer. Chem. Phys. Lett. **213**, 401 (1993).

[72] E. I. Altman and R. J. Colton. The Interaction of C_{60} with Noble Metal Surfaces. Surf. Sci. **295**, 13 (1993).
[73] J. A. Gardener, G. A. D. Briggs, and M. R. Castell. Scanning Tunnelling Microscopy Studies of C_{60} Monolayers on Au(111). Phys. Rev. B **80**, 235434 (2009).
[74] S. D. Kevan and R. H. Gaylord. High-Resolution Photoemission Study of the Electronic Structure of the Nobel-Metal (111) Surface. Phys. Rev. B **36**, 5809 (1987).
[75] R. Paniago, R. matzdorf, and A. Goldmann. Localization of d-Like Surface Resonances on Reconstructed Au(111). Europhys. Lett. **26**, 63 (1994).
[76] S. LaShell, B. A. McDougall and E. Jensen. Spin Splitting of an Au(111) Surface State Band Observed with Angle Resolved Photoelectron Spectroscopy. Phys. Rev. Lett. **77**, 3419 (1996).
[77] p. Borghetti, J. Lobo-Checa, E. Goiri, A. Mugarza, F. Schiller, J. E. Ortega, and E. E. Krasovskii. Effect of Surface Reconstruction on the Photoemission Cross-Section of the Au(111) Surface State. J. Phys.: Condens. Matter **24**, 395006 (2012).
[78] D. Fujita, K. Amemiya, T. Yakabe, and H. Nejoh. Anisotropic Standing-Wave Formation on an Au(111)-23×$\sqrt{3}$ Reconstructed Surface. Phys. Rev. Lett. **78**, 3904 (1997).
[79] W. Chen, V. Madhavan, T. Jamneala, and M. F. Crommie. Scanning Tunnelling Microscopy Observation of An Electronic Superlattice at the Surface of Clean Gold. Phys. Rev. Lett. **80**, 1469 (1998)
[80] D. Fujita, K. Amemiya, T. Yakabe, H. Nejoh, T. Sato, and M. Iwatsuki. Observation of Two-Dimensional Fermi Contour of a Reconstructed Au(111) Surface Using Fourier Transform Scanning Tunnelling Microscopy. Surf. Sci. **423**, 160 (1999).
[81] P. J. Kowalczyk, M. Puchalski, W. Kozłowski, P. Dabrowski, Z. Klusek, and W. Olejniczak. Investigation of the Schockley Surface State on Clean and Air-Exposed Au(111). Appl. Surf. Sci. **254**, 4572 (2008).
[82] K. Schouteden, P. Lievens, and C. V. Haesendonck. Fourier-Transform Scanning Tunnelling Microscopy Investigation of the Energy Versus Wave Vector Dispersion of Electrons at the Au(111) Surface. Phys. Rev. B **79**, 195409 (2009).
[83] N. Takeuchi, C. T. Chan, and K. M. Ho. Au(111): A Theoretical Study of the Surface Reconstruction and the Surface Electronic Structure. Phys. Rev. B **43**, 13899 (1991).
[84] R. Mazzarello, A. D. Corso, and E. Tosatti. Spin-Orbit Modifications and Splitting of Deep Surface States on Clean Au(111). Surf. Sci. **602**, 893 (2008).
[85] Z. Li, S. Gong, and Z. Yang. Large Spin-Orbit Splitting of Surface States in Ultrathin Au(111) Films. Phys. Rev. A , **377**, 129 (2012).
[86] Y. Hasegawa and Ph. Avouris. Direct Observation of Standing Wave Formation at Surface Step Using Scanning Tunnelling Spectroscopy. Phys. Rev. Lett. **71**, 1071 (1993).
[87] L. C. Davis, M. P. Everson, and R. C. Jaklevic. Theory of the Local Density of Surface States on A Metal: Comparison with Scanning Tunnelling Spectroscopy of A Au(111) Surface. Phys. Rev. B **43**, 3821 (1991).
[88] P. Avouris and I. Lyo. Observation of Quantum-Size Effects at Room Temperature on Metal Surfaces with STM. Science **264**, 942 (1994).

[89] L. Bürgi, H. Brune, and K. Kern. Imaging of Electron Potential Landscapes on Au(111). Phys. Rev. Lett. **89**, 176801 (2002).
[90] P. Hohenberg and W. Kohn. Inhomogeneous Electron Gas. Phys. Rev. **136**, B864 (1964).
[91] T. Michely, M. Hohage, M. Bott, and G. Comsa. Inversion of Growth Speed Anisotropy in Two Dimensions. Phys. Rev. Lett. **70**, 3943(1993).
[92] V. Repain, J. M. Berroir, S. Rousset, and J. Lecoeur. Interaction between Steps and Reconstruction on Au(111). Europhys. Lett. **47**, 435 (1999).
[93] V. Repain, J. M. Berroir, S. Rousset, J. Lecoeur. Reconstruction, Step Edges and Self-Organization on the Au(111) Surface. Appl. Surf. Sci. **162**, 30 (2000).
[94] M. Giesen. Step and Island Dynamics at Solid/Vacuum and Solid/Liquid Interface. Prog. Surf. Sci. **68**, 1 (2001).
[95] S. Rousset, V. Repain, G. Baudot, Y. Garreau, and J. Lecoeur. Self-Ordering of Au(111) Vicinal Surfaces and Application to Nanostructure Organized Growth. J. Phys.: Condens. Matter **15**, 53363 (2003).
[96] F. Yin, R. E. Palmer, and Q. Guo. Faceting of Nanoscale Fingers on the (111) Surface of Gold. Surf. Sci. **600**, 1504 (2006).
[97] M. Giesen, C. Steimer, and H. Ibach. What Does One Learn from Equilibrium Shapes of Two-Dimensional Islands on Surfaces. Surf. Sci. **471**, 80 (2001).
[98] E. Holland-Moritz, J. Gordon II, G. Borges, and R. Sonnenfeld. Motion of Atomic Steps of Au(111) Films on Mica. Langmuir **7**, 301 (1991).
[99] Z. Wang and M. Moskovits. Scanning Tunnelling Microscope-Promoted Growth of Nanometer-Scale, Uniform Gold Stripes on Reconstructed Au(111) Surfaces. J. Appl. Phys. **71**, 5401 (1992).
[100] Q. Guo, F. Yin, and R. E. Palmer. Beyond the Herringbone Reconstruction: Magic Gold Gingers. Small **1**, 76 (2005).
[101] A. Bartolini, F. Ercolessi, and E. Tosatti. "Magic" Vicinal Surfaces Stabilized by Reconstruction. Phys. Rev. Lett. **63**, 872 (1989).
[102] S. Rousset, F. Pourmir, J. M. Berroir, J. Klein, J. Lecoeur, P. Hecquet, and B. Salanon. Self-Organization on Au(111) Vicinal Surfaces and the Role of Surface Stress. Surf. Sci. **422**, 33 (1999).
[103] W. J. Kaiser and R. C. Jaklevic. Direct Observation of An Ordered Step Surface Reconstruction on Au(111) by Scanning Tunnelling Microscopy. Surf. Sci. Lett. **182**, L227 (1987).
[104] S. Rousset, J. M. Berroir, V. Repain, Y. Garreau, V. H. Etgens, J. Lecoeur, and R. Pinchaux. Thermal Faceting Behavior of Au(455). Surf. Sci. **443**, 265 (1999).
[105] F. Pourmir, S. Rousset, S. Gauthier, M. Sotto, and J. Klein. Periodic Faceting of Au(4,3,3) Observed by Scanning Tunnelling Microscopy. Microsc. Microanal. Microstruct. **5**, 269 (1994).
[106] F. Pourmir, S. Rousset, S. Gauthier, M. Sotto, J. Klein, J. Lecoeur, and J. P. Bellier. Superperiodicity in the Thermal Faceting of Au(111) Vicinal Surfaces. Surf. Sci. **324**, L337 (1995).
[107] W. Xiao, P. Ruffieux, K. Aït-Mansour, O. Gröning, K. Palotas, W. A. Hofer, P. Gröning, and R. Fasel. Formation of A Regular Fullerene Nanochain Lattice. J. Phys. Chem. B **110**, 21394 (2006).
[108] L. Zhang, Z. Cheng, Q. Huan, X. He, X. Lin, L. Gao, Z. Deng, N. Jiang, Q. Liu, S. Du, H. Guo, and H. Gao. Site- and Configuration-Selective Anchoring of Iron-

Phthalocyanine on the Step Edges of Au(111) Surface. J. Phys. Chem. C **115**, 10791 (2011).
[109] S. Linden, D. Zhong, A. Timmer, N. Aghdassi, J. H. Franke, H. Zhang, X. Feng, K. Müllen, H. Fuchs, L. Chi, and H. Zacharia. Electronic Structure of Spatially Aligned Graphene Nanoribbons on Au(788). Phys. Rev. Lett. **108**, 216801 (2012).
[110] M. Treier, P. Ruffieux, R. Schillinger, T. Greber, K. Müllen, and R. Fasel. Living on the Edge: A Nanographene Molecule Adsorbed across Gold Step Edges. Surf. Sci. **602**, L84 (2008).
[111] R. Gaspari, C. A. Pignedoli, R. Fasel, M. Treier, and D. Passerone. Atomistic Insight into the Adsorption Site Selectivity of Stepped Au(111) Surfaces. Phys. Rev. B **82**, 041408 (2010).
[112] S. Linden, D. Zhong, A. Timmer, N. Aghdassi, J. H. Franke, H. Zhang, X. Feng, K. Müllen, H. Fuchs, L. Chi, and H. Zacharias. Electronic Structure of Spatially Aligned Graphene Nanoribbons on Au(788). Phys. Rev. Lett. **108**, 216801 (2012).
[113] R. Emch, J. Nogami, M. M. Dovek, C. A. Lang and C. F. Quate. Characterization of Gold Surfaces for Use as Substrates in Scanning Tunnelling Microscopy Studies. J. Appl. Phys. **65**, 79 (1989).
[114] C. A. Lang, M. M. Dovek, J. Nogami, and C. F. Quate. Au(111) Autoepitaxy Studied by Scanning Tunnelling Microscopy. Surf. Sci. Lett. **224**, L947 (1989).
[115] R. C. Jaklevic and L. Elie. Scanning Tunnelling Microscope Observation of Surface Diffusion on An Atomic Scale: Au on Au(111). Phys. Rev. Lett. **60**, 120 (1988).
[116] J. Gong. Structure and Surface Chemistry of Gold-Based Model Catalysts. Chem. Rev. **112**, 2987 (2012).
[117] S. Duffe, N. Grönhagen, L. Patryarcha, B. Sieben C. Yin, B. Issendorff, M. Moseler, and H. Hövel. Penetration of Thin C_{60} Films by Metal Nanoparticles. Nat. Nanotech. **5**, 335 (2010).
[118] N. Grönhagen, T. T. Järvi, N. Miroslawski, H. Hövel, and M. Moseler. Decay Kinetics of Cluster-Beam-Deposited Metal Particles. J. Phys. Chem. C **116**, 19327 (2012).
[119] K. Morgenstern, G. Rosenfeld, E. Lægsgaard, F. Besenbacher, and G. Comsa. Measurement of Energies Controlling Ripening and Annealing on Metal Surfaces. Phys. Rev. Lett. **80**, 556 (1998).
[120] K. Morgenstern, G. Rosenfeld, G. Comsa, M. R. Sørensen, B. Hammer, E. Lægsgaard, and F. Besenbacher. Kinetics of Fast Island Decay on Ag(111). Phys. Rev. B **63**, 045412 (2001).
[121] M. M. Dovek, C. A. Lang, J. Nogami, and C. F. Quate. Epitaxial Growth of Ag on Au(111) Studied by Scanning Tunnelling Microscopy. **40**, 11973 (1989).
[122] H. Cercellier, Y. Fagot-Revurat, B. Kierren, D. Malterre, and F. Reinert. Shockley State in Epitaxial Ag Films on Au(111). Surf. Sci. **566-568**, 520 (2004).
[123] Y. Borensztein, T. Lopez-Rios, and G. Vuye. Comparative Study of Ag Growth on (111) Au and Cu Substrates. Phys. Rev. B **37**, 6235 (1988).
[124] Q. M. Magnussen, J. Hotlos, R. J. Nichols, D. M. Kolb, and R. J. Behm. Atomic Structure of Cu Adlayers on Au(100) and Au(111) Electrodes Observed by In Situ Scanning Tunnelling Microscopy. Phys. Rev. Lett. **64**, 2929 (1990).

[125] X. H. Xia, L. Nagle, R. Schuster, O. M. Magnussen, and R. J. Behm. The Kinetics of Phase Transitions in Underpotentially Deposited Cu Adlayers on Au(111). Phys. Chem. Phys. Chem. **2**, 4387 (2000).
[126] N. Vasiljevic, L. T. Viyannalage, N. Dimitrov, and K. Sieradzki. High Resolution Electrochemical STM: New Structural Results for Underpotentially Deposited Cu on Au(111) in Acid Sulfate Solution. J. Electroanal. Chem. **613**, 118 (2008).
[127] J. Rodriguez. Physical and Chemical Properties of Bimetallic Surfaces. Surf. Sci. Rep. **24**, 223 (1996).
[128] F. Grillo, H. Früchtl, S. M. Francis and N. V. Richardson. Site Selectivity in the Growth of Copper Islands on Au(111). New J. Phys. **13**, 013044 (2011).
[129] D. D. Chambliss, R. J. Wilson, and S. Chiang. Nucleation of Ordered Ni Island Arrays on Au(111) by Surface-Lattice Dislocation. Phys. Rev. Lett. **66**, 1721 (1991).
[130] W. G. Cullen and P. N. First. Island Shapes and Intermixing for Submonolayer Nickel on Au(111). Surf. Sci. **420**, 53 (1999).
[131] J. A. Meyer, I. D. Baikie, E. Kopatzki, and R. J. Behm. Preferential Island Nucleation at the Elbows of the Au(111) Herringbone Reconstruction through Place Exchange. Surf. Sci. **365**, L647 (1996).
[132] A. G. Trant, T. E. Jones, J. Gustafson, T. C. Q. Noakes, P. Bailey, and C. J. Baddeley. Alloy Formation in the Au{111}/Ni System – An Investigation with Scanning Tunnelling Microscopy and Medium Energy Ion Scattering. Surf. Sci. **603**, 571 (2009).
[133] D. N. Tafen and L. J. Lewis. Structure and Energetics of Ni and Au Nanoclusters Deposited on the (001), (110), and (111) Surfaces of Au and Ni: A Molecular Dynamics Study. Phys. Rev. B **77**, 075429 (2008).
[134] M. Ø. Pedersen, S. Helveg, A. Ruban, I. Stensgaard, E. Lægsgaard, J. K. Nørskov, F. Besenbacher. How A Gold Substrate Can Increase the Reactivity of A Pt Overlayer. Surf. Sci. **426**, 395 (1999).
[135] Y. Nahas, V. Repain, C. Chacon, Y. Girard, and S. Rousset. Interplay between Ordered Growth and Intermixing of Pt on Patterned Au Surfaces. Surf. Sci. **604**, 829 (2010).
[136] A. Mathur and J. Erlebacher. Effects of Substrate Shape, Curvature and Roughness on Thin Heteroepitaxial Films of Pt on Au(111). Surf. Sci. **602**, 2863 (2008).
[137] D. Friebel, D. J. Miller, D. Nordlund, H. Ogasaware, and A. Nilsson. Degradation of Bimetallic Model Electrocatalysts: An In Situ X-Ray Absorption Spectroscopy Study. Angew. Chem. Int. Ed. **50**, 10190 (2011).
[138] H. Häkkinen. Atomic and Electronic Structure of Gold Clusters: Understanding Flakes, Cages and Superatoms from Simple Concepts. Chem. Soc. Rev. **37**, 1847 (2008).
[139] M. A. Brown, E. Carrasco, M. Sterrer, and H. J. Freund. Enhanced Stability of Gold Clusters Supported on Hydroxylated MgO(001) Surfaces. J. Am. Chem. Soc. **132**, 4064 (2010).
[140] S. C. Parker and C. T. Campbell. Kinetic Model for Sintering of Supported Metal Particles with Improved Size-Dependent Energetics and Applications to Au on TiO_2(110). Phys. Rev. B **75**, 035430 (2007).
[141] A. T. Bell. The Impact of Nanoscience on Heterogeneous Catalysis. Science **299**, 1688 (2003).

[142] T. S. Kim, J. D. Stiehl, C. T. Reeves, R. J. Meyer, and C. B. Mullins. Cryogenic CO Oxidation on TiO_2-Supported Gold Nanoclusters Precovered with Atomic Oxygen. J. Am. Chem. Soc. **125**, 2018 (2003).
[143] M. Pan, H. C. Ham, W. Y. Yu, G. S. Hwang, and C. B. Mullins, Highly Selective Facile NO_2 Reduction to NO at Cryogenic Temperatures on Hydrogen Precovered Gold. J. Am. Chem. Soc. **135**, 436 (2013).
[144] A. Fielicke, A. Kirilyuk, C. Ratsch, J. Behler, M. Scheffler, G. Helden, and G. Meijer. Structure Determination of Isolated Metal Clusters via Far-Infrared Spectroscopy. Phys. Rev. Lett. **93**, 023401 (2004).
[145] H. Häkkinen and U. Landman. Gold Clusters (Au_N, 2≤N≤10) and Their Anions. Phys. Rev. B **62**, 2287 (2000).
[146] J. Wang, G. Wang, and J. Zhao. Density –Functional Study of Au_n (n= 2-20) Clusters: Lowest-Energy Structures and Electronic Properties. Phys. Rev. B **66**, 035418 (2002).
[147] P. Gruene, D. M. Rayner, B. Redlich, A. F. G. van der Meer, J. T. Lyon, G. Meijer, and A. Fielicke. Structures of Neutral Au_7, Au_{19}, and Au_{20} Clusters in the Gas Phase. Science, **321**, 674 (2008).
[148] S. Gilb, P. Weis, F. Furche, R. Ahlrichs, and M. M. Kappes. Structures of Small Gold Cluster Cations (Au_n^+, n<14): Ion Mobility Measurements versus Density Functional Calculations. J. Chem. Phys. **116**, 4094 (2002).
[149] F. Furche, R. Ahlrichs, P. Weis, C. Jacob, S. Gilb, T. Bierweiler, and M. M. Kappes. The Structures of Small Gold Cluster Anions as Determined by A Combination of Ion Mobility Measurements and Density Functional Calculations. J. Chem. Phys. **117**, 6982 (2002).
[150] H. Häkkinen, M. Moseler, and U. Landman. Bonding in Cu, Ag, and Au Clusters: Relativistic Effects, Trends, and Surprises. Phys. Rev. Lett. **89**, 033401 (2002).
[151] H. Häkkinen, B. Yoon, and U. Landman, X. Li, H. Zhai, and L. Wang. On the Electronic and Atomic Structures of Small Au_{N^-} (N=4-14) Clusters: A Photoelectron Spectroscopy and Density-Functional Study. J. Phys. Chem. A **107**, 6168 (2003).
[152] H. M. Lee, M. Ge, B. R. Sahu, P. Tarakeshwar, and K. S. Kim. Geometrical and Electronic Structures of Gold, Silver, and Gold-Silver Binary Clusters: Origins of Ductility of Gold and Gold-Silver Alloy Formation. J. Phys. Chem. B **107**, 9994 (2003).
[153] M. Walter, P. Frondelius, K. Honkala, and H. Häkkinen. Electronic Structure of MgO-Supported Au Clusters: Quantum Dots Probed by Scanning Tunnelling Microscopy. Phys. Rev. Lett. **99**, 096102 (2007).
[154] W. Huang and L. Wang. Probing the 2D to 3D Structural Transition in Gold Cluster Anions Using Argon Tagging. Phys. Rev. Lett. **102**, 153401 (2009).
[155] X. Li, H. Wang, X. Yang, Z. Zhu, and Y. Tang. Size Dependence of the Structures and Energetic and Electronic Properties of Gold Clusters. J. Chem. Phys. **126**, 084505 (2007).
[156] E. M. Fernández, J. M. Soler, I. L. Garzón, and L. C. Balbás. Trends in the Structure and Bonding of Noble Metal Clusters. Phys. Rev. B **70**, 165403 (2004).
[157] A. Moghaddasi and M. Zahedi. Theoretical Study of Site Dependency on Charge Transfer at Au(111) Nanoclusters. J. Phys. Chem. C **116**, 5014 (2012).

[158] D. F. Mukhamedzyanova, N. K. Ratmanova, D. A. Pichugina, and N. E. Kuz'menko. A Structural and Stability Evaluation of Au_{12} from An Isolated Cluster to the Deposited Material. J. Phys. Chem. C **116**, 11507 (2012).
[159] A. Martínez. Size Matters, but Is Being Planar of Any Relevance? Electron Donor-Acceptor Properties of Neutral Gold Clusters up to 20 Atoms. J. Phys. Chem. C **114**, 21240 (2010).
[160] D. J. Miller, H. Öberg, S. Kaya, H. S. Casalongue, D. Friebel, T. Anniyev, H. Ogasaware, H. Bluhm, L. G. M. Pettersson, and A. Nilsson. Oxidation of Pt(111) under Near-Ambient conditions. Phys. Rev. Lett. **107**, 195502 (2011).
[161] Z. Zhu, F. Tao, F. Zheng, R. Chang, Y. Li, L. Heinke, Z. Liu, M. Salmerson, and G. A. Somorjai. Formation of Nanometer-Sized Surface Platinum Oxide Clusters on A Stepped Pt(557) Single Crystal Surface Induced by Oxygen: A High-Pressure STM and Ambient-Pressure XPS Study. Nano. Lett. **12**, 1491 (2012).
[162] M. Bowker. Catalysis Resolved Using Scanning Tunnelling Microscopy. Chem. Soc. Rev. **36**, 1656 (2007).
[163] S. Helveg, H. T. Lorensen, S. Horch, E. Lægsgaard, I. Stensgaard, K. W. Jacobsen, J. K. Nørskov, and F. Bensenbacher. Oxygen Adsorption on Pt(110)-(1×2): New High-Coverage Structures. Surf. Sci. **430**, 533 (1999).
[164] W. X. Li, L. Österlund, E. K. Vestergaard, R. T. Vang, J. Matthiesen, T. M. Pedersen, E. Lægsgaard, B. Hammer, and F. Bensenbacher. Oxidation of Pt(110). Phys. Rev. Lett. **93**, 146104 (2004).
[165] N. Takahashi, H. Shinjoh, T. Lijima, T. Suzuke, K. Yamazaki, K. Yokota, H. Suzuke, N. Miyoshi, S. Matsumoto, T. Tanizawa, T. Tanaka, S. Tateishi, and K. Kasahara. The New Concept 3-Way Catalyst for Automotive Lean-Burn Engine: NO_x Storage and Reduction Catalyst. Catal. Today **27**, 63 (1996).
[166] J. K. Nørskov, J. Rossmeisl, A. Logadottir, L. Lindqvist, J. R. Kitchin, T. Bligaard, and H. Jónsson. Origin of the Overpotential for Oxygen reduction at a Fuel-Cell Cathode. J. Phys. Chem. B **108**, 17886 (2004).
[167] J. K. Nørskov, T. Bligaard, J. Rossmeisl, and C. H. Christensen. Towards the Computational Design of Solid Catalysts. Nat. Chem. **1**, 37 (2009).
[168] Y. S. Kim, A. Bostwick, E. Rotenberg, P. N. Ross, S. C. Hong, and B. S. Mun. The Study of Oxygen Molecules on Pt(111) Surface with High Resolution X-Ray Photoemission Spectroscopy. J. Chem. Phys. **133**, 034501 (2010).
[169] J. Wintterlin, R. Schuster, and G. Ertl. Existence of A "Hot" Atom Mechanism for the Dissociation of O_2 on Pt(111). Phys. Rev. Lett. **77**, 123 (1996).
[170] J. Wintterlin, S. Völkening, T. V. W. Janssens, T. Zambelli, and G. Ertl. Atomic and Macroscopic Reaction Rates of a Surfae-Catalyzed Reaction. Science **278**, 1931 (1997).
[171] N. Materer, U. Starke, A. Barbieri, R. Döll, K. Heinz, M. A. Van Hove, and G. A. Somorjai. Reliability of Detailed LEED Structural Analyses: Pt(111) and Pt(111) – p(2×2)-O Surf. Sci. **325**, 207 (1995).
[172] J. Bandlow, P. Kaghazchi, and T. Jacob. Oxidation of Stepped Pt(111) Studied by X-Ray Photoelectron Spectroscopy and Density Functional Theory. Phys. Rev. B **83**, 174107 (2011).
[173] P. J. Feibelman, S. Esch, and T. Michely. O Binding Sites on Stepped Pt(111) Surfaces. Phys. Rev. Lett. **77**, 2257 (1996).

[174] P. Gambardella, Ž. Šljivančanin, B. Hammer, M. Blanc, K. Kuhnke, and K. Kern. Oxygen Dissociation at Pt Steps. Phys. Rev. Lett. **87**, 056103 (2001).
[175] A. T. Gee and B. E. Hayden. The Dynamics of O_2 Adsorption on Pt(533): Step Mediated Molecular Chemisorption and Dissociation. J. Chem. Phys. **113**, 10333 (2000).
[176] B. C. Stipe, M. A. Rezaei, W. Ho, S. Gao, M. Persson, and B. I. Lundqvist. Single-Molecule Dissociation by Tunnelling Electrons. Phys. Rev. Lett. **78**, 4410 (1997).
[177] T. Zambelli, J. V. Barth, J. Wintterlin, and G. Ertl. Complex Pathways in Dissociative Adsorption of Oxygen on Platinum. Nature **390**, 495 (1997).
[178] H. W. Kroto, J. R. Heath, S. C. O'Brien, R. F. Curl, and R. E. Smalley. C_{60}: Buckminsterfullerene. Nature **318**, 162 (1985).
[179] W. Krätschmer, L. D. Lamb, K. Fostiropoulos, and D. R. Huffman. Solid C_{60}: a New Form of Carbon. Nature **347**, 354 (1990).
[180] R. Taylor, G. J. Langley, H. W. Kroto, and D. R. M. Walton. Formation of C_{60} by Pyrolysis of Naphthalene. Nature **366**, 728 (1993).
[181] J. B. Howard, J. T. McKinnon, Y. Makarovsky, A. L. Lafleur, and M. E. Johnson. Fullerenes C_{60} and C_{70} in Flames. Nature **352**, 139 (1991).
[182] J. B. Howard, J. T. McKinnon, M. E. Johnson, Y. Makarovsky, A. L. Lafleur. Production of C_{60} and C_{70} Fullerenes in Benzene-Oxygen Flames. J. Phys. Chem. **96**, 6657 (1992).
[183] L. T. Scott, Methods for the Chemical Synthesis of Fullerenes. Angew. Chem. Int. Ed. **43**, 4994 (2004).
[184] R. Taylor. Lecture Notes on Fullerene Chemistry: a Handbook for Chemists. Imperial College Press, London (1999).
[185] R. D. Johnson, G. Meijer, and D. S. Bethune. C_{60} Has Icosahedral Symmetry. J. Am. Chem. Soc. **112**, 8983 (1990).
[186] C. S. Yannoni, P. P. Bernier, D. S. Bethune, G. Meijer, and J. R. Salem. NMR Determination of the Bond Lengths in C_{60}. J. Am. Chem. Soc. **113**, 3190 (1991).
[187] C. S. Yannoni, R. D. Johnson, G. Meijer, D. S. Bethune, and J. R. Salem. ^{13}C NMR Study of the C_{60} Cluster in the Solid State: Molecular Motion and Carbon Chemical Shift Anisotropy. J. Phys. Chem. **95**, 9 (1991).
[188] K. Hedberg, L. Hedberg, D. S. Bethune, C. A. Brown, H. C. Dorn, R. D. Johnson, and M. De Vries. Bond Lengths in Free Molecules of Buckminsterfullerene, C_{60}, from Gas-Phase Electron Diffraction. Science, **254**, 410 (1991).
[189] M. S. Dresselhaus, G. Dresselhaus, and P. C. Eklund. Science of Fullerenes and Carbon Nanotubes. Academic Press, London (1996).
[190] W. I. F. David, R. M. Ibberson, J. C .Matthewman, K. Prassides, T. J. S. Dennis, J. P. Hare, H. W. Kroto, R. Taylor, and D. R. M. Walton. Crystal Structure and Bonding of Ordered C_{60}. Nature, **353**, 147 (1991).
[191] P. A. Heiney, J. E. Fischer, A. R. McGhie, W. J. Romanow, A. M. Denenstein, J. P. McCauley, Jr., and Amos B. Smith, III. Orientational Ordering Transition in Solid C_{60}. Phys. Rev. Lett. **66**, 2911 (1991).
[192] H. Kroto. Space, Stars, C_{60}, and Soot. Science, **242**, 1139 (1988).
[193]J. E. Fischer, P. A. Heiney, A. R. McGhie, W. J. Romanow, A. M. Denenstein, J. P. McCautley, JR., and Amos B. Smith III. Nature, **252**, 1288 (1991).

[194] G. A. Samara, J. E. Schirber, B. Morosin, L. V. Hansen, D. Loy, and A. P. Sylwester. Pressure Dependence of the Orientational Ordering in Solid C_{60}. Phys. Rev. Lett. **67**, 3136 (1991).
[195] D. M. Poirier, D. W. Owens, and J. H. Weaver. Alkali-Metal-Fulleride Phase Equilibria. Phys, Rev. B **51**, 1830 (1991).
[196] A. Cheng, M. L. Klein, and C. Caccamo. Prediction of the Phase Diagram of Rigid C_{60} Molecules. Phys. Rev. Lett. **71**, 1200 (1993).
[197] M. H. J. Hagen, E. J. Meijer, G. C. A. M. Mooij, D. Frenkel, and H. N. W. Lekkerkerker. Does C_{60} Have a Liquid Phase? Nature **365**, 425 (1993).
[198] F. Moshary, N. H. Chen, I. F. Silvera, C. A. Brown, H. C. Dorn, M. S. de Vries, and D. S. Bethune. Gap Reduction and the Collapse of Solid C_{60} to a New Phase of Carbon under Pressure, Phys. Rev. Lett. **69**, 466 (1992).
[199] B. L. Zhang, C. Z. Wang, C. T. Chan, and K. M. Ho. Thermal Disintegration of Carbon Fullerenes. Phys. Rev. B **48**, 11381 (1993).
[200] P. A. Heiney, G. B. M. Vaughan, J. E. Fischer, N. Coustel, D. E. Cox, J. R. D. Copley, D. A. Neumann, W. A. Kamitakahara, K. M. Creegan, D. M. Cox, J. P. McCauley, Jr, and Amos B. Smith, III. Discontinuous Volume Change at the Oreientational-Ordering Transition in Solid C_{60}. Phys. Rev. B **45**, 4544 (1992).
[201] F. Gugenberger, R. Heid, C. Meingast, P. Adelmann, M. Braun, H. Wühl, M. Haluska, and H. Kuzmany. Glass Transition in Single-Crystal C_{60} Studied by High-Resolution Dilatometry. Phys. Rev. Lett. **69**, 3774 (1992).
[202] J. Lu, X. Li, and R. M. Martin. Ground State and Phase Transitions in Solid C_{60}. Phys. Rev. Lett. **68**, 1551 (1992).
[203] W. I. F. David, R. M. Ibberson, T. J. S. Dennis, J. P. Hare, and K. Prassides. Structure Phase Transitions in the Fullerene C_{60}. Europhys. Lett. **18**, 219 (1992).
[204] W. I. F. David, R. M. Ibberson, T. J. S. Dennis, J. P. Hare, and K. Prassides. Addendum for Structure Phase Transitions in the Fullerenes C_{60}. Europhys. Lett. **18**, 735 (1992).
[205] X. D. Shi, A. R. Kortan, J. M. Williams, A. M. Kini, B. M. Savall, and P. M. Chaikin. Sound Velocity and Attenuation in Single-Crystal C_{60}. Phys. Rev. Lett. **68**, 827 (1992).
[206] G. B. Alers, B. Golding, A. R. Kortan, R. C. Haddon, F. A. Theil. Existence of an Orientional Electric Dipolar Response in C_{60} Single Crystal. Science, **257**, 511 (1992).
[207] W. Schranz, A. Fuith, P. Dolinar, and H. Warhanek. Low Frequency Elastic Properties of the Structural and Freezing Transitions in Single-Crystal C_{60}. Phys. Rev. Lett. **71**, 1561 (1993).
[208] R. F. Curl and R. E. Smalley. Probing C_{60}. Science **242**, 1017 (1988).
[209] D. L. Lichtenberger, K. W. Nebesny, C. D. Ray, D. R. Huffman, and L. D. Lamb. Valence and Core Photoelectron Spectroscopy of C_{60}, Buckminsterfullerene. Chem. Phys. Lett. **176**, 203 (1991).
[210] J. H. Weaver, J. L. Martins, T. Komeda, Y. Chen, T. R. Ohno, G. H. Kroll, N. Troullier, R. E. Haufler, and R. E. Smalley. Electronic Structure of Solid C_{60}: Experiment and Theory. Phys. Rev. Lett. **66**, 1741 (1991).
[211] J. H. Weaver. Fullerenes and Fullerides: Photoemission and Scanning Tunnelling Microscopy Studies. Acc. Chem. Res. **25**, 143 (1992).

[212] J. H. Weaver. Electronic Structures of C_{60}, C_{70} and the Fullerides: Photoemission and Inverse Photoemission Studies. J. Phys. Chem. Solids **53**, 1433 (1992).
[213] R. C. Haddon, L. E. Brus, and K. Raghavachari. Electronic Structure and Bonding in Icosahedral C_{60}. Chem. Phys. Lett. **125**, 459 (1986).
[214] S. Saito and A. Oshiyama. Cohesive Mechanism and Energy ands of Solid C_{60}. Phys. Rev. Lett. **66**, 2637 (1991).
[215] Q. M. Zhang, J. Y. Yi, and J. Bernholc. Structure and Dynamics of Solid C_{60}. Phys. Rev. Lett. **66**, 2633 (1991).
[216] S. G. Louie and E. L. Shirley. Electron Excitation Energies in Fullerites: Many-Electron and Molecular Orientational Effects. J. Phys. Chem. Solids **54**, 1767 (1993).
[217] L. Wang, J. Conceicao, C. Jin, and R. E. Smalley. Threshold Photodetachment of Cold C_{60}^-. Chem. Phys. Lett. **182**, 5 (1991).
[218] M. S. Dresselhaus, G. Dresselhaus, and P. C. Eklund. Fullerenes. J. Mater. Res. **8**, 2054 (1993).
[219] R. E. Haufler, L. Wang, L. P. F. Chibante, C. Jin, J. Conceicao, Y. Chai, and R. E. Smalley. Fullerene Triplet State Production and Decay: R2PI Probes of C_{60} and C_{70} in A Supersonic Beam. Chem. Phys. Lett. **179**, 449 (1991).
[220] R. W. Lof, M. A. van Veenendaal, B. Koopmans, H. T. Honkman, and G. A. Sawatzky. Band Gap, Excitons, and Coulomb Interaction in Solid C_{60}. Phys. Rev. Lett. **68**, 3924 (1992).
[221] T. R. Ohno, Y. Chem, S. E. Harvey, G. H. Kroll, J. H. Weaver, R. E. Haufler and R. E. Smalley. C_{60} Bonding and Energy-Level Alignment on Metal and Semiconductor Surfaces. Phys. Rev. B **44**, 13747 (1991).
[222] G. Gensterblum, J. J. Pireaux, P. A. Thiry, R. Caudano, J. P. Vigneron, Ph. Lambin, A. A. Lucas, and W. Krätschmer. High-Resolution Electron-Energy-Loss Spectroscopy of Thin Films of C_{60} on Si(100). Phys. Rev. Lett. **67**, 2171 (1991).
[223] E. I. Altman and R. J. Colton. Nucleation, Growth, and Structure of Fullerene Films on Au(111). Surf. Sci. **279**, 49 (1992).
[224] E. I. Altman and R. J. Colton. Determination of the Orientation of C_{60} Adsorbed on Au(111) and Ag(111). Phys. Rev. B **48**, 18244 (1993).
[225] D. Fujita, T. Yakabe, H. Nejoh, T. Sato, and M. Iwatsuki. Scanning Tunnelling Microscopy Study on the Initial Adsorption Behavior of C_{60} Molecules on a Reconstructed Au(111)-(23×√3) Surface at Various Temperatures. Surf. Sci. **366**, 93 (1996).
[226] R. J. Wilson, G. Meijer, D. S. Bethune, R. D. Johnson, D. D. Chambliss, M. S. de Vries, H. E. Hunziker, and H. R. Wendt. Imaging C_{60} Clusters on A Surface Using a Scanning Tunnelling Microscope. Nature **348**, 621 (1990).
[227] J. L. Wragg, J. E. Chamberlain, H. W. White, W. Krätschmer, and D. R. Huffman. Scanning Tunnelling Microscopy of Solid C_{60}/C_{70}. Nature **348**, 623 (1990).
[228] A. Fartash. In-Plane Orientational Order across C_{60}(111)/Au(111) Interfaces. Thin Solid Films **323**, 296 (1998).
[229] C. T. Tzeng, W. S. Lo, J. Y. Yuh, R. Y. Chu and K. D. Tsuei. Photoemission, Near-Edge X-Ray-Adsorption Spectroscopy, and Low-Energy Electron-Diffraction Study of C_{60} on Au(111) Surfaces. Phys. Rev. B **61**, 2263 (2000).

[230] G. Schull and R. Berndt. Orientationally Ordered (7×7) Superstructure of C_{60} on Au(111). Phys. Rev. Lett. **99**, 226105 (2007).
[231] M. J. Weaver, X. Gao, and Y. Zhang. Scanning Tunnelling Microscopy of Carbon Molecule (C_{60} and C_{70}) on Ordered Gold(111) and Gold(110): Molecular Structure and Electron Transmission. J. Phys. Chem. **96**, 510 (1992).
[232] I. D. Hands, J. L. Dunn, and C. A. Bates. Calculation of Images of Oriented C_{60} Molecules Using Molecular Orbital Theory. Phys. Rev. B **81**, 205440 (2010)
[233] H. Wang, C. Zeng, B. Wang, J. G. Hou, Q. Li, and J. Yang. Orientational Configurations of the C_{60} molecules in the (2×2) Superlattice on A Solid C_{60}(111) Surface at Low Temperature. Phys. Rev. B **63**, 085417 (2001).
[234] C. Chiutu, A. M. Sweetman, A. J. Lakin, A. Stannard, S. Jarvis, L. Kantorovich, J. L. Dunn, and P. Moriarty. Precise Orientation of A Single C_{60} Molecule on the Tip of A Scanning Probe Microscope. Phys. Rev. Lett. **108**, 268302 (2012).
[235] S. J. Chase, W. S. Bacsa, M. G. Mitch, L. J. Pilione, and J. S. lannin. Surface-Enhanced Raman Scattering and Photoemission of C_{60} on Noble-Metal Surfaces. Phys. Rev. B **46**, 7873 (1992).
[236] A. J. Britton, A. Rienzo, J. N. O'Shea, and K. Schulte. Charge Transfer between the Au(111) Surface and Adsorbed C_{60}: Resonant Photoemission and New Core-Hole Decay Channels. J. Chem. Phys. **133**, 094705 (2010).
[237] C. Rogero, J. I. Pascual, J. Gómez-Herrero, and A. M. Baró. Resolution of Site-Specific Bonding Properties of C_{60} Adsorbed on Au(111). J. Chem. Phys. **116**, 832 (2002).
[238] X. Lu, M. Grobis, K. H. Khoo, S. G. Louie, and M. F. Crommie. Charge Transfer and Screening in Individual C_{60} Molecules on Metal Substrates: A Scanning Tunnelling Spectroscopy and Theoretical Study. Phys. Rev. B **70**, 115418 (2004).
[239] I. F. Torrente, K. J. Franke, and J. I. Pascual. Spectroscopy of C_{60} Single Molecules: the Role of Screening on Energy Level Alignment. J. Phys. Condens. Matter. **20**, 184001 (2008).
[240] L. Wang and H. Cheng. Density Functional Study of the Adsorption of a C_{60} Monolayer on Ag(111) and Au(111) Surfaces. Phys. Rev. B **69**, 165417 (2004).
[241] I. Hamada and M. Tsukada. Adsorption of C_{60} on Au(111) Revisited: A van der Waals Density Functional Study. Phys. Rev. B **83**, 245437 (2011).
[242] E. Abad, J. Ortega, Y. J. Dappe, F. Flores. Dipoles and Band Alignment for Benzene/Au(111) and C_{60}/Au(111) Interfaces. Appl. Phys. A **95**, 119 (2009).
[243] X. Shi, M. A. Van Hove, and R. Zhang. Adsorbate-Induced Reconstruction by C_{60} on Close-Packed Metal Surfaces: Mechanism for Different Types of Reconstruction. Phys. Rev. B **85**, 075421 (2012).
[244] X. Torreles, M. Pedio, C. Cepek, and R. Felici. $(2\sqrt{3}\times 2\sqrt{3})R30°$ Induced Self-Assembly Ordering by C_{60} on A Au(111) Surface: X-Ray Diffraction Structure Analysis. Phys. Rev. B **86**, 075461 (2012).
[245] L. Tang, X. Zhang, Q. Guo, Y. Wu, L. Wang, and H. Cheng. Two Bonding Configurations for Individually Adsorbed C_{60} Molecules on Au(111). Phys. Rev. B **82**, 125414 (2010).
[246] M Hinterstein, X. Torrelles, R. Felici, J. Rius, M. Huang, S. Fabris, H. Fuess, and M. Pedio. Looking underneath Fullerenes on Au(110): Formation of Dimples in the Substrate. Phys. Rev. B **77**, 153412 (2008).

[247] L. Tang, Y. Xie, and Q. Guo. Complex Orientational Ordering of C_{60} Molecules on Au(111). J. Chem. Phys. **135**, 114702 (2011).
[248] L. Tang, Y. Xie, and Q. Guo. Probing the Buried C_{60}/Au(111) Interface with Atoms. J. Chem. Phys. **136**, 214706 (2012).
[249] A. Tamai, A. P. Seitsonen, F. Baumberger, M. Hengsberger, Z. X. Shen, T. Greber, and J. Osterwalder. Electronic Structure at the C_{60}/Metal Interface: An Angle-Resolved Photoemission and First-Principles Study. Phys. Rev. B **77**, 075134 (2008).
[250] T. Hashizume, K. Motai, X. D. Wang, H. Shinohara, Y. Saito, Y. Maruyama, K. Ohno, Y. Kawazoe, Y. Nishina, H. W. Pickering, Y. Kuk, and T. Sakurai. Intramolecular Structures of C_{60} Molecules Adsorbed on the Cu(111) – (1×1) Surface. Phys. Rev. Lett. **71**, 2959 (1993).
[251] J. A. Larsson, S. D. Elliott, J. C. Greer, J. Repp, G. Meyer, and R. Allenspach. Orientation of Individual C_{60} Molecules Adsorbed on Cu(111): Low Temperature Scanning Tunnelling Microscopy and Density Functional Calculations. Phys. Rev. B **77**, 115434 (2008).
[252] R. Fasel, P. Aebi, R. G. Agostino, D. Naumović, J. Osterwalder, A. Santaniello, and L. Schlapbach. Orientation of Adsorbed C_{60} Molecules Determined via X-Ray Photoelectron Diffraction. Phys. Rev. Lett. **76**, 4733 (1996).
[253] W. W. Pai, C. Hsu, M. C. Lin, K. C. Lin, and T. B. Tang. Structural Relaxation of Adlayers in the Presence of Adsorbate–Induced Reconstruction: C_{60}/Cu(111). Phys. Rev. B **69**, 125405 (2004).
[254] L. L. Wang and H. P. Cheng. Rotation, Translation, Charge Transfer, and Electronic Structure of C_{60} on Cu(111) Surface. Phys. Rev. B **69**, 045404 (2004).
[255] K. Tsuei, J. Yuh, C. Tzeng, R. Chu, S. Chung, and K. Tsang. Photoemission and Photoabsorption Study of C_{60} Adsorption on Cu(111) Surfaces. Phys. Rev. B **56**, 15412 (1997).
[256] T. Sakurai, X. D. Wang, T. Hashizume, V. Yurov, H. Shinohara, H. W. Pickering. Adsorption of Fullerenes on Cu(111) and Ag(111) Surfaces. Appl. Surf. Sci. **87-88**, 405 (1995).
[257] H. I. Li, K. Pussi, K. J. Hana L. L. Wang, D. D. Johnson, H. P. Cheng, H. Shin, S. Curtarlolo, W. Moritz, J. A. Smerdon, R. McGrath, and R. D. Diehl. Surface Geometry of C_{60} on Ag(111). Phys. Rev. Lett. **103**, 056101 (2009).
[258] L. Sánchez, R. Otero, J. M. Gallego, R. Miranda, and N. Martín. Ordering Fullerenes at the Nanometer Scale on Solid Surfaces. Chem. Rev. **109**, 2081 (2009).
[259] N. Nėel, J. Kröger, and R. Berndt. Fullerene Nanowires on A Vicinal Gold Surface. Appl. Phys. Lett. **88**, 163101 (2006).
[260] X. Zhang, L. Tang, and Q. Guo. Low-Temperature Growth of C_{60} Monolayers on Au(111): Island Orientation Control with Site-Selective Nucleation. J. Phys. Chem. C **114**, 6433 (2010).
[261] J. Lu, P. S. E. Yeo, Y. Zheng, Z. Yang, Q. Bao, C. K. Gan and K. P. Loh. Using the Graphene Moiré Pattern for the Trapping of C_{60} and Homoepitaxy of Graphene. ACS Nano **6**, 944 (2012).
[262] J. A. Theobald, N. S. Oxtoby, M. A. Phillips, N. R. Champness, and P. H. Beton. Controlling Molecular Deposition and Layer Structure with Supramolecular Surface Assemblies. Nature **424**, 1029 (2003).

[263] D. Bonifazi, H. Spillmann, A. Kiebele, M. de Wild, P. Seiler, F. Cheng, H. Güntherodt, T. Jung, and F. Diederich. Supramolecular Patterned Surfaces Driven by Cooperative Assembly of C_{60} and Porphyrins on Metal Substrates. Angew. Chem. Int. Ed. **43**, 4759 (2004).
[264] L. Piot, F. Silly, L. Tortech, Y. Nicolas, P. Blanchard, J. Roncali, and D. Fichou. Long-Range Alignments of Single Fullerenes by Site-Selective Inclusion into a Double-Cavity 2D Open Network. J. Phys. Chem. Soc. **131**, 12864 (2009).
[265] J. M .Macleod, O. Ivasenko, C. Fu, T. Taerum, F. Rosei, and D. F. Perepichka. Supramolecular Ordering in Oligothiophene-Fullerene Monolayers. J. Phys. Chem. Soc. **131**, 16844 (2009).
[266] B. Baris, J. Jeannoutot, V. Luzet, F. Palmino, A. Rochefort, and F. Chérioux. Noncovalent Bicomponent Self-Assemblies on A Silicon Surface. ACS Nano. **6**, 6905 (2012).
[267] W. Chen, H. L. Zhang, H. Huang, L. Chen, and A. T. S. Wee. Self-Assembled Organic Donor/Acceptor Nanojuction Arrays. Appl. Phys. Lett. **92**, 193301 (2008).
[268] G. Koller, S. Berkebile, M. Oehzelt, P. Puschnig, C. Ambrosch-Draxl, F. P. Netzer, M. G. Ramsey. Intra- and Intermolecular Band Dispersion in An Organic Crystal. Science **317**, 351 (2007).
[269] B. Xu, C. Tao, W. G. Cullen, J. E. Reutt-Robey, and E. D. Williams. Chiral Symmetry Breaking in Two-Dimensional C_{60}- ACA Intermixed Systems. Nano. Lett. **5**, 2207 (2005).
[270] B. Xu, C. Tao, E. D. Williams, and J. E. Reutt-Robey. Coverage Dependent Supramolecular Structures: C_{60}:ACA Monolayers on Ag(111). J. Am. Chem. Soc. **128**, 8493 (2006).

Chapter 3. Experimental Techniques and Methodology

All the STM experiments are carried out in an ultra high vacuum to ensure the cleanness of the sample. Due to the UHV condition, we follow certain procedures for the preparation of STM tips and samples. The main content of this chapter include the basic physics principles related to ultra-high vacuum (UHV), the general practice in operation, and the procedures of sample preparation. Two STM systems – the VT STM and the LT STM – are used to fulfil the requirements for different experimental conditions.

3.1 The Ultra-High Vacuum

3.1.1 The Definition of Ultra-High Vacuum

Surface science sometimes involves the study of surfaces more or less free of condensation from background adsorption, and this requires a vacuum environment. A vacuum is associated with limited amount of gas in a confined space and specified in the pressure unit. The ultra-high vacuum is in the range of equal to or below 10^{-9} mbar. The knowledge of the kinetics of atoms and molecules is essential for a good understanding of the vacuum systems.

The molecule or atom flux in the unit of monolayer (ML) per second (s) can be described by the Hertz-Knudsen equation

$$Z_W = \frac{p}{\sqrt{2\pi m k_B T}}, \tag{3.1}$$

which embodies the mass of a molecule m, the environment temperature T, and the pressure p [1]. Generally speaking, at a pressure of about 1×10^{-6} mbar, a surface can be fully covered by molecules in only one second assuming that

molecules adhere to the surface once they hit the surface at 300 K [1]. If the vacuum pressure is about 1×10^{-10} mbar, the surface can stay intact for about one hour. The UHV condition is also necessary for electron spectroscopy measurement. As detecting electrons need a transit path in the order of 1 metre from the sample to the detector when the detecting electrons should be free of any collision with the molecules in the vacuum. This travel length corresponds to the physics term – the mean free path λ

$$\lambda = \frac{k_B T}{\sqrt{2}\pi\sigma p}, \tag{3.2}$$

where σ is the collision cross section equal to the square of a molecular diameter [2]. At pressure of 1.0×10^{-10} mbar and room temperature (~ 300 K), the mean free path is about 500 km which is far above the vacuum standard for electron spectroscopy.

3.1.2 Attaining UHV

To achieve and maintain UHV, a joint cooperation of vacuum pumps and pressure gauges is essential. Vacuum pumps are classified into two categories – gas transfer vacuum pumps and gas-binding vacuum pumps. Each pump has its own pumping speed and pressure region of maximum working efficiency. In the air-tight chamber of the Omicron STM used in our experiments, the system is equipped with an ion pump and a Ti sublimation pump (TSP) to maintain the vacuum. These two pumps belong to the category of gas-binding pumps. The ion pump ionizes molecules by a high electrical field (typically 3kV, 5 kV and 7 kV) between its cathode and anode. The ions are accelerated and then either collected by the cathode or buried in the wall of the pump. Ti is an active metal that most gas molecules bind with irreversibly. Our TSP pump has three Ti filaments. When it

works, Ti is sublimed from the filament, forming a thin layer of Ti on the inner wall of a metal cylinder usually assembled to vacuum chamber. Gases are absorbed by the fresh layer of Ti. In order to extend the service life of Ti filaments, TSP pump usually work at vacuum better than 10^{-7} mbar. Because there is outgas from the chamber wall and other subtle leaks through connections, a UHV chamber depends on these two pumps – the ion pump and TSP to maintain the vacuum.

There are inlets of the STM UHV chamber, which are used for sample transfer from outside to the UHV chamber, for chemical vapour deposition and for pumping down the chamber before it reaches UHV condition. In these cases, the vacuum in the chamber deteriorates to high vacuum level in the range of 10^{-7} to 10^{-5} mbar when the ion pump needs to be switched off. A pumping station, consisting of a mass transfer pump and a rough pump that is used as a backing pump, is put into use during those operations. A rough pump is connected at the outlet of the mass transfer pump. Our UHV chamber is equipped with a turbo pump and a rotary pump. When the rotary pump reaches the required backing vacuum ($10^{-2} \sim 10^{-3}$ mbar), the turbo pump accelerates to its peak speed. The rotary pump can work at atmospheric pressure with a high throughput. A good backing pressure can assist the performance of the turbo pump. Turbo pump has a better pumping efficiency on heavy molecules than in light molecules such as He and H_2. The vacuum chamber can be kept at about 10^{-8} mbar when the pumping station is working.

3.1.3 Venting and Baking

Venting a UHV chamber is necessary sometimes, to change or fix parts inside it. To prevent contamination to the parts inside the vacuum chamber, it should be

vented with nitrogen gas. Water vapor from air sticks to the vessel wall, which is difficult to remove following evacuation.

If the UHV chamber is opened and gets contact with the atmosphere, a bakeout step is a must to achieve UHV standard (≤ 10^{-10} mbar) with cooperation of three types of pumps at different pumping stages. During bakeout, the STM system is covered with heat shields. After the vacuum is better than 10^{-5} mbar, an oven inside the bakeout cover gradually heats the whole system at a temperature increment rate of 1 °C/min. The ultimate bakeout temperature is set to be 140 °C to 150 °C and the heating lasts for 24 hours to 60 hours in accordance with the volume of the chamber and what kinds of gases the chamber has been exposed to. This process helps to remove water with increased desorption and diffusion efficiency. The bakeout controller monitors the bakeout process from heating to cooling. Before start, all the glass windows and ceramic parts are covered with alumina foil and all the unbakeable parts, made of plastic or having magnetic property, need to be taken off from the system. And all the electronic connect cables are protected with metal plugs to avoid harmful discharge. During the cooling period at about 70 °C, the ion pump and TSP are degassed by starting the devices at different work powers for a short time, until they can work without causing a pressure increase. Because of the requirement that the materials in UHV environment need to have a low outgas rate and high temperature resistance, stainless steel components and metal seals (e.g. Cu) must be used. Molybdenum, Tantalum, and Tungsten are also appropriate.

The whole UHV system is protected by the interlock. In case of power failure or other emergencies that can cause damage, all the gauges and pumps will be shut

down automatically when the vacuum exceeds the minimum base pressure for operation.

3.1.4 The Leakage Detection

The UHV system is very sensitive to leakage due to the large pressure difference between the space inside and outside of the chamber. Air leakage disturbs the normal functioning of the UHV STM system. Usually, leakage is subtle with pressure increase of one or two orders of magnitude, which requires sensitive measuring methods to locate where the leakage happens. The common method we use employs the mass spectrometer and test gas Helium. He is chosen as the test gas because it is non-active, non-toxic and takes up a small share in air. Because He is lighter than the average mass of air and therefore flows upwards, leak detection should start from the highest point of all the suspected parts. He atoms can quickly diffuse through the leak to the detector of the mass spectrometer, which is located inside the chamber. The controller of mass spectrometer, connected with the detector through a port, has an audible indicator, which increases the sound pitch when He concentration rises. Leakage can also be confirmed from mass spectrum of the gas molecules in the UHV chamber when the ratio of the peaks of nitrogen (mass = 28) and oxygen (mass = 32) is 4/1, near the ratio of the two gases in air.

3.2 Tip Treatment

There are mainly two ways to prepare an STM tip. The commonly used method is the DC chemical etching method, where tungsten wire is etched in a NaOH or KOH solution. Normally, an Ir/Pt tip, it is mechanically cut using a clipper. When cutting the wire, there should be an angle between the wire and the cut direction. The smaller the angle is, the sharper the tip will be. This is a relatively more

straightforward method than chemical etching. And the tip can function very well to get clear STM images. Chemical etching is a more controllable method. It is easy to get a sharp tip. The aspect ratio of the etched tip is controlled by the concentration of the solution, the length immersed in the solution, and etching voltage.

3.2.1 Tungsten Tip – Electrochemical Etching

In our UHV experiments, the W tip is made by chemical etching using 2M NaOH solution. Distilled water is used to dissolve 40 g NaOH pellets. The solution needs 24 hours to become uniform. The setup is shown in Figure 3.1. It consists of two electrodes and a connecting vessel. The connecting vessel is filled with NaOH solution with some space left in the connecting pipe. A W wire of 0.4 mm in diameter is held by a metal rod, partly immersed in the solution on one side of the vessel and connected to the anode of a power supply. On the other side of the vessel, the cathode of the power supply is connected to a W wire bent as shown in Figure 3.1a, where hydrogen gas forms during etching. One advantage of the connecting vessel is that it can prevent the hydrogen bubbles on the cathode from disturbing the meniscus around the W wire. A small section of W wire (connected to the anode) at the air-solution interface is gradually dissolved by NaOH solution when a direct current is applied at the voltage of about 10 V. As soon as the lower part of the tungsten wire drops off (Figure 3.1b), the power supply immediately cuts the power to prevent further etching as the tip may still contact with the solution surface. A sharp tip forms for both parts, one held by the rod and the other at the bottom of the vessel (Figure 3.1b).

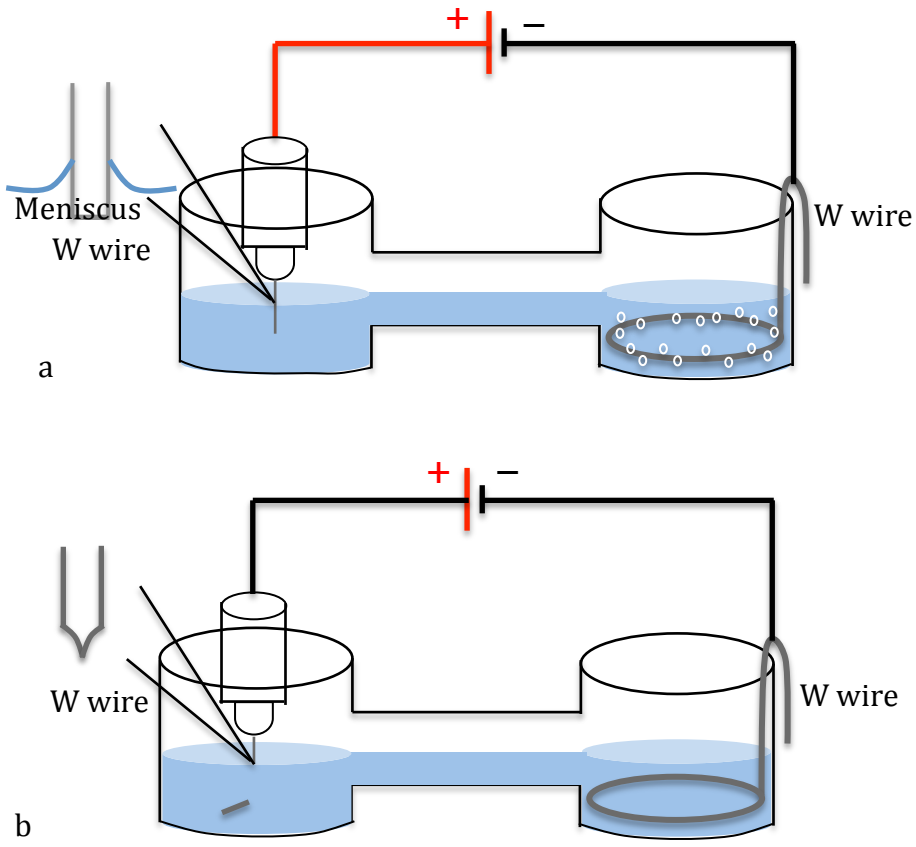

Figure 3.1 The tip etching kit. (a) The tip is connected to an anode where the part at the interface of air and solution is etched. A meniscus forms when the wire is inserted into the solution. At the cathode, a long W wire bent into a circle is immersed in the solution, where during etching, hydrogen bubbles are released. (b) When the lower part of the W wire drops off, the power supply is cut off.

The whole chemical reaction is as follows [3]:

Cathode $6H_2O + 6e^- \rightarrow 3H_2 \uparrow + 6OH^-$

Anode $W + 8OH^- \rightarrow WO_4^{2-} + 2H_2O + 6e^-$

Overall $W + 2OH^- + 2H_2O \rightarrow WO_4^{2-} + H_2 \uparrow$

During etching, the etching kit should be isolated from any vibration, because vibration causes the perturbation of the meniscus (the zoom-in image of the interface of the wire and the solution in Figure 3.1a) and thus an irregular shape of

the tip after etching. The NaOH residual on the tip is removed by dipping the tip in distilled water and then ethanol several times. The tip is also degassed inside the high vacuum preparation chamber at 150 ˚C for 30 minutes. Now the tip can be used in the VT STM to image. But for the tip used in the LT STM, the tungsten oxide layer on its surface is further removed by high-temperature treatment.

3.2.2 Tip Treatment – High Temperature Annealing

The tip is heated in a vacuum of 10^{-7} mbar. The annealing device is shown schematically in Figure 3.2. The end of the tip is placed in contact with a tungsten wire of larger diameter (Figure 3.2a). The tip has the highest resistance of the device. When current passes through the wire, the tip gets heated first. A current of about 6.3 A is flashed through the tip wire when the temperature of the tip reaches ~ 1000 ˚C in a bright orange colour for 3 seconds. Then the current is kept at about 3.5 A, when the tip just glows in dark orange colour (about 600 °C) for five minutes for the purpose of degassing (Figure 3.3b).

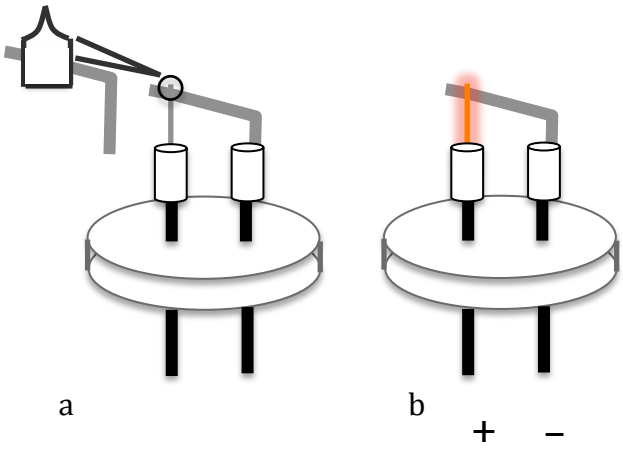

Figure 3.2 A simple device for tip annealing. (a) A flange with a freshly made W tip is placed as part of a circuit, where the thin wire (the W tip) has the highest resistance in the circuit. The apex of the tip is positioned as shown in the zoom-in image, which

can guarantee that the temperature of the pinpoint is high enough to evaporate the W oxide there. (b) When a current flows through the tip, it is resistively heated. A temperature of about 1000 °C is achieved when a current of 6.3 A is applied and the tip glows in bright orange colour.

This baking process removes the tungsten oxide layer from the tip, after which the sharp end of the tip exhibits metal surface of a shiny white colour. The W metal has a high melting point (3410 °C). Tungsten oxide (WO_2) sublimes at a temperature above 800°C [3]. At last the tip is taken out from the vacuum and transferred into the preparation chamber of the UHV STM chamber, where it is gently annealed at about 150 °C to remove adsorbates from air.

The quality of the STM tip is important in order to get atomic resolution and a stable tunneling condition. There are a number of ways to sharpen a tip from practical experiences. STM tip can be treated by controlled collision [3]. After the collision there is usually a crater left on the surface. A high bias is suddenly applied to the tip and kept for several scans, during which there is a strong interaction between the tip and the sample. And then the bias is reduced to the normal value, ~ ±1 V. Usually after this treatment, the tip becomes better, with a stable tunneling junction. Improvement of tip resolution can also be induced by increasing the tunneling current by a factor of two for a few seconds. Both of these sharpening processes may cause the tip to move to a new position. For new tips, it is easier to get atomic resolution of the Au(111) surface perhaps due to the large curvature of the tip at the apex.

The resolution of the STM can be improved with the decoration of H atoms at the tip apex [4, 5, 6]. Weiss et al. carried out a low temperature experiment at 5 ~ 10 K

to image 3,4,9,10-perylenete-tracarboxylic-dianhydride (PTCDA) on Au(111) with an H-sensitized tip[4]. The attachment of a hydrogen atom is accomplished by filling the STM chamber with molecular hydrogen, and the dissociative adsorption of hydrogen molecule to the tip [6]. They managed to observe the intramolecular structure with the resolution of carbon rings, which may result from local molecular interaction [4].

3.3 Sample Preparation

The samples – Au thin films on HOPG, used in the experiments were prepared in a high vacuum Edwards evaporator. Metal and molecule evaporation is accomplished in the UHV STM chamber.

3.3.1 The Preparation of the Clean Au(111) Surface

The Edwards evaporator is a high vacuum system with a base pressure of around 1×10^{-7} mbar pumped by a molecular turbo pump together with a rotary pump. The vacuum level is monitored by a Pirani gauge in the pipeline that connects the rotary pump and the turbo pump (Figure 3.3). A Penning gauge is used to check the vacuum in the chamber when the vacuum is below 10^{-3} mbar. Below is a simplified diagram of the vacuum system, Figure 3.3. One gas line is for venting and the other is for pumping.

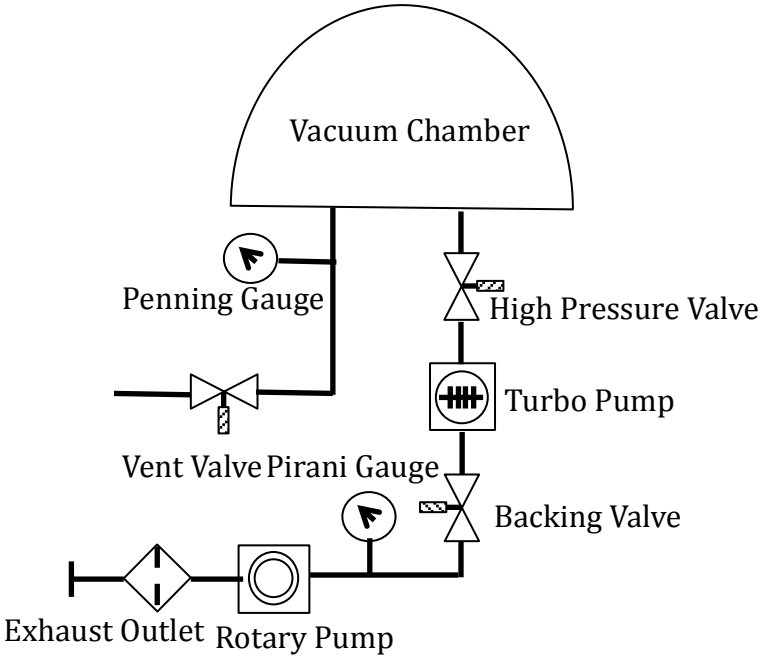

Figure 3.3 A simplified diagram of the Edwards vacuum pumping system [7]. One gas line is used to vent the chamber. Besides the venting valve, there are other valves (not shown) in this line controlled by interlock. The other gas line is for pumping the chamber.

A clean and flat HOPG surface, confirmed by visual inspection, was prepared by cleaving with adhesive tape. The freshly cleaved HOPG was placed on top of the copper base of a sample holder and fixed by a copper plate with two rectangular voids in the centre. The copper base can be heated by a tungsten wire attached at the back and isolated from the copper base by two mica sheets. During deposition, the temperature of the HOPG substrate was maintained at around 250 °C measured by a thermocouple resting in a small hole drilled in the copper base. Au wire of 99.99% purity was loaded in a Mo boat positioned directly below the HOPG substrate with a separation of about 7 cm. There was a shutter in between the sample and the source.

When the vacuum in the chamber reached 1×10^{-7} mbar, the HOPG substrate was gently heated to 250 °C to remove adsorbates. An elevated substrate temperature ensures sufficient surface mobility of Au atoms on the flat surface of HOPG, and the Au thin films obtained always have flat terraces of the area of up to 1 μm^2. The Au wire was degassed at a temperature about 20 °C below the evaporation temperature for 20 minutes with a direct current flowing through the Mo boat. The temperature of the source was measured with an optical pyrometer. The shutter between the substrate and the Au source was always closed before the start of deposition. After finishing the deposition, samples were kept in the vacuum chamber until the temperature of the sample decreased to room temperature. Then the sample was taken out from the evaporator and transferred to the UHV chamber of the STM. Practical experience shows that Au thin film prepared following this procedure always exhibits large flat terraces under the observation by STM.

The Au sample is put on an UHV sample holder with a resistive heating plate below the sample, which is used in variable temperature experiments to heat the sample. In the UHV chamber of the STM, the Au thin film is further cleaned by Ar^+ sputtering and high-temperature annealing at 1000 K for several cycles until the herringbone reconstruction of Au (111) can be seen by STM. A 4-5 kV voltage is applied between the anode and cathode of an ion gun to discharge Ar gas, and the Ar ions are accelerated by an electrical field of 1 kV. The size of the sample is 0.5 cm^2 and an ion beam current is about 10 ~ 14 μA, which amounts to 6.25×10^{13} ions per second sputtering on the surface of the Au sample. After removing the top few layers, the annealing process allows the Au thin film to recover, recrystallize, and release impurities in the bulk. The sputtering and annealing process needs to

be repeated for a few cycles until a clean Au surface with the herringbone reconstruction can be observed by STM.

3.3.2 Au Atom and C_{60} Molecule Deposition

In-situ deposition inside the UHV chamber is fulfilled with Knudsen cells (K cells), which are used to thermally evaporate sources of low partial pressure. The Knudsen cell for depositing C_{60} molecules is homemade. C_{60} powder (commercially available) is contained in a pocket made of tantalum. A K-type thermocouple is welded near the nozzle to measure the temperature of the metal pocket. Before every deposition, the C_{60} source is degassed at about 600 K for 10 minutes. During deposition, the cell is heated to about 750 K with the background vacuum in the range of 10^{-8} mbar. At such a temperature, the deposition rate is approximately 0.05 ML per minute. The deposition time corresponds to the extent of the coverage. The Knudsen (high temperature effusion) cell for Au atom deposition was purchased from CreaTech. Au wire of 99.99% purity is placed in an alumina crucible. The control unit can accurately change the temperature of the Au source. A manually controlled shutter is installed in front of the orifice of the cell. Before deposition, the Au source is degassed at 1120 °C for 5 minutes and deposited at 1100 °C. The deposition rate of Au atoms at 1100 °C is about 0.012 ML per minute as measured from the Au coverage in STM images.

3.4 The VT and LT STM System

In this section, the VT STM and LT STM are discussed, which are specifically designed for different experiments in various conditions. The VT STM is useful when studying the thermal response of a sample at different temperatures, where the STM can follow the changes on the surface. A high-resolution image with

molecular structure, and stable STS, can only obtained at low temperature using the LT STM. The atomic resolution of both systems is achieved with the combination of electronic control and mechanical design as well as the quantum tunneling effect.

The electronic control for both VT STM and LT STM is similar. There are three connections between the control unit and the STM stage. One is the preamplifier (VT PRE) for the amplification of the tunneling current. A second cable is the cable for the control signals of the piezo scanner and the coarse motion motor. The movement of the piezo in the z direction is controlled by a feedback loop to maintain constant current or height during scanning. A third is the heating/cooling control cable, which is useful during variable temperature experiments and for a defined sample potential with the connection to earth. In the VT system, the sample is held at virtual ground while the tip is at a changeable potential controlled by a computer interface.

An important part in the mechanical design of the STM is vibration isolation. Mechanical noise from the surrounding environment causes disturbance to the tunneling junction. Vibration isolation is achieved via adoption of several damping stages. First of all is the foundation isolation. The whole STM system is placed on a special stage with a damping suspension for both vertical and horizontal motion. Acoustic noise is prevented by the lab walls which have panels that adsorb sound. A second isolation is with the STM stage, where four springs are used for suspending the STM stage during scanning. A push-and-pull motion (PPM) drive is used to lock the STM stage when exchanging samples and tips, and unlock the STM stage during scanning. An eddy current damper made of copper plates and permanent magnets is mounted around the STM stage. When a ring of copper

plates moves in the magnetic field, eddy current is induced in the conductor, and damping forces in the opposite direction to the relative movement direction of the copper and the magnet are generated through interaction between the eddy current and the magnetic field, to damp the motion of the STM stage.

Besides noise from environment, there is also electrical noise from tunneling gap fluctuation due to instability of the tip. Bright streaks on STM images come from the movement of adsorbates on the tip or the sample that disturbs the tunneling junction.

3.4.1 The Features of the VT STM

A simple top view of the VT STM chamber is shown in Figure 3.4. This system is relatively compact compared with that for the LT STM. Samples and tips are transferred to the vacuum chamber through the Fast Entry lock (FEL) (on the top of Figure 3.4). The small chamber of the FEL is at ambient condition when a sample is put at the transfer folk from outside. Then the FEL chamber is sealed with three knurled screws through the door flange, and is pumped by a rotary and turbo pumping station. There is a gate valve between the FEL and the UHV chamber. After at least 20 minutes' pumping, the gate valve is slowly opened and the sample can be taken out and put in the carousel by a wobble stick, which is a transferring tool for samples and tip within the vacuum chamber.

The manipulator is an important part associated with the chamber. It can hold the tip and sample at the heating stage for annealing treatment at temperatures from room temperature to about 1100 K by indirect heating. During Ar^+ sputtering and molecule dosing in the gas phase, the sample surfaces can be positioned towards different ports where ions or molecules enter the UHV chamber with primary

(polar) rotation of the manipulator. A carousel with twelve spaces is used for parking samples and tips. Au samples can stay clean and free of any contamination for several days inside the chamber.

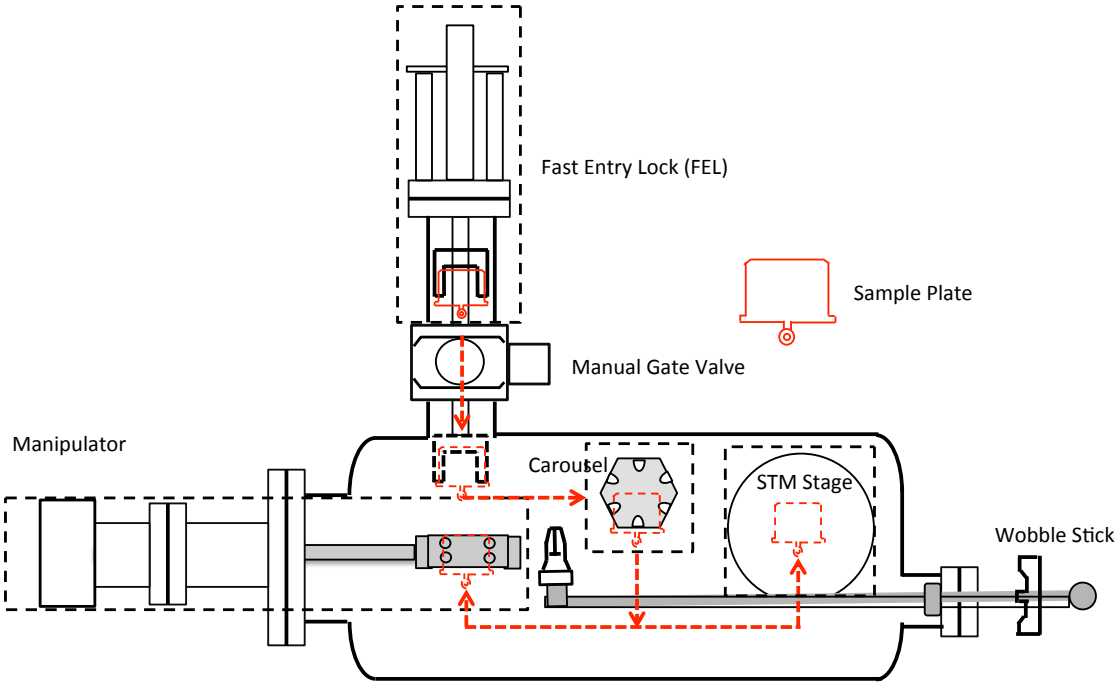

Figure 3.4 A simple diagram of the UHV VT STM main chamber. A top view of the sample plate is shown on the right. The paths for sample or tip transfer from the ambient to the UHV chamber and within the chamber are indicated by red dashed lines with arrows. The fast entry lock is used to transfer objects from the ambient to the UHV chamber and there is a manually operated gate valve separating the small chamber of FEL and the main chamber. The manipulator has a heater stage and can be rotated to let the sample or tip face different ports. The wobble stick can move sample and tip within the UHV chamber.

The VT STM system has cooling and heating facilities to achieve temperatures from 25 K to 1500 K. For low temperatures between 100 K and room temperature,

cooling can be fulfilled with liquid nitrogen (LN_2). There is a bath cryostat mounted on the base flange (Figure 3.5). A copper braid connected with the cryostat is used to transfer cooling power. The sample holder is clamped with a metal block (Figure 3.6b) and the sample holder with the sample is exclusively cooled, while the rest parts of the STM stage beside the tip remain at room temperature. An integral heater is fitted to the heat exchanger, which is controlled by a temperature controller. Any temperature between room temperature and 100 K can be achieved by regulating the LN_2 flow and output power of the heater.

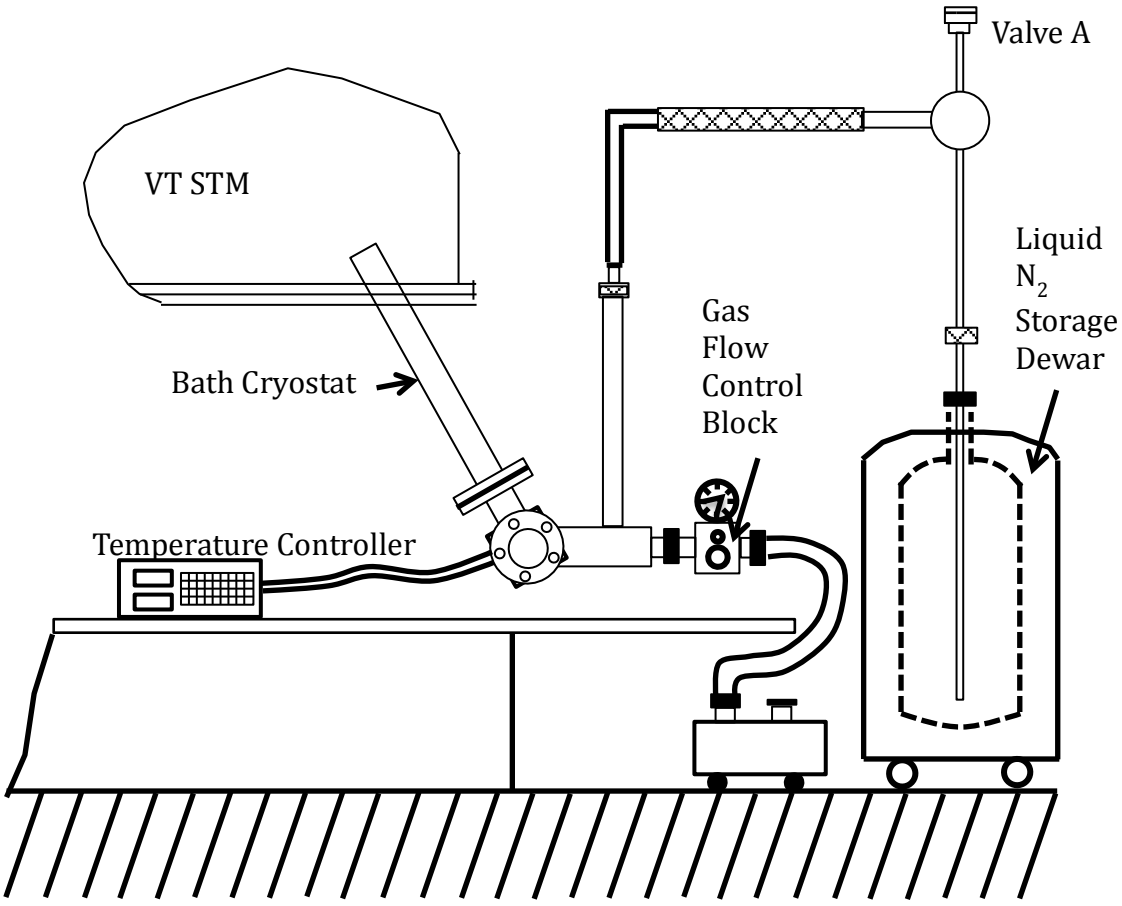

Figure 3.5 Schematic diagram for LN_2 cooling.

The whole cooling setup is schematically shown in Figure 3.5. The valve A can regulate the LN_2 flow out of the LN_2 storage dewar. A gas flow control block regulates the N_2 gas flow from the bath cryostat. A rotary pump drives the gas flow. When a thermal equilibrium is reached, the temperature of the sample is about 20 K higher than that of the cryostat as measured with a silicon diode. The temperature controller displays the temperatures at the sample stage and at the cryostat. To achieve a temperature below 100 K and above 40 K, liquid He (LHe) is required. It takes hours to reach the lowest temperature. In order to eliminate thermal drift during scanning, the tip is positioned at the place near the tunneling position during the cooling process when the tip can be indirectly cooled. The tip gradually retracts from the sample surface if the sample temperature continuously decreases until a thermal balance is reached.

There are two ways to heat a sample. One is direct heating, with current flowing directly through the sample (Figure 3.6c), which is commonly used for samples (e.g. silicon) that have large resistance. The other is indirect resistive heating, in which current flows through a pyrolytic boron nitride (PBN) plate placed above the sample (Figure 3.6d) with the sample facing downwards. Indirect heating is used when the sample resistance is lower than 2 Ω. The sample holder for indirect heating is specially designed as shown in Figure 3.6a, with a heat shield to prevent heat radiation and a PBN heating component integrated. The contact brush is for electric conduction. Indirect heating can achieve highest temperature of 750 K.

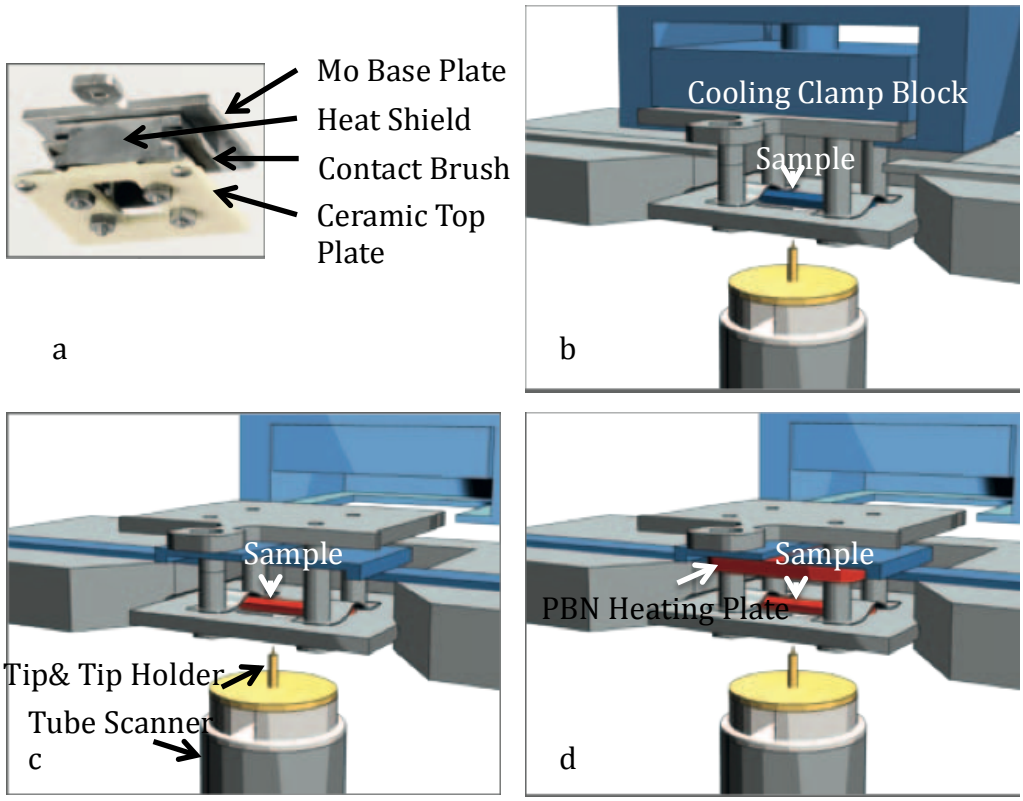

Figure 3.6 Schematic diagrams of the sample holder and the VT STM functioning at cooling or heating conditions. (a) A sample holder for indirect resistive heating. (b) The sample is cooled by a clamp block and the tip (yellow) is scanning the sample (blue) at low temperatures. (c) The sample is heated by a direct current flowing through the sample (red). (d) An indirect resistive heating method used with current passing through the PBN plate (red) above the sample for radioactive heating the sample (red). [Images from Omicron VT STM manual]

When there is a temperature gradient between the sample and tip, thermal drift due to thermal contraction or expansion of the sample always occurs. The scan frame needs to be adjusted manually to compensate for thermal drift, and to centralize the area of interest during scanning. From Figure 3.6b we can see that only the sample is heated or cooled while the STM stage stays at room temperature.

3.4.2 The Features of the LT STM

The LT STM is designed for low temperature experiments. The LT STM is operated at 77 K with LN_2 cooling or at 5 K with LHe cooling. Unlike the VT STM, the entire STM stage including the vibration isolation is kept at the same low temperature. Therefore, the system has an outstanding thermal stability.

Two separate and concentric bath cryostats enclose the working stage. The outer cryostat is filled with LN_2 for thermal shielding, the inner cryostat for cooling filled with either LN_2 for experimentation at 77 K or LHe for experimentation at 5 K. The shielding from the outer cryostat can substantially extend the usage of expensive LHe in the inner cryostat during experiment. Other temperatures between 5 K to 60 K and 77 K to room temperature are also achievable using the LT STM. There is a heater fitted to the scanning stage with a silicon diode for temperature measurement. Elevated temperatures have an increased cost in the LN_2 or LHe consumption.

There is a preparation chamber associated with the analysis chamber where the STM stage is, with a gate valve separating the two. Sample and tip are transferred into the preparation chamber first through a small fast entry lock. The manipulator equipped with the preparation chamber has two stages, one for heating and the other one for cooling. The heating stage has a resistive heating element and electrical connection with external power supply and other measurement devices. An Au sample or a Si sample needs to be placed at the heating stage for cleaning. The cooling stage is used when deposition onto a substrate at low temperature is required. In addition to the polar rotation movement, the manipulator can move in the horizontal direction to transfer objects from preparation chamber to analysis chamber.

Operation at low temperature needs a lot of care. The scan range of the tip is limited to 1.2 μm for LT STM (compared to 4 μm for VT STM). The surface sticking probability almost equals to 1 at 50 K or below. The vacuum in the analysis chamber is maintained at 10^{-12} mbar to avoid residual gas adsorption onto the cold surface. If atoms are picked up by the tip at low temperature, they are hard to get rid of in normal tunneling conditions. On the other hand, atoms are more stable than they are at room temperature.

References

[1] K. W. Kolasinski. Surface Science: Foundations of Catalysis and Nanoscience. Second Edition, Wiley, (2008).
[2] J. A. Venables. Introduction to Surface and Thin Film Processes. Cambridge University Press, Cambridge (2003).
[3] C. J. Chen. Introduction to Scanning Tunneling Microscopy. Second Edition, Oxford University Press, Oxford 315 (2008).
[4] C. Weiss, C. Wagner, R. Temirov, and F. S. Tautz. Direct Imaing of Intermolecular Bonds in Scanning Tunneling Microcopy. J. Am. Chem. Soc. **132**, 11864 (2010).
[5] C. Weiss, C. Wagner, C. Kleimann, M. Rohlfing, F. S. Tautz, and R. Temirov. Imaging Puali Repulsion in Scanning Tunneling Microscopy. Phys. Rev. Lett. **105**, 086103 (2010).
[6] J. I. MartÍnez, E. Abad, C. González, F. Flores, and J. Ortega. Improvement of Scanning Tunneling Microscopy Resolution with H-Sensitized Tips. Phys. Rev. Lett. **108**, 246102 (2012).
[7] BOC EDWARDS. Instruction Manual AUTO 306 Vacuum Coater with Turbomolecular Pumping System. Issue G, **1**, 5.

Chapter 4. Probing the C_{60}/Au(111) Interface with Au Atoms

The interfaces between C_{60} single layer and various metal substrates have been widely studied using different surface analytic techniques, as reviewed in Chapter 2. Scanning tunnelling microscopy is an ideal technique to study the growth and nucleation of the C_{60} layer. However, the interface structure buried beneath the C_{60} layer is out of the reach of STM. The interface information can be derived indirectly from spectroscopy and diffraction patterns, as well as theoretical simulations about the electronic, chemical and physical properties of the interface. This chapter introduces the experiment of study on the C_{60}/Au(111) surface.

All STM images in this chapter are presented in gold-scale colour of the raw data, with plane subtraction to remove tilt. Streaks on the STM images are due to the perturbation of the tunnelling junction by Au atoms or C_{60} molecules in proximity to the tip at work.

4.1 C_{60} Monolayer on the Au(111) Surface

Due to the high chemical and physical stability of C_{60} molecules, they can be thermally evaporated and readily form hexagonally compact islands on the Au(111) surface. However, due to the size difference between the C_{60} molecule (about 10.02 Å in diameter) and the Au atom (about 2.35 Å in diameter), the C_{60} epilayer is not always commensurate with the Au(111) surface. So far, three superstructures of C_{60} monolayer on Au(111) have been widely recognized [1, 2]. Only in the $2\sqrt{3}\times2\sqrt{3}$-R30° superstructure do all the C_{60} molecules occupy the same lattice site

on Au(111). Due to the strong interaction between C_{60} and metallic surfaces, a dim and bright contrast or height contrast is widely observed by the STM for C_{60} layer on the surfaces of various metals such as Cu, Ag, and Au. One explanation for the observation is that the bright C_{60} molecule occupies a top site over an Au atom having a weaker bonding with the surface while the dim C_{60} molecule sits over a nanopit (an Au vacancy in the (111) surface) with a stronger bonding via a facilitated charge transfer from the metal substrates [3, 4, 5]. To properly describe a close packed C_{60} layer on Au(111), one needs to know: i) the close-packing direction of the molecules relative to the close-packing direction of Au atoms in the substrate; ii) the distribution of dim and bright molecules. Based on i), we can classify C_{60} layers into 38×38-R0°, $2\sqrt{3}\times2\sqrt{3}$-R30°, and 7×7-R14° rotational domains. Based on ii), we can further describe a C_{60} domain as a contrast uniform phase, contrast disordered phase, and periodic phase. Here the contrast uniform phase or uniform phase represents a domain where C_{60} molecules have the same height apart from a very small fraction of dim looking molecules. The contrast disordered phase refers to a domain consisting of a random mixture of bright (high) and dim (low) molecules. The periodic phase refers to a domain where the dim molecules are equally spaced from each other. Here the domain indicates a region of close packed C_{60} molecules in the same orientation with respect to the substrate. This section introduces the observations of the different phases of the C_{60} layer on Au(111) and the diffusion of Au atoms at the C_{60}/Au(111) interface at room temperature.

4.1.1 C_{60} Molecular Phases

A majority of the freshly deposited C_{60} monolayer on Au(111) shows the 38×38-R0° structure, as islands initially grow out from Au steps a high density of which are in the close packing directions, via a hit and stick manner. Molecules inside the 38×38-R0° domain appear uniform in contrast. The rest of the C_{60} monolayer takes on the disordered and periodic phases. A thermal annealing process promotes the transformation of the C_{60} layer in the 38×38-R0° phase of poor lattice matching, to the $2\sqrt{3}\times2\sqrt{3}$-R30° commensurate phase. A large C_{60} domain can sometimes exhibit two phases at the same time, when phase transition is not complete, as seen in Figure 4.1a. Two zoom-in images at the phase boundary are shown in Figure 4.1b and 4.1c. Imaging at positive bias 1.2 V, Figure 4.1b shows an obvious dim and bright contrast among the molecules and the distribution of dim and bright molecules at the phase boundary between the disordered phase and the uniform phase seems quite random.

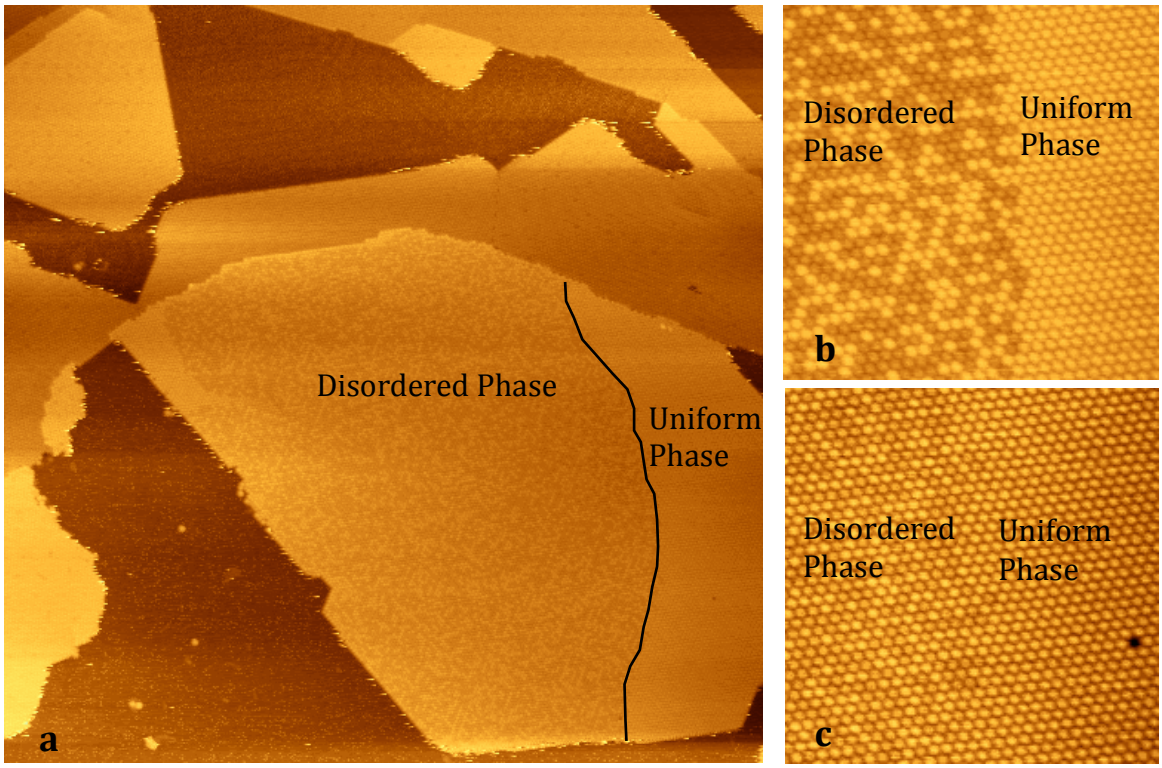

Figure 4.1 Submonolayer C_{60} on Au(111) without annealing. (a) Au surface is not fully covered. On the terrace, a large C_{60} island is in two phases with the phase boundary indicated by a solid black line. On the left of the phase boundary is a disordered phase and on the right a uniform phase without dim C_{60} molecule. (Image size: 200 nm × 200 nm, tunnelling bias V_{sample}: 1.2V, tunnelling current I_t: 0.03nA) (b) An irregular boundary between the disordered phase and the uniform phase. (Image size: 29 nm× 29 nm, V_{sample}: 1.2 V, I_t: 0.03 nA) (c) Image obtained at negative bias -1.2V. The dim and bright contrast is vague compared to the image b obtained at positive bias 1.2 V. (Image size: 29 nm × 29 nm, V_{sample}: -1.2 V, I_t: 0.03 nA)

After annealing at about 300 °C, dim molecules can be observed in all the domains as shown in Figure 4.2. The image includes three phases and there is a step running vertically. The domains marked A on the lower terrace and A' on the upper terrace are in the uniform phase with scattered distribution of the dim

molecules. The dim molecules in domain B (Figure 4.2) show an indication of long-range order with an average separation of about 6 ~ 7 molecules. The contrast disorder in domain C (Figure 4.2) results from the random intermixture of dim and bright molecules, in which the dim molecules make up about 52 ~ 55 % of the total in the disordered phase.

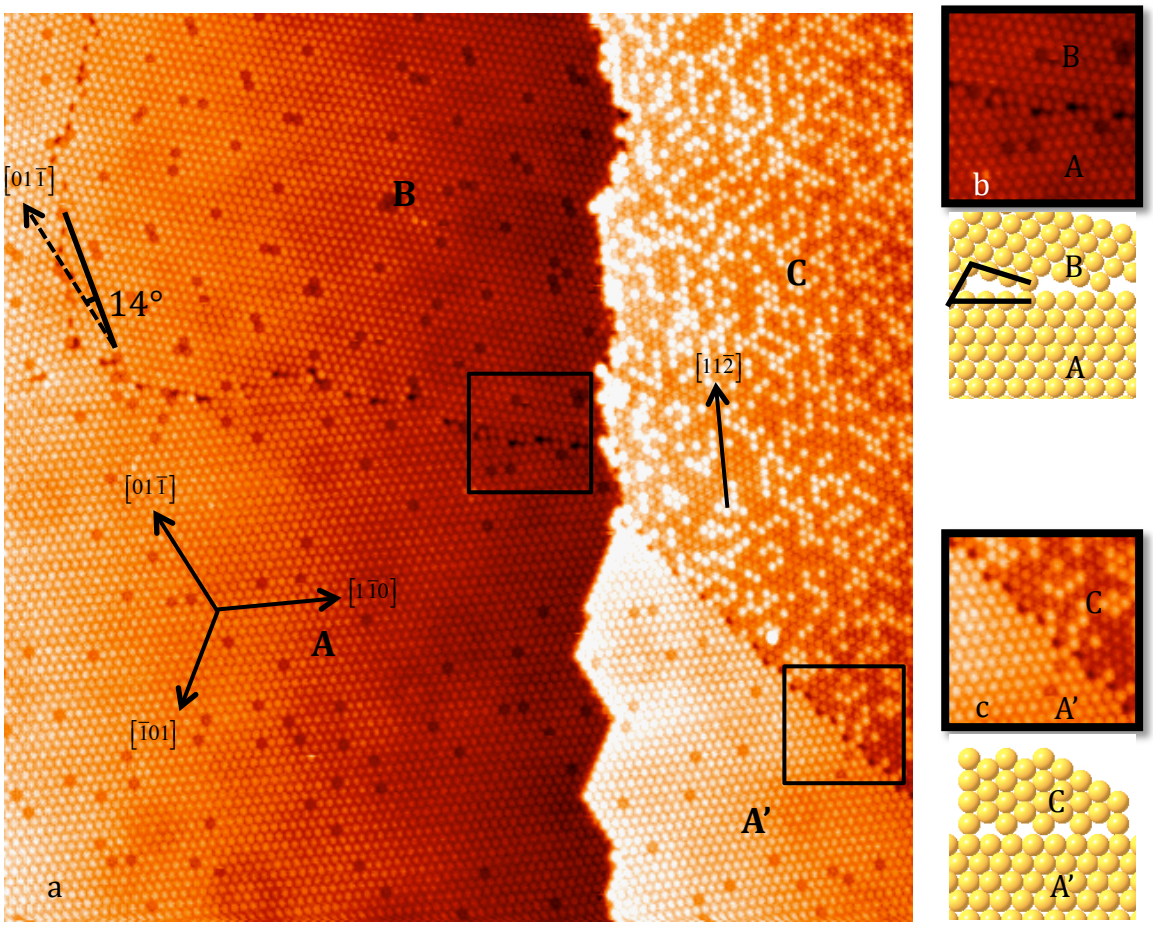

Figure 4.2 STM image of C_{60} monolayer on Au(111) after annealing at 300 °C for 15 minutes. (a) Image shows four domains marked A, A', B and C. The A and A' domains are in the uniform phase, B domain in the periodic phase and C domain in the disordered phase. (b) Zoom-in image of the domain boundary between the unifrom phase and periodic phase. Below the STM image is a schematic diagram with an acute-triangle shape of the void at the boundary. The solid lines mark the molecules

at the periphery of the acute triangle. (c) A zoom-in image of the domain boundary between the disordered and uniform phases. The void at the boundary is about the size of a C_{60} molecule in the centre of a polygon.

The three phases have been assigned to three superstructures introduced in Chapter 2, i.e., 38×38-R0° superstructure for the uniform phase, $2\sqrt{3}\times2\sqrt{3}$-R30° superstructure for the disordered phase and 7×7-R14° for the periodic phase. There is a pattern that a particular rotational domain tends to exist in a preferred phase. For example, the 7×7-R14° domain is always linked to the periodic phase. The residual discommensurate lines (DLs) are good references to measure the rotational angle of each domain in relation to the close packed direction of Au(111). Boundaries between different rotational domains have characteristic structures. Mainly there are two kinds of domain boundaries with different shapes of voids. The void shape at the boundary between the uniform R0° and periodic R14° domains (Figure 4.2b) is an acute triangle. The numbers of C_{60} molecules on the periphery of the acute triangle are roughly three, five and six for each side. The void at the boundary between R0° and R30° domains is about one molecular size and approximate in the centre of a pentagon (Figure 4.2c).

The features of the C_{60} monolayer on Au(111) indicates a complex interface structure. The uniform R0° phase with only a few dim molecules seems a metastable configuration of the C_{60} monolayer on Au(111). The disordered R30° phase is found to be the most stable phase with the highest commensurability and the largest proportion of dim molecules. From STM images, a few periodic phases with different periodicities of the ordered structure formed by dim C_{60} molecules have been observed, as discussed in the next section.

4.1.2 The Periodic Phases

From LT STM experiments [6], dim molecules are observed to be in the configuration of a hexagonal carbon ring in parallel with the Au(111) surface. Different theoretical calculations proposed that the occupation site of the dim C_{60} molecule could be the on-top site [7] or the hollow site [8] on the (111) surface. With the assumption that the dim molecules in the periodic phase take on the same adsorption site, an optimised superstructure can be assigned to each periodic phase observed, considering the physical dimensions of the C_{60} molecule 10.02 Å in diameter and lattice constant of Au(111) 2.88 Å. In comparison with the interactions between the C_{60} monolayer and the (111) surface of metals such as copper, silver and platinum, the interaction with the Au(111) surface is weakest, and large periodic domains with relatively uniform arrangements of dim molecules have been observed on the (111) surface of copper, silver and platinum where C_{60} molecules are strongly attached. The periodic phase of the C_{60} layer on Au(111) has short range order, Figure 4.3a and b. In Figure 4.3a, a blue rhombus marks the smallest unit ($\sqrt{7}\times\sqrt{7}$) (in terms of the lattice constant of C_{60} layer) of the periodic structure regarding the dim C_{60} molecules within the close packed layer. Along the close packing directions (two black lines in Figure 4.3a) the average interval between two dim molecules is seven molecules. If the periodic structure evenly spreads over the layer, the dim molecules are positioned as is shown in the ball model Figure 4.3c where the red balls correspond to the dim molecules. The interval between two neighbouring dim molecules along the close packing directions can be accurately counted to be 7 C_{60} molecules. A second

periodic phase in Figure 4.3b has a unit cell ($\sqrt{13}\times\sqrt{13}$). A C_{60} layer in an ideal periodic phase with an uninterrupted periodic arrangement of dim molecules is drawn in Figure 4.3d with reference to Figure 4.3b. Accordingly, there is one dim C_{60} molecule in every 13 C_{60} molecules along the close packing direction.

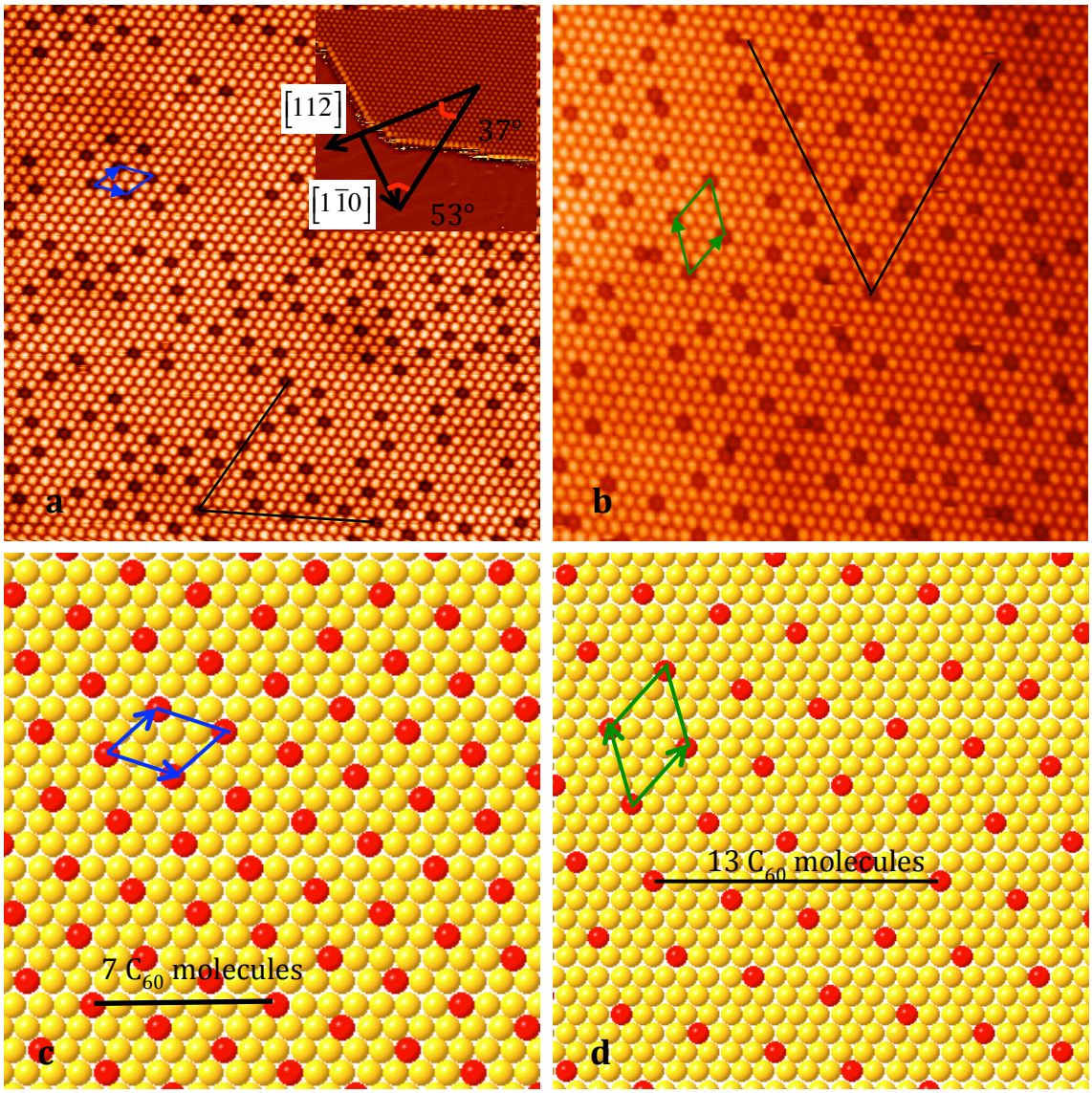

Figure 4.3 STM images of two C_{60} domains in periodic phases. (a) The periodicity is kept in a short range. And the unit cell is ($\sqrt{7}\times\sqrt{7}$). The two black lines are along two equivalent close packing directions, which indicate an average separation of six molecules in between two dim molecules along these two directions. The inset shows

the relatively rotational angle of the close packed direction of the C_{60} layer with respect to that ($[1\bar{1}0]$) of Au(111). (b) A second periodic phase with a unit cell ($\sqrt{13}\times\sqrt{13}$). Along the two close packing directions marked by two black lines, there is one dim C_{60} molecule in every ten ~ thirteen C_{60} molecules. The ball models c and d show the morphologies of the C_{60} layer if dim molecules are evenly distributed in a periodic manner, where the red balls correspond to the dim C_{60} molecules. The unit cells for the two periodic phases are indicated with two rhombuses in blue c and green d respectively. Along the close packing directions the separation between two neighbouring dim molecules is six-molecule for c and twelve-molecule for d.

If the dim molecules occupy the same lattice site, based on the method proposed by Schull and Berndt [2], Figure 4.4 is a map representing the commensurability of a row of close packed C_{60} molecules on the non-reconstructed Au(111) lattice. The unit lattice vectors $\vec{\boldsymbol{\imath}}$ and $\vec{\boldsymbol{\jmath}}$ are as shown in the inset of Figure 4.4. The vector $\vec{\boldsymbol{r}}$ for a superstructure in terms of $\vec{\boldsymbol{\imath}}$ and $\vec{\boldsymbol{\jmath}}$ has the form $\vec{\boldsymbol{r}} = m\vec{\boldsymbol{\imath}} + n\vec{\boldsymbol{\jmath}}$ where m and n are integers. The commensurability C is defined by the quantity $1 - |m\vec{\boldsymbol{\imath}} + n\vec{\boldsymbol{\jmath}}|/(kb)$ where b is the molecular diameter 10.02 Å and k is an integer that minimizes the absolute value of C. The centre-to-centre distance between two adjacent Au atoms in the (111) plane is 2.88 Å, the same as the Au lattice constant in bulk. The closer the C is to zero, the smaller the mismatch. A positive value of C means that the normal C_{60} layer needs to expand to revise the commensurability C to be zero, while a negative value of C indicates the necessity of compression of the C_{60} layer to make C zero. In Figure 4.4 the colour blocks from dark red to dark blue represent the commensurability C from 0.5 to about -0.5, and the light green squares are the most commensurable superstructures of C_{60} layer on Au(111). On

the map the (20,7) point marks the superstructure with the denotation ($\sqrt{589}\times\sqrt{589}$)-R14.5° with a periodicity of 7 C_{60} molecules and a mismatch of 0.35% [2].

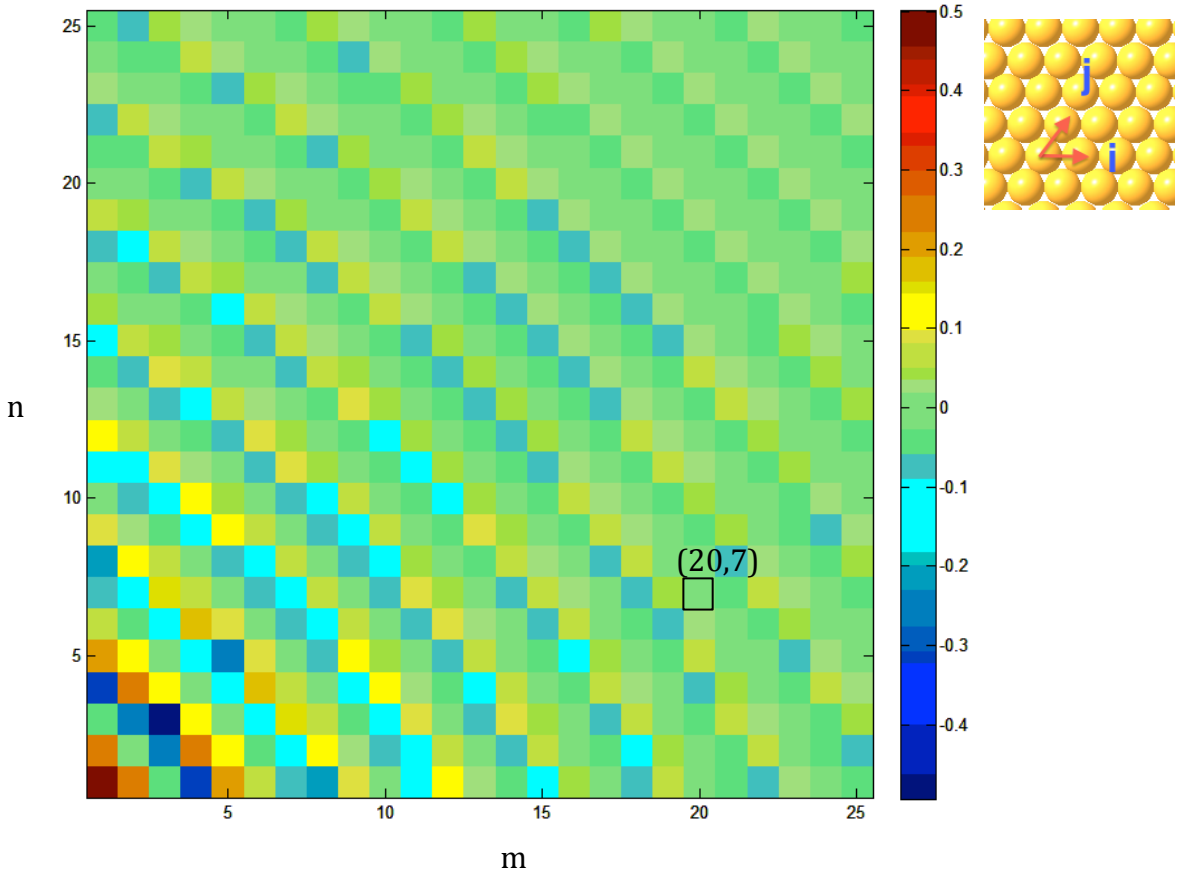

Figure 4.4 Commensurability map of C_{60} overlayer on Au(111). Color blocks on the graph correspond to the degree of commensurability $C = 1 - |m\vec{i} + n\vec{j}|/kb$ where b is the C_{60} intermolecular distance 10.02Å in bulk, and k is the integer that results in the smallest absolute value of C. The color to red is positive and the color to blue is negative. The smaller the absolute value of C, the more commensurate the superstructure. Assuming that the Au(111) surface is rigid, a positive value of C means that in order to become a commensurate layer, the intermolecular distance in the superstructure needs to be larger than the bulk value of intermolecular distance 10.02 Å, while negative value means that the intermolecular distance in the

superstructure needs to be smaller than that in the bulk. The inset shows the lattice vectors on the Au(111) surface. The color block (20;7) corresponds to the ($\sqrt{589}\times\sqrt{589}$)-R14.5° superstructure proposed by Schull and Berndt. [2]

Based on the experimental observation and the commensurability map of C_{60} overlayer on Au(111), we can generally assign a superstructure to each of the two periodic phases in Figure 4.3. There are a few possible structures on the map in Figure 4.4 for a C_{60} layer with the same periodicity regarding the occupation sites of C_{60} molecules on Au(111). Obviously the smaller the unit cell is for the superstructure, the more likely it is to be observed.

In the commensurability map (Figure 4.4), within the range of $0\leq m\leq 25$ and $0\leq n\leq 25$, the smallest mismatch for the periodic phase in which every 7 C_{60} molecule occupies the same lattice site is 0.09%, in which case (m,n) equals (12,16) and the rotational angle is 37.8° anti-clockwise from the vector $\vec{\imath}$. Therefore, the superstructure can be denoted as $16\sqrt{2}\times16\sqrt{2}$-R37.8° in terms of the 2D lattice of Au(111). Figure 4.5 is a colour graph for the periodic phase where the average separation between the C_{60} molecules on the same lattice site is the distance of six C_{60} molecules. In Figure 4.5 the values of m and n are confined within 26 as superstructures. The background colour in light green represents other periodic phases of different commensurability where the separation between dim molecules is either larger or smaller than six molecules in the close packing direction. The colour scale bar on the right of Figure 4.5 shows that the degree of mismatch is in the range of ±7%. The two data points (12,16) and (16,12) highlighted by two black squares are the most commensurable structure for the 7-molecule periodic phase. The periodic phase in Figure 4.3a exhibits a periodicity of

7 molecules in the superstructure formed by dim molecules. The inset there indicates that the close packed direction of the C_{60} layer in the periodic phase is shifted by about 53° or 7°. From the commensurability map the point (m,n)=(4,22) is the most commensurable structure with a rotational angle 8.2° and a mismatch value 0.43%.

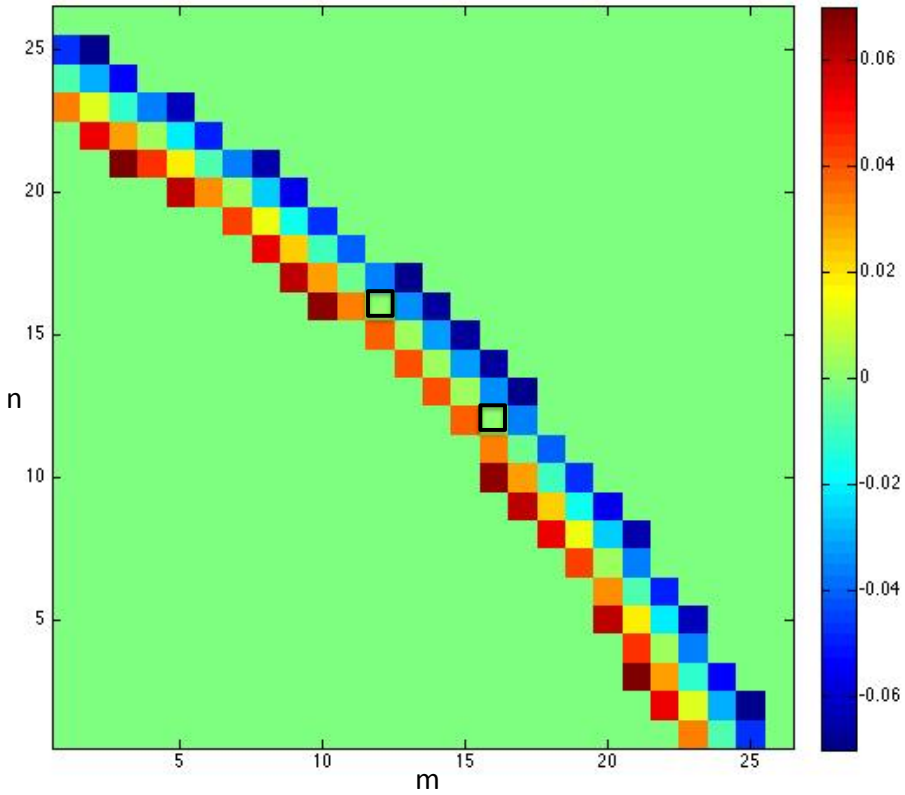

Figure 4.5 Map for the periodic phase where every 7 C_{60} molecules occupy the same lattice site on Au(111) along the close packed direction of C_{60} layer. The two black square on the map mark the most commensurable structure of the 7-molecule periodic phase. Each colour block represents one superstructure for the 7 molecule periodic phase. The rest area in green represents other periodic phases of different commensurability where the separation between dim molecules is either larger or smaller than six molecules in the close packing direction.

Another periodic phase in Figure 4.3b shows a short-range periodicity of the dim C_{60} molecules in the overlayer. The STM image (Figure 4.3b) indicates a distance of about 10 C_{60} molecules between two adjacent dim molecules in the close packing direction. The superstructures for the periodic phase in Figure 4.3b with the least mismatch between the C_{60} layer and Au(111) are when (m,n) equals (5,32) or (17,23), with a mismatch of 0.06%. The corresponding rotational angles for the two superstructures (5,32) and (17,23) are 52.8° and 35.0° respectively. If the dim molecules are arranged like the pattern and shape of the unit cell highlighted by a rhombus in green in Figure 4.3b, the corresponding ball model (Figure 4.3d) reveals that the separation between two neighbouring dim molecules is 13 molecules. This periodic phase is associated with a large unit cell on Au(111) which is (12,38) or (22,30). The rotational angles for the superstructure (12,38) and (22,30) are 46.7° and 35.1° respectively. Numerical data for the commensurability of C_{60} layer on Au(111) are listed in the Appendix.

The commensurability maps about the periodic phase assume an ideal Au(111) surface without reconstruction, no changes of the lattice constants of both the close-packing Au and C_{60} layer, and do not take into account the energy cost for different occupations of C_{60} molecules on the (111) surface. In reality, with stress from the adsorption of C_{60} layer the arrangement of Au atoms of the (111) surface may have small fluctuations in both vertical and lateral positions. However, the commensurability map gives a general guidance when considering the superstructures for different phases of C_{60} domains. This simple geometric model can provide a qualitative understanding of complex overstructures. In empirical researches, from both geometric and energetic considerations, the most stable phase for C_{60} single layer on Au(111) is the disordered R30° phase.

4.1.3 Au Atom Diffusion on C_{60}/Au(111) Substrate at Room Temperature

In order to probe the properties of the interface between the C_{60} layer and Au(111), another experiment in which Au atoms were deposited on the post-annealed C_{60} monolayer covered Au(111) substrate was carried out. At room temperature, after the deposition of Au atoms at a rate of 0.012 ML per minute, few Au atoms are observed on top of the C_{60} layer, which means that Au atoms penetrate the C_{60} layer and reach the C_{60}/Au interface, where they diffuse laterally to merge with the step edge or get trapped by surface defects. The interstitial site formed by three molecules in the close packed C_{60} layer is a little smaller than the metallic radius of gold atom (1.44 Å). At room temperature, C_{60} molecules move constantly around equilibrium positions within the layer, and the deposited Au atoms have the chance to reach the C_{60}/Au interface through the interstitial sites. On large terraces, Au islands that grow out from surface defects can be observed, two examples as shown by Figure 4.6. The surface dislocations are the nucleation sites where Au islands form.

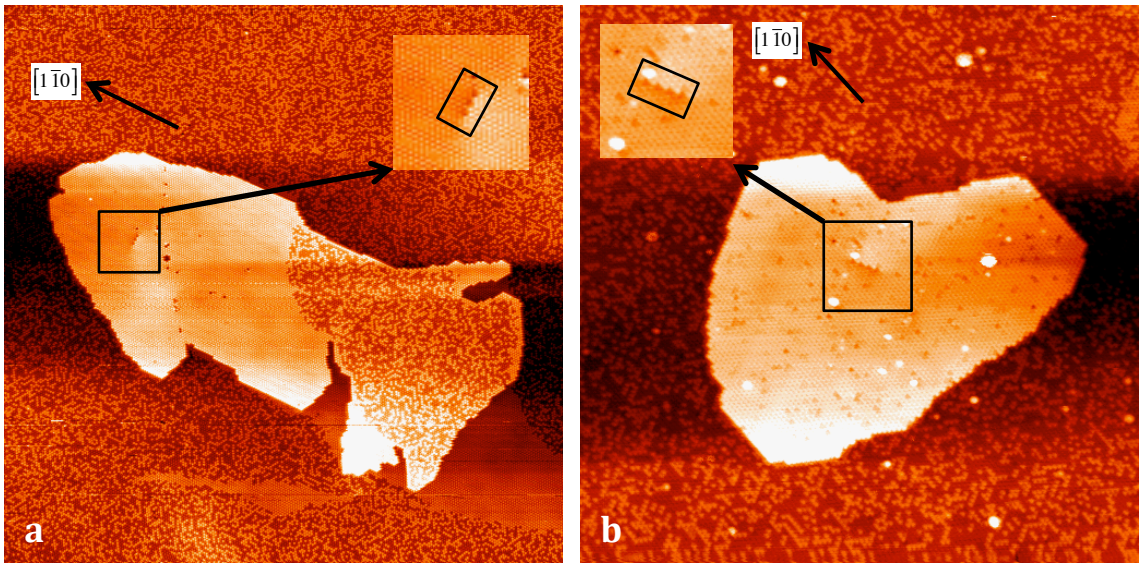

Figure 4.6 Au islands formed on large terraces after Au atom deposition at room temperature. The black shadows are due to background subtraction. On both Au islands, surface dislocations can be observed as shown on the two insets on each image and the defects are highlighted by rectangles. The close-packing direction $[1\bar{1}0]$ *of the Au(111) substrate is shown on each image. (a) The C_{60} overlayer on top of the gold island is partially in disordered phase. (b) The C_{60} overlayer on top of the gold island takes on the uniform phase in contrast to the C_{60} layer around the Au island, which is in disordered phase.*

The two insets in Figure 4.6 show the surface dislocations on the Au(111) surface and the C_{60} molecules on top of the surface dislocations look like in depression. Although these two Au islands formed within the C_{60} domains of disordered phase, C_{60} molecules that cover the Au islands are in the uniform phase before the transition from the uniform phase to the disordered phase happens. The insertion of Au atoms beneath the close packed C_{60} layer leads to the phase change of the molecular layer from disordered phase to uniform phase. However, the disordered phase is more energetically favored. The C_{60} domain in the uniform phase was observed to turn into the disordered phase at elevated substrate temperatures. In Figure 4.6, due to the difference between the close packing direction of Au(111) and that of the C_{60} layer, the contour of the step of the Au islands are not always straight but faceted. There are segments of straight steps which run along the close packing direction $[1\bar{1}0]$ of the Au(111) substrate. This type of Au step is energetically favoured.

Figure 4.7 shows a series of STM images acquired at various sample temperatures. The substrate temperature was further increased gradually from room

temperature to about 390 K, during which both the phase of the C_{60} domain on the Au island and the shape of the Au island changed gradually (Figure 4.7 below). This phase transition is thermally activated. The relaxation of the Au islands is constrained by the C_{60} overlayer.

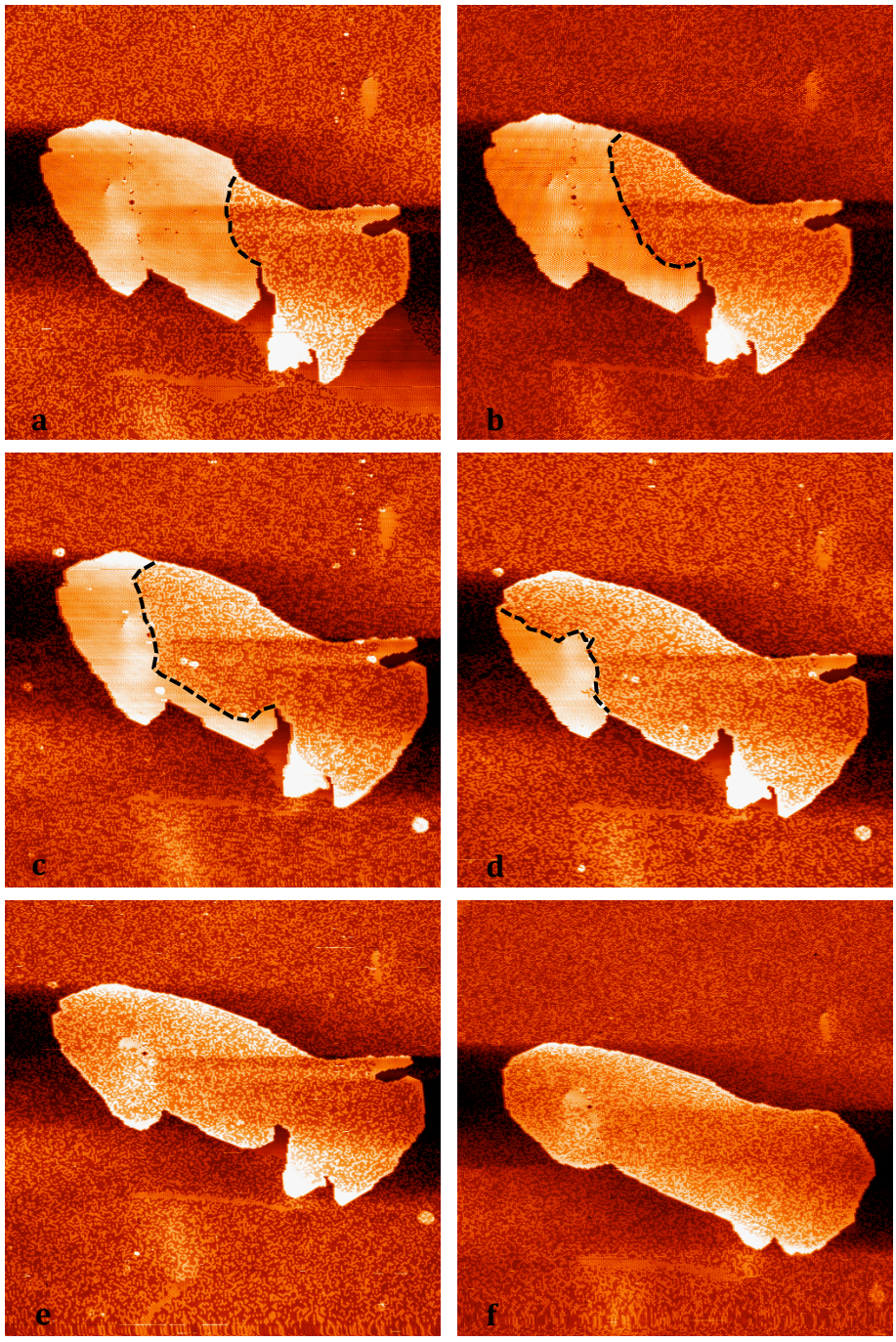

Figure 4.7 STM images obtained at increasing substrate temperatures. Both image a and image b are obtained at room temperature. A dashed line highlights the boundary between the uniform phase and disordered phase. By comparing image a and b, a clear phase transition happens from right-hand side with the shift of the phase boundary. Image c and d are obtained separately at temperature of 297 K and 302 K. During the annealing process, the phase transition continues but is hindered by an irregular domain boundary at the lower part of the island. After the phase transition is complete, image e and f show a ripening process during which the shape of the gold island became more compact.

First of all, a gradual phase transition occurs for the C_{60} overlayer in the uniform phase, with few dim molecules at room temperature, as indicated in Figure 4.7a-d on which a dashed line highlights the phase boundary. The phase transition proceeds from right to left which can happen at room temperature (Figure 4.7a and b). The directional transition implies a correlation within adjacent C_{60} molecules in the close packed layer, as the phase transition doesn't happen randomly in the C_{60} layer of the uniform phase but from one side. The domain boundary can hinder the phase transition, as indicated in Figure 4.7c and d. On the lower part of the phase boundary on Figure 4.7d is a domain boundary with small gaps of the size of a C_{60} molecule between adjacent domains. Then at elevated substrate temperatures and after an extended period of time, the phase transition is complete, with the C_{60} overlayer on top of the Au island entirely in the disordered phase. And finally, the Au island itself changes to a more compact structure, Figure 4.7f. Due to the constraint of the C_{60} overlayer, and therefore limited Au atom diffusion, the ripening process of the Au island seems slow.

As demonstrated above, deposition of Au onto C_{60}/Au(111) can form single layer Au islands on the flat terraces. Many Au atoms are found to have diffused to existing surface steps, and a step flow type of growth takes place, Figure 4.8. The nucleation of Au atoms on the lower terrace leads to the lifting of C_{60} molecules on the lower terrace. The lifted C_{60} layer conserves its original phase. If the C_{60} domains on the upper and lower Au terraces are in different phases, a clear domain as well as a phase boundary forms at the initial step, as is highlighted in Figure 4.8 by dashed lines. The C_{60} molecules beside the Au step edge have a stronger interaction with the adjacent molecules on the lower terrace than with the adjacent molecules on the upper terrace, which is the reason why they can remain in their original phase. If the C_{60} domains on the lower and the upper terraces are in the same phase, there is no boundary, but an extended Au terrace (Figure 4.8c). The domain boundary in Figure 4.8a is obvious and like the boundary between a R0° phase (denoted by α) and a R14° phase (denoted by β) as has been pointed out in connection with Figure 4.2, while the domain boundary in Figure 4.8b is very vague as the relative rotational angle between the close-packing directions of the two phases (β and γ) is small, and only a few gaps exist at the boundary as shown in the inset of Figure 4.8b. There it seems that the dim molecules on the extended terrace are arranged in what approaches an ordered manner. The interaction between the C_{60} overlayer and the Au(111) surface is not strong enough to form a well ordered phase, as compared to the cases of C_{60} monolayer on either Pt(111) [9, 10] or Cu(111) [11]. Another phase boundary of the C_{60} layer between C_{60} domains in the periodic phase δ and in the uniform phase is shown in Figure 4.8c, where a step flow growth of an Au terrace covered by the C_{60} layer in the uniform phase does not show a boundary between the original C_{60}

domain on the upper terrace and the lifted C_{60} domain on the lower terrace (the top inset of Figure 4.8c).

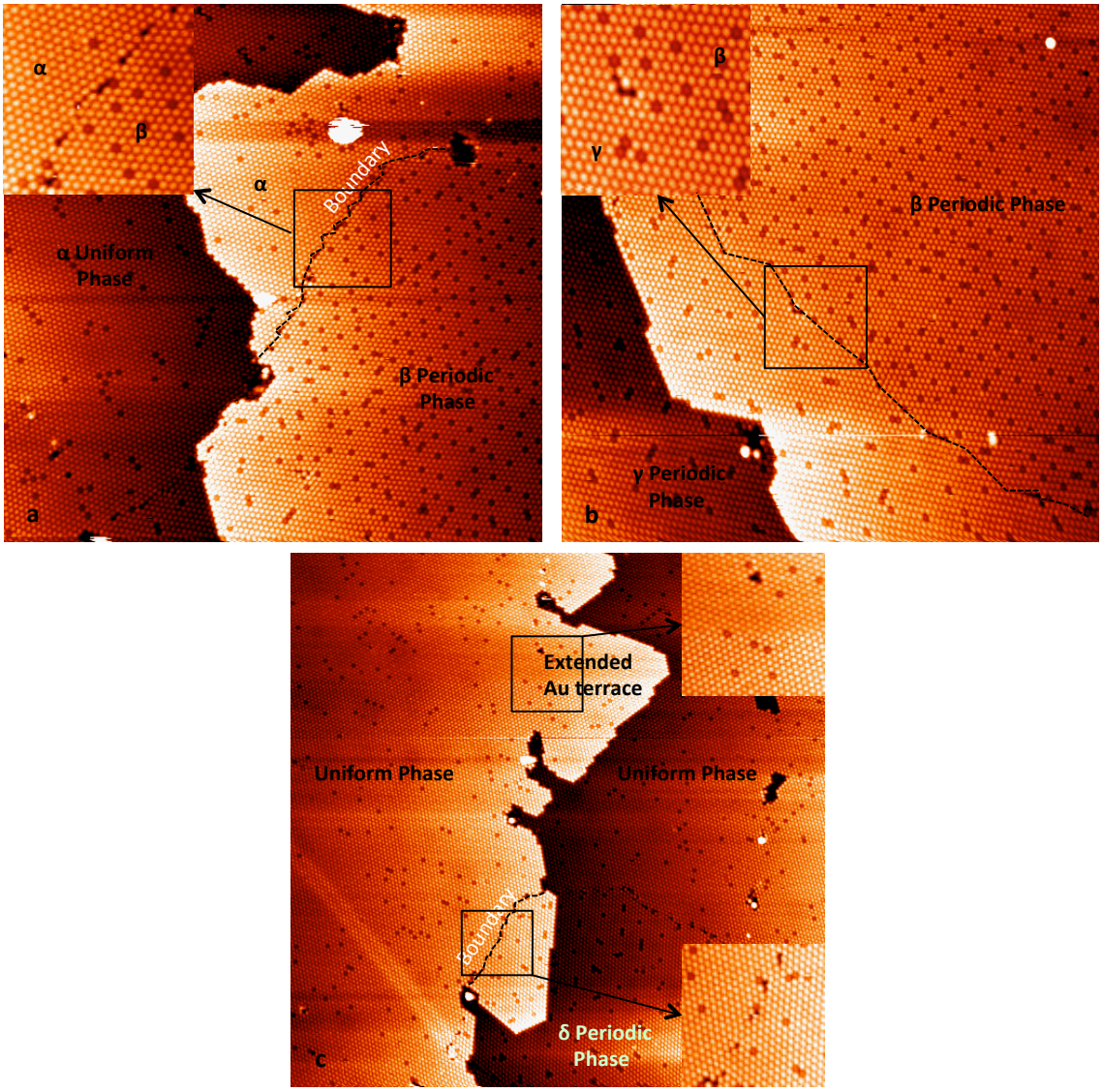

Figure 4.8 Nucleation of deposited Au atoms at the step edges. Images a and b show two areas near together as the periodic phase β is from the same domain. When Au atoms diffuse to the step edge, Au step edges extend on the lower terrace and the extended Au terraces lift C_{60} molecules originally on the lower terrace. The lifted C_{60} layer conserves its original phase. All the boundaries are marked by dashed lines. (a) A domain and phase boundary is highlighted with a rectangle, which separates a

uniform phase α with random distribution of dim molecules and a periodic phase β with superstructure of dim molecules in long-range order. (b) A domain and phase boundary separates two periodic phases β and γ of different periodicities. (c) Step flow growth of the Au terrace covered by C_{60} layer in different phases. The C_{60} domains on the upper and lower Au terraces share the same phase – the uniform phase; there is an extended Au step with no boundary (the upper inset). A clear boundary (zoom-in image shown in the lower inset) between the C_{60} domains in the uniform phase (upper terrace) and the periodic phase δ (lower terrace) forms after the C_{60} molecules on the lower terrace are lifted by the extended Au terrace.

At room temperature Au atoms cannot be confined at the C_{60}/Au(111) interface unless they are trapped by surface defects on the Au(111) substrate. The diffusion barriers at the C_{60}/Au(111) interface with the C_{60} layer in different phases are lower than the kinetic energy of Au atoms at room temperature, and therefore there is no difference in the nucleation of the deposited Au atoms at the C_{60}/Au(111) interface. The kinetic energy of the deposited Au atoms is reduced after they land on the cold C_{60}/Au(111) substrate, and a divergence of the morphology of Au islands formed by the deposited Au atoms under the C_{60} layer in different phases indicates a different bonding configuration of the C_{60} layer with the Au(111) substrate.

4.2 Au Island Sandwiched at the Interface of C_{60}/Au(111) at Low Temperature

Substrate temperature plays a vital role in the diffusion of Au atoms and affects the final structure of the Au island at the interface. At room temperature, a large fraction of the Au atoms deposited on the C_{60}/Au(111) substrate diffuse to the step

edges, and only a small portion form Au islands on the terrace, anchored by surface dislocations. In the following, I will present results from another experiment where Au are deposited on the substrate at low temperatures.

4.2.1 The Au Islands beneath the C_{60} Overlayer in the R30° Disordered Phase

I first introduce findings on the disordered R30° phase. Au atom deposition on the post-annealed C_{60}/Au(111) sample was carried out at substrate temperature 122 K. The coverage of Au atoms deposited is about 0.11 ML. In the disordered phase, besides the brightness contrast among the C_{60} molecules within the layer, extra bright features are observed after Au atom deposition (Figure 4.9a-e). These are attributed to C_{60} molecules sitting on top of small Au islands, because the height of the extra bright features has been measured to be the same as that of single-layer Au. Based on the physical dimensions of the molecule and the atom, the average size of a compact Au island beneath one C_{60} molecule should be around 12 atoms. The substrate temperature was gradually increased to study Au atoms diffusion in the disordered phase. At 122 K, only about 13 % of the deposited Au atoms (0.11 ML) are found staying at the C_{60}/Au(111) interface based on the number of the extra bright C_{60} molecules in disordered domains (Figure 4.9a). When the substrate temperature reaches 188 K, there are more C_{60} molecules raised by Au atoms (Figure 4.9b). These emerging Au atoms could possibly be trapped at the interstitial sites and they penetrate the C_{60} layer during the process of temperature rising from 122 K to 188 K forming Au islands at the C_{60}/Au(111) interface. At 228 K (Figure 4.9c) and room temperature (295 K, Figure 4.9d), more small Au islands form at the C_{60}/Au(111) interface and the Au steps become less smooth compared with the Au steps at lower temperatures (Figure 4.9a and b) due to the

incorporation of the deposited Au atoms. Extra bright C_{60} molecules have disappeared in the disordered phase when the temperature reached 388 K and, at the same time, Au terraces grow outwards. We find that the number of the extra bright C_{60} molecules increases with the rise in sample temperature from 122 K to 295 K, and so it is with the population of bright C_{60} molecules within the C_{60} layer in disordered phase, which results from the conversion of dim C_{60} molecules to bright C_{60} molecules. This finding can be explained as follows. After Au deposition at 122 K, a majority of the deposited Au atoms are trapped at interstitial sites formed by groups of three C_{60} molecules in contact. As the sample temperature increases, these trapped Au atoms are gradually released to the C_{60}/Au(111) interface. The conversion of dim molecules to bright molecules is accomplished by filling the Au vacancies underneath the dim C_{60} molecules with the Au atoms at the C_{60}/Au(111) interface. The change of the ratio of the extra bright C_{60} molecules over the total area and that of the bright C_{60} molecule according to sample temperature is plotted in Figure 4.9f. Above room temperature, clusters of Au atoms that support the extra bright C_{60} molecules gradually disintegrate and integrate with step edges. Therefore, we see the reduction of the number of the extra bright C_{60} molecules seen in Figure 4.9f.

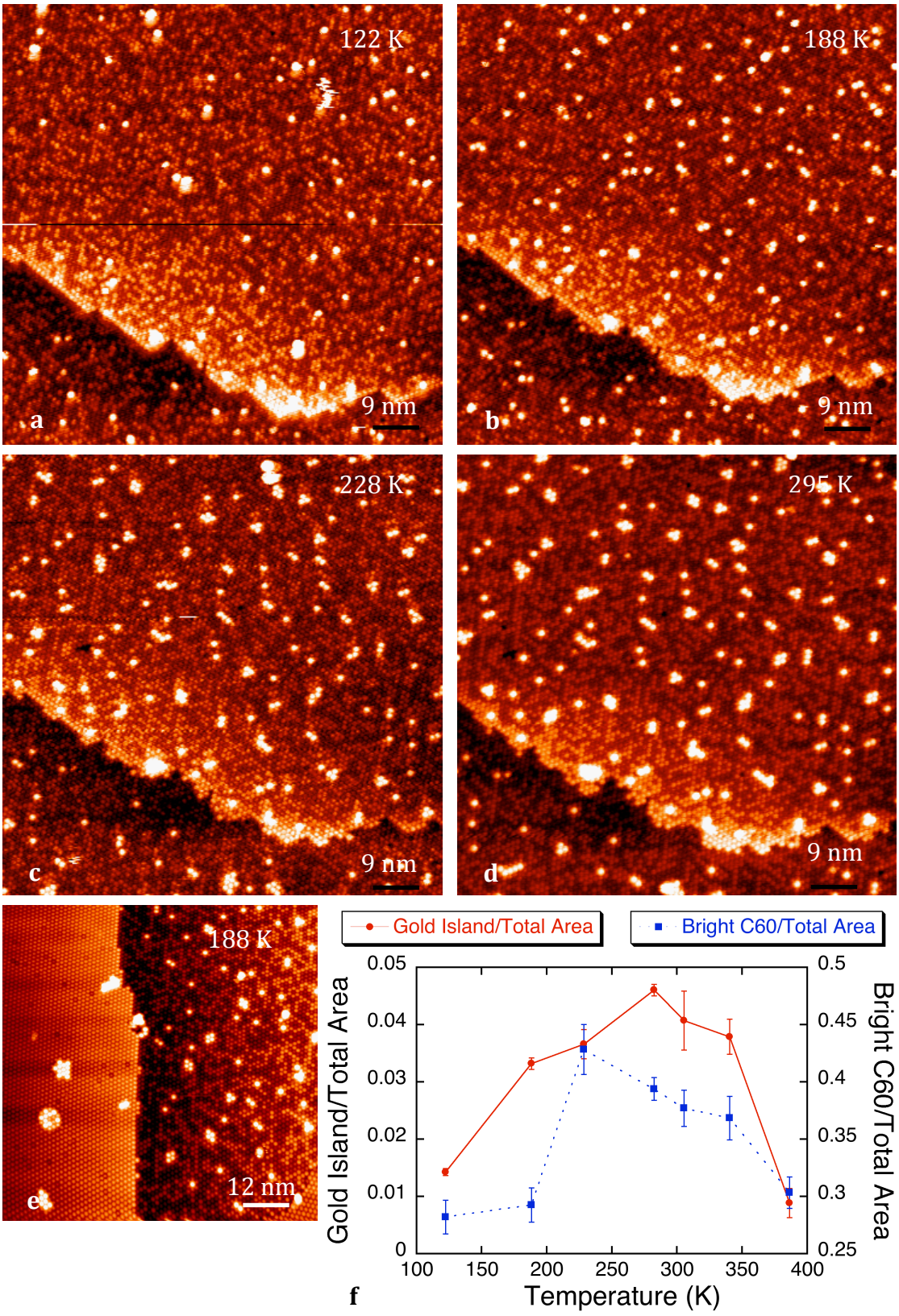

Figure 4.9 STM images showing the morphologies of sample surface at different substrate temperatures (from 122 K to 295 K) after Au atom deposition. All images show extra bright C_{60} molecules that sit above small Au islands of single-layer height.

These extra bright C_{60} molecules are about 0.24 nm higher than the background C_{60} layer where molecules are imaged dim or bright. The larger size of the Au islands in the uniform phase (left part of e) compared with that in the disordered phase (right part of e) indicates a lower degree of diffusion confinement for Au atoms at the C_{60}/Au(111) interface there. Small Au islands can stay in the disordered phase at room temperature d until the substrate temperature reaches 388 K, accompanying the Au terrace outgrowth.

In contrast to the formation of small Au islands beneath C_{60} molecules in disordered phase, the Au islands in the uniform phase (Figure 4.9e) are relatively large. The interfacial diffusion length of Au atoms in the uniform phase is larger than that in the disordered phase due to the lower content of dim molecules there. The dim molecules in the disordered phase play an important role in the formation of isolated small Au islands at the interface, which further validates the assumption that the dim molecule has stronger bonding with the substrate. There is thus a higher barrier against Au atom insertion beneath the dim molecule and, in the end, a shorter diffusion length of Au atoms at the interface.

The diffusion and nucleation of the deposited Au atoms reveal the buried different interfacial structures of the rotational C_{60} domains in the disordered and in the uniform phase. When we vary the substrate temperature during Au atom deposition and the quantity of deposited Au atoms, additional interesting features appear on the C_{60}/Au(111) substrate presented in the following section.

4.2.2 The Au Islands beneath the C_{60} Overlayer in the R0° Uniform Phase

In this section, I will examine the morphology of Au islands formed underneath the 38×38-R0° uniform phase of C_{60} monolayer. Less than a complete layer of C_{60} was prepared by deposition of molecules onto Au(111) at room temperature. No post-annealing was performed. Because the coverage is less than one layer, there are residual bare Au(111) surface areas left. Therefore, we can use the herringbone structure to tell the relative orientation of a C_{60} domain with respect to the Au(111) substrate.

In Figure 4.10a, the STM image shows the morphology of the substrate after the sublimation of about 0.24 ML of Au atoms. During the Au atom deposition, the substrate was kept at 136 K. Due to the submonolayer coverage of C_{60} molecules, some bare Au(111) surface still existed. Au atoms landed on the bare Au(111) surface could diffuse across the Au surface and nucleate at the step edges of C_{60} layer as pointed by the black arrows in Figure 4.10a. The substrate temperature, 136 K was not low enough to inhibit Au-atom diffusion on the Au(111) surface. Au atoms that landed on the C_{60} monolayer, diffused through the layer and eventually settled on the Au(111) surface, where they nucleated into Au islands. The C_{60} molecules in the close packed layer were lifted up by the newly formed Au islands.

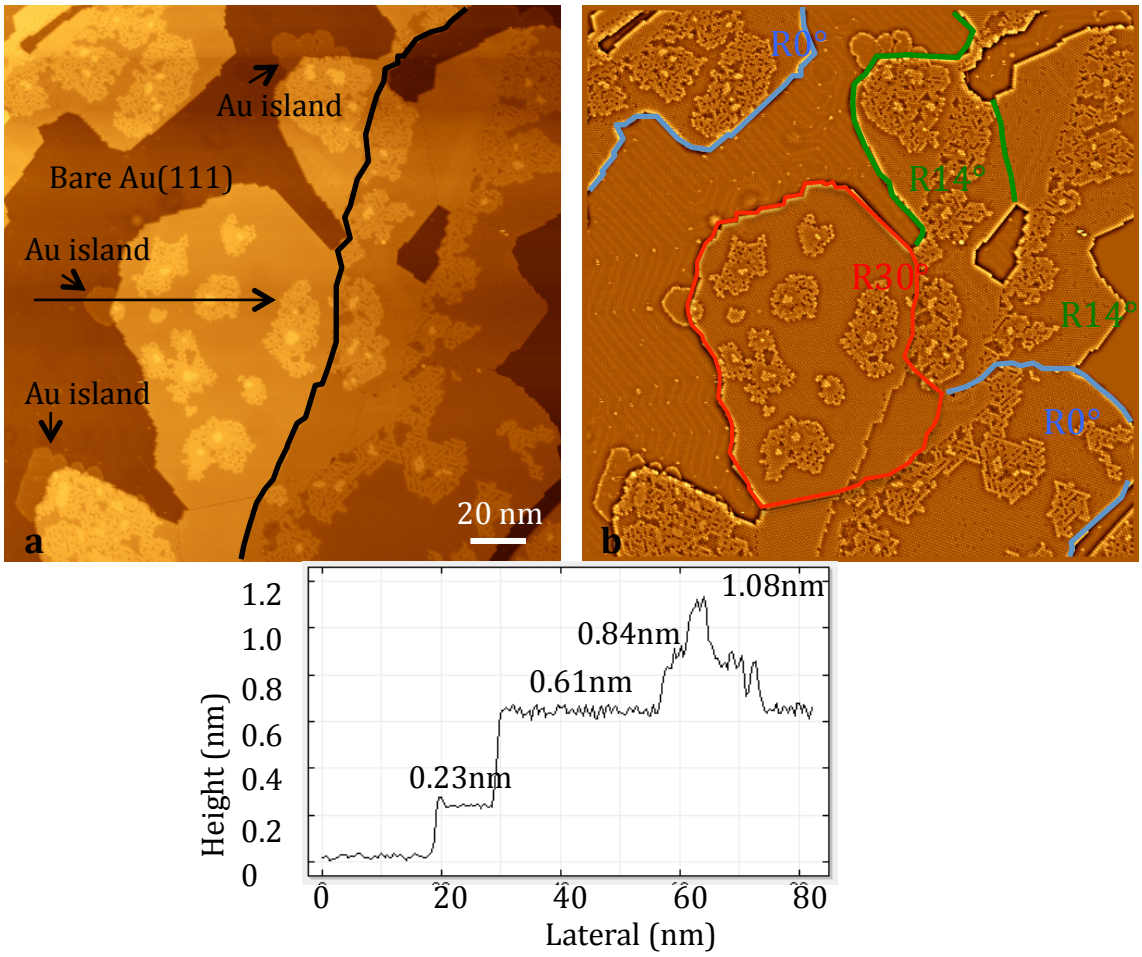

Figure 4.10 Surface morphology of the C_{60}/Au(111) sample after Au atom deposition at a substrate temperature of 136 K. (a) On the STM image, the black line separates the upper and lower terraces. The C_{60} layer does not completely cover the Au(111) Surface. Small Au islands are attached to the step edges of the C_{60} layer. These Au islands are formed by the deposited Au atoms. (b) The STM image is processed by the function of unsharp mask to set all the terraces on the same level. Solid lines of different colours are used to outline C_{60} domains in the R0° (red line), R14° (green line) and R30° (red line) phases. (c) A height profile along the yellow line on a. The height of the bare Au(111) surface is set to be zero. The height of the Au island is about 0.23 nm. The C_{60} layer is measured to be about 0.63 nm. And there are C_{60} islands that are 0.21 nm and 0.45 nm higher than that of C_{60} layer on Au(111), which correspond to C_{60} molecules raised up by single, and double Au layers respectively.

The small second Au layer is grown on top of the first Au layer on the Au(111) substrate. (I_t: 0.03nA, V_{sample}: -2.0V)

The line profile in Figure 4.10c is plotted along the yellow line in Figure 4.10a from left to right. The heights of various features on the sample surface indicate that C_{60} molecules sit on three levels of Au terraces or Au islands. Along the yellow line from left to right, the height profile firstly shows the height of the bare Au(111) surface which is set to zero. The next rise in height corresponds to the Au island 0.23 nm attached to the C_{60} layer. The height of the C_{60} layer is measured to be 0.64 nm. Above the initial C_{60} layer, there are two kinds of C_{60} molecules of different height 0.21 nm and 0.405 nm which are close to the height of single and double Au(111) step(s). The large C_{60} islands with porous structures are lifted by one Au layer and a few C_{60} molecules sit on top of double Au layers, a result of long-time Au deposition (20 minutes) such that incoming Au atoms nucleate on top of the freshly formed Au islands at the interface of the C_{60} layer and the Au(111) surface. On the right of the black solid line in Figure 4.10a are lower Au terraces where similar features also exist.

Figure 4.10b has been processed with the function of unsharp mask, to enhance the contrast of surface features by offsetting all terraces to the same level. Three phases of C_{60} layers are observed as highlighted on the image. The blue lines outline the regions of C_{60} layer in the uniform R0° phase, the red lines a region of C_{60} layer in the disordered R30° phase and there are C_{60} domains in the periodic R14° phase on the upper right of Figure 4.10b. Close examination reveals that the porous structure in each of the three phases differs. In the uniform R0° phase, two types of porous structures have been observed. The “pores” in the porous

structures refer to C_{60} molecules that are not lifted by Au islands at the interface while the C_{60} molecules that surround the pores are lifted. The height difference is reflected as brightness contrast in the STM images. One type of the porous structures is shown in Figure 4.11, which is populated with bright C_{60} rows i.e. with linear Au islands underneath. The Au islands are one atomic layer high. Such linear Au islands seldom exist in the other two phases. In the R0° phase, due to the coincidence between the close packed directions of the Au(111) substrate and that of the C_{60} overlayer, the growth of the Au islands at the interface are partially guided by the close packed C_{60} rows. Therefore, the long edges of the narrow Au islands extend along the close-packing direction of the Au(111) substrate. However, the length of the linear Au islands is limited due to the intersection with other islands because Au islands can grow in three equivalent close packing directions at the interface. This configuration of the linear Au islands resembles that of the narrow gold fingers [12]. The gold fingers a single Au layer high are apt to grow along the close-packing directions of Au(111), driven by the force exerted by the scanning STM tip. The difference between these two linear structures lies in the growth mode. Here, the C_{60} layer encloses the Au islands and thus subsequent Au atoms added to the Au island during the process of expanding need to overcome the barrier to lift up the C_{60} molecules beside the steps of the Au island. The bonding of the C_{60} molecules with the Au atomic steps is another major factor for the growth of Au islands. For this reason, underlayer growth of Au structures at low temperature (110 K to 150 K) does not lead to the formation of large compact islands.

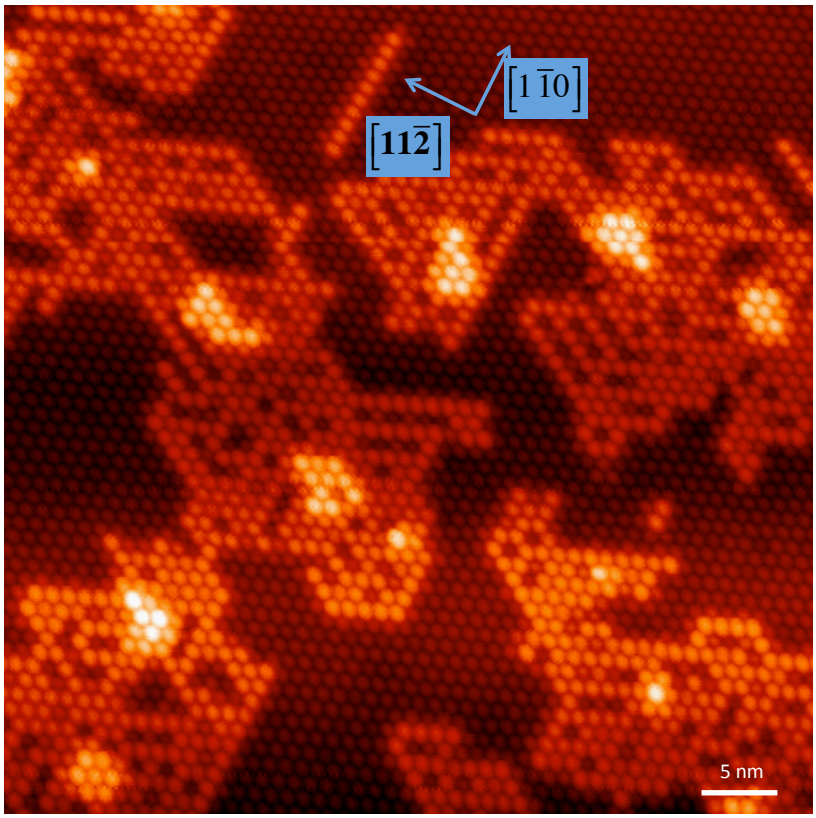

Figure 4.11 The porous structure of Au islands at the interface. The formation of this structure is through the intersection of one-dimensional Au islands.

The ball model with straight Au islands and raised C_{60} rows in Figure 4.12 explains the formation of the porous structure in Figure 4.11. In the model, Au atoms are multicoloured, denoting to two types of atoms. Au atoms in tangerine are close packed to represent the Au(111) substrate, while others in light tangerine are the Au atoms inserted below the C_{60} molecules. C_{60} molecules in two vertical levels are distinguished by their colours, those in light grey sitting on top of the Au islands, and those in dark grey sitting directly on the Au(111) substrate. Others that cover the Au(111) substrate are not shown.

After a row of C_{60} molecules is lifted by a narrow Au island (Figure 4.12a), the two rows of C_{60} molecules beside the narrow Au island are now further anchored by the steps of the island, the contribution from the C_{60}-step interaction increasing

the stability of these molecules. Therefore, the barrier for incoming Au atoms to lift these molecules is higher than for other C_{60} molecules that only contact with the Au(111) substrate. The thermodynamic energy of course influences the barrier for the insertion of Au atoms. At room temperature, Au atoms can freely lift C_{60} molecules and compact Au islands instead of porous islands form at the interface.

After a second row of C_{60} molecules is lifted (Figure 4.12b), the C_{60} molecules sandwiched between the Au islands are further stabilized by the interaction with the two Au steps on the two sides of the C_{60} row. The continuation of this process creates the 2D porous network observed (Figure 4.12c). Due to the three fold symmetry of the (111) surface, the narrow Au island can extend along its length, or switch its growth direction by 120°. The large network has a complex long-range structure but the linear feature is retained at the local scale.

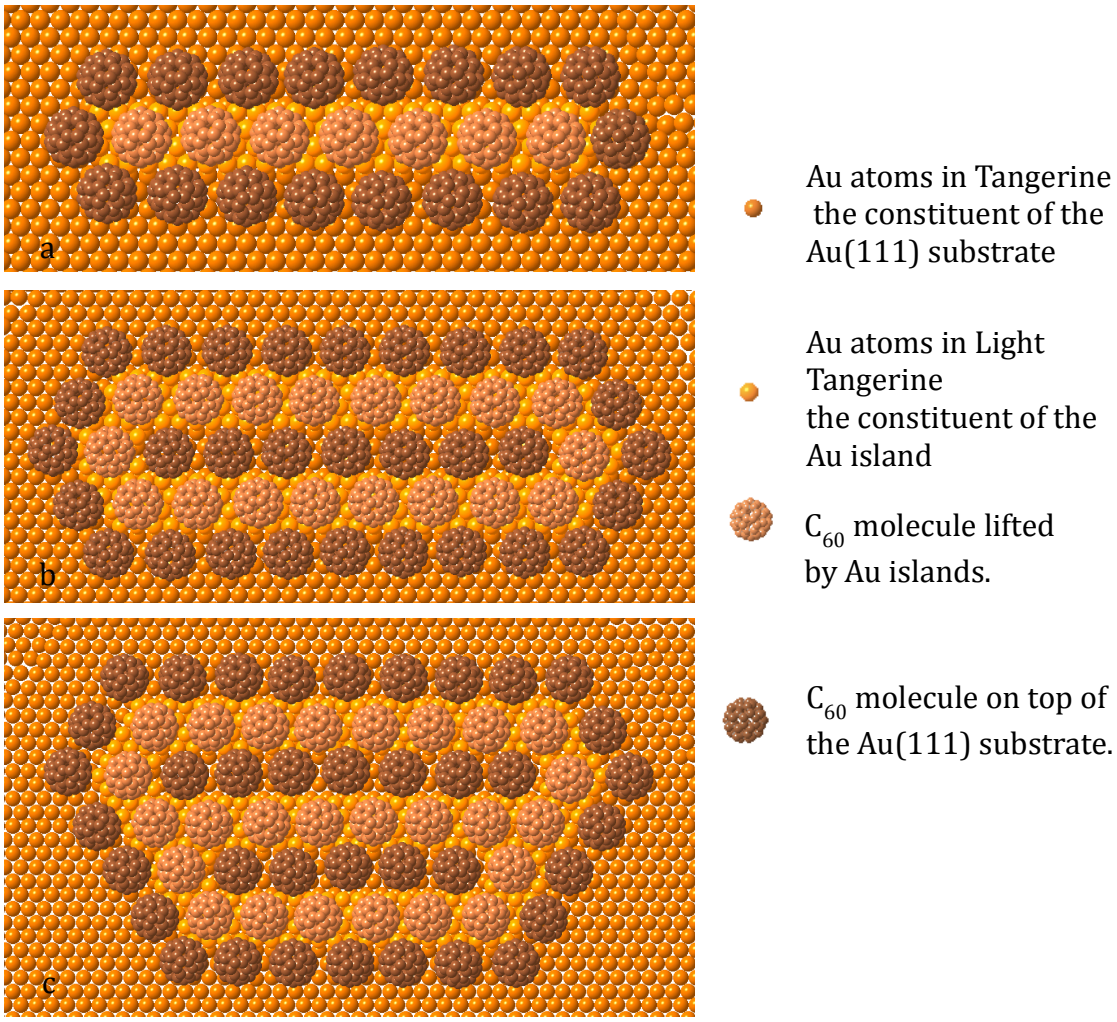

Figure 4.12 The ball models for the linear structures.

Another porous structure is the honeycomb structure, as shown in Figure 4.13a and b below. In the honeycomb structure, C_{60} molecules are lifted according to another pattern. In Figure 4.13a, C_{60} molecules are in three levels of increasing brightness: the background C_{60} layer, C_{60} molecules lifted up by one layer of Au islands at the interface of the C_{60} layer and the Au(111) substrate, and a few C_{60} molecules sitting on top of double Au layers. The zoom-in image in Figure 4.13b from the area in Figure 4.13a enclosed by a black rectangle shows more clearly the honeycomb structure, where the bright protrusions are the C_{60} molecules lifted by a single-layer Au island and the black holes are where the C_{60} molecules sit on top

of the original Au(111) substrate. To elucidate the formation of this structure, we need to recall the findings about the molecular orientations of C_{60} molecules in the close packed layer on Au(111). In the uniform R0° phase, seven C_{60} molecules cluster into one group with a certain pattern of molecular orientations, as indicated in the STM image (Figure 4.13c) and the corresponding ball model Figure 4.13d.

The internal structures of the C_{60} molecules obtained from STM images have been applied to deduce the molecular orientations [2]. The molecule in the centre of the group with a well defined structure of three bright lobes, takes on the most stable orientation with a hexagonal ring in direct contact with the Au(111) substrate. At the same time the other six molecules all exhibit a three-lobe structure with two bright lobes and one dim lobe, which indicates that the molecules are not in the position of hexagonal ring parallel to the substrate but tilted by a small angle as demonstrated in the ball model (Figure 4.13d). These molecules have a C=C double bond facing the Au(111) substrate. In the ball model Figure 4.13d the six surrounding molecules are placed on the background Au(111) substrate with a C=C double bond and the pentagon rings in yellow colour represent the bright lobes while the six pentagonal rings in light brown correspond to the dim lobes in the STM image. From the ball model we can see that the two molecules at the two opposite sides of the central molecule along the close packed direction tilt in the same direction. When Au atoms diffuse to these molecules at the interface, the tilted C_{60} molecules are more likely to capture the Au atoms. The central molecule has a large area, i.e., more carbon atoms in direct interaction with the Au surface, which builds a higher barrier for the diffusing Au atoms. After Au atoms lift the tilted molecules, as a direct result the stability of the molecule in the central of the

group is further enhanced by the step edges of the Au islands below the raised molecules. A ring-like structure (or a hexagonal structure with a hollow in the centre) of the underlayer Au island forms beneath the six raised C_{60} molecules as shown in Figure 4.13e.

As indicated in Figure 4.13e outside the hexagonal shaped Au island, there are 12 molecules (drawn as circles) in contact with the step edge of the Au island. These 12 molecules can be divided into two groups according to the strength of their bonding with the Au step edge. The molecules next to the sides of the Au island indicated with filled circles in Figure 4.13e are strongly attached, with more coordination between the molecule and the Au atoms in the step edge compared with the other six molecules attached to the corners of the hexagonal Au island. As a result, when more Au atoms come near the Au island, the molecules in contact with the corners of the Au island are more likely to be lifted by Au atoms and the molecules represented by the filled circles can stay attached to the Au(111) substrate. Following this pattern, the honeycomb structure spreads on the surface. Figure 4.13f shows a larger Au island in a structure of two interconnected hexagonal rings, supporting ten C_{60} molecules (indicated by circles). The edge of this honeycomb structure has a zigzag shape as shown inside the blue rectangle in Figure 4.13a. There is no extended honeycomb network due to the short range of the C_{60} superstructure with periodic molecular orientations (Figure 4.13c) and the disturbance from the randomly distributed dim molecules that are hard to lift by interfacial Au atoms.

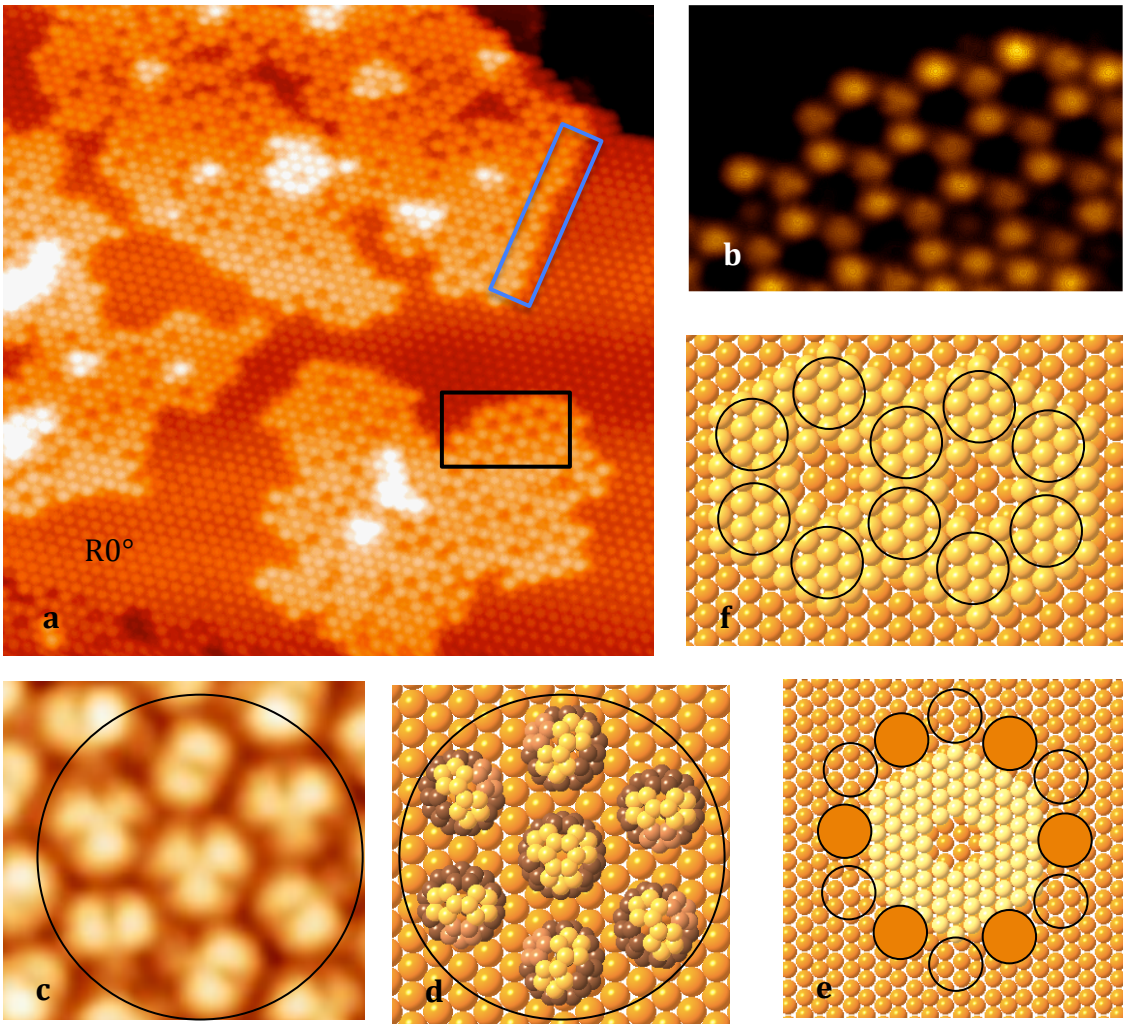

Figure 4.13 A second porous structure – the honeycomb structure of Au islands at the interface. (a) STM image showing the porous structure after the deposition of 0.45 ML of Au atoms at 135 K. The blue rectangle highlights the zigzag boundary of the C_{60} island that sit on top of the Au island. A small area of the porous structure enclosed in the black rectangle is enlarged and shown in the STM image b. (c) STM image with internal molecular structure. The circle encloses a group of seven C_{60} molecules. (d) A ball model for the group of seven C_{60} molecules in the image c. (e) and (f) Two structural models to explain the formation of the honeycomb structure. The background is the Au(111) substrate (tangerine colour). The Au islands are made of Au atoms (light yellow colour). Both the blank circles and the circles in orange represent the positions of C_{60} molecules.

The structures of the Au islands indicate general trends in the bonding strength of the C_{60} layer to the Au(111) substrate, where the interfacial stress for both the close packed top Au(111) layer and C_{60} layer plays a role. For the disordered R30° phases every C_{60} molecule occupies an area of a $2\sqrt{3}\times2\sqrt{3}$-R30° unit cell. The diagonal length of the unit cell is about 9.98 Å (taking the Au lattice constant as 2.88 Å). The molecule diameter in bulk is 10.02 Å. If the Au(111) surface is rigid, the close packed C_{60} layer needs to contract by about 0.4 % to ensure that all the C_{60} molecules occupy the same lattice site on the Au(111). Similarly the C_{60} layer in the uniform R0° phase (38×38-R0°) also experiences compression by about 0.7%. On the contrary, the Au(111) surface experiences the tensile stress exerted by the C_{60} overlayer.

In fact both the C_{60} layer and the Au(111) surface are not rigid. The system of C_{60}/Au(111) is dynamically stable to reach an optimized condition. Before the adsorption of C_{60} layer, Au atoms in the (111) surface are compressed along three equivalent directions to form the herringbone structure. The coverage of C_{60} layer leads to anisotropic stress due to the misorientation between the close packed direction of the C_{60} layer and the direction of the tension in the Au(111) surface. The elimination of the herringbone construction due to adsorption of C_{60} indicates that the compression stress in the Au(111) surface between the Au(111) and the vacuum surface has been relieved. However, the stress at the interface between Au(111) and the C_{60} overlayer gradually accumulates. The interfacial stress has a local effect on the interface in the C_{60}/Au(111) system, and the formation of the dim C_{60} molecule is a way to release the interfacial tension. The interfacial stress can cause subtle vertical movement of Au atoms within the layer and changes of

C_{60} molecules in geometrical position on the surface, molecular orientations and molecular electronic structures. The nucleation of the deposited Au atoms at the interface is affected by the interfacial structure induced partly by the stress. The two types of short-range porous structures of Au islands reflect the local variation of the interface structures of the C_{60}/Au(111).

4.3 Electron Irradiation of C_{60} Molecule in Monolayer on Au(111)

When a second layer of C_{60} grows on top of the first layer, molecules in the second layer sit, not in line with the molecules in the first layer, but with an offset of one third of the molecular diameter to form close packed FCC stacking. In Figure 4.14, the line profile along the solid line indicates that the bright C_{60} island is a second layer with a height of about 0.6 nm. Along the dashed lines, we can see that the rows of C_{60} molecules in the second layer are situated at the troughs of the lower layer.

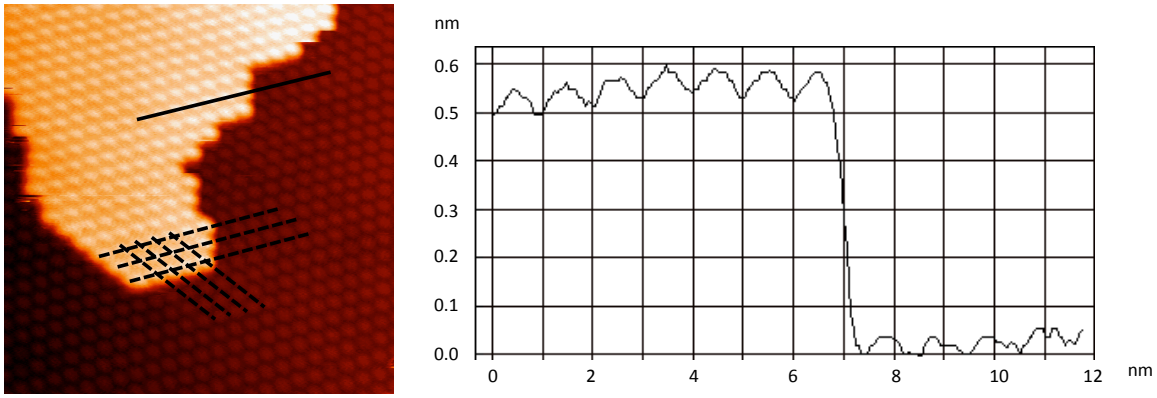

Figure 4.14 STM image of a double-layer C_{60} sample. The line profile along the solid line indicates that the bright C_{60} island is a second layer with a height of about 0.6 nm. The dashed lines are along the close packed C_{60} rows in the second layer and along the troughs of the under layer.

Sometimes there are small C_{60} islands with bright colour and a larger height than the surrounding C_{60} molecules in the monolayer, one of which is highlighted by a square, as shown in Figure 4.15a. One interesting characteristic of these bright C_{60} island is that they pack in line with the C_{60} layer on Au(111) as indicated in Figure 4.15b by dashed lines. Figure 4.15b is Figure 4.15a after being treated with the unsharp mask to place all the features at the same level and the arrangement of the bright C_{60} molecules can be clearly seen. This alignment proves that the islands are not a second layer of C_{60} molecules, because as has been shown in Figure 4.14, C_{60} molecules in the second C_{60} layer should sit at the troughs of the under layer.

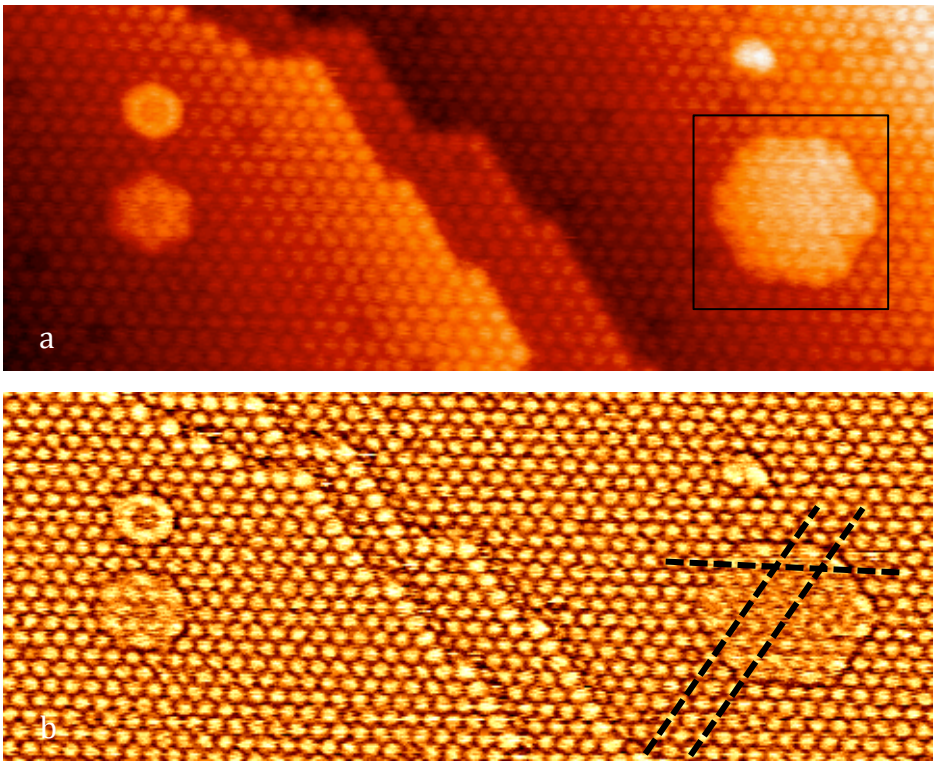

Figure 4.15 A STM image with bright C_{60} islands in the first molecular layer. (a) A few bright features of C_{60} molecules are observed in the freshly formed C_{60} monolayer on Au(111). There are two steps on the image. On the lower terrace a bright C_{60} island (highlighted by a square) of about 47 molecules, while on the higher terrace two

small bright islands of C_{60} molecules occur. A few dim molecules are also visible at positive bias 1.2 V. (b) The STM image is processed with the unsharp mask that all the surface features are pressed to the same level. Dashed lines mark the bright C_{60} molecules arranged in line with the molecules on the Au(111) surface.

What is the reason for the formation of these bright islands of C_{60} molecules? The explanation that the bright C_{60} molecules are lifted by Au atoms beneath is ruled out by the height profile of the islands, which is measured to be about 1.5 Å at 1.5 V (height profile in Figure 4.16). More importantly, the height of the island varies with the imaging bias and tunnelling current. The bias dependence of the heights of these bright C_{60} molecules is similar to that of the dim C_{60} molecules, because both the dim C_{60} molecules and the bright C_{60} islands are visible when the surface is imaged at positive bias (about 1.5 V), while at low bias (about 0.2 V) both become faint (Figure 4.16). The background C_{60} layer remains constant in both tunnelling conditions. The height of the bright C_{60} island changes with the applied bias. At 1.5 V, the height of the island is about 0.15 nm while at 0.2 V, it becomes about 0.12 nm through the calculation of height difference between the bright C_{60} molecule in the centre of the bright island and one C_{60} molecule in the background C_{60} layer on the same terrace. The heights of the C_{60} molecules along the solid line in Figure 4.16b have a symmetrical distribution about the central C_{60} molecule as shown in the height profile on the right of the image.

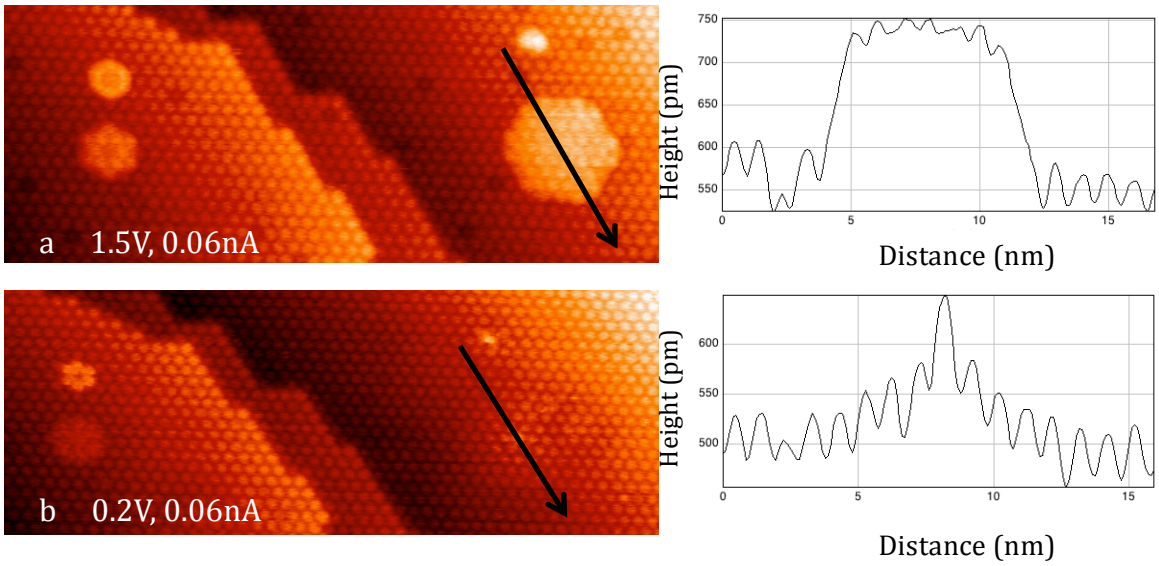

Figure 4.16 STM images showing the topography of C_{60} monolayer on Au(111), obtained at 1.5 V a and 0.2 V b separately. On the right of each images is the line profile along the solid line with an arrow end. Comparing the two STM image reveals the bright feature of the C_{60} islands closely related with the imaging bias: (a) at 1.5 V these bright C_{60} molecules are about 1.5 Å higher than background molecules in the layer on the same terrace; (b) at low imaging bias the bright feature becomes invisible, except the molecule in the centre which is of about 1.2 Å in height seen from the line profiles.

The six STM images shown in Figure 4.17 display the appearance of the bright C_{60} islands at different positive bias, but with the same tunnelling current (0.06 nA). When the imaging bias is in the range from 1.5 V to 1.0 V (Figure 4.17a – c), there is no obvious change of the bright C_{60} island on the bottom terrace. When the imaging bias is 0.8 V or 0.6 V, the STM images no longer show the molecules in the islands, instead the features of molecular orbitals of the C_{60} molecules appear (Figure 4.17d and e). The C_{60} molecule in the centre of the island always appears

bright even at a small bias 0.4 V (Figure 4.317f) while the others look the same as the background molecules.

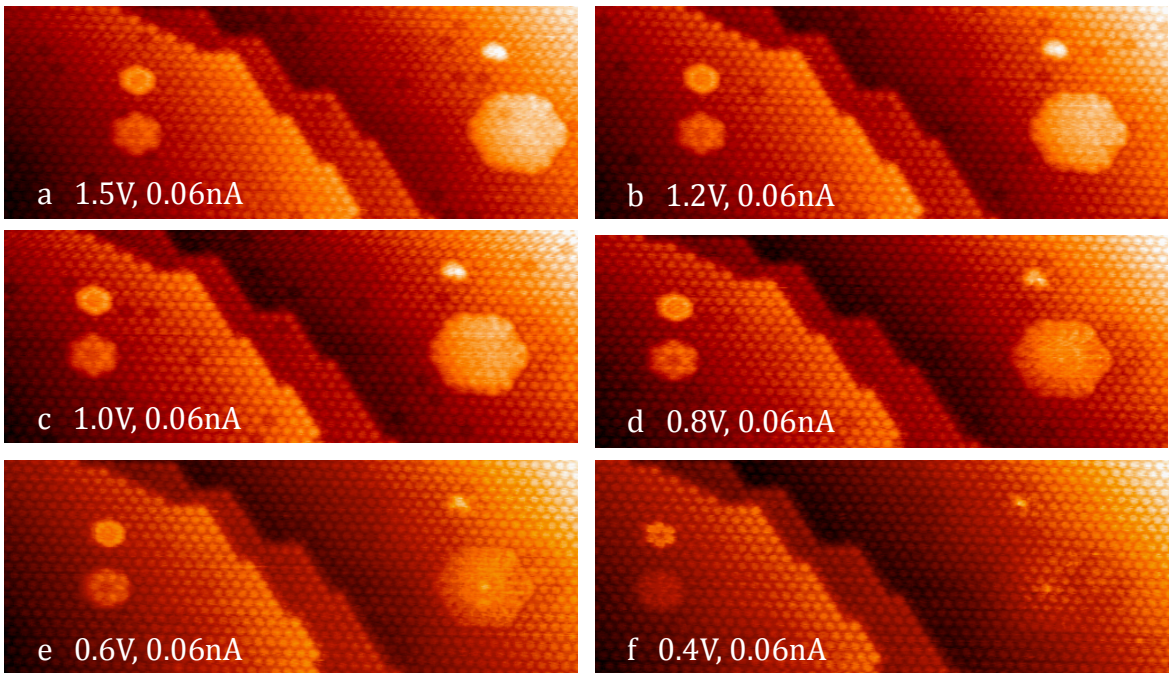

Figure 4.17 A series of STM images with decreasing tunnelling bias from a 1.5 V, b 1.2 V, c 1.0 V, d 0.8 V, e 0.6 V to f 0.4 V and the same tunnelling current 0.06 nA. The bright C_{60} island on the lower terrace becomes faint with decreasing bias and only the C_{60} molecule in the centre remains bright.

The changing heights of the C_{60} molecule in the centre of the bright island versus bias are listed in table 4.1 and range from 130 pm to 197 pm (the heights in table 4.3.1 are averaged values of four measurements at each bias).

Bias/V	-1.5	-1	-0.8	-0.6	-0.4	0.2	0.4	0.6	0.8	1	1.2	1.5
Height/pm	130.4	130.7	146.2	143.2	129.8	145.9	164.2	162.1	169.2	172.7	179.0	197.0

Table 4.1 Averaged height difference between the bright C_{60} molecule in the centre of the bright island and the molecule in the background C_{60} layer on the lower terrace (Figure 4.17).

The relation between the tunnelling bias and the height is plotted in the Chart 4.1 below. The chart clearly reveals the trend of a positive increase of the heights at increasing positive sample biases. The changes of the heights at negative biases are relatively smooth and the fluctuations are within 17 pm.

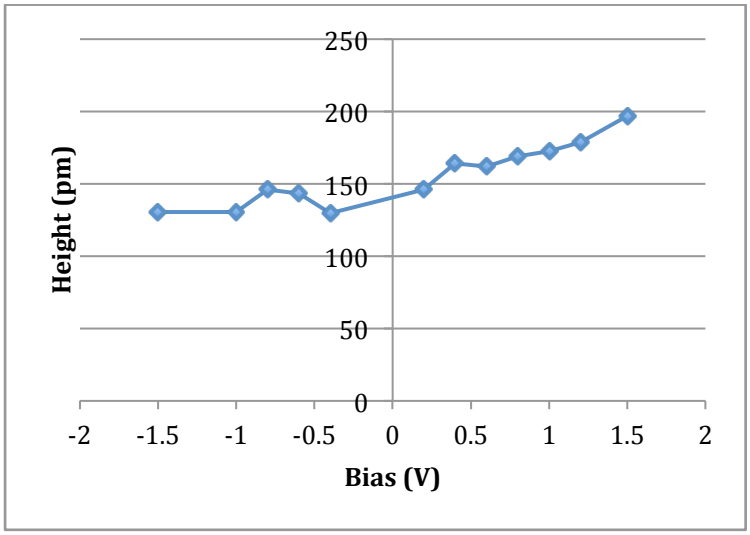

Chart 4.1 Variations of the height differences between the C_{60} molecule in the centre and the background C_{60} layer with imaging biases. At positive bias, the height difference increases with bias while at negative bias the height difference does not change much.

Similar observations existed for electron irritated C_{60} films of 4 to 5 layers grown on Si(111)$\sqrt{3}\times\sqrt{3}$-R30°-Ag surface [13]. From this study by Nakaya et al. it is assumed that the bright C_{60} molecules come from polymerization with the C_{60}

molecules in the underneath layer excited by high-energy electrons (100 eV to 2 KeV). The bright C_{60} molecule in the centre of the cluster show larger heights at negative sample bias than at positive sample bias (Figure 4.18b), which indicates the change of the LUMO, i.e., extra electrons transferred to the LUMO. The authors did conductance spectra for both the pristine C_{60} molecule (spectra A in Figure 4.18a) and the irritated C_{60} molecule (spectra B in Figure 4.18a). The two spectra in Figure 4.18 demonstrate that after electrons were injected into the C_{60} molecules, their LUMO and HOMO had been altered significantly.

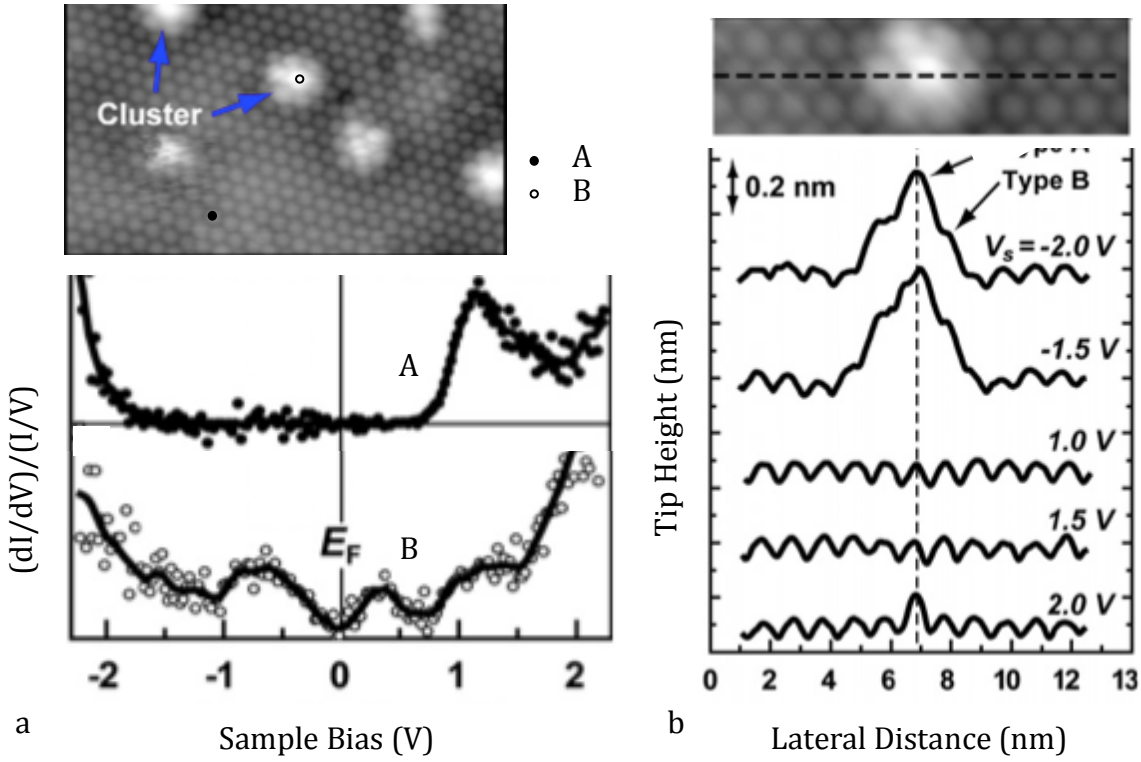

Figure 4.18 (a) Normalized conductance spectra for two types of C_{60} molecules. The spectra A is taken over the pristine molecule and the Spectra B is taken over the bright C_{60} molecule in the centre of the cluster. (b) Height profile across the cluster of bright C_{60} molecules at different imaging biases. Largest variation of height for the bright C_{60} molecule happens at -2.0V. (All images and spectra taken from [13].)

In our experiment, the molecular structure of bright C_{60} molecules should also be altered, and that is why we can observe the bias-dependent appearance changes of the bright C_{60} molecules. The occurring of the bright C_{60} molecules can be attributed to small residuals from carbon fragments of C_{60} molecules after Ar^+ sputtering on the C_{60}/Au(111) substrate. When the Au(111) surface still has some carbon impurities on the terrace, this kind of bright C_{60} islands can be easily observed. These defects on the Au surface affect the charge distribution of the C_{60} molecules around the defects and also the molecular states. In our study, the significant dependency between the positive sample bias and the height of the excited molecules indicates the change of the HOMO which can affect the tunneling current when electrons tunnels from the tip to the sample. If the electrons in the HOMO are taken away from a C_{60} molecule by the carbon fragments, which is in contrast to the irritated C_{60} molecules where electrons are injected into the LUMO, the C_{60} molecule has a higher conductance (compared with pristine C_{60} molecules) or a brighter look in STM images when electrons are injected from the tip (corresponding to a positive sample bias), as the molecule has more available states in HOMO to accommodate the electrons.

References

[1] E. I. Altman, R. J. Colton. Nucleation, Growth, and Structure of Fullerene Films on Au(111). Surf. Sci. **279**, 49 (1992).
[2] G. Schull and R. Berndt. Orientationally Ordered (7×7) Superstructure of C_{60} on Au(111). Phys. Rev. Lett. **99**, 226105 (2007).
[3] J. A. Gardener, G. A. D. Briggs, and M. R. Castell. Scanning Tunneling Microscopy Studies of C_{60} Monolayers on Au(111). Phys. Rev. B **80**, 235434 (2009).

[4] X. Shi, M. A. Van Hove, and R. Q. Zhang. Adsorbate-Induced Reconstruction by C_{60} on Close-Packed Metal Surfaces: Mechanism for Different Types of Reconstruction. Phys. Rev. B **85**, 075421 (2012).
[5] X. Torrelles, M. Pedio, C. Cepek, and R. Felici. $(2\sqrt{3}\times2\sqrt{3})R30^{\circ}$ Induced Self-Assembly Ordering by C_{60} on a Au(111) surface: X-Ray Diffraction Structure Analysis. Phys. Rev. B **86**, 075461 (2012).
[6] L. Tang, Y. Xie, and Q. Guo. Probing the Buried C_{60}/Au(111) Interface with Atoms. J. Chem. Phys. **136**, 214706 (2012).
[7] L. Wang and H. Cheng. Density Functional Study of the Adsorption of A C_{60} monolayer on Ag(111) and Au(111). Phys. Rev. B **69**, 165417 (2004).
[8] I. Hamada and M. Tsukada. Adsorption of C_{60} on Au(111) Revisted: A van der Waals Density Functional Study. Phys. Rev. B **83**, 245437 (2011).
[9] R. Felici, M Pedio, F. Borgatti, S. Iannotta, M. Capozi, G. Ciullo, and A. Stierle. X-Ray Diffraction Characterization of Pt(111) Surface Nanopatterning induced by C_{60} Adsorption. Nature Mater. **4**, 688 (2005).
[10] C. Liu, Z. Qin, J. Chen, Q. Guo, Y. Yu, and G. Cao Molecular Orientations and Interfacial Structure of C_{60} on Pt(111). J. Chem. Phys. **134**, 044707 (2011).
[11] W. W. Pai, C. Hsu, M. C. Lin, K. C. Lin, and T. B. Tang. Structural Relaxation of Adlayers in the Presence of Adsorbate-Induced Reconstruction: C_{60}/Cu(111). Phys. Rev. B **69**, 125405 (2004).
[12] F. Yin, R. E. Palmer, and Q. Guo. Critical Stability of Gold Nanofingers on a Zero-Gradient Stepped Surface. J. Phys. Condens. Mater.: **21**, 445001 (2009).
[13] M. Nakaya, M. Aono, and T. Nakayama. Scanning Tunnelling Microscopy and Spectroscopy of Electron-Irradiated Thin Films of C_{60} Molecules. Carbon, **49**, 1829 (2011).

Chapter 5. Self-Defined $(C_{60})_m(Au)_n$ Nanoclusters

The C_{60} molecule has been anticipated to be a component for nano-devices and when combined with other atoms and molecules, many novel structures have been discovered (as stated in the literature review). The realization of these nano-structures is the first step toward the final goal of nano-device fabrication. In chapter 5 the study about the self-defined nanoclusters made of C_{60} molecules and Au clusters is discussed. We took advantage of the Au(111) surface with the unique herringbone reconstruction to grow well ordered arrays of the nanoclusters. The Au(111) surface plays an important role in the formation and the properties of the nano-clusters. The experiment was carried out with the VT STM.

5.1 The Fabrication Process

5.1.1 In-Situ Deposition of C_{60} Molecules and Au Atoms

C_{60} molecules are thermally evaporated from a pocket made of Tantalum foil at a temperature of about 650 K measured with a thermocouple attached to the body of the pocket. A diagram of the simple C_{60} pocket evaporator is drawn in Figure 5.1. The pocket is made of tantalum foil. Two tantalum wings are used as the electrical contacts between the pocket and the copper rods fixed to a flange, which is mounted on the STM base. The joints of the pocket are welded and only a small opening is left where C_{60} molecules can escape. Inside the pocket is the C_{60} powder with a purity of 99.9% (product from MER Corp. US). The deposition rate for C_{60} molecules is controlled at around 0.05 ML per minute.

Before deposition, the C_{60} source is preheated to 575 K and degassed for 5 minutes to remove contaminations. During deposition, the temperature of the source is increased to 650 K, while the vacuum is kept below 2×10^{-9} mbar.

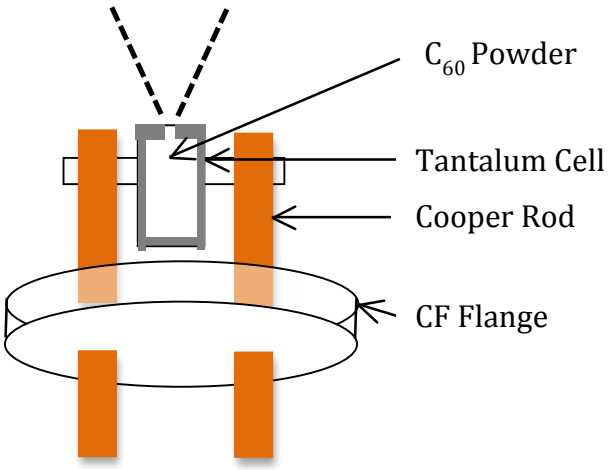

Figure 5.1 Simplified diagram of the C_{60} pocket evaporator, which is mounted at the base of the STM stage and the opening of the pocket is pointed to the sample on the scanning stage. The pocket is made of tantalum 0.1 mm thickness and only a small opening is left on one side of the pocket, with the other sides (in grey shadow) welded. This design can sufficiently control the deposition angle to prevent spreading C_{60} molecules on the STM stage. Two wings (horizontal bars) are the electrical connections between the pocket and the copper rods of the flange. Current flows from one copper rod through the pocket and back through another copper rod.

The deposition rate of the C_{60} molecule was generally estimated from STM images after deposition, and the coverage of the molecules can be roughly controlled by tuning the deposition temperature of the pocket evaporator. A single effusion cell (from CreaTec) can accurately control the temperature of the Au source during deposition. An Al_2O_3 crucible is used to hold small pieces of Au wire of 99.99%

purity. The degassing of the Au source is carried out at 1365 K and the deposition is at 1385 K with a deposition rate of about 0.02 ML per minute.

5.1.2 The Formation of the C_{60}/Au Nanocluster

Au clusters of tens of atoms cannot stay at the elbow sites of Au(111) herringbone reconstruction at room temperature, nor can smaller clusters of C_{60} molecules. They will diffuse to the terrace edges. Therefore, to inhibit the thermal energy of both Au atoms and C_{60} molecules on Au (111), the Au substrate was cooled down to 113 K by the liquid nitrogen bath cryostat. Both C_{60} molecules and Au atoms were deposited while the sample is held in the scanning stage (in-situ deposition) and kept at 113 K.

The Au(111) surface was cleaned following the standard procedure by Ar^+ ion sputtering and thermal annealing at 1000 K. The cleanness of the surface was further checked by STM until clear herringbone reconstruction was observed. Au atoms were deposited at a rate of 0.02 ML per minute for 1 minute and 20 seconds, i.e., 0.027 ML of Au atoms. The surface after the Au atom deposition is shown in Figure 5.2a. The bright dots on the surface are clusters of Au atoms, which stay at the elbow sites. A few are attached to step edges of Au terraces. Large Au clusters also exist on the surface at the place where the DLs are distorted. A height profile across three Au clusters along the line AB (Figure 5.2b) indicates that the Au clusters are a single layer high 0.228 nm. A close look at the elbow sites where Au clusters stay reveals that at the bulged elbow site Au clusters are in the FCC region while at the pinched elbow site they are in the HCP region (the inset in Figure 5.2a). At both sites there are dislocations near which Au atoms are trapped when

they diffuse across the surface. This nucleation phenomenon is also true for some other metals on the Au(111) surface.

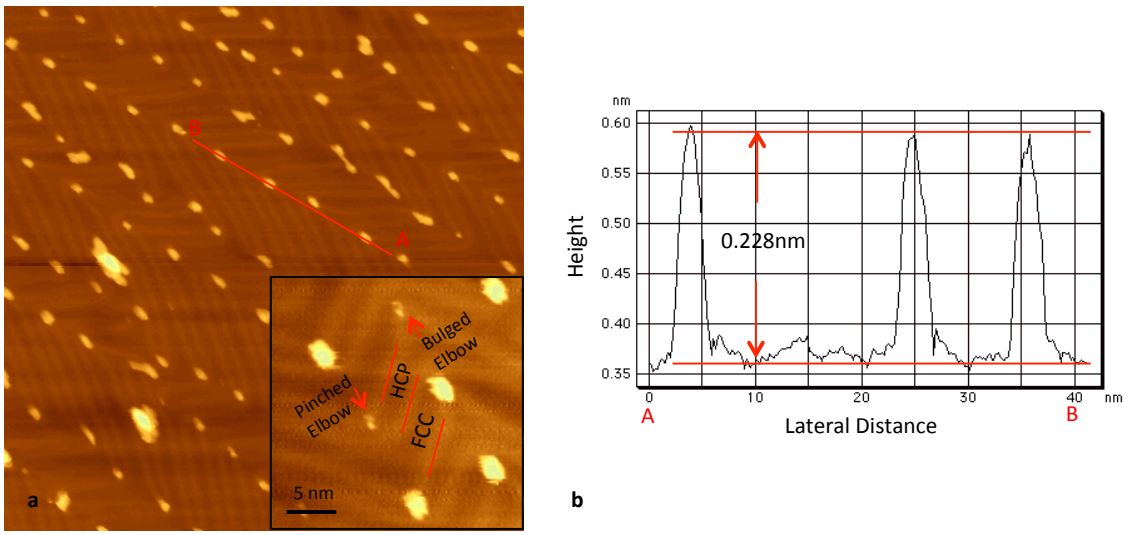

Figure 5.2 Morphology of the Au(111) substrate after Au atom deposition. STM image is obtained at 113 K. The size of STM image a is 100 nm ×100 nm. The inset shows main features of the reconstructed Au(111) surface, clearly showing the adsorption sites of Au clusters at the two types of elbow sites, i.e., the FCC region at the bulged elbow and the HCP region at the pinched elbow. The height profile in b along the red line in image a indicates that the Au cluster is one layer high, 0.228 nm.

After confirmation of the existence of Au clusters on the Au(111) substrate, C_{60} molecules were deposited at the same substrate temperature 113 K. The diffusion length for the molecules on the cold sample surface is shortened as their kinetic energy is consumed quickly through dissipation to the substrate. But it is long enough for the C_{60} molecules to find the preformed Au clusters at the elbow sites. In the temperature range 120 K to 170 K, we observed C_{60}/Au clusters in various sizes and shape. Most of the time the Au clusters cannot be directly imaged due to

the attachment of C_{60} molecules. But their positions on the surface can be indirectly assigned from the appearances of the C_{60}/Au clusters. The STM images in Figure 5.3 display the general features of C_{60}/Au clusters.

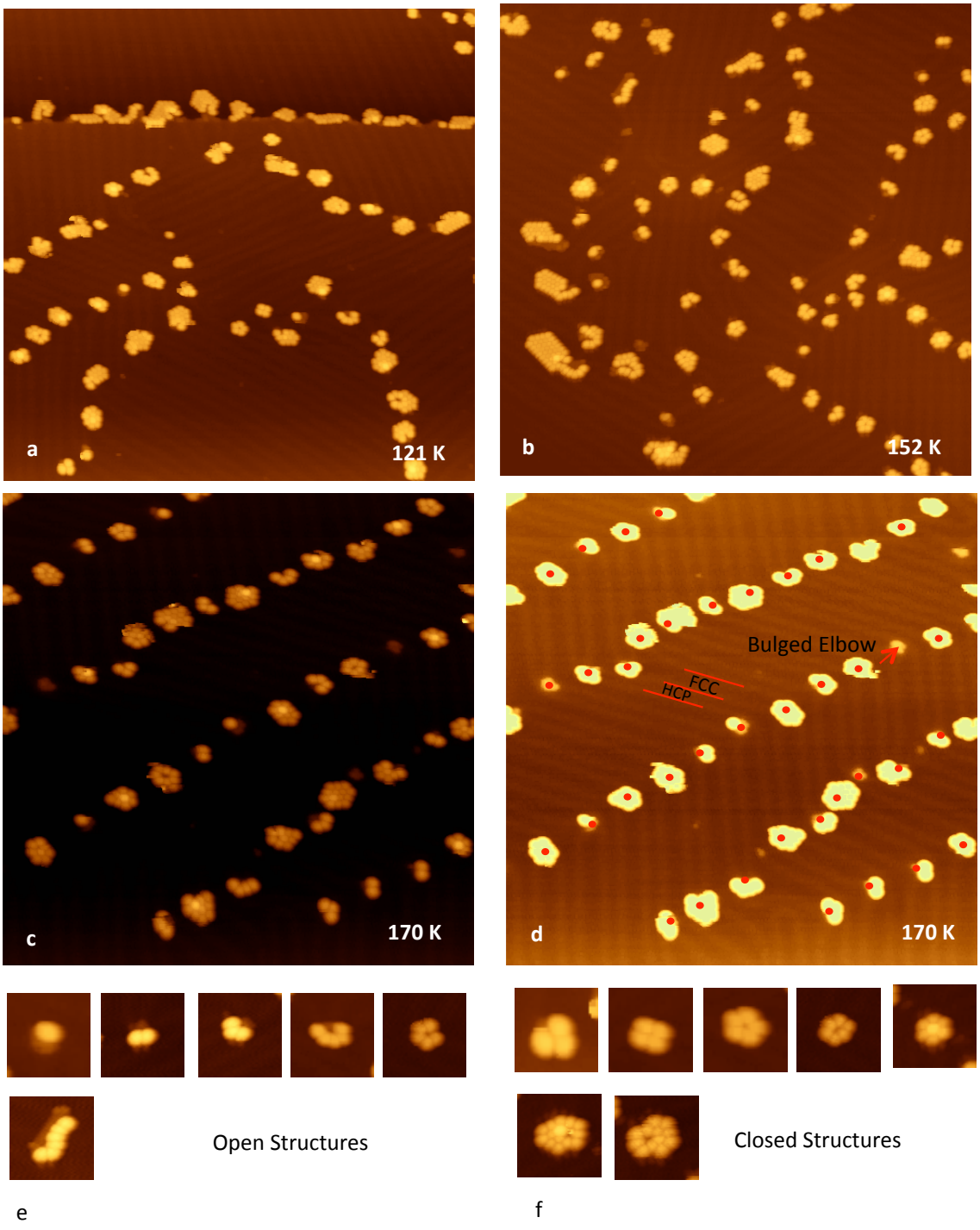

Fig. 5.3. C_{60}/Au clusters formed on Au (111) at various substrate temperatures. Temperature on each image is the temperature of the substrate during imaging. C_{60} molecules on top of Au clusters are brighter than C_{60} molecules on the Au(111) substrate. When C_{60} molecules are around a gold cluster, there is a hole due to the height difference between the molecule and the Au cluster. (a) The C_{60} molecules stay at the elbow sites or attached to Au step edge. The step edge decorated with Au clusters is not straight and the adsorption of C_{60} molecules to the step edge doesn't show any preference to the FCC regions in the step edge. (b) Image is obtained at 152 K with small isolated C_{60}/Au clusters and large clusters at the bottom left. Image c and d are one STM image with different brightness contrast. The red dots on image d are the positions of Au clusters. The majority of the Au clusters still stay at the places when they first formed at 120 K, i.e., FCC region at the bulged elbow and HCP region at the pinched elbow. The structures of C_{60}/Au clusters in e are open and in f are closed at temperatures from 120 K to 170 K.

There is no specific structure for the C_{60}/Au clusters except that the C_{60} molecules are close packed when forming islands around the Au clusters (Figure 5.3a-d). At the Au terrace edge, the deposited Au atoms are not fully integrated with the step to form a straight edge at 121 K. Instead they form isolated clusters attached to the step edge and, when C_{60} molecules diffuse to the "rough" edge, they organize into close packed islands around protrusions of Au clusters, or into rows of irregular shapes along the step edge as can be seen in Figure 5.3a, in which a horizontal Au step edge is on the top part of the image. For C_{60} molecules attached to the step edge (Figure 5.3a), there is no preference for the FCC region of the step edge compared to their adsorption behaviour to step edge at room temperature when,

at low coverage, isolated rows of C_{60} molecules form at the FCC regions of the Au step edges and no molecules stay at the HCP regions of the Au step edges [1]. Some single C_{60} molecules are brighter than others (Figure 5.3c) on the same terrace, as these brighter molecules are sitting on top of Au clusters of single-layer height.

After the deposition of C_{60} molecules, Au clusters are hard to see directly in STM images. Their existence can be determined through the appearances of the C_{60}/Au clusters. As has been mentioned above, for a C_{60}/Au cluster, if the C_{60} molecules are not in the same degree of brightness, the brighter C_{60} molecules have Au clusters underneath while the others sit on the Au(111) substrate. Moreover, when C_{60} molecules are around a void, there is an Au cluster at the void, which prevents the molecules forming a close packed structure. Based on this knowledge, by comparing the two images in Figure 5.3c and d, we can generally see the distribution of Au clusters after the adsorption of C_{60} molecules. Figure 5.3c and d, obtained at 170 K, is one STM image with a different brightness contrast. From Figure 5.3c the structures of C_{60}/Au clusters can be clearly resolved while from Figure 5.3d the locations of the Au clusters are readily known because of the clear view of the herringbone. The red dots in Figure 5.3d mark the location of Au clusters and one bulged elbow is indicated. In Figure 5.3d a majority of Au clusters remain in the FCC regions at the bulged elbow and the HCP region at the pinched elbow at 170 K.

At low temperature from 120 K to 170 K, the structures of C_{60}/Au clusters can be classified into two categories. One is open structure (Figure 5.3e) and the other is closed structure (Figure 5.3f). The “open” structure means that the Au cluster is not fully surrounded by C_{60} molecules, and the “closed” means that the Au cluster is fully enclosed by C_{60} molecules, with or without the coverage of molecules on the

top. For open structures (Figure 5.3e), the number of C_{60} molecules attached to a small Au clusters ranges from one to five and part of the Au clusters are still sometimes visible. Large clusters (the two clusters at the bottom of Figure 5.3e) with large Au clusters and more C_{60} molecules frequently form at the elbow sites which are connected with long and straight discommensurate lines (DLs). For the closed structures (Figure 5.3f) the Au clusters are usually out of the reach of the STM tip, due to the attachment of C_{60} molecules and their small area. A C_{60} molecule (~ 7 Å in height on Au(111)) is about three times higher than an Au atom (2.35 Å in diameter). Occasionally the closed structure on the right side of Figure 5.3f with one bright C_{60} molecule surrounded by six molecules is observed at low temperature.

In order to get the thermodynamic stable structures of the C_{60}/Au clusters which can be more uniform, the substrate temperature is gradually raised to room temperature.

5.2 The C_{60}/Au Nanocluster at Room Temperature

At room temperature, the interactions with the Au substrate are weak enough for C_{60} molecules and Au atoms to diffuse on the surface, and strong enough to direct the reorganization of the C_{60}/Au clusters through a surface template effect. One structure with one bright C_{60} molecule and six molecules around the bright one populates the surface.

5.2.1 Close-Shell Structure of $(C60)_7(Au)_{19}$

The introduction of a slow annealing treatment from about 170 K to room temperature 295 K leads to significant changes of the C_{60}/Au clusters on the Au(111) substrate so that a large portion of one type of C_{60}/Au cluster prevails as

shown in Figure 5.4a. In Figure 5.4a, all the clusters stay at the elbow sites and the space in between these clusters are the bare Au surface. In order to clearly show the features of the typical cluster, the background is dark but the herringbone reconstruction of the Au(111) substrate is still visible at the bottom of the STM image (Figure 5.4a). A height profile across the cluster proves that the bright C_{60} molecule is sitting on top of an Au cluster of single layer height, because the bright C_{60} molecule is about 0.220 nm, the height of an Au atomic layer, higher than the surrounding C_{60} molecules. The surrounding six C_{60} molecules that are on the substrate, are about 0.747 nm in height with reference to the Au(111) surface. This is the height of a C_{60} molecule attached to an Au step.

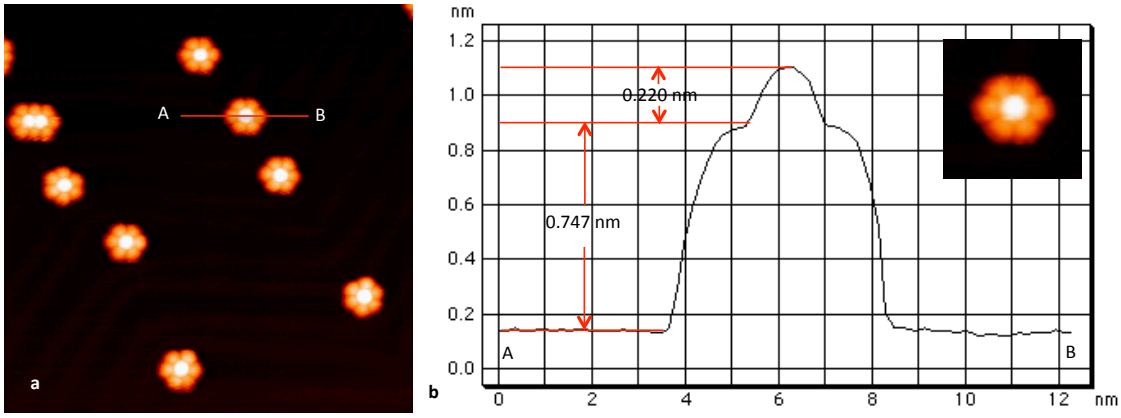

Figure 5.4 (a) STM image of some C_{60}/Au clusters on the Au(111) surface at room temperature. One typical cluster with one bright C_{60} molecule and six surrounding molecules populates substrate. (b) Height profile across a cluster indicates that the bright C_{60} molecule sits on top of an Au cluster of single layer height, as it is about 0.220 nm higher than the surrounding molecules. The height difference is close to the height of an atomic Au layer.

At the top left corner of Figure 5.4a, there is also a larger C_{60}/Au cluster with two bright C_{60} molecules and eight surrounding C_{60} molecules. More compact C_{60}/Au

clusters have been discovered on the sample surface, which will be discussed in section 5.2.3. The number of C_{60} molecules in each cluster can be accurately counted, but the size of the Au cluster underneath the bright C_{60} molecule cannot be seen directly. With the knowledge of the C_{60} monolayer on Au(111), a general estimation of the number of Au atoms underneath the bright C_{60} molecule is possible. For a close packed C_{60} layer on Au(111), each C_{60} molecule takes up the area of 12 Au atoms in the (111) surface. The number of 12 atoms is an average value for one C_{60} molecule. The number of Au atoms that one C_{60} molecule interacts with should be more than 12 as there are Au atoms that are shared by other molecules. A ball model for the typical C_{60}/Au cluster is shown in Figure 5.5c, with one brown C_{60} molecule on top of an Au island in yellow colour. The Au atoms in the Au(111) substrate are in purple except 18 Au atoms, around the yellow Au cluster, that are in red. We name this cluster the $(C_{60})_7(Au)_{19}$ cluster. The 19 Au atoms organize into a hexagonal island and six molecules each attach to one side of the Au hexagonal island. The cavity formed by the six surrounding molecules is just the right space to fit in one C_{60} molecule. Figure 5.5a is a zoom-in image of the smallest and most compact C_{60}/Au cluster on the substrate at room temperature. In the ball model, the bright C_{60} molecule occupies atop site over an Au atom (the red Au atom in the centre of the Au cluster in Figure 5.5b) in the Au cluster, while the other six C_{60} molecules around the Au cluster all sit over the hollow sites on the Au(111) substrate. Each of the six hollow sites is formed by three Au atoms, as indicated in Figure 5.5b – the six groups of three Au atoms in red. We place all the seven C_{60} molecules as shown in Figure 5.5c, i.e., a hexagonal carbon ring of the cage being parallel to the (111) surface and the C-C edges of the hexagonal ring in the parallel orientation to the step edges of the hexagonal Au cluster. The

configuration of the six C_{60} molecules on the Au(111) substrate is from theoretical simulation concluded to be the most stable geometry for the C_{60} single layer on Au(111) [2, 3].

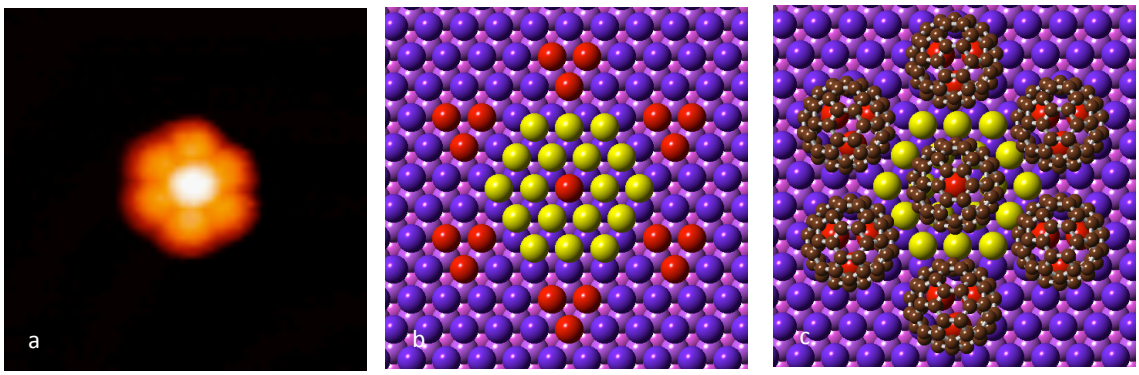

Figure 5.5 The $(C_{60})_7(Au)_{19}$ cluster and corresponding ball models. (a) A zoom-in STM image of the cluster. (b) Structure of the Au cluster on the Au(111) substrate without showing any C_{60} molecules. The Au atoms of the Au cluster are in yellow except the centre one, which is red. 19 Au atoms form a hexagonal island on the Au(111) substrate. Background purple balls are Au atoms that form the Au(111) surface. 18 Au atoms in red in the Au(111) substrate highlight the occupation sites of the six C_{60} molecules around the Au cluster. (c) Overall structure of the $(C_{60})_7(Au)_{19}$ cluster. All C_{60} molecules have one hexagonal carbon ring in direct contact with Au substrate. The C_{60} molecule on the top of the Au cluster occupies a top site and the other six molecules occupy the hollow sites on Au substrate.

When conceiving the ball model, both the Au atoms and the C_{60} molecules are set to be close packed. The nearest distance between a carbon atom of the C_{60} molecule and an Au atom at the step edge of the Au cluster is one key factor in deciding the size of the Au cluster while keeping the distance for two neighbouring

molecules around 10.03 Å. According to the theoretical calculation about the optimized configuration of C_{60} molecules on Au(111), the centre-to-centre distance from a carbon atom to its nearest Au atom is about 2.3 Å [2]. In the model (Figure 5.5c) the C_{60} molecules are placed on the surface with the nearest C-Au distance being 2.3 Å. A schematic diagram is given in Figure 5.6, where only the 19 Au atoms that form the Au cluster, and the 18 Au atoms that define the adsorption sites of the C_{60} molecules on the substrate, are left. The diagram is the view when the remaining structure is seen from the bottom. Therefore, the red Au atoms are at the front of the diagram and the hexagonal carbon ring that is used to locate the C_{60} molecule is clear. The distance between the Au1 atom and one of the two orange carbon atoms is about 2.30 Å. The six carbon atoms of the hexagonal carbon ring can be grouped into three pairs (the inset at the bottom right side of Figure 5.6) and each pair is at the same distance from the Au2 atom that is in the middle of the step edge of the Au cluster. The two carbon atoms, in black colour, shared by one hexagonal ring and one pentagonal ring, are nearest to the Au2 atom and the separation is about 2.50 Å as seen in the table in Figure 5.6. The two carbon atoms in blue and two carbon atoms in orange of the hexagonal carbon ring are further away, 3.19 Å and 3.79 Å respectively, from the Au2 atom compared with the two carbon atoms in black. The separation 2.5 Å is an acceptable value for the carbon atoms to bind with the Au atoms.

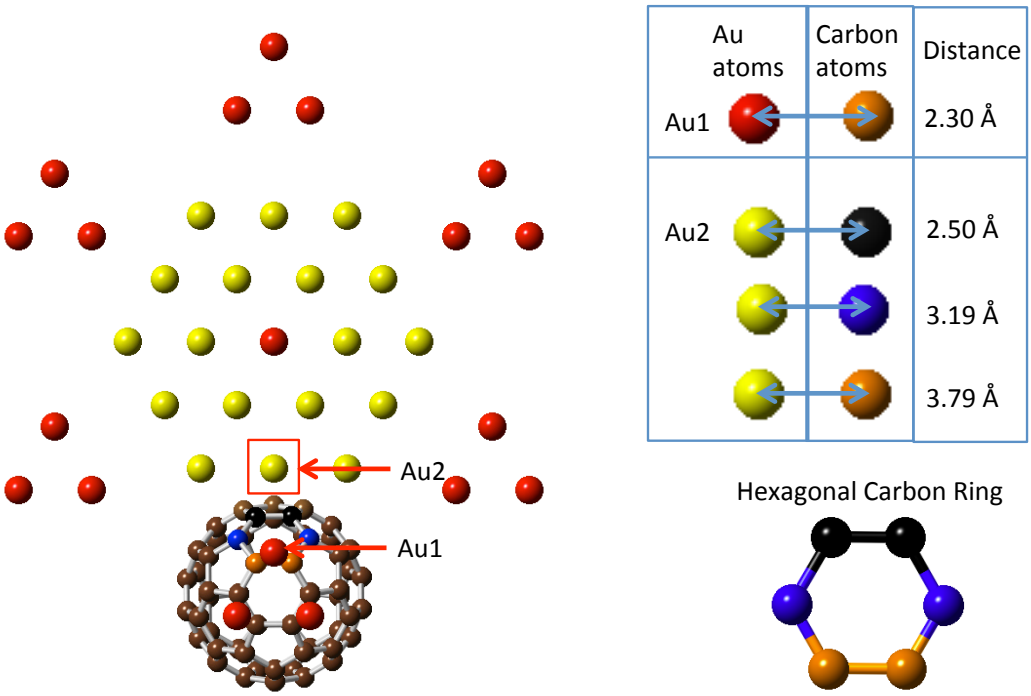

Figure 5.6 Schematic diagram for the distance between the carbon atoms and the relevant Au atoms. Red and yellow balls are Au atoms at the same positions as in Figure 5.5b and c. Other Au atoms are removed in order to show the carbon rings that are near the step edge of Au cluster more clearly. Carbon atoms, in yellow, blue and black, of the hexagonal carbon ring concern the shortest separation between a carbon atom and an Au atom in the step edge of the Au cluster, and the centre-to-centre distances between each of the six carbon atoms and the Au2 atom are listed in the table above. The shortest distance is 2.5 Å between one of the carbon atoms in black and the Au2 atom

The formation of $(C_{60})_7(Au)_{19}$ depends the size of the Au cluster in the centre and interactions between molecule-molecule, Au atom-atom, and molecule-atom as well as the balancing of all the energies involved. This cluster is one of the stable structures on the substrate, which will be presented in the next section.

5.2.2 Large C_{60}/Au Clusters

Besides the compact small C_{60}/Au clusters, large C_{60}/Au clusters due to their stable size can also survive on the (111) surface at room temperature. These large clusters always have large Au islands and sometimes with open structures. Open structures with a small Au cluster are seldom observed on the surface at room temperature.

The STM image in Figure 5.7a is an overview of the sample at room temperature. All the clusters are trapped at the elbow sites. Due to the distortion of the herringbone, the distribution of the clusters is not uniform. A few large clusters with large Au islands can be clearly seen with C_{60} molecules fully enclosing or partially enclosing the Au islands. Figure 5.7b reveals the features of the large clusters. The large clusters highlighted by red circles have the step edge of the Au islands fully covered with C_{60} molecules. The height profile along the line AB demonstrates that the height of the Au island in the centre is 0.22 nm, the same as that of a single-layer Au island, and the C_{60} molecules closely around the Au island are 0.72 nm high. The other large C_{60}/Au clusters enclosed by the yellow circles always have openings around the Au islands where no C_{60} molecules cover the step edge of the Au islands. From Figure 5.7c, which is Figure 5.7b processed by unsharp mask to make the herringbone structure more clear, we can see that the bare step edges of the Au islands are totally or partly in the HCP regions of the Au(111) substrate, no matter which type of elbow sites the clusters are anchored by. At a low coverage of C_{60} molecules on Au(111), they tend to decorate the step edge in the FCC regions first, before they adsorb to the step edges in the HCP regions, which is the same case for C_{60} adsorption around the Au clusters on Au(111).

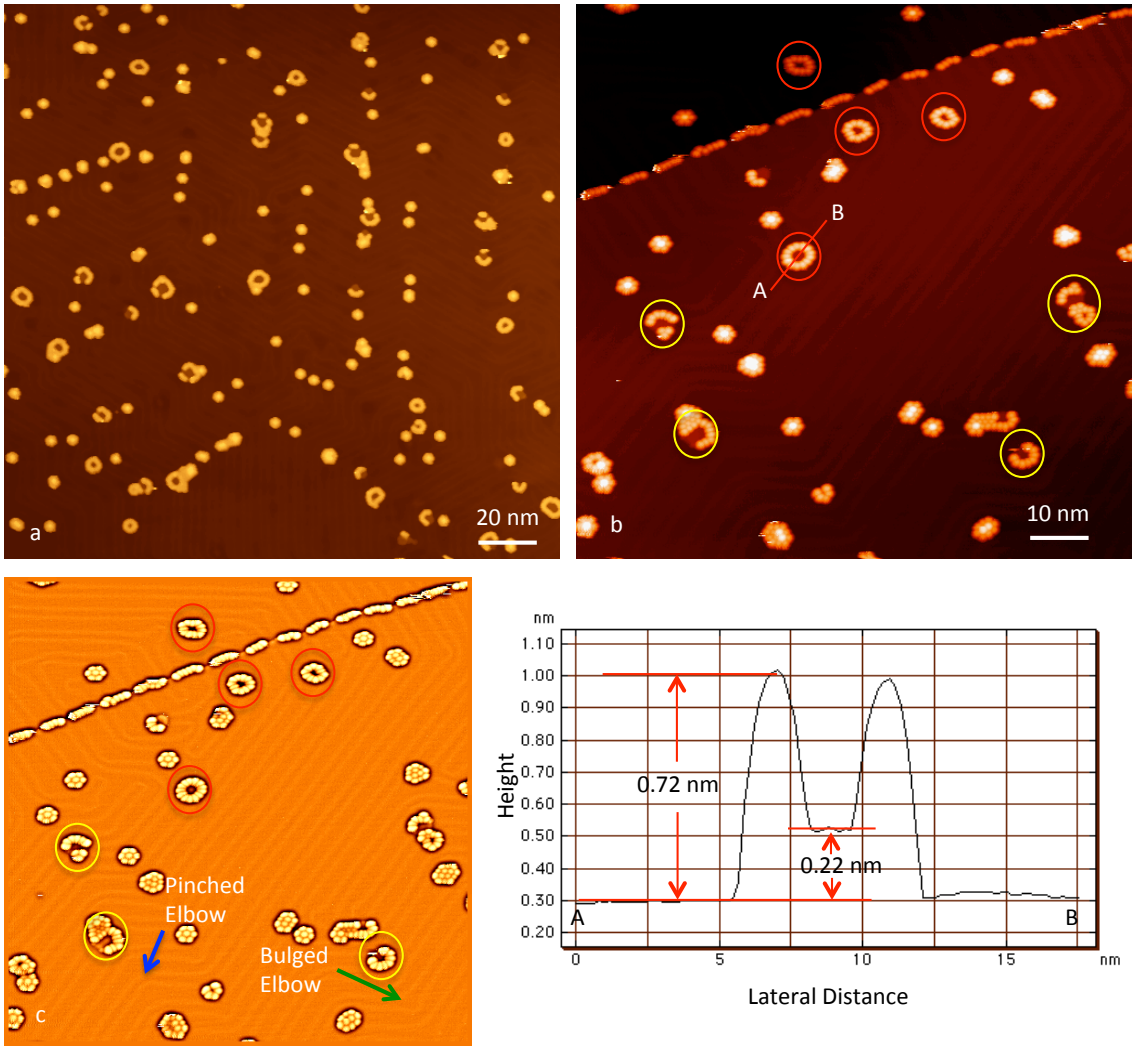

Figure 5.7 STM images of the Au(111) substrate with decoration of C_{60}/Au clusters at room temperature. (a) Overview of the substrate at room temperature. Sizes of C_{60}/Au clusters can be simply grouped in two categories: one the big C_{60}/Au clusters with large Au islands, where Au islands are large enough to be visible on the STM image; the other compact C_{60}/Au clusters. (b) There is an Au step on the STM image. Short rows of C_{60} molecules adsorb to the step edge and the gaps between these C_{60} rows are HCP regions of the herringbone reconstruction. Red circles enclose large C_{60}/Au clusters in closed structures with edge of the Au islands fully covered by C_{60} molecules. Yellow circles highlight other large clusters in open structures. The profile below the STM image along the line AB on the image b indicates that the Au island is

single layer high. (c) The STM image b is processed by unsharp mask to show clearly the herringbone reconstruction. Openings at the edge of large clusters marked by yellow circles are in HCP regions of the substrate. At low coverage of C_{60} on Au(111), C_{60} molecules prefer to stay in or adsorb to the FCC regions over the HCP regions.

We also studied the thermal stability of the C_{60}/Au clusters at elevated substrate temperatures up to about 410 K. Some of these large clusters grow even larger with a supply of Au atoms from other C_{60}/Au clusters that physically decompose. At 410 K, there are large Au islands of some clusters having the discommensurate lines visible, and the width of the Au island, although not in the shape of a polygon or circle, is about 10 nm. The change of two large clusters followed by STM with increasing substrate temperature is shown in Figure 5.8. The four images on the top are the appearances of one cluster from room temperature, about 295 K, to 330 K. The four STM images below are of a second large cluster. The biggest change of the cluster in Figure 5.8a1 is the detachment of a compact cluster at 330 K (Figure 5.8d1), and there are more C_{60} molecules around the Au island in the centre. Another cluster in Figure 5.8a2 has an Au island with a corner at room temperature. With increasing temperature of the substrate, the sharp corner of the Au island gradually disappears and the shape of the Au island becomes near to a circle. The C_{60} molecules that are not attached to the Au island are detached from the C_{60}/Au cluster. At 316 K (Figure 5.8c2), there are one bright molecule on the big Au island and one bright molecule on the small Au island forming a $(C_{60})_7(Au)_{19}$ cluster aside the big Au island. At 330 K, the movement of C_{60} molecules in the tunnelling junction causes streaks on the images.

The surface area changes of the Au islands of the two clusters (Figure 5.8a1 and a2) are plotted in Figure 5.8e. The substrate temperatures range from room temperature 295 K to 330 K. The blue line with the data points marked by blue diamonds shows the area change of the Au island in Figure 5.8a1-d1. The red line with the data points marked by red squares corresponds to the other cluster in Figure 5.8a2-d2. For the Au islands, the general tendency is to become bigger at higher temperature than at room temperature. There are fluctuations of the surface areas measured at various substrate temperatures due to slight distortion of STM images, but the chart can show the tendency that the Au island can grow bigger at high substrate temperatures due to the capturing of Au atoms that diffuse on the substrate. This annealing process can eliminate the unstable molecules and atoms and promote the ripening of the nanostructures on the substrate. More results concerning the evolution of small C_{60}/Au clusters are presented in section 5.3.

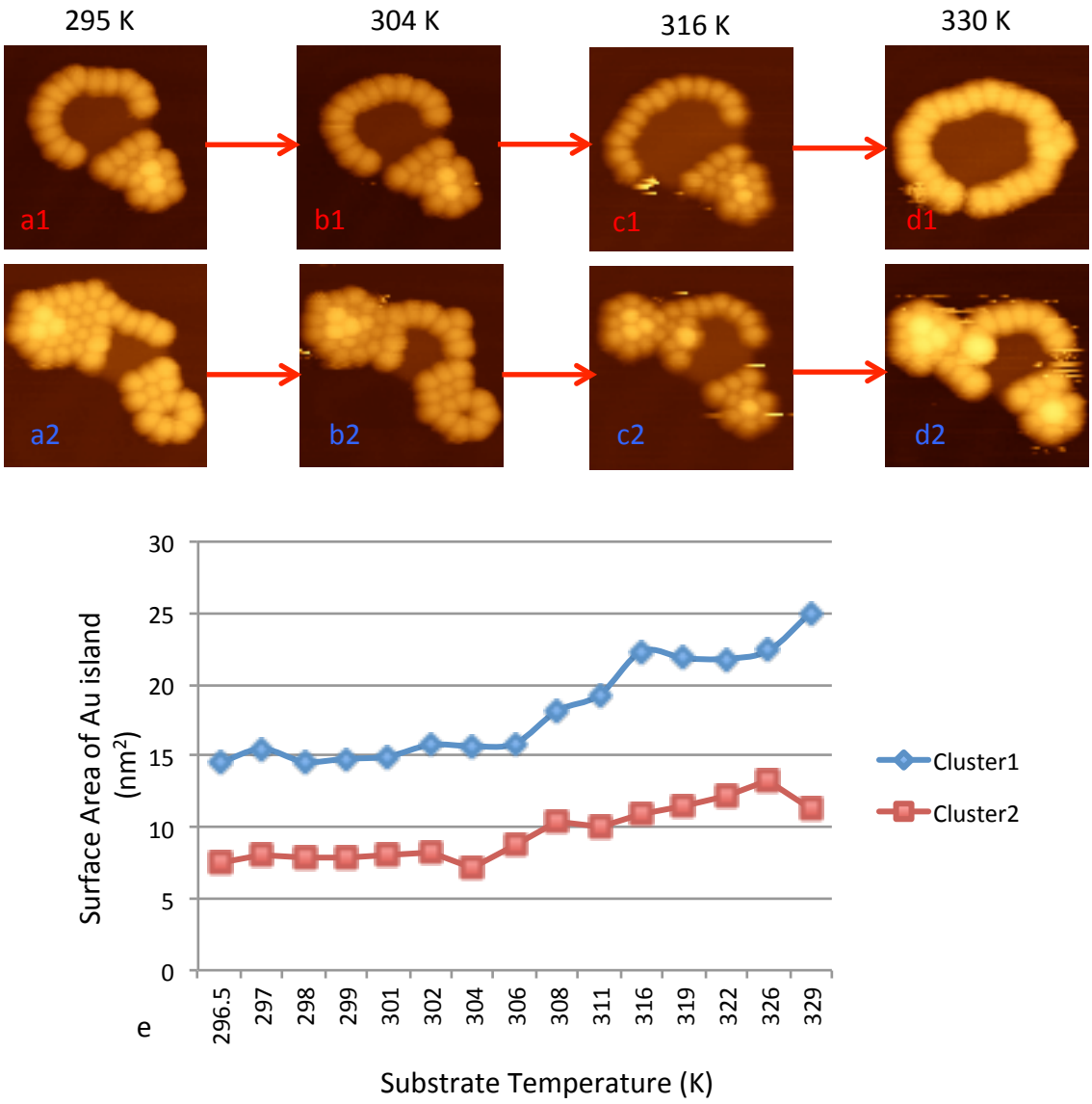

Figure 5.8 Surface area changes of two C_{60}/Au clusters with increasing substrate temperature from 295 K to 330 K. Surface areas of two big Au islands measured from STM images obtained at different substrate temperatures are plotted in e. Each line corresponds to one set of data for one cluster, the red line for the cluster1 in a1 - d1 and the blue line for the cluster2 in a2 - d2. The surface area of the Au island of cluster1 grows bigger at elevated temperatures. There is molecule detachment from both clusters and reorganization of the Au islands. The substrate temperature when each image was obtained is indicated on the top of the image.

At temperature up to 410 K, there is increasing proportion of large C_{60}/Au clusters on the substrate due to the decomposition of the small compact C_{60}/Au clusters. The openings at the edge of the Au island is supposed to be the place where incoming Au atoms are merged into the Au island. C_{60} molecules can also move around the Au island for the cluster to reorganize. The restructuring of the large cluster follows the process of Ostwald ripening [4].

5.2.3 Relocation of C_{60}/Au Clusters

As aforementioned at low temperature, Au clusters stay in the HCP regions of the pinched elbows and the FCC regions of the bulged elbows of the herringbone reconstruction. When the substrate temperature reached room temperature almost no Au clusters stay in the HCP regions at either type of elbows from the statistics of hundreds of STM images, which means that during the process of heating the sample from 115 K to 295 K, some C_{60}/ Au clusters with Au islands in the HCP regions move to a nearby location (FCC region) with a local minimum energy activated by increasing thermal kinetic energy. From the STM image in Figure 5.9a, rows of C_{60}/Au clusters can be clearly distinguished as marked by the white rectangles. The type of the elbows where C_{60}/Au clusters are anchored are written inside the rectangles. The brightness contrast of the STM image (Figure 5.9b) is adjusted to make the herringbone structures more clear. Among all the clusters in Figure 5.9b only three C_{60}/Au clusters have their Au clusters in the HCP regions at the pinched elbow as marked with circles. Other Au clusters at the pinched elbows stay in the FCC regions with the relocation of the Au clusters of these C_{60}/Au clusters from the HCP regions to the adjacent FCC regions over the discommensurate lines. One interesting observation is that two additional elbow

sites (highlighted by two squares in Figure 5.9b) form by the discommensurate lines free of surface dislocations. The pair of discommensurate lines has one line with dislocations at the elbow sites and the other one without dislocations. This phenomenon could be caused by the adsorption of C_{60}/Au clusters at the elbow sites, which induces the creation of new surface dislocations due to the change of surface strain.

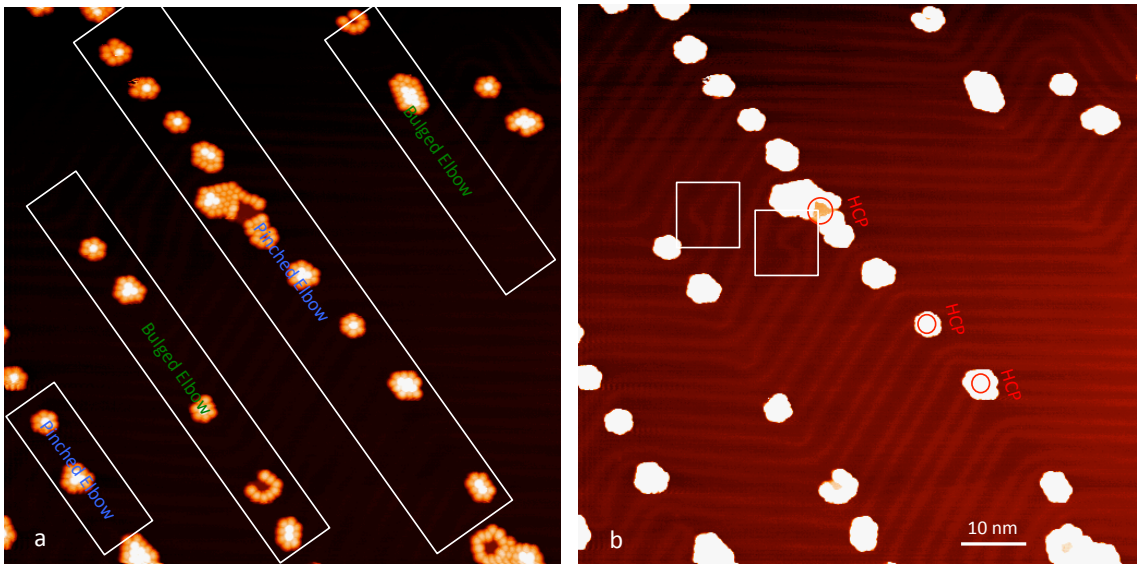

Figure 5.9 Relocation of Au islands of the C_{60}/Au clusters at the pinched elbows. The STM image obtained at room temperature. (a) The Au(111) substrate with rows of C_{60}/Au clusters at two types of elbow sites arranged in an alternative manner. (b) To make the herringbone structure more clear on the image, the brightness contrast is adjusted. Among all the C_{60}/Au clusters there are only three clusters that have their Au islands in the HCP regions of the pinched elbows as highlighted by three red circles. Two white squares highlight the two elbows formed by the discommensurate line free of surface dislocation.

The Au clusters prefer to stay in the FCC region to have the most compatible overlayer configuration for the stability of the clusters as a whole. The closed structure of the $(C_{60})_7(Au)_{19}$ cluster makes it stable on the substrate. This conclusion can be proved not only by the fact that it is the most popular structure on the substrate at room temperature, but also by the observation that the cluster can move slightly across the surface as a unit. In Figure 5.10, a series of STM images obtained at different substrate temperatures exhibit the movement of one cluster – the third from top, where white lines are used to indicate the relative positions of the clusters. In Figure 5.10a, obtained at the substrate temperature 313 K, the third cluster is at the left side of the white line. In Figure 5.10b and c, it moves to a new place so that one C_{60} molecule of the cluster is at the right side of the white line. At 322 K (Figure 5.10d) it has moved back to its original place. During imaging the third cluster is the only molecule that causes streaks on the images when the tip scans over the cluster.

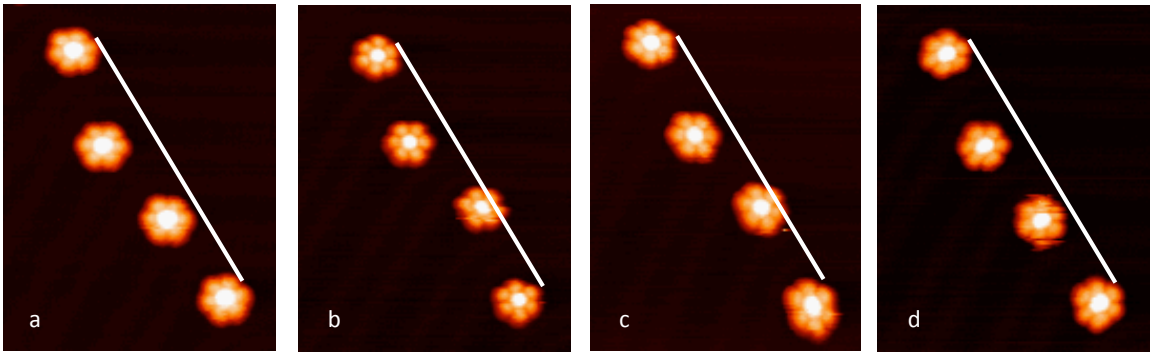

Figure 5.10 Movement of a C_{60}/Au cluster as a unit. The four STM images are obtained at the substrate temperature, from a to d, 313 K, 316 K, 319 K, and 322 K. The white line is the reference to mark the positions of the clusters. The third $(C_{60})_7(Au)_{19}$ cluster down slightly shifts its position to the right side of the white line in b and c and come back in d.

Because the limited resolution of the herringbone structures around the C_{60}/Au clusters it is hard to tell what the reason is behind the movement of the cluster. However, what can be concluded from this observation is the high stability and the strong internal binding strength of the $(C_{60})_7(Au)_{19}$ cluster as a unit.

5.3 Structural Evolution of the $(C_{60})_m(Au)_n$ Clusters at Elevated Temperatures

During the annealing process of the sample, the selection of stable clusters in particular structures and the evolution of the remaining clusters in metastable structures have been observed as the STM follows changes in the clusters continuously from room temperature to about 330 K. With the substrate temperature in the range 330 K to 410 K, the sample is heated to the desired temperature and kept at that temperature for about 1 hour, and STM imaging is taken after the sample is cooled down to room temperature.

5.3.1 Vanishing of the Open Structure

The compact $(C_{60})_7(Au)_{19}$ cluster has six molecules around the Au cluster in the centre. What if the step edge of a small Au cluster is not fully protected by C_{60} molecules? The disintegration of a $(C_{60})_6(Au)_n$ cluster is displayed in Figure 5.11 when increasing substrate temperature from room temperature 295 K to 304 K. In Figure 5.11 the cluster has one C_{60} molecule, imaged brightest, on top of the Au cluster and there are five C_{60} molecules, dimer than the centre molecule, around the Au cluster. These five C_{60} molecules are too few to entirely cover the step edges of the Au cluster and therefore there is a gap between two of them. The gap is observed to change its place around the Au cluster due to the movement of the five C_{60} molecules. The bonding of the carbons atoms of the C_{60} molecule to the Au atoms at the step edge of the Au cluster and the van der Waals interaction between

adjacent molecules are large enough to prevent the molecules to detach from the step edge, but not enough to prohibit the diffusion of the molecules around the step edge. It seems that adding one molecule to the five molecules at the circumference of the Au cluster is all that is needed to change this restless C_{60}/Au cluster to a compact cluster of relative high stability. When the substrate temperature reaches 304 K (the STM image at the right bottom of Figure 5.11), this cluster collapses and disappears from view. The scanning tip may impact on the disintegration of the cluster. However, the imaging parameter -1.8 V and 0.03 nA should not impose a large force on the cluster as the tip is farther from the sample surface compared with the imaging conditions for atom manipulation. The structure of this $(C_{60})_6(Au)_n$ is not stable in nature.

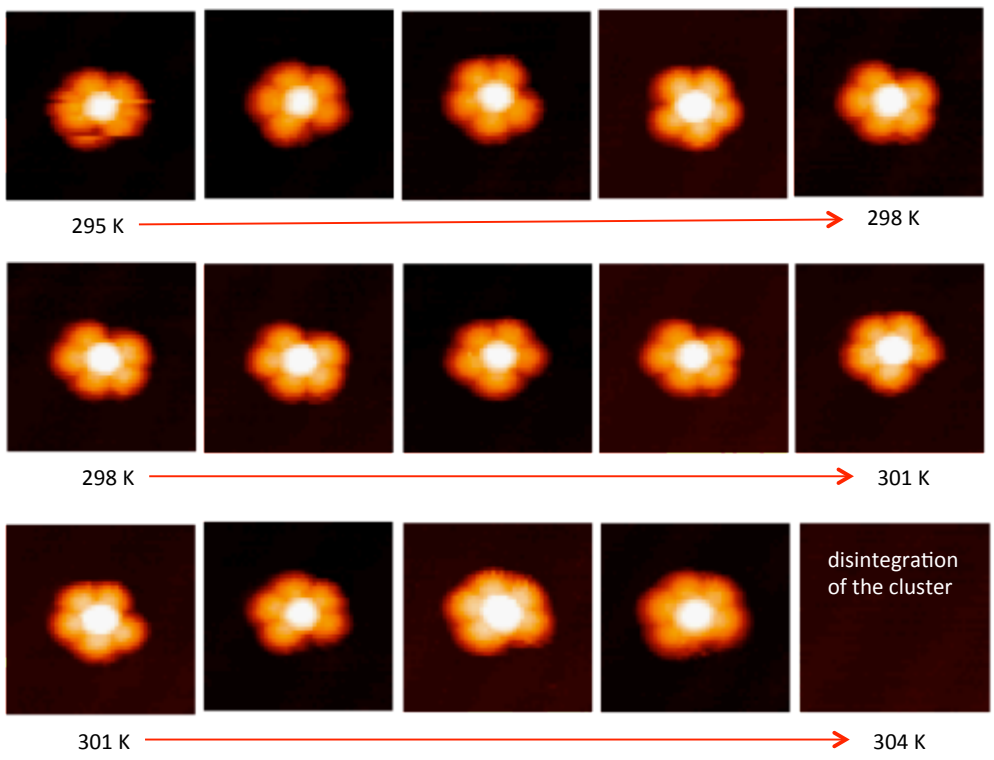

Figure 5.11 Series of STM images focusing on one C_{60}/Au cluster denoted $(C_{60})_6(Au)_n$. The substrate temperature is raised from 295 K (the top left image) to 204 K (the

bottom right image). The cluster has one bright C_{60} molecule on top of the Au cluster and five C_{60} molecules around the Au cluster. These five C_{60} molecules on the Au(111) substrate are not closely packed, and there is a gap between two of them leaving the step edge of the Au cluster not fully covered by molecules. This gap is seen moving around the Au cluster due to the movement of the five molecules at the circumference of the Au cluster. This cluster is not stable and at 304 K collapses disappearing completely from view.

For the $(C_{60})_7(Au)_{19}$ cluster the movement of C_{60} molecules around the Au cluster is not observed because of their compact configuration. The formation of the $(C_{60})_6(Au)_n$ cluster may be the result of a smaller Au cluster whose atom number n is less than 19, without enough room left at the step edge to accommodate one extra molecule.

5.3.2 Structural Reorganization from Unstable to Stable during Annealing

During the annealing process the reorganization of both C_{60} molecules and Au clusters have been observed. The resulting structures are the thermodynamically stable structures.

If one C_{60} molecule attaches to the compact $(C_{60})_7(Au)_{19}$ cluster, this extra molecule can move around the cluster as displayed in Figure 5.12. This cluster is denoted $(C_{60})_8(Au)_{19}$. The extra molecule can stay at any one of the six sites formed by two adjacent C_{60} molecules around the step edge of the Au cluster. At about 306 K, this molecule escapes from the cluster, leaving behind the compact and stable core – the $(C_{60})_7(Au)_{19}$ cluster.

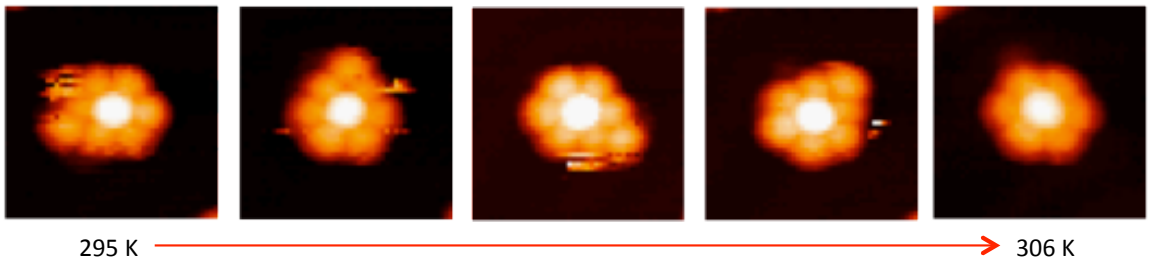

Figure 5.12 Detachment of one C_{60} molecule. Cluster shown in the first image at 295 K can be divided into a compact $(C_{60})_7(Au)_{19}$ cluster, plus one extra C_{60} molecule. This extra molecule is observed to wandering around the compact cluster until, at 306 K, it leaves the cluster.

Small thermal activation is enough to refine the structure of C_{60}/Au clusters in metastable state as is demonstrated in Figure 5.12. More dramatic changes of C_{60}/Au clusters have also been observed to demonstrate the evolution promoted by thermal activation. Figure 5.13 are ten STM images showing the response of three C_{60}/Au clusters, denoted A, B and C at the beginning, to thermal annealing. The cluster C at the bottom of the first STM image (Figure 5.13), which was obtained at 295 K, is the $(C_{60})_7(Au)_{19}$ cluster with little reaction to the thermal treatment at temperatures up to 330 K. The cluster A at the top of the first STM image in Figure 5.13 has a ring like structure with seven C_{60} molecules around an Au cluster. These seven C_{60} molecules stayed intact during imaging without changing their relative positions. At about 309 K one of the seven molecules managed to jump up to the top of the Au cluster and then a new $(C_{60})_7(Au)_{19}$ cluster formed on the substrate. A third cluster B is a large cluster that have five C_{60} molecules attached to a $(C_{60})_7(Au)_{19}$ cluster. These five molecules randomly wandered around the stable core – the $(C_{60})_7(Au)_{19}$ cluster – during imaging, and

at 309 K the five molecules left the stable core. When the substrate temperature reached 310 K, three $(C_{60})_7(Au)_{19}$ clusters existed on the surface in the same size, shape and composition.

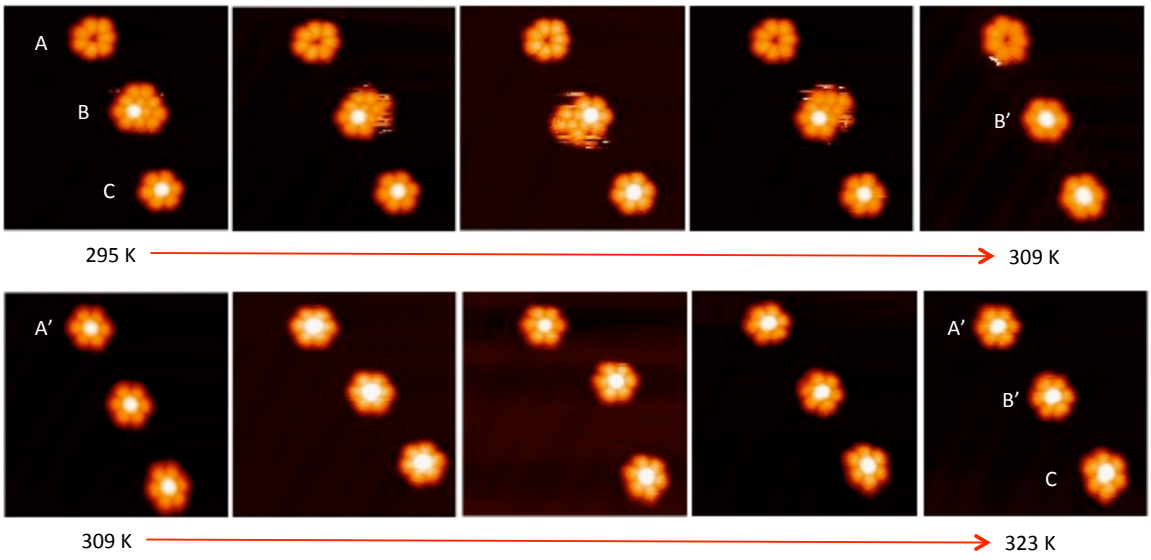

Figure 5.13 Series of STM images showing the response of three C_{60}/Au clusters to thermal annealing treatment. At first there were three clusters A, B, and C of different sizes and shapes. The cluster C in the first image is the $(C_{60})_7(Au)_{19}$ cluster which stayed intact during the whole process when the substrate temperature was raised from 295 K to 330 K (STM image not shown). The cluster A is in a ring like structure with seven molecules around an Au cluster. One of the seven molecules managed to jump up to the top of the Au cluster and formed a $(C_{60})_7(Au)_{19}$ cluster. A third cluster B at 295 K has five C_{60} molecules around the core – $(C_{60})_7(Au)_{19}$ cluster. These five molecules constantly wandered around the core until they were detached at 309 K. At last, in the image on the bottom right there are three $(C_{60})_7(Au)_{19}$ clusters on the surface in the same size, shape, and composition.

With increasing substrate temperatures, fewer and fewer $(C_{60})_7(Au)_{19}$ clusters existed on the surface, but they can survive on the Au(111) surface up to the temperature of about 410 K. Besides the detachment or reorganization of C_{60} molecules the restructuring of Au clusters also happened as shown in the next two figures (Figure 5.14 and Figure 5.15).

The first series of STM images (Figure 5.14) shows the process involving the detachment of both C_{60} molecules and Au atoms from the C_{60}/Au complex. The cluster in Figure 5.14a1 has nine C_{60} molecules around the Au cluster and one bright molecule on the top of the Au cluster. These molecules were not in the hexagonally close-packed structure. The surface area of the Au cluster is large enough to support one molecule but cannot accommodate two. Without forming a compact structure with its neighbouring molecules on the Au(111) substrate, the bright molecule was observed to hop back and forth during imaging, as seen in Figure 5.14b2 and b3. When the substrate temperature was 306 K one molecule that was around the Au cluster left the complex and at the same time some Au atoms escaped from the Au cluster. And the structure of the C_{60}/Au cluster (Figure 5.14b5) remaining on the substrate became more compact than it was at room temperature 295 K. When the substrate temperature reached 316 K a second molecule was detached (Figure 5.14c4) and the structure of the C_{60}/Au cluster changed to the combination of a $(C_{60})_7(Au)_{19}$ structure plus one C_{60} molecule (Figure 5.14c5) which is the same as the cluster in Figure 5.12. Up until 330 K the extra molecule still adhered to the compact $(C_{60})_7(Au)_{19}$ core. However, one possible prediction for the final structure of the cluster in Figure 5.14c5 is that of the stable $(C_{60})_7(Au)_{19}$ cluster.

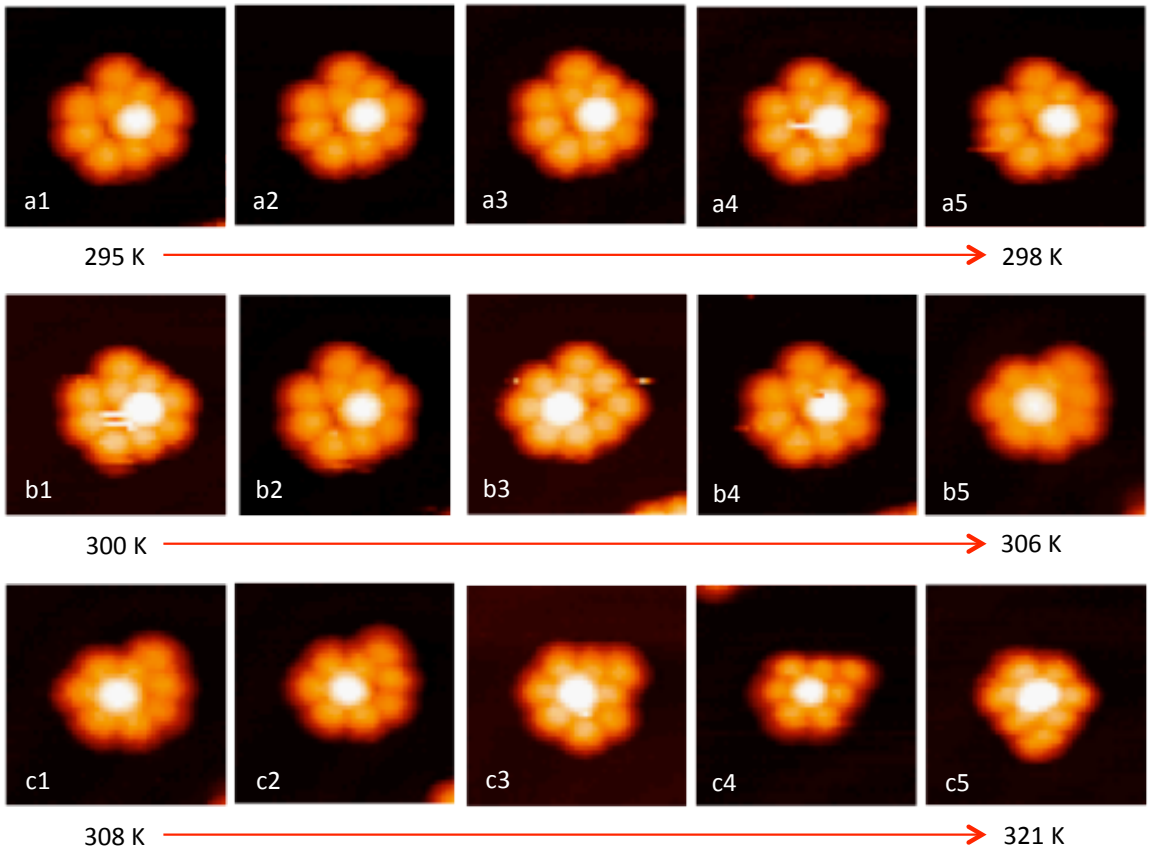

Figure 5.14 Series of STM images with increasing substrate temperatures from 295 K to 312 K. The Au cluster in the C_{60}/Au cluster gradually evolved to a small size. At 295 K a1, the step edge of the Au cluster is fully covered by C_{60} molecules but not in the hexagonally close-packed form. There are nine C_{60} molecules around the Au cluster and one bright molecule on the top of the Au cluster – labelled as $(C_{60})_{10}(Au)_n$. The bright molecule without forming close packed structure with neighbouring molecules on the Au(111) substrate was observed to hop back and forth during imaging b2 and b3. At 306 K one C_{60} molecule left the cluster simultaneously with the shrinkage of the Au cluster, and there remains eight molecules around the Au cluster. At 316 K c3 a similar process – detachment of both C_{60} molecule and Au atoms, happened to the C_{60}/Au cluster and the resulting cluster is labelled as $(C_{60})_7(Au)_{19}$ cluster plus one C_{60} molecule. Remaining cluster acted as what is shown in Figure 5.12.

If the Au cluster does not take on a stables structure due to the confinement by the attached C_{60} molecules on top of and around the Au cluster, thermal treatment can promote the transition from metastable structure to stable structure. The Au cluster in the large C_{60}/Au cluster in Figure 5.15 can support five C_{60} molecules. At room temperature the shape of the five bright molecules was near a polygon. At 306 K two C_{60} molecules that were marked by two red dots in Figure 5.15b2 were missing, which seemed to cause disturbance to the structure of the Au cluster. The cluster changed a lot in Figure 5.15c2, which was obtained five minutes after Figure 5.15b2 at the same substrate temperature. The C_{60} molecules that had been affected are marked by dots in different colours (Figure 5.15c2). In Figure 5.15c2 the red dots marks the place where two molecules was in the cluster but missing latter compared with Figure 5.15b2. The blue dots mark the two molecules that newly joint there, and the green dot is the molecule that was originally sitting on top of the Au cluster in Figure 5.15b2. The organization of the Au cluster changed from Figure 5.15b2 to Figure 5.15c2, and raised one molecule that was next to the molecule highlighted by the green dot (Figure 5.15c2).

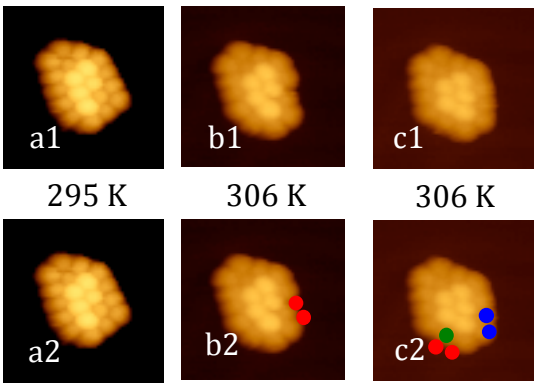

Figure 5.15 Rearrangement of both the Au cluster and the C_{60} molecule in the C_{60}/Au cluster. The second row of images a2 –c2 is the same as the first row a1 – c1 except that there are dots on the images to mark the reorganization of the molecules. By comparing the cluster in a1 and b1, we can see that two molecules marked by two red dots in b2 moved away from the cluster. From b1 to c1, two more molecules marked by two red dots in image c2 disappeared and two molecule marked by blue dots jointed the cluster. The green dot in c2 highlights the molecule that was originally on top of the Au cluster. The Au cluster reorganized and raised another molecule that was next to the green dot.

The shape of the new Au cluster in Figure 5.15c1 is a trapezoid seen from the couture of the raised C_{60} molecules. This is the common structure of Au clusters that can accommodate five C_{60} molecules on top, as observed from many images. The reorganization of the Au cluster is the result of a thermodynamic process to fulfil the energetic equilibrium minimum of the combined complex.

All the above observations emphasize the self-refining process of the C_{60}/Au clusters during the annealing treatment. The phenomenon shows the balance of the interactions between the C_{60} molecule and the Au atom, and the coherence between the C_{60}/Au complex and the Au(111) substrate.

5.4 The Importance of the Template - the Au(111) Substrate

The Au(111) substrate plays a vital role in the formation, the stability, and the size distribution of the clusters during the process of seeking the thermodynamic and kinetic equilibrium on the substrate.

5.4.1 Role in the Size Distribution of the Clusters

At low temperatures, clusters formed at the bulged site cannot be distinguished from those at the pinched site due to the kinetic confinement of the movement of the molecules and atoms. Both the size and shape of the C_{60}/Au clusters are irregular as can be seen from Figure 5.3. In great contrast to what has been observed at low temperature, at room temperature the morphology of the cluster changes to what is shown in Figure 5.16. Figure 5.16a is an STM image processed by unsharp mask, to make both the clusters and the herringbone structure clear. In Figure 5.16a the two types of elbow sites are distinguished by rectangles of different colours. The blue rectangles highlight the bulged elbow while the green rectangles mark the pinched elbows. There is a clear difference in the distribution of the C_{60}/Au clusters in size and shape at the two types of elbow sites. On one hand, at the bulged elbow nearly 100% of the clusters there are compact $(C_{60})_7(Au)_{19}$ clusters. On the other hand, the pinched elbow sites lead to the formation of C_{60}/Au clusters of larger size and irregular shape. A clear view (images without unsharp mask processing) of the clusters in the first two rows in Figure 5.16a is shown below Figure 5.16b.

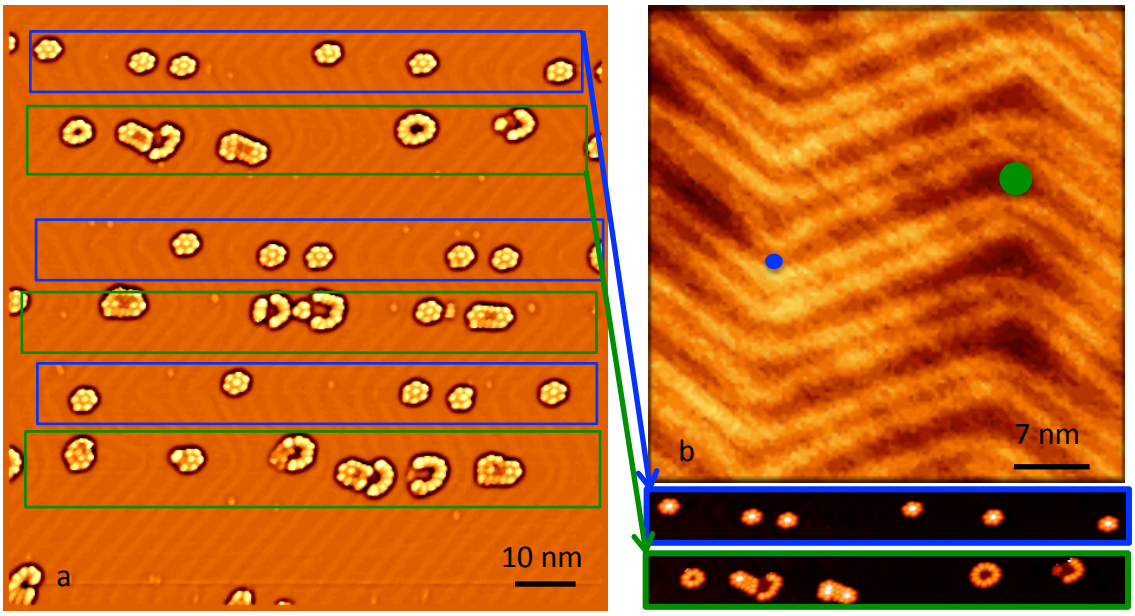

Figure 5.16 STM image showing the distribution of the C_{60}/Au clusters in size and shape at the two types of elbow sites. The image is processed by the function of unsharp mask to show both the clusters and the herringbone structure clearly. (a) Rectangles in two colours each mark one type of elbow site. The blue rectangles highlight the rows of bulged elbow sites, and the green rectangles single out the pinched elbows. A clear view (without unsharp mask processing) of the clusters at the two types of elbows is shown below image b. The clusters staying at the bulged elbows are all the compact $(C_{60})_7(Au)_{19}$ clusters while the other clusters at the pinched elbows have larger sizes and irregular shapes. (b) A STM image of Au(111) with the herringbone reconstruction. The blue dot indicates the area of the FCC region at the bulged elbow. The green dot at the pinched elbow shows that the area of the FCC regions is larger than that at the pinched elbow, formed by the same two DLs.

What is the possible reason behind the observed distribution? The sizes of the Au clusters decide the sizes of the C_{60}/Au complex because they are the anchors for

C_{60} molecules and they also pin the clusters during the ripening process from low to room temperature. As the majority of Au clusters stay in the FCC regions at the elbows, the difference in the area of the FCC regions at the bulged elbow and the pinched elbow (Figure 5.15b) possibly contributes to the final evolution of the clusters from the meta-equilibrium state at low temperatures to the equilibrium state at room temperature. The two dots in Figure 5.15b indicate the size of FCC regions at the two types of elbow sites. The area of the FCC region at the bulged elbow is obviously smaller than that at the pinched elbow. Therefore, the Au clusters are confined to smaller sizes at the bulged elbows than those at the pinched elbows, especially during the time when the structures of clusters evolve at elevated temperatures. At the stage when the C_{60}/Au clusters ripen due to thermal activation, the properties of the elbow sites are one of the key factors leading to the formation of the well defined structures.

5.4.2 Role in the Stability of the Clusters

The stability of a C_{60}/Au cluster is determined by many factors including its size, structure, and its local environment, i.e., the type of the elbow site where the cluster is attached. During annealing treatment to the sample at a temperature above room temperature, the clusters at the bulged sites exhibit less stability than those at the pinched elbow as demonstrated in Figure 5.17 of four STM images obtained sequentially at temperatures from 295 K to 333 K. The specific substrate temperature during imaging is written on the respective image. Due to the thermal drift at changing substrate temperatures, the scanning range on the sample is not exactly the same, but from the four images shown in Figure 5.17 the vanishing of some C_{60}/Au clusters from the surface can be seen. In Figure 5.17a the C_{60}/Au

clusters are aligned in three rows as grouped by three rectangles. The blue rectangle marks the clusters at the bulged elbows and the two green rectangles the clusters at the pinched elbows.

At room temperature, 295 K (Figure 5.17a) the clusters at the bulged elbows take on three structures – the compact $(C_{60})_7(Au)_{19}$ structure, the structure of the $(C_{60})_7(Au)_{19}$ cluster plus one C_{60} molecule, and the structure of a large cluster with three molecules on top of and nine molecules around an Au cluster. The other clusters at the pinched elbows have various structures besides the structure defined by the compact $(C_{60})_7(Au)_{19}$ cluster and two of the clusters are anchored by two Au islands. When the substrate temperature reached 310 K and the scanning conditions became stable with only a little thermal drift, we found that the two clusters were missing from the scanning range as indicated in Figure 5.17b, and the positions of the two missing clusters are marked by two white dots. At 316 K, another two clusters disassembled from the bulged elbow sites (Figure 5.17c). A fifth cluster had disappeared from the view of STM at 333 K in Figure 5.17d.

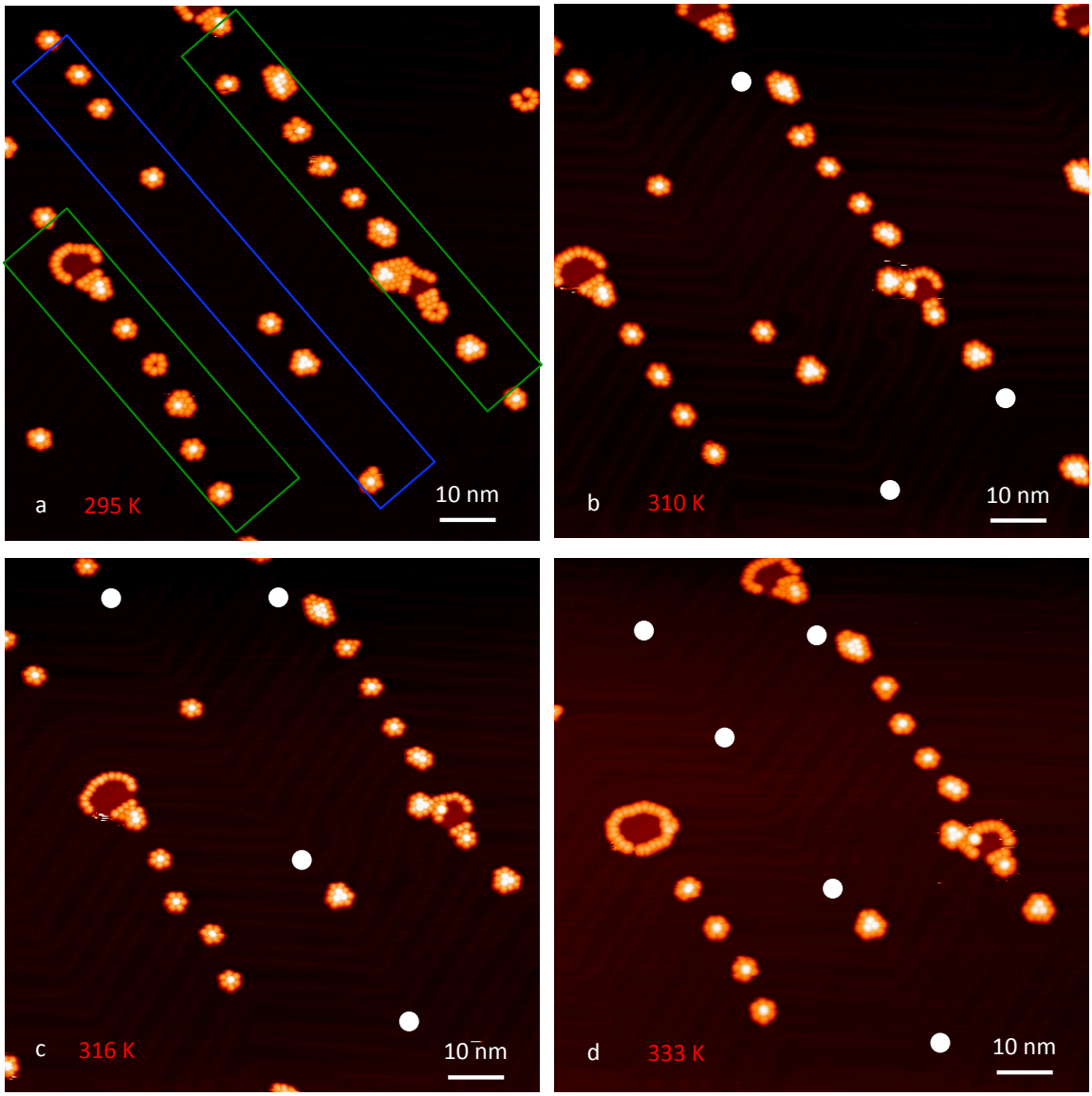

Figure 5.17 Series of STM images obtained on the same area at increasing substrate temperature. The temperature of the substrate when the image was taken is indicated on each image. All the images include three rows of clusters that stay at two types of elbow sites on the Au(111) substrate. (a) The blue rectangle marks the row of clusters at the bulged elbow sites and the two green rectangles indicate the clusters at the pinched elbow. As the substrate temperature increases, the numbers of clusters at both elbows decrease. The large portion of the disappeared clusters was originally fixed at the bulged elbow sites by comparing the images obtained at 295 K a and 333 K d. At 333 K only one large C_{60}/Au cluster with three bright C_{60} molecules

on top of the Au cluster and nine C_{60} molecules around the Au cluster survived at the bulged elbow site.

Compared with Figure 5.17a obtained at 295 K, Figure 5.17d obtained at 333 K gives a clear contrast in the numbers of clusters at the bulged elbows, fewer clusters remaining there except one cluster that has a large Au island to support three C_{60} molecules and nine molecules protect the edge of the Au island. A close look at the clusters at the pinched elbows discloses the structural rectification of the clusters during the annealing process from 295 K to 333 K. There are new compact $(C_{60})_7(Au)_{19}$ clusters emerging at the pinched elbows in Figure 5.17d, which are transferred from C_{60}/Au clusters in metastable structures. And the shape of the Au clusters of the large clusters gradually evolved to shapes with rounded edges.

When the substrate temperature reaches about 356 K, almost no clusters can hold to their positions at the bulged elbows. Figure 5.18 is obtained at 356 K. The brightness contrast of the image is adjusted to show the herringbone clearly. These blue rectangles highlight the bulged elbows, which are nearly clear of any C_{60}/Au clusters. In contrast, the pinched elbows can still anchor large numbers of clusters. At this stage the C_{60}/Au clusters need to be either large with C_{60} molecules protecting the Au cluster edge or compact with C_{60} molecules fully enclosing the Au cluster.

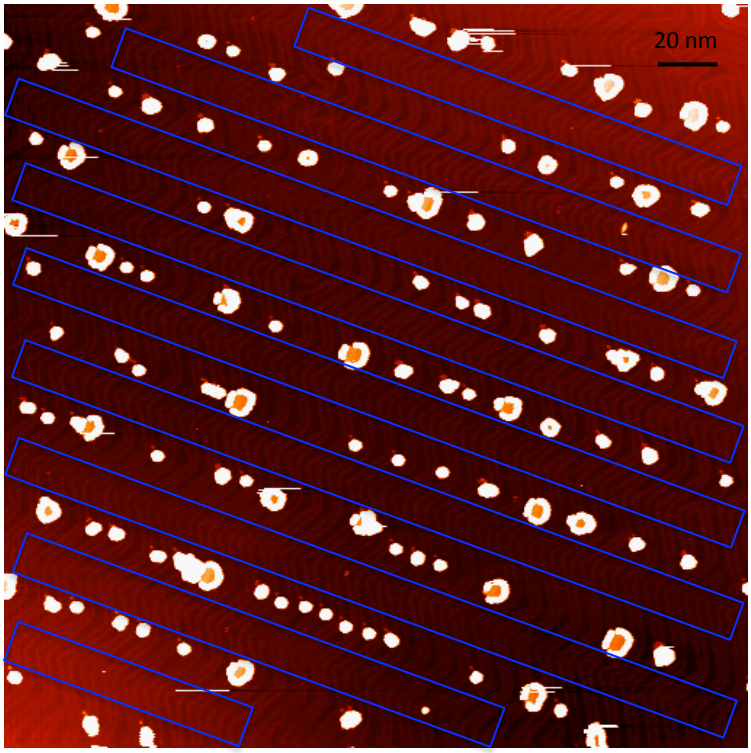

Figure 5.18 STM image obtained at substrate temperature 356 K. Due to brightness contrast, the detailed structures of the clusters are not clear, but the herringbone is distinct. The blue rectangles mark the bulged elbows where C_{60}/Au clusters hardly exist. In contrast, the pinched elbows can still anchor the clusters there.

We want to ascertain the highest temperature at which the compact and stable $(C_{60})_7(Au)_{19}$ cluster are completely removed from the Au(111) substrate. The sample was heated to 410 K when, after checking several areas of the surface, no $(C_{60})_7(Au)_{19}$ cluster could be found. The decomposition of the $(C_{60})_7(Au)_{19}$ cluster is a gradual process, due to the variation in stability originating in how they integrate with the substrate, even though they may adapt similar physical structures within the clusters. The complexity of this process needs more experiments as well as theoretical calculations to achieve a good understanding of the factors behind it.

5.5 Other Self-Defined Structures

The stable C_{60}/Au clusters on Au (111) form partly due to the tendency of close packing of both Au atoms and C_{60} molecules within the clusters. With the amount of Au atoms – about 0.029 ML, the majority of the C_{60}/Au clusters take on the structure of the $(C_{60})_7(Au)_{19}$ cluster, which is the smallest compact structure on the substrate. Due to the irregular configuration of the elbow sites of the herringbone structure in some areas, the sizes of Au clusters vary dependent on the density of the elbow sites around them. In addition to the $(C_{60})_7(Au)_{19}$ cluster, other compact clusters as seen in Figure 5.19 also form on the substrate with larger Au clusters to support more C_{60} molecules, the number of which ranges from two to eight. The interesting feature of these compact clusters is their unique structure. When the number of bright C_{60} molecules on top of the Au clusters is less than five, from STM observation the general structure is certain (Figure 5.19a – d) with only one row of C_{60} molecules protect each step edge of the Au cluster and all the molecules closely packed. If five C_{60} molecules sit on top of an Au cluster, the shape of the Au cluster can be arranged into the shape of a triangle (Figure 5.19e) or a parallelogram (Figure 5.19f) seen from the contours of the group of C_{60} molecule. Seven C_{60} molecules are organized into a hexagon beneath which the Au cluster should take on a shape close to a hexagon (Figure 5.19g). One additional molecule can be added to the seven bright C_{60} molecules in Figure 5.19g and the resulting shape of the cluster is as shown in Figure 5.19h.

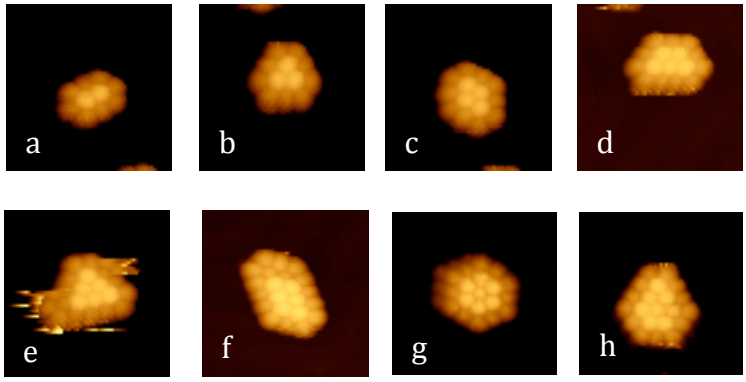

Figure 5.19 Zoom-in STM images of compact C_{60}/Au clusters that coexisted with the commonly observed $(C_{60})_7(Au)_{19}$ cluster. The size of the Au cluster for each C_{60}/Au cluster increases from two to eight one by one as the number of C_{60} molecules supported on the Au cluster increases.

Based on the model for the $(C_{60})_7(Au)_{19}$ cluster, the structures for the larger C_{60}/Au clusters above in Figure 5.19 can be easily obtained as demonstrated in Figure 5.20.

Similar to the description of the ball model in Figure 5.5b, Figure 5.20 only indicates the structures of the Au clusters and the adsorption sites for each C_{60} molecules, which are eliminated to show the structures of the Au clusters clearly. In the four ball models (Figure 5.20), all the C_{60} molecules on top of the Au clusters are at the top site over an Au atom (the red ball in the centre of the Au atoms in yellow) while the rest molecules around the Au clusters are sitting at the hollow site (the site within three Au atoms, in red, of the Au substrate), all with a hexagonal ring facing parallel to the Au(111) substrate.

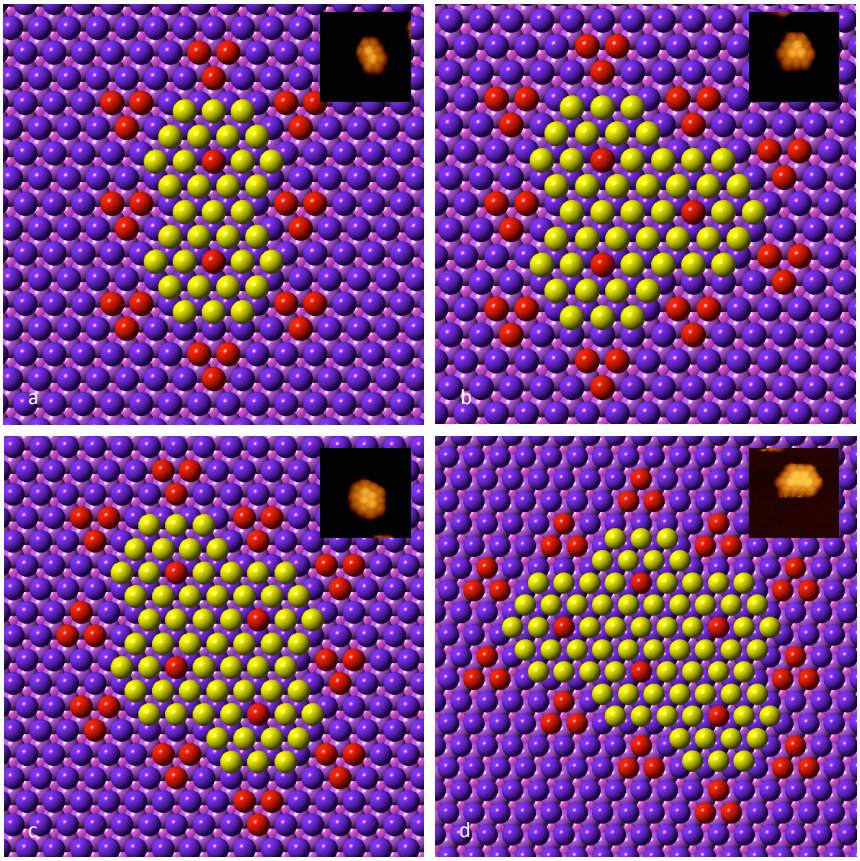

Figure 5.20 Ball model for Au clusters that are covered by C_{60} molecules (not shown in the model). The structures of the Au clusters from a – d correspond to the C_{60}/Au clusters whose images are attached to the right upper corner of each model. The $(C_{60})_m(Au)_n$ denotations for each cluster a – d are $(C_{60})_{10}(Au)_{35}$, $(C_{60})_{12}(Au)_{49}$, $(C_{60})_{14}(Au)_{63}$ and $(C_{60})_{16}(Au)_{77}$, respectively. The yellow balls and the red balls encompassed by the yellow balls are Au atoms forming the Au clusters. The background Au atoms in the (111) surface are in purple except the Au atoms in groups of three in the red colour, which are used to indicate the adsorption sites of C_{60} molecules on Au(111).

The proposed models for the observed C_{60}/Au clusters have merit in the geometric configurations of the molecules and the Au atoms, considering their dimensions, the preferred adsorption sites of C_{60} on Au(111), and the range of interaction

between molecules and atoms. The pattern of C_{60} molecules within the clusters can be unambiguously resolved by STM. For one type of C_{60}/Au cluster, there can be more than one structure of the Au cluster. However, the structure of the Au cluster we introduced could be the primary structure among all the possible arrangements of Au atoms underneath the molecule(s).

The C_{60} molecule is free of ligands for directional bonding, but the C_{60}/Au clusters can still take on certain compact structures as described above and one reason for this tendency is that both Au atoms and C_{60} molecules incline to form close-packed structures of high stability with optimized coordination between the two components. If the two components are separated and placed on the Au(111) substrate, they cannot stay at the elbow sites at temperatures above room temperatures. Thermal stability of the bi-component clusters is justified by molecule-atom and cluster-substrate interactions.

References

[1] N. Néel, J Kröger, and R. Berndt. Highly Periodic Fullerene Nanomesh. Adv. Mater. **18**, 174 (2006).
[2] L. Wang and H. Cheng. Density Functional Study of the Adsorption of a C_{60} Monolayer on Ag(111) and Au(111) Surfaces. Phys. Rev. B **69**, 165417 (2004).
[3] I. Hamada and M. Tsukada. Adsorption of C_{60} on Au(111) Revisted: A van der Waals Density Functional Study. Phys. Rev. B **83**, 245437 (2011).
[4] K. W. Kolasinski, Surface Science foundations of Catalysis and Nanoscience Second Edition, John Wiley & Sons, England (2008).

Chapter 6: Summary and Future Work

6.1 Summary

This thesis gives a detailed account of the study of the interface between the C_{60} monolayer and the Au(111) substrate, and the self-assembled structures of Au/C_{60} complex supported on the Au(111) substrate.

The change of the herringbone reconstruction upon adsorption of C_{60} makes the experimental investigation more complicated. We predict the molecule configurations in the overlayer through a pure geometric view of commensurism that is lattice registry between the overlayer and the substrate. Although consideration of the energetic optimisation and of the characterization of detailed structure are missing, the geometric modelling offers a possible explanation of the relative structures of the C_{60} overlayer on the Au(111) substrate. The various superstructures of dim C_{60} molecules within the close packed layer indicate complex interfacial structures between the two. Following the STM observations of the C_{60} monolayer on Au(111), Au atoms are used as a probe to explore the interfacial properties of C_{60}/Au. Their diffusion behaviour within constraint of kinetic energy, and the nano-structures at the interface, indirectly give information on the different binding strength among the ordinary and dim C_{60} molecules in various phases of the C_{60} layer. The stress exerted at both the Au substrate and the C_{60} overlayer makes the porous nano-structures – the honeycomb and the linear structures – of Au islands at the interface, exhibiting short-range orders. The study is important in the investigation of nanoscale devices or electronics involving the

interface properties. Other surface science techniques are needed to further explore the detailed interface structure of the C_{60} layer on Au(111).

The second part of the work concerns the self assembled nano-structures of C_{60}/Au clusters supported on the Au(111) substrate fabricated by sequential deposition of Au atoms and C_{60} molecules at low substrate temperatures, when both elements on the cold substrate can be confined at the elbow sites of the herringbone which is the unique feature of the clean Au(111) surface. The characteristics of the C_{60}/Au clusters including their size, shape and compositions are thoroughly studied at changing kinetic energies of the system by varying the substrate temperature from 110 K to about 410 K. One particular nanocluster consisting of six C_{60} molecules around an Au cluster and one C_{60} molecule on top of the Au cluster – denoted $(C_{60})_7(Au)_{19}$ cluster – existed abundantly on the substrate at the elbow sites, forming well-ordered arrays of nanoclusters of uniform size and shape. A model is proposed for the $(C_{60})_7(Au)_{19}$ cluster with the Au_{19} cluster of single Au layer high in a hexagonal shape, one C_{60} molecule on the top of the Au_{19} cluster and six other around it. The model is based on the existing knowledge of the bond length between a carbon atom and a Au atom, the physical and chemical structure of the C_{60} molecule.

During the ripening process at temperatures above room temperature (~ 295 K), the disassembling of some metastable structures, and the evolution of the metastable structures to one specific nano-structure of the $(C_{60})_7(Au)_{19}$ cluster reveal the intrinsic stability of the $(C_{60})_7(Au)_{19}$ cluster with the optimized coordination between the molecules and the Au atoms in the close-shell structure.

Large C_{60}/Au clusters, the Au clusters of which are large enough to be visible under STM observation, also experienced changes of size and shape due to thermal activation at elevated temperature.

The importance of the herringbone reconstruction is emphasized in the last part of Chapter 5. At an early stage during the formation of C_{60}/Au clusters, the elbow sites confine the movements of the molecules and the Au atoms there. During the ripening process, the elbow sites play the role, besides stabilizing, of regulating the organization of the clusters, as the discommensurate lines can impact the transportation of the molecules and atoms moving across the surface. At low temperature, the DLs are like walls of potential well so that the atoms and molecules inside can only move inside the well.

6.2 Future Plan

Further experiments as well as theoretical calculations are necessary for more information concerning the self-assembled structures of C_{60}/Au clusters presented in this thesis. The electronic structures of each the seven C_{60} molecules in the $(C_{60})_7(Au)_{19}$ cluster are important, as their changes compared to pristine C_{60} molecules in bulk reveal the interaction between the molecules and the Au atoms via charge transfer, which is the binding pathway for the C_{60} monolayer on Au(111). Scanning tunnelling spectroscopy (STS) is a useful tool to study the electronic structures of an individual atom or molecule. The experiment needs to be carried out at low temperatures in order to freeze the rotational motion of the C_{60} molecule and to insure a stable tunnelling junction during data acquisition. Theoretical calculations based on STM observations (and STS measurements) can

provide insight into the forces or energies that act during the formation of the bi-component C_{60}/Au clusters.

The fabrication of the C_{60}/Au cluster of one size and structure may be possible via proper choice of deposition methods such as size selected cluster source, which can produce a uniform size distribution of Au clusters on the substrate at low temperatures. Which size of the C_{60}/Au clusters is abundant on the substrate can be tuned by changing the Au cluster sizes. Some large and compact C_{60}/Au clusters, for example the $(C_{60})_{10}(Au)_{35}$ cluster that has two C_{60} molecules on top of the Au cluster, can also widely exist on the Au(111) substrate if, at the beginning, the size of the Au clusters is large enough (about 35 atoms). The nano-template can also be tuned to guide more ordered growth of nanostructures [1, 2].

Self-assembly of bi-component clusters is a promising research subject as they can be used to design and fabricate nano devices on surfaces. By changing the components of the cluster various structures may be produced and the physical, chemical and electronic features of each element or the cluster can be modified according to the needs of the actual application.

References

[1] H. Brune, M. Giovannini, K. Bromann, and K. Kern. Self-Organized Growth of Nanostructure Arrays on Strain-Relief Patterns. Nature **394**, 451 (1998).
[2] M. Corso, L. Fernández, F. Schiller, and J. E. Ortega. Au(111)- Based Nanotemplates by Gd Alloying. ACS Nano. **4**, 1603 (2010).

Appendix

I. Formation of Pt Oxide in Two Phases Supported on Au(111): A Low Oxygen Pressure STM Study

The metal Pt is of great scientific, technological and industrial interest for its vital role in catalysing many chemical reactions [i, ii, iii]. Many experiments concerning the formation of Pt oxide have been carried out on various crystallographic surfaces of Pt crystal, where the step is found to be the preferential adsorption and reaction site for Pt oxide [iii, iv]. In our study, we deposit oxygen and Pt atoms at the same time on the inert Au(111) surface, in order to study the formation of Pt oxide by STM. An STM experiment [v] has revealed the formation of Pt/Au alloy via replacing Au atoms with Pt atoms in the Au substrate, and the increased Pt reactivity with assistance from the Au substrate. The replacement of Au atoms by Pt atoms is possible as Pt and Au are adjacent metals in the periodic table, and their atomic diameters are very close to each other.

I.1 Oxygen Dosing through A Hot Pt Tube on Au(111)

We designed an oxygen deposition device as shown in Figure I.1, and mount it on the UHV STM chamber. A thin Pt tube of diameter 4 mm is welded to a flange, and connected to a copper rod through Pt wire to form a circuit for heating. A disk with a small circular opening in the centre is placed in front of the tube, as shown in Figure I.1 to confine the deposition angle. A leak valve precisely controls the oxygen pressure. The oxygen gas of 99.999% purity is from Argo.

During oxygen deposition, the outlet of the Pt tube is heated by direct current to about 1300 K while oxygen gas flows through the Pt tube. The oxygen pressure in the UHV chamber is in the range from 2.0×10^{-8} mbar to 2.0×10^{-6} mbar and the deposition time is 2 minutes. A clean Au sample is placed at the manipulator inside the UHV chamber, facing directly towards the oxygen source during dosing. After oxygen dosing the sample is immediately transferred to the STM stage for imaging.

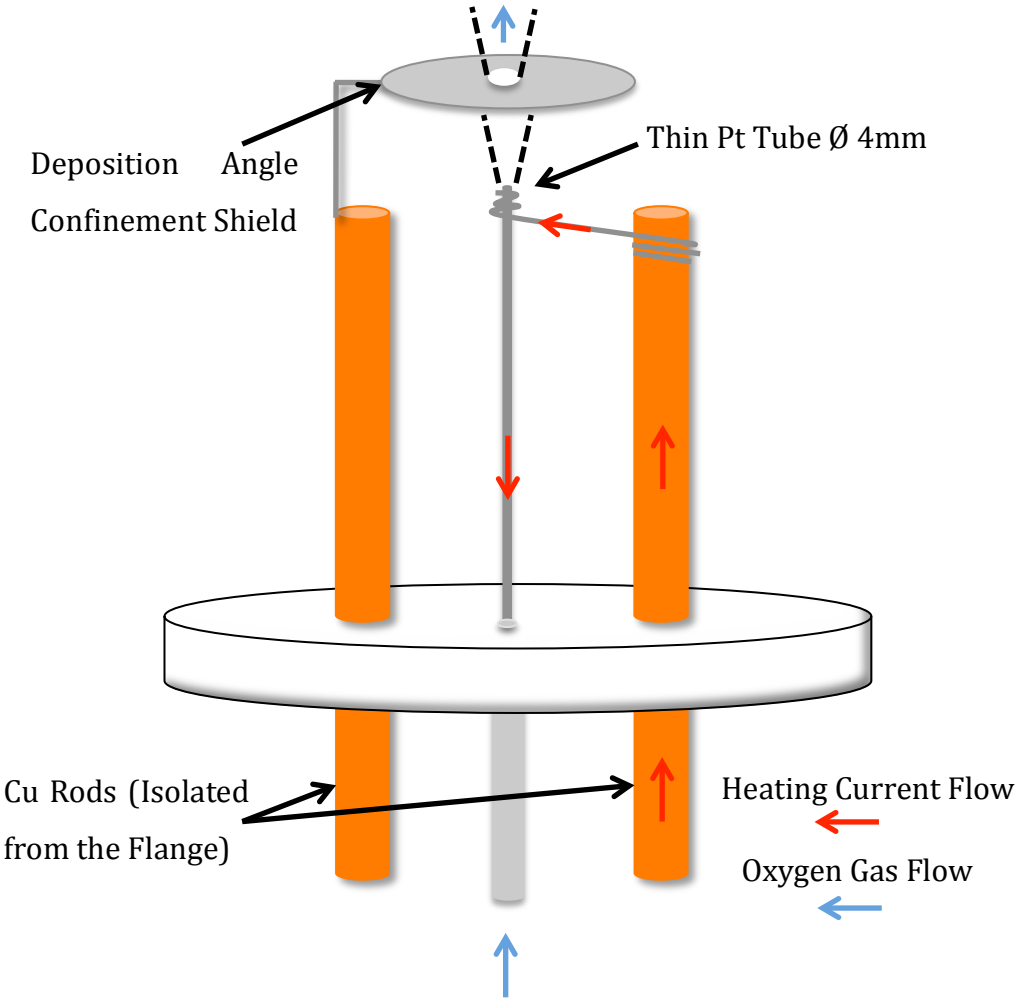

Figure I.1 Schematic Diagram of the oxygen dosing device. A Pt tube of diameter 4 mm is welded to the flange with two copper rods (isolated from the flange). The Pt tube is connected with one copper rod through thin thread of Pt wires. The other copper rod is used to fix a shield to confine the dosing angle. During oxygen dosing, a direct current passes through the Pt tube to heat the tube to about 1300 K while oxygen gas flows through the Pt tube. The whole setup is mounted on the UHV chamber.

I.2 The Pt oxide on Au(111)

At pressure 2.0×10^{-8} mbar, after oxygen dosing through the Pt tube heated at about 1300 K for two minutes, the surface morphology of the sample is as shown in Figure I.2. An overview of the Au surface (Figure I.2a) shows that bright islands form on Au terraces and the Au step edges become rough. From the heights of these small and isolated islands, we can characterise them as either Au islands or

Pt/Au islands with small fractions of Pt atoms. A closer look at the Au surface reveals the existence of bright dots (Figure I.2b). We do not succeed in obtaining atomic resolution of both the bright dots and the Au(111) surface. However, from zoom-in STM images, the bright dots are about 0.3 Å higher than the Au surface. According to the observations of Pedersen et al. [v], these bright dots are Pt atoms. And the formation of the small islands of Au or of a mixture of Au atoms and Pt atoms is due to the substitutional alloying of Pt atoms in the Au surface layer. Besides the Au islands and Pt atoms, there are also small amounts of some amorphous substances attached to Au step edges or on the top of these small Au islands. These amorphous substances inhibit the diffusion of Au atoms leading to the formation of the roughened Au step edges and irregular shapes of the small Au islands on the Au(111) terraces.

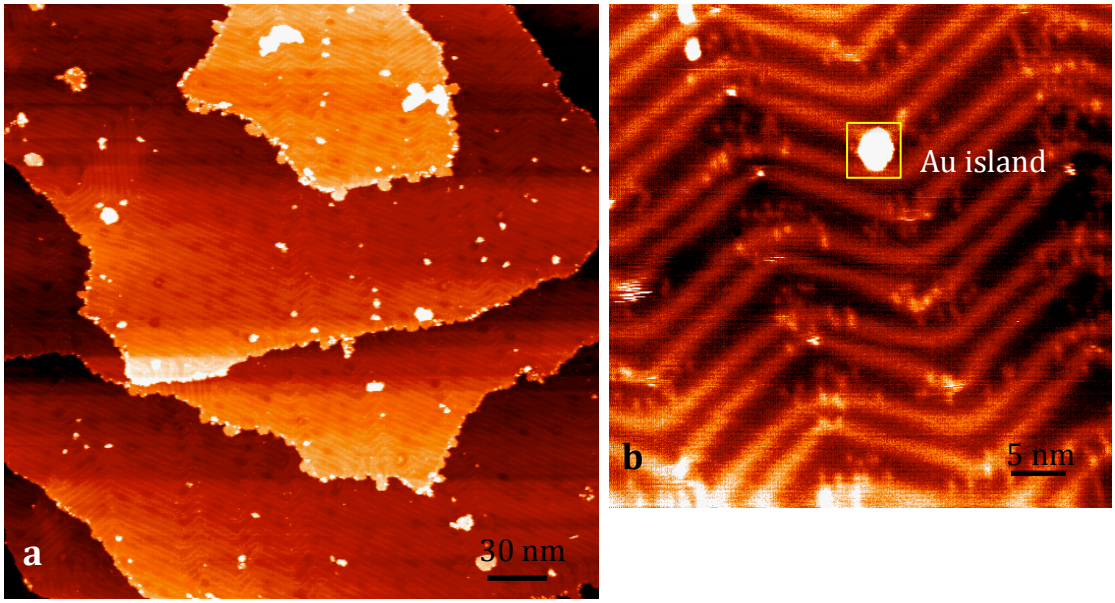

Figure I.2 Oxygen dosing through a hot (1300 K) Pt tube at 2.0×10^{-8} mbar. (a) Large area of the sample surface after oxygen dosing. Small Au islands form on Au terraces, and Au step edges become roughened. (b) Zoom-in STM image shows bright dots on the Au(111) surface.

We increase the oxygen pressure, keeping the vacuum in the STM chamber at 6.0×10^{-7} mbar during dosing. New complexes and features appear on the Au(111) substrate as seen in Figure I.3. There are mainly three types of complexes formed on the Au(111) substrate after the oxygen/Pt deposition, and a majority of them

stay in the FCC regions. A large portion of the new substances is amorphous (as highlighted by the green square in Figure I.3), and may be a mixture of metals (Pt, Au) and metal oxides, as their heights are usually larger than the height of single layer Au. We also observe clusters of some complex roughly in the shape of a sphere as shown in the inset of Figure I.3. They don't have directional bonding, and just randomly gather together. The most interesting feature is a linear structure highlighted by the blue rectangle in Figure I.3. Only a small amount of this type of linear structure exists in such oxygen dosing conditions.

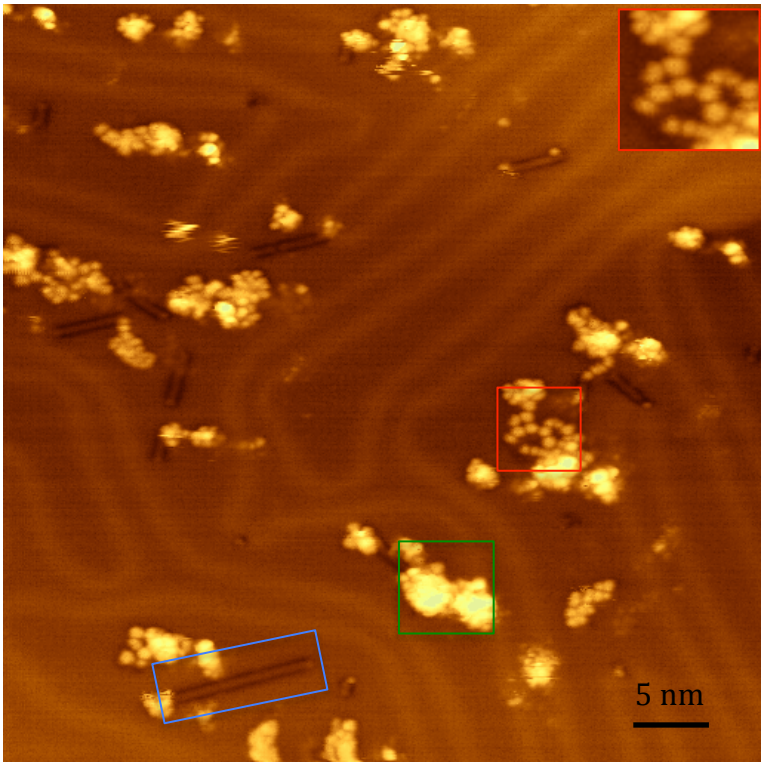

Figure I.3 Oxygen dosing through a hot Pt tube at pressure 6.0×10^{-7} mbar. Three types of substances form on Au(111).

In order to obtain more linear structures, we increase the partial pressure of oxygen, so that the vacuum pressure is 2.0 ×10^{-6} mbar during oxygen dosing. The temperature of the Pt tube and the dosing time is constant through out these experiments. The surface morphology of the sample is shown in Figure I.4a, and the existence of Pt oxide changes the patterns of the herringbone reconstruction, i.e., the FCC area in between two discommensurate lines (Figure I.4b).

All the complexes in linear structure are in the FCC regions, and align with the close packing directions $\langle 1\bar{1}0 \rangle$ of Au(111) as indicated in Figure I.4b. A height profile along the line AB in Figure I.4b indicates that the height of the linear structure on Au(111) is 0.056 nm. A similar linear structure is also observed for oxygen dosing on Pt(557) (Figure I.4d [iv]). Making comparison to the Pt oxide observed by Zhu et al., and because of the fact that no such linear structure has been observed if there is no oxygen passing through the hot Pt tube, we ascribe the substances in the linear structure (Figure I.4c) to 1D Pt oxide. The average separation of the brightness maxima along the linear structure is about 0.29 nm, close to that of 0.25 nm measured by Zhu et al. [iv]. The Pt oxide in linear structure vanishes from the surface after a few hours, and only the amorphous oxide remains.

The height of the amorphous complex (Figure I.4e) is 0.161 nm, lower than that of single layer Au, 0.235 nm. There is no fixed value for the height of the amorphous complexes, and they may be a 2D surface phase of Pt oxide.

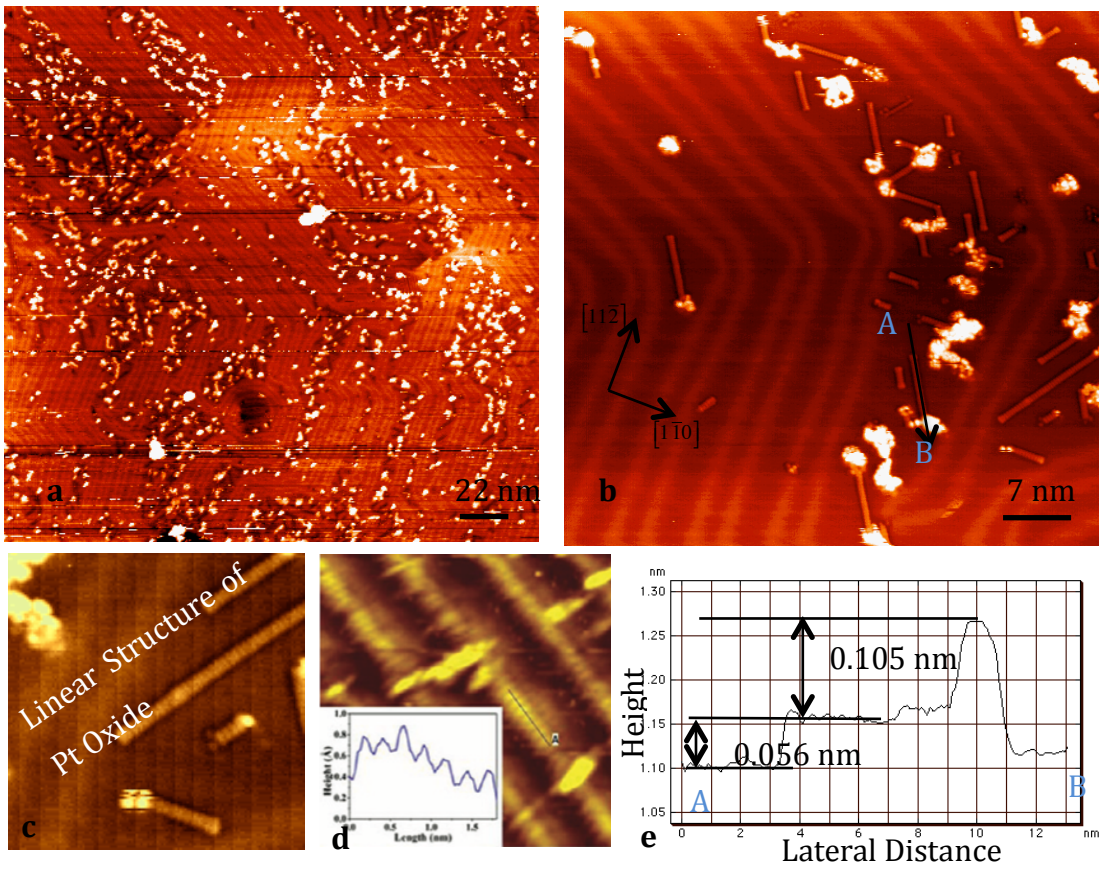

Figure I.4 Oxygen dosing through a hot Pt tube at 2.0×10^{-6} mbar. There are two types of Pt oxide. One is Pt oxide in a linear structure and the other is amorphous Pt oxide.

From STM observation, we cannot yet decide the structure and the index for each element in the Pt oxide. Other techniques for the detection of the chemical composition are needed to confirm the nature of the complexes observed.

II. Abbreviations

AFM	Atomic Force Microscopy
DSG	Double Sine Gordon
FCC	Face-Centred Cubic
FEL	Fast Entry Lock
FT	Fourier Transform
HCP	Hexagonal Close Packed
HOMO	Highest Occupied Molecular Orbital
HOPG	Highly Oriented Pyrolytic Graphite
HRARPES	High-Resolution Angle Resolved Photoemission Spectroscopy
HRHAS	High-Resolution Helium Atom Scattering
IPES	Inverse Photoemission Spectroscopy
K-cell	Knudsen cell
LEED	Low Energy Electron Diffraction
LHe	Liquid Helium
LN_2	Liquid Nitrogen
LT	Low Temperature
LUMO	Lowest Unoccupied Molecular Orbital
ML	Monolayer
NMR	Nuclear Magnetic Resonance
PBN	Pyrolytic Boron Nitride
PPM	Push and Pull Motion
STM	Scanning Tunneling Microscopy
STS	Scanning Tunneling Spectroscopy

TED	Transmission Electron Diffraction
TEM	Transmission Electron Microscope
TSP	Ti Sublimation Pump
VT	Variable Temperature
XPS	X-Ray Photoelectron Spectroscopy
UHV	Ultra High Vacuum

III. The Commensurability of the C_{60} Single Layer on Au(111)

n \ m	1	2	3	4	5
1	0.5022	0.2395	-0.0363	-0.3171	0.1998
2	0.2395	0.0043	-0.2529	0.2395	0.1025
3	-0.0363	-0.2529	-0.4935	0.1258	-0.0060
4	-0.3171	0.2395	0.1258	0.0043	-0.1224
5	0.1998	0.1025	-0.0060	-0.1224	-0.2446
6	0.0576	-0.0363	-0.1407	0.1648	0.0860
7	-0.0850	-0.1763	0.1484	0.0761	-0.0003
8	-0.2279	0.1219	0.0564	-0.0139	-0.0882
9	0.0860	0.0277	-0.0363	-0.1049	0.1170
10	-0.0094	-0.0669	-0.1296	0.1025	0.0494
11	-0.1049	-0.1616	0.0826	0.0333	-0.0187
12	0.0996	0.0576	0.0121	-0.0363	-0.0874
13	0.0279	-0.0137	-0.0585	-0.1062	0.0749
14	-0.0438	-0.0850	0.0966	0.0589	0.0194
15	-0.1155	0.0749	0.0398	0.0027	-0.0363
16	0.0502	0.0177	-0.0170	-0.0537	-0.0922
17	-0.0072	-0.0395	-0.0739	0.0748	0.0431
18	-0.0646	-0.0967	0.0576	0.0277	-0.0037
19	0.0649	0.0383	0.0101	-0.0196	-0.0506
20	0.0171	-0.0094	-0.0374	-0.0669	0.0592
21	-0.0308	-0.0572	0.0700	0.0450	0.0188
22	-0.0786	0.0529	0.0292	0.0043	-0.0216
23	0.0344	0.0120	-0.0116	-0.0363	-0.0620
24	-0.0066	-0.0290	-0.0525	0.0576	0.0353
25	-0.0477	-0.0699	0.0433	0.0220	-0.0002
26	0.0474	0.0279	0.0076	-0.0137	-0.0357

27	0.0115	-0.0079	-0.0282	-0.0493	0.0478
28	-0.0244	-0.0438	0.0542	0.0356	0.0162
29	-0.0603	0.0403	0.0224	0.0038	-0.0154
30	0.0256	0.0084	-0.0094	-0.0279	-0.0471
31	-0.0064	-0.0235	-0.0412	0.0463	0.0291
32	-0.0383	-0.0553	0.0342	0.0177	0.0006
33	0.0368	0.0215	0.0056	-0.0109	-0.0279
34	0.0081	-0.0072	-0.0231	-0.0395	0.0396
35	-0.0207	-0.0359	0.0439	0.0290	0.0136
36	-0.0494	0.0321	0.0178	0.0030	-0.0123
37	0.0199	0.0060	-0.0083	-0.0231	-0.0383
38	-0.0062	-0.0201	-0.0343	0.0383	0.0244
39	-0.0324	0.0410	0.0279	0.0145	0.0006
40	0.0297	0.0171	0.0040	-0.0094	-0.0232
41	0.0058	-0.0068	-0.0199	-0.0333	0.0335
42	-0.0182	-0.0308	0.0365	0.0242	0.0115
43	0.0380	0.0264	0.0144	0.0021	-0.0105
44	0.0159	0.0043	-0.0076	-0.0199	-0.0325
45	-0.0062	-0.0178	-0.0297	0.0325	0.0208
46	-0.0283	0.0344	0.0233	0.0120	0.0003
47	0.0246	0.0139	0.0028	-0.0085	-0.0201
48	0.0041	-0.0066	-0.0177	-0.0290	0.0288
49	-0.0164	-0.0271	0.0311	0.0205	0.0097
50	0.0322	0.0222	0.0119	0.0014	-0.0094

n \ **m**	6	7	8	9	10
1	0.0576	-0.0850	-0.2279	0.0860	-0.0094
2	-0.0363	-0.1763	0.1219	0.0277	-0.0669
3	-0.1407	0.1484	0.0564	-0.0363	-0.1296
4	0.1648	0.0761	-0.0139	-0.1049	0.1025
5	0.0860	-0.0003	-0.0882	0.1170	0.0494
6	0.0043	-0.0797	-0.1656	0.0604	-0.0060
7	-0.0797	-0.1616	0.0659	0.0017	-0.0634
8	-0.1656	0.0659	0.0043	-0.0585	-0.1224
9	0.0604	0.0017	-0.0585	-0.1201	0.0537
10	-0.0060	-0.0634	-0.1224	0.0537	0.0043
11	-0.0730	0.0966	0.0502	0.0027	-0.0458
12	0.0875	0.0433	-0.0023	-0.0490	-0.0967
13	0.0330	-0.0105	-0.0553	0.0823	0.0431
14	-0.0219	-0.0646	0.0761	0.0383	-0.0003

15	-0.0770	0.0674	0.0312	-0.0060	-0.0440
16	0.0564	0.0218	-0.0139	-0.0506	0.0673
17	0.0101	-0.0241	-0.0593	0.0610	0.0292
18	-0.0363	-0.0701	0.0529	0.0223	-0.0091
19	-0.0829	0.0432	0.0137	-0.0166	-0.0477
20	0.0318	0.0035	-0.0257	-0.0557	0.0494
21	-0.0083	-0.0363	-0.0652	0.0420	0.0154
22	-0.0485	0.0583	0.0333	0.0076	-0.0187
23	0.0474	0.0233	-0.0015	-0.0269	-0.0530
24	0.0121	-0.0117	-0.0363	-0.0616	0.0334
25	-0.0232	-0.0469	0.0478	0.0256	0.0028
26	-0.0585	0.0382	0.0167	-0.0054	-0.0279
27	0.0277	0.0069	-0.0144	-0.0363	0.0472
28	-0.0038	-0.0244	-0.0456	0.0394	0.0194
29	-0.0353	0.0498	0.0308	0.0114	-0.0084
30	0.0398	0.0215	0.0027	-0.0166	-0.0363
31	0.0114	-0.0068	-0.0255	-0.0447	0.0325
32	-0.0170	-0.0351	0.0421	0.0248	0.0071
33	-0.0455	0.0332	0.0164	-0.0008	-0.0184
34	0.0237	0.0074	-0.0093	-0.0264	-0.0439
35	-0.0022	-0.0184	-0.0350	0.0356	0.0197
36	-0.0281	-0.0442	0.0277	0.0121	-0.0037
37	0.0339	0.0191	0.0040	-0.0114	-0.0272
38	0.0101	-0.0046	-0.0196	-0.0349	0.0302
39	-0.0137	-0.0283	0.0370	0.0229	0.0085
40	-0.0374	0.0289	0.0152	0.0011	-0.0132
41	0.0204	0.0070	-0.0067	-0.0206	-0.0349
42	-0.0015	-0.0149	-0.0285	0.0320	0.0188
43	-0.0235	-0.0368	0.0246	0.0118	-0.0014
44	0.0292	0.0169	0.0043	-0.0085	-0.0216
45	0.0088	-0.0035	-0.0160	-0.0288	0.0277
46	-0.0116	-0.0238	0.0328	0.0209	0.0088
47	-0.0320	0.0254	0.0138	0.0019	-0.0101
48	0.0177	0.0064	-0.0052	-0.0170	-0.0290
49	-0.0014	-0.0127	-0.0242	0.0288	0.0175
50	-0.0204	-0.0317	0.0220	0.0110	-0.0002

n \ **m**	11	12	13	14	15
1	-0.1049	0.0996	0.0279	-0.0438	-0.1155
2	-0.1616	0.0576	-0.0137	-0.0850	0.0749

3	0.0826	0.0121	-0.0585	0.0966	0.0398
4	0.0333	-0.0363	-0.1062	0.0589	0.0027
5	-0.0187	-0.0874	0.0749	0.0194	-0.0363
6	-0.0730	0.0875	0.0330	-0.0219	-0.0770
7	0.0966	0.0433	-0.0105	-0.0646	0.0674
8	0.0502	-0.0023	-0.0553	0.0761	0.0312
9	0.0027	-0.0490	0.0823	0.0383	-0.0060
10	-0.0458	-0.0967	0.0431	-0.0003	-0.0440
11	-0.0952	0.0455	0.0032	-0.0396	-0.0829
12	0.0455	0.0043	-0.0374	-0.0797	0.0379
13	0.0032	-0.0374	-0.0786	0.0397	0.0035
14	-0.0396	-0.0797	0.0397	0.0043	-0.0314
15	-0.0829	0.0379	0.0035	-0.0314	-0.0668
16	0.0344	0.0009	-0.0331	-0.0676	0.0353
17	-0.0033	-0.0363	-0.0699	0.0339	0.0037
18	-0.0412	0.0604	0.0313	0.0017	-0.0282
19	0.0556	0.0273	-0.0015	-0.0307	-0.0603
20	0.0220	-0.0060	-0.0345	0.0548	0.0287
21	-0.0117	-0.0394	0.0510	0.0256	-0.0003
22	-0.0456	0.0462	0.0214	-0.0038	-0.0294
23	0.0403	0.0162	-0.0084	-0.0334	0.0472
24	0.0100	-0.0139	-0.0383	0.0433	0.0206
25	-0.0205	-0.0442	0.0385	0.0164	-0.0060
26	-0.0510	0.0330	0.0114	-0.0105	-0.0327
27	0.0266	0.0056	-0.0158	-0.0375	0.0367
28	-0.0010	-0.0219	-0.0431	0.0321	0.0122
29	-0.0287	-0.0494	0.0269	0.0074	-0.0123
30	0.0396	0.0209	0.0019	-0.0174	-0.0370
31	0.0143	-0.0042	-0.0231	-0.0422	0.0268
32	-0.0110	-0.0294	0.0392	0.0218	0.0040
33	-0.0363	0.0333	0.0162	-0.0011	-0.0187
34	0.0268	0.0101	-0.0068	-0.0241	-0.0416
35	0.0035	-0.0131	-0.0299	0.0335	0.0174
36	-0.0199	-0.0363	0.0279	0.0122	-0.0037
37	0.0370	0.0219	0.0065	-0.0091	-0.0249
38	0.0154	0.0004	-0.0149	-0.0304	0.0285
39	-0.0062	-0.0211	-0.0363	0.0233	0.0088
40	-0.0278	0.0318	0.0178	0.0035	-0.0110
41	0.0255	0.0118	-0.0022	-0.0164	-0.0308
42	0.0054	-0.0083	-0.0222	0.0328	0.0194

43	-0.0147	-0.0284	0.0273	0.0142	0.0008
44	-0.0349	0.0214	0.0086	-0.0045	-0.0177
45	0.0153	0.0027	-0.0101	-0.0231	0.0284
46	-0.0036	-0.0161	-0.0289	0.0233	0.0110
47	-0.0224	0.0298	0.0179	0.0058	-0.0065
48	0.0238	0.0121	0.0003	-0.0117	-0.0240
49	0.0061	-0.0055	-0.0173	-0.0293	0.0198
50	-0.0116	-0.0232	0.0260	0.0147	0.0033

n \ **m**	16	17	18	19	20
1	0.0502	-0.0072	-0.0646	0.0649	0.0171
2	0.0177	-0.0395	-0.0967	0.0383	-0.0094
3	-0.0170	-0.0739	0.0576	0.0101	-0.0374
4	-0.0537	0.0748	0.0277	-0.0196	-0.0669
5	-0.0922	0.0431	-0.0037	-0.0506	0.0592
6	0.0564	0.0101	-0.0363	-0.0829	0.0318
7	0.0218	-0.0241	-0.0701	0.0432	0.0035
8	-0.0139	-0.0593	0.0529	0.0137	-0.0257
9	-0.0506	0.0610	0.0223	-0.0166	-0.0557
10	0.0673	0.0292	-0.0091	-0.0477	0.0494
11	0.0344	-0.0033	-0.0412	0.0556	0.0220
12	0.0009	-0.0363	0.0604	0.0273	-0.0060
13	-0.0331	-0.0699	0.0313	-0.0015	-0.0345
14	-0.0676	0.0339	0.0017	-0.0307	0.0548
15	0.0353	0.0037	-0.0282	-0.0603	0.0287
16	0.0043	-0.0269	-0.0585	0.0308	0.0023
17	-0.0269	-0.0579	0.0319	0.0038	-0.0244
18	-0.0585	0.0319	0.0043	-0.0235	-0.0515
19	0.0308	0.0038	-0.0235	-0.0510	0.0291
20	0.0023	-0.0244	-0.0515	0.0291	0.0043
21	-0.0264	-0.0529	0.0283	0.0039	-0.0207
22	-0.0553	0.0266	0.0027	-0.0215	-0.0458
23	0.0240	0.0006	-0.0231	-0.0470	0.0262
24	-0.0023	-0.0255	-0.0490	0.0248	0.0030
25	-0.0287	0.0439	0.0227	0.0012	-0.0204
26	0.0407	0.0199	-0.0011	-0.0224	-0.0439
27	0.0164	-0.0042	-0.0251	0.0410	0.0215
28	-0.0079	-0.0284	0.0383	0.0191	-0.0003
29	-0.0324	0.0351	0.0162	-0.0028	-0.0221
30	0.0312	0.0127	-0.0060	-0.0249	0.0363

31	0.0087	-0.0097	-0.0283	0.0335	0.0159
32	-0.0139	-0.0322	0.0302	0.0130	-0.0045
33	-0.0366	0.0264	0.0095	-0.0076	-0.0249
34	0.0222	0.0056	-0.0113	-0.0283	0.0292
35	0.0011	-0.0154	-0.0321	0.0259	0.0101
36	-0.0199	-0.0363	0.0223	0.0067	-0.0091
37	0.0333	0.0182	0.0028	-0.0127	-0.0284
38	0.0137	-0.0014	-0.0166	-0.0320	0.0222
39	-0.0060	-0.0210	0.0330	0.0186	0.0041
40	-0.0257	0.0288	0.0147	0.0005	-0.0139
41	0.0243	0.0104	-0.0036	-0.0177	-0.0321
42	0.0058	-0.0079	-0.0219	0.0288	0.0154
43	-0.0127	-0.0264	0.0248	0.0116	-0.0016
44	-0.0312	0.0205	0.0076	-0.0055	-0.0187
45	0.0159	0.0032	-0.0097	-0.0227	0.0251
46	-0.0015	-0.0141	-0.0269	0.0213	0.0089
47	-0.0189	0.0292	0.0172	0.0050	-0.0072
48	0.0246	0.0128	0.0009	-0.0112	-0.0234
49	0.0082	-0.0035	-0.0154	-0.0275	0.0181
50	-0.0082	-0.0199	0.0256	0.0142	0.0028

n \ m	21	22	23	24	25
1	-0.0308	-0.0786	0.0344	-0.0066	-0.0477
2	-0.0572	0.0529	0.0120	-0.0290	-0.0699
3	0.0700	0.0292	-0.0116	-0.0525	0.0433
4	0.0450	0.0043	-0.0363	0.0576	0.0220
5	0.0188	-0.0216	-0.0620	0.0353	-0.0002
6	-0.0083	-0.0485	0.0474	0.0121	-0.0232
7	-0.0363	0.0583	0.0233	-0.0117	-0.0469
8	-0.0652	0.0333	-0.0015	-0.0363	0.0478
9	0.0420	0.0076	-0.0269	-0.0616	0.0256
10	0.0154	-0.0187	-0.0530	0.0334	0.0028
11	-0.0117	-0.0456	0.0403	0.0100	-0.0205
12	-0.0394	0.0462	0.0162	-0.0139	-0.0442
13	0.0510	0.0214	-0.0084	-0.0383	0.0385
14	0.0256	-0.0038	-0.0334	0.0433	0.0164
15	-0.0003	-0.0294	0.0472	0.0206	-0.0060
16	-0.0264	-0.0553	0.0240	-0.0023	-0.0287
17	-0.0529	0.0266	0.0006	-0.0255	0.0439
18	0.0283	0.0027	-0.0231	-0.0490	0.0227

19	0.0039	-0.0215	-0.0470	0.0248	0.0012
20	-0.0207	-0.0458	0.0262	0.0030	-0.0204
21	-0.0455	0.0269	0.0040	-0.0191	-0.0422
22	0.0269	0.0043	-0.0184	-0.0413	0.0244
23	0.0040	-0.0184	-0.0409	0.0250	0.0040
24	-0.0191	-0.0413	0.0250	0.0043	-0.0165
25	-0.0422	0.0244	0.0040	-0.0165	-0.0372
26	0.0232	0.0032	-0.0170	-0.0374	0.0234
27	0.0017	-0.0182	-0.0383	0.0229	0.0041
28	-0.0199	-0.0396	0.0219	0.0033	-0.0154
29	-0.0416	0.0204	0.0021	-0.0163	-0.0349
30	0.0184	0.0004	-0.0178	-0.0361	0.0208
31	-0.0018	-0.0197	-0.0377	0.0195	0.0024
32	-0.0221	0.0344	0.0178	0.0009	-0.0160
33	0.0320	0.0156	-0.0009	-0.0177	-0.0345
34	0.0130	-0.0033	-0.0197	0.0328	0.0171
35	-0.0060	-0.0222	0.0307	0.0153	-0.0003
36	-0.0251	0.0282	0.0130	-0.0023	-0.0177
37	0.0254	0.0104	-0.0047	-0.0199	0.0294
38	0.0075	-0.0074	-0.0224	0.0273	0.0130
39	-0.0105	-0.0253	0.0248	0.0107	-0.0036
40	-0.0285	0.0220	0.0081	-0.0060	-0.0202
41	0.0189	0.0051	-0.0087	-0.0227	0.0242
42	0.0019	-0.0117	-0.0255	0.0217	0.0085
43	-0.0151	-0.0287	0.0189	0.0059	-0.0072
44	0.0286	0.0159	0.0030	-0.0099	-0.0230
45	0.0125	-0.0001	-0.0129	-0.0258	0.0189
46	-0.0035	-0.0161	-0.0289	0.0162	0.0039
47	-0.0196	0.0252	0.0132	0.0011	-0.0110
48	0.0218	0.0100	-0.0019	-0.0139	-0.0261
49	0.0065	-0.0052	-0.0171	0.0251	0.0137
50	-0.0088	-0.0205	0.0221	0.0108	-0.0006

n \ **m**	26	27	28	29	30
1	0.0474	0.0115	-0.0244	-0.0603	0.0256
2	0.0279	-0.0079	-0.0438	0.0403	0.0084
3	0.0076	-0.0282	0.0542	0.0224	-0.0094
4	-0.0137	-0.0493	0.0356	0.0038	-0.0279
5	-0.0357	0.0478	0.0162	-0.0154	-0.0471
6	-0.0585	0.0277	-0.0038	-0.0353	0.0398

7	0.0382	0.0069	-0.0244	0.0498	0.0215
8	0.0167	-0.0144	-0.0456	0.0308	0.0027
9	-0.0054	-0.0363	0.0394	0.0114	-0.0166
10	-0.0279	0.0472	0.0194	-0.0084	-0.0363
11	-0.0510	0.0266	-0.0010	-0.0287	0.0396
12	0.0330	0.0056	-0.0219	-0.0494	0.0209
13	0.0114	-0.0158	-0.0431	0.0269	0.0019
14	-0.0105	-0.0375	0.0321	0.0074	-0.0174
15	-0.0327	0.0367	0.0122	-0.0123	-0.0370
16	0.0407	0.0164	-0.0079	-0.0324	0.0312
17	0.0199	-0.0042	-0.0284	0.0351	0.0127
18	-0.0011	-0.0251	0.0383	0.0162	-0.0060
19	-0.0224	0.0410	0.0191	-0.0028	-0.0249
20	-0.0439	0.0215	-0.0003	-0.0221	0.0363
21	0.0232	0.0017	-0.0199	-0.0416	0.0184
22	0.0032	-0.0182	-0.0396	0.0204	0.0004
23	-0.0170	-0.0383	0.0219	0.0021	-0.0178
24	-0.0374	0.0229	0.0033	-0.0163	-0.0361
25	0.0234	0.0041	-0.0154	-0.0349	0.0208
26	0.0043	-0.0149	-0.0342	0.0216	0.0035
27	-0.0149	-0.0340	0.0221	0.0041	-0.0139
28	-0.0342	0.0221	0.0043	-0.0135	-0.0314
29	0.0216	0.0041	-0.0135	-0.0312	0.0209
30	0.0035	-0.0139	-0.0314	0.0209	0.0043
31	-0.0147	-0.0320	0.0205	0.0041	-0.0123
32	-0.0331	0.0198	0.0036	-0.0127	-0.0290
33	0.0186	0.0027	-0.0134	-0.0296	0.0195
34	0.0014	-0.0145	-0.0305	0.0189	0.0037
35	-0.0159	-0.0317	0.0179	0.0029	-0.0122
36	-0.0333	0.0166	0.0017	-0.0132	-0.0282
37	0.0149	0.0003	-0.0145	-0.0293	0.0172
38	-0.0015	-0.0160	-0.0307	0.0160	0.0020
39	-0.0179	0.0283	0.0146	0.0007	-0.0132
40	0.0264	0.0128	-0.0008	-0.0146	-0.0284
41	0.0108	-0.0027	-0.0163	0.0273	0.0142
42	-0.0048	-0.0182	0.0256	0.0127	-0.0003
43	-0.0205	0.0236	0.0109	-0.0019	-0.0148
44	0.0214	0.0088	-0.0038	-0.0166	0.0248
45	0.0065	-0.0060	-0.0186	0.0230	0.0109
46	-0.0084	-0.0208	0.0210	0.0091	-0.0030

47	-0.0233	0.0188	0.0070	-0.0049	-0.0169
48	0.0164	0.0047	-0.0071	-0.0190	0.0206
49	0.0021	-0.0095	-0.0212	0.0186	0.0073
50	-0.0121	-0.0237	0.0164	0.0053	-0.0060

n \ m	31	32	33	34	35
1	-0.0064	-0.0383	0.0368	0.0081	-0.0207
2	-0.0235	-0.0553	0.0215	-0.0072	-0.0359
3	-0.0412	0.0342	0.0056	-0.0231	0.0439
4	0.0463	0.0177	-0.0109	-0.0395	0.0290
5	0.0291	0.0006	-0.0279	0.0396	0.0136
6	0.0114	-0.0170	-0.0455	0.0237	-0.0022
7	-0.0068	-0.0351	0.0332	0.0074	-0.0184
8	-0.0255	0.0421	0.0164	-0.0093	-0.0350
9	-0.0447	0.0248	-0.0008	-0.0264	0.0356
10	0.0325	0.0071	-0.0184	-0.0439	0.0197
11	0.0143	-0.0110	-0.0363	0.0268	0.0035
12	-0.0042	-0.0294	0.0333	0.0101	-0.0131
13	-0.0231	0.0392	0.0162	-0.0068	-0.0299
14	-0.0422	0.0218	-0.0011	-0.0241	0.0335
15	0.0268	0.0040	-0.0187	-0.0416	0.0174
16	0.0087	-0.0139	-0.0366	0.0222	0.0011
17	-0.0097	-0.0322	0.0264	0.0056	-0.0154
18	-0.0283	0.0302	0.0095	-0.0113	-0.0321
19	0.0335	0.0130	-0.0076	-0.0283	0.0259
20	0.0159	-0.0045	-0.0249	0.0292	0.0101
21	-0.0018	-0.0221	0.0320	0.0130	-0.0060
22	-0.0197	0.0344	0.0156	-0.0033	-0.0222
23	-0.0377	0.0178	-0.0009	-0.0197	0.0307
24	0.0195	0.0009	-0.0177	0.0328	0.0153
25	0.0024	-0.0160	-0.0345	0.0171	-0.0003
26	-0.0147	-0.0331	0.0186	0.0014	-0.0159
27	-0.0320	0.0198	0.0027	-0.0145	-0.0317
28	0.0205	0.0036	-0.0134	-0.0305	0.0179
29	0.0041	-0.0127	-0.0296	0.0189	0.0029
30	-0.0123	-0.0290	0.0195	0.0037	-0.0122
31	-0.0289	0.0198	0.0042	-0.0116	-0.0274
32	0.0198	0.0043	-0.0113	-0.0269	0.0186
33	0.0042	-0.0113	-0.0268	0.0189	0.0042
34	-0.0116	-0.0269	0.0189	0.0043	-0.0103

35	-0.0274	0.0186	0.0042	-0.0103	-0.0250
36	0.0181	0.0038	-0.0106	-0.0251	0.0181
37	0.0030	-0.0112	-0.0255	0.0179	0.0042
38	-0.0120	-0.0262	0.0173	0.0038	-0.0098
39	-0.0272	0.0166	0.0032	-0.0103	-0.0238
40	0.0155	0.0023	-0.0110	-0.0244	0.0167
41	0.0011	-0.0121	-0.0253	0.0160	0.0033
42	-0.0133	-0.0264	0.0151	0.0025	-0.0102
43	0.0263	0.0139	0.0015	-0.0111	-0.0237
44	0.0125	0.0002	-0.0122	-0.0247	0.0147
45	-0.0013	-0.0136	-0.0259	0.0136	0.0017
46	-0.0151	0.0240	0.0123	0.0006	-0.0112
47	0.0224	0.0109	-0.0007	-0.0124	-0.0242
48	0.0092	-0.0023	-0.0139	0.0233	0.0122
49	-0.0040	-0.0155	0.0219	0.0108	-0.0003
50	-0.0173	0.0203	0.0093	-0.0017	-0.0127

n \ **m**	36	37	38	39	40
1	-0.0494	0.0199	-0.0062	-0.0324	0.0297
2	0.0321	0.0060	-0.0201	0.0410	0.0171
3	0.0178	-0.0083	-0.0343	0.0279	0.0040
4	0.0030	-0.0231	0.0383	0.0145	-0.0094
5	-0.0123	-0.0383	0.0244	0.0006	-0.0232
6	-0.0281	0.0339	0.0101	-0.0137	-0.0374
7	-0.0442	0.0191	-0.0046	-0.0283	0.0289
8	0.0277	0.0040	-0.0196	0.0370	0.0152
9	0.0121	-0.0114	-0.0349	0.0229	0.0011
10	-0.0037	-0.0272	0.0302	0.0085	-0.0132
11	-0.0199	0.0370	0.0154	-0.0062	-0.0278
12	-0.0363	0.0219	0.0004	-0.0211	0.0318
13	0.0279	0.0065	-0.0149	-0.0363	0.0178
14	0.0122	-0.0091	-0.0304	0.0233	0.0035
15	-0.0037	-0.0249	0.0285	0.0088	-0.0110
16	-0.0199	0.0333	0.0137	-0.0060	-0.0257
17	-0.0363	0.0182	-0.0014	-0.0210	0.0288
18	0.0223	0.0028	-0.0166	0.0330	0.0147
19	0.0067	-0.0127	-0.0320	0.0186	0.0005
20	-0.0091	-0.0284	0.0222	0.0041	-0.0139
21	-0.0251	0.0254	0.0075	-0.0105	-0.0285
22	0.0282	0.0104	-0.0074	-0.0253	0.0220

23	0.0130	-0.0047	-0.0224	0.0248	0.0081
24	-0.0023	-0.0199	0.0273	0.0107	-0.0060
25	-0.0177	0.0294	0.0130	-0.0036	-0.0202
26	-0.0333	0.0149	-0.0015	-0.0179	0.0264
27	0.0166	0.0003	-0.0160	0.0283	0.0128
28	0.0017	-0.0145	-0.0307	0.0146	-0.0008
29	-0.0132	-0.0293	0.0160	0.0007	-0.0146
30	-0.0282	0.0172	0.0020	-0.0132	-0.0284
31	0.0181	0.0030	-0.0120	-0.0272	0.0155
32	0.0038	-0.0112	-0.0262	0.0166	0.0023
33	-0.0106	-0.0255	0.0173	0.0032	-0.0110
34	-0.0251	0.0179	0.0038	-0.0103	-0.0244
35	0.0181	0.0042	-0.0098	-0.0238	0.0167
36	0.0043	-0.0095	-0.0235	0.0172	0.0039
37	-0.0095	-0.0233	0.0174	0.0042	-0.0090
38	-0.0235	0.0174	0.0043	-0.0088	-0.0220
39	0.0172	0.0042	-0.0088	-0.0219	0.0167
40	0.0039	-0.0090	-0.0220	0.0167	0.0043
41	-0.0095	-0.0223	0.0165	0.0042	-0.0081
42	-0.0229	0.0161	0.0039	-0.0083	-0.0207
43	0.0155	0.0034	-0.0088	-0.0210	0.0160
44	0.0027	-0.0094	-0.0215	0.0156	0.0040
45	-0.0102	-0.0222	0.0150	0.0035	-0.0081
46	-0.0231	0.0143	0.0028	-0.0087	-0.0202
47	0.0133	0.0020	-0.0094	-0.0208	0.0146
48	0.0009	-0.0103	-0.0217	0.0139	0.0030
49	-0.0114	-0.0227	0.0130	0.0022	-0.0087
50	0.0227	0.0120	0.0012	-0.0095	-0.0204

n \ **m**	41	42	3	44	45
1	0.0058	-0.0182	0.0380	0.0159	-0.0062
2	-0.0068	-0.0308	0.0264	0.0043	-0.0178
3	-0.0199	0.0365	0.0144	-0.0076	-0.0297
4	-0.0333	0.0242	0.0021	-0.0199	0.0325
5	0.0335	0.0115	-0.0105	-0.0325	0.0208
6	0.0204	-0.0015	-0.0235	0.0292	0.0088
7	0.0070	-0.0149	-0.0368	0.0169	-0.0035
8	-0.0067	-0.0285	0.0246	0.0043	-0.0160
9	-0.0206	0.0320	0.0118	-0.0085	-0.0288
10	-0.0349	0.0188	-0.0014	-0.0216	0.0277

11	0.0255	0.0054	-0.0147	-0.0349	0.0153
12	0.0118	-0.0083	-0.0284	0.0214	0.0027
13	-0.0022	-0.0222	0.0273	0.0086	-0.0101
14	-0.0164	0.0328	0.0142	-0.0045	-0.0231
15	-0.0308	0.0194	0.0008	-0.0177	0.0284
16	0.0243	0.0058	-0.0127	-0.0312	0.0159
17	0.0104	-0.0079	-0.0264	0.0205	0.0032
18	-0.0036	-0.0219	0.0248	0.0076	-0.0097
19	-0.0177	0.0288	0.0116	-0.0055	-0.0227
20	-0.0321	0.0154	-0.0016	-0.0187	0.0251
21	0.0189	0.0019	-0.0151	0.0286	0.0125
22	0.0051	-0.0117	-0.0287	0.0159	-0.0001
23	-0.0087	-0.0255	0.0189	0.0030	-0.0129
24	-0.0227	0.0217	0.0059	-0.0099	-0.0258
25	0.0242	0.0085	-0.0072	-0.0230	0.0189
26	0.0108	-0.0048	-0.0205	0.0214	0.0065
27	-0.0027	-0.0182	0.0236	0.0088	-0.0060
28	-0.0163	0.0256	0.0109	-0.0038	-0.0186
29	0.0273	0.0127	-0.0019	-0.0166	0.0230
30	0.0142	-0.0003	-0.0148	0.0248	0.0109
31	0.0011	-0.0133	0.0263	0.0125	-0.0013
32	-0.0121	-0.0264	0.0139	0.0002	-0.0136
33	-0.0253	0.0151	0.0015	-0.0122	-0.0259
34	0.0160	0.0025	-0.0111	-0.0247	0.0136
35	0.0033	-0.0102	-0.0237	0.0147	0.0017
36	-0.0095	-0.0229	0.0155	0.0027	-0.0102
37	-0.0223	0.0161	0.0034	-0.0094	-0.0222
38	0.0165	0.0039	-0.0088	-0.0215	0.0150
39	0.0042	-0.0083	-0.0210	0.0156	0.0035
40	-0.0081	-0.0207	0.0160	0.0040	-0.0081
41	-0.0206	0.0162	0.0042	-0.0077	-0.0197
42	0.0162	0.0043	-0.0075	-0.0195	0.0154
43	0.0042	-0.0075	-0.0194	0.0156	0.0042
44	-0.0077	-0.0195	0.0156	0.0043	-0.0070
45	-0.0197	0.0154	0.0042	-0.0070	-0.0183
46	0.0151	0.0040	-0.0072	-0.0184	0.0151
47	0.0036	-0.0075	-0.0186	0.0150	0.0043
48	-0.0080	-0.0191	0.0147	0.0040	-0.0067
49	-0.0196	0.0142	0.0036	-0.0070	-0.0176
50	0.0135	0.0031	-0.0074	-0.0180	0.0142

n \ m	46	47	48	49	50
1	-0.0283	0.0246	0.0041	-0.0164	0.0322
2	0.0344	0.0139	-0.0066	-0.0271	0.0222
3	0.0233	0.0028	-0.0177	0.0311	0.0119
4	0.0120	-0.0085	-0.0290	0.0205	0.0014
5	0.0003	-0.0201	0.0288	0.0097	-0.0094
6	-0.0116	-0.0320	0.0177	-0.0014	-0.0204
7	-0.0238	0.0254	0.0064	-0.0127	-0.0317
8	0.0328	0.0138	-0.0052	-0.0242	0.0220
9	0.0209	0.0019	-0.0170	0.0288	0.0110
10	0.0088	-0.0101	-0.0290	0.0175	-0.0002
11	-0.0036	-0.0224	0.0238	0.0061	-0.0116
12	-0.0161	0.0298	0.0121	-0.0055	-0.0232
13	-0.0289	0.0179	0.0003	-0.0173	0.0260
14	0.0233	0.0058	-0.0117	-0.0293	0.0147
15	0.0110	-0.0065	-0.0240	0.0198	0.0033
16	-0.0015	-0.0189	0.0246	0.0082	-0.0082
17	-0.0141	0.0292	0.0128	-0.0035	-0.0199
18	-0.0269	0.0172	0.0009	-0.0154	0.0256
19	0.0213	0.0050	-0.0112	-0.0275	0.0142
20	0.0089	-0.0072	-0.0234	0.0181	0.0028
21	-0.0035	-0.0196	0.0218	0.0065	-0.0088
22	-0.0161	0.0252	0.0100	-0.0052	-0.0205
23	-0.0289	0.0132	-0.0019	-0.0171	0.0221
24	0.0162	0.0011	-0.0139	0.0251	0.0108
25	0.0039	-0.0110	-0.0261	0.0137	-0.0006
26	-0.0084	-0.0233	0.0164	0.0021	-0.0121
27	-0.0208	0.0188	0.0047	-0.0095	-0.0237
28	0.0210	0.0070	-0.0071	-0.0212	0.0164
29	0.0091	-0.0049	-0.0190	0.0186	0.0053
30	-0.0030	-0.0169	0.0206	0.0073	-0.0060
31	-0.0151	0.0224	0.0092	-0.0040	-0.0173
32	0.0240	0.0109	-0.0023	-0.0155	0.0203
33	0.0123	-0.0007	-0.0139	0.0219	0.0093
34	0.0006	-0.0124	0.0233	0.0108	-0.0017
35	-0.0112	-0.0242	0.0122	-0.0003	-0.0127
36	-0.0231	0.0133	0.0009	-0.0114	0.0227
37	0.0143	0.0020	-0.0103	-0.0227	0.0120
38	0.0028	-0.0094	-0.0217	0.0130	0.0012

39	-0.0087	-0.0208	0.0139	0.0022	-0.0095
40	-0.0202	0.0146	0.0030	-0.0087	-0.0204
41	0.0151	0.0036	-0.0080	-0.0196	0.0135
42	0.0040	-0.0075	-0.0191	0.0142	0.0031
43	-0.0072	-0.0186	0.0147	0.0036	-0.0074
44	-0.0184	0.0150	0.0040	-0.0070	-0.0180
45	0.0151	0.0043	-0.0067	-0.0176	0.0142
46	0.0043	-0.0065	-0.0174	0.0145	0.0040
47	-0.0065	-0.0173	0.0147	0.0043	-0.0062
48	-0.0174	0.0147	0.0043	-0.0061	-0.0165
49	0.0145	0.0043	-0.0061	-0.0164	0.0143
50	0.0040	-0.0062	-0.0165	0.0143	0.0043

References

[i] J. Inukai, D. A. Tryk, T. Abe, M. Wakisaka, H. Uchida, and M. Watanabe. Direct STM Elucidation of the Effects of Atomic-Level Structure on Pt(111) Electrodes for Dissolved CO Oxidation. J. Am. Chem. Soc. **135**, 1476 (2013).

[ii] D. J. miller, H. Öberg, L.-Å. Näslund, T. Anniyev, H. Ogasawara. L. G. M. Pettersson, and A. Nilsson. Low O_2 Dissociation Barrier on Pt(111) Due to Adsorbate-Adsorbate Interactions. J. Chem. Phys. **133**, 224701 (2010).

[iii] J. G. Wang, W. X. Li, M. Borg, J. Gustafson, A. Mikkelsen, T. M. Pedersen, E. Lundgren, J. Weissenrieder, J. Klilovits, M. Schmid, B. Hammer, and J. N. Andersen. One-Dimensional PtO_2 at Pt Steps: Formation and Reaction with CO. Phys. Rev. Lett. **95**, 256102 (2005).

[iv] Z. Zhu, F. Tao, F. Zheng, R. Chang, Y. Li, L. Heinke, Z. Liu, M. Salmeron, and G. A. Somorjai. Formation of Nanometer-Sized Surface Platinum Oxide Clusters on A Stepped Pt(558) Single Crystal Surface Induced by Oxygen: A High-Pressure STM and Ambient-Pressure XPS Study. Nano Lett. **12**, 1491 (2012).

[v] M. Ø. Pedersen, S. Helveg, A. Ruban, I. Stensgaard, E. Lægsgaard, J. K. Nørskov, F. Besenbacher. How A Gold Substrate Can Increase the Reactivity of A Pt Overlayer. Surf. Sci. **426**, 395 (1999).